Investigation of Metalloid Additives for Nuclear Metal Fuels to Mitigate Neodymium Interactions with the Cladding Alloy HT9

A Dissertation

Presented in Partial Fulfillment of the Requirement for the

Degree of Doctor of Philosophy

with a

Major in Materials Science and Engineering

in the

College of Graduate Studies

by

Nathan D. Jerred

Major Professor: Indrajit Charit, Ph.D.

Committee Members: Samrat Choudhury, Ph.D.; Michael T. Benson, Ph.D.;

Haiyan Zhao, Ph.D.

Department Administrator: Mark Roll, Ph.D.

August 2021

Authorization to Submit Dissertation

This dissertation of Nathan D. Jerred, submitted for the degree of Doctor of Philosophy with a Major in Materials Science and Engineering and titled "Investigation of Metalloid Additives for Nuclear Metal Fuels to Mitigate Neodymium Interactions with the Cladding Alloy HT9," has been reviewed in final form. Permission, as indicated by the signatures and dates below, is now granted to submit final copies to the College of Graduate Studies for approval.

Major Professor: Indrajit Charit — Date: 7/12/2021
Indrajit Charit, Ph.D.

Committee Members: Schoudhury — Date: 7/13/2021
Samrat Choudhury, Ph.D.

Michael T. Benson — Date: 7-12-21
Michael T. Benson, Ph.D.

Haiyan Zhao — Date: 7/12/21
Haiyan Zhao, Ph.D.

Department Administrator: Mark R Roll — Date: 7/14/2021
Mark Roll, Ph.D.

Abstract

The metalloid elements: antimony (Sb), tellurium (Te), and arsenic (As); along with the nonmetal element selenium (Se), are evaluated as fuel-based additives to mitigate the deleterious effects from chemical interactions that have been observed to occur at the fuel-cladding interface of the U-Zr metallic fuel system; a phenomenon known as fuel-cladding chemical interaction (FCCI). Lanthanide fission products, neodymium (Nd), cerium (Ce), praseodymium (Pr), and lanthanum (La), have been found to exhibit a high rate of interdiffusion with the primary cladding constituents, iron (Fe), chromium (Cr), and nickel (Ni). The FCCI phenomenon has been found to adversely affect the performance of metallic fuels due to the formation of both brittle and low-melting intermetallic phases. The formation of such phases leads to a loss of cladding wall integrity and can eventually lead to cladding failure. Alloying fuels with additives that will bind with and form high temperature stable compounds with lanthanide fission products, effectively stabilizing them within the fuel structure, has the potential to mitigate the major effects of the FCCI phenomenon.

This research focuses on the efficacy of Sb, Te, and As additives and their stabilizing effects on the lanthanide Nd and ameliorate its interaction with the cladding alloy HT9. To evaluate the additive interactions and additive-lanthanide interactions within the U-Zr fuel structure, both U-10Zr-X and U-10Zr-X-Nd (wt.%) alloys, where ‘X’ denotes the additive, are fabricated. It is observed that X-Nd compounds preferentially form at a 1:1 atomic ratio within the U-Zr system. The ability of the additives to bind with Nd and alleviate its participation in FCCI is evaluated through isothermal diffusion couple studies carried out between U-10Zr-X-Nd alloys and the cladding alloy HT9 at temperatures up to 675°C. Although Fe is observed to diffuse to some degree into several of the additive-containing fuel alloys, Fe and Cr interaction with X-Nd phases was not observed. Further, atomistic models predicted both As and Se to be effective additives and further research on As found that within the U-Zr-As-Nd alloy the NdAs compound preferentially formed. Subsequent diffusion experiments between U-Zr-As-Nd against HT9 found the NdAs phase remains stable and no interaction with Fe or Cr was observed.

Acknowledgements

First, I would like to express my profound gratitude to my advisor, Dr. Indrajit Charit. I am deeply grateful for his guidance, encouragement and confidence through this academic journey and greatly appreciate the opportunity to work on such a fascinating project. I would like to thank my committee members, Dr. Samrat Choudhury, Dr. Michael Benson, and Dr. Haiyan Zhao as well, for their commitment and guidance through my research. I would like to acknowledge Dr. Rabi Khanal, for his support and his modeling work which helped to drive my own research work. I am also equally grateful for the academic support provided by Alice Allen and numerous others at the University of Idaho's Idaho Falls campus over the course of my academic journey.

I would like to offer my sincere thanks to various staff members of the Center for Advanced Energy Studies (CAES), both former and current, for their support in the execution of my experimental work at the facility; they include Kristi Moser-McIntire, Jatu Burns, Megha Dubey, Mason Jaussi, Bryan Forsmann, Jeremy Burgener, and Yaqiao Wu.

I wish to thank the support I received from Dr. J. Stephen Herring, director of the Center for Space Nuclear Research (CSNR), Tim Hyde, director of the Fuel Fabrication division of Idaho National Laboratory (INL), and Patrick Hogan, manager of the Advanced Fuel Manufacturing and Development department of INL's Fuel Fabrication division; the support and encouragement received from each of you was of tremendous help to me in accomplishing this goal.

Finally, I would like to acknowledge the funding support to accomplish this work was provided by the U.S. Dept. of Energy's Nuclear Energy University Programs (NEUP) under contract DE-NE0008557. Beyond the financial support, this research made use of resources located at the CAES facility, Materials and Fuel Complex (MFC) of INL and that of the High-Performance Computing center (HPC) of INL which is supported by the Office of Nuclear Energy of the U.S. Dept. of Energy under Contract No. DE-AC07-05ID14517.

Dedication

This dissertation is dedicated to my wife and daughters.

To my beautiful wife, Sara, if not for your continuous support, encouragement and sacrifice this work would have remained beyond reach.

To my wonderful daughters, Scarlett, Eden and Delaney, you have been my greatest cheerleaders your continuous praise kept me going. I hope that you will always have inquisitive minds and never cease learning.

A special thanks to family and friends, I am extremely grateful for your support of both me and my girls through this long journey

Publication of Chapters

The following dissertation is comprised of research carried out under a Nuclear Energy University Program (NEUP) funded project. A primary goal of this research was to periodically publish the research work. To that end, this dissertation is comprised of the following publications:

I. **N.D. Jerred**, R. Khanal, M.T. Benson, E.E. Perez, J.A. King, M. Dubey, J. Burns, I. Charit, S. Choudhury, and Robert D. Mariani, "Evaluation of Tellurium as a Fuel Additive in Neodymium-Containing U-Zr Metallic Fuel," *Scientific Reports* (Nature Publishing Group), 9 (2019) 16403.

II. **N.D. Jerred**, R. Khanal, M.T. Benson, R.D. Mariani, S. Choudhury, and I. Charit, "Nd, SbNd, and Sb_3Nd_4, and their interactions with the cladding alloy HT9," *Journal of Nuclear Materials*, 541 (2020) 152387.

III. **N.D. Jerred**, M.T. Benson, R. Khanal, R.D. Mariani, S. Choudhury, and I. Charit, "Evaluation of Sb-Nd and Te-Nd phases within the U-Zr fuel matrix and their interactions with HT9," BEING PREPARED FROM CHAPTER 4 FOR SUBMISSION TO A JOURNAL.

Statement of Contributions

This dissertation is comprised of the research and experimental work carried out by the author, Nathan Jerred. However, the research was conducted with contributions from several collaborators. Work performed by some collaborators has been added in subsequent chapters to enhance and strengthen the experimental work conducted by the author for publication purposes. The following statement aims to describe the contributions provided by each collaborator and give each the credit that is deserved. Computational modeling efforts and subsequent data analysis from modeling that has been added in chapters 2, 3 and 4 was conducted by Dr. Rabi Khanal, previously a post-doctoral student at the University of Idaho and now a post-doctoral research associate at Oak Ridge National Laboratory. Publications authored by Dr. Khanal led to the experimental work covered in chapter 5. Dr. Khanal was guided by Dr. Samrat Choudhury, professor in the Materials Science and Engineering department at the University of Idaho and project lead on the computational and atomistic modeling efforts. Overall project administration, funding acquisition and my advisor for this work was Dr. Indrajit Charit, professor of the Materials Science and Engineering department at the University of Idaho. Dr. Michael Benson, senior research scientist at the Idaho National Laboratory, provided guidance on experimental efforts and fabricated the various uranium-based alloys that were used for analysis and to execute the diffusion-based experiments. Original idea conceptualization is credited to Dr. Bob Mariani of the Fuel Development Department at Idaho National Laboratory. All collaborators provided reviews and comments on chapters 2, 3 and 4 before being submitted for publication.

Table of Contents

Authorization to Submit Dissertation ii

Abstract iii

Acknowledgements iv

Dedication v

Publication of Chapters vi

Statement of Contributions vii

Table of Contents viii

Table of Figures xii

Table of Tables xviii

Chapter 1 Introduction 1

1.1 Research Motivation and Objectives 1

1.1.1 Dissertation arrangement 2

1.2 Sodium-Cooled Fast Reactors 3

1.2.1 Metallic fuels for SFRs 4

1.3 Metallic Fuel Performance 5

1.3.1 Irradiation of metal fuels 5

1.3.2 Lanthanide migration 10

1.4 FCCI in Metallic Fuels 12

1.4.1 Role of fission products in FCCI 13

1.4.2 Role of fuel constituents in FCCI 15

1.4.3 Role of cladding constituents in FCCI 18

1.4.4 Additional diffusion mechanisms 21

1.5 Controlling FCCI 21

1.5.1 Diffusion barriers 21

1.5.2 Fuel-based additives 23

Chapter 2 Nd, SbNd and Sb_3Nd_4 and their Interactions with the Cladding Alloy HT9 31

2.1 Introduction 32

2.2 Materials and Methods 33

2.2.1 Materials 33

2.2.2 Experimental details 34

2.2.3 Characterization details 35

2.2.4 Electronic structure calculations 36

2.3 Results and Discussion 37

2.3.1 Initial conditions of Nd and Sb-Nd alloy 37

2.3.2 Nd interaction with HT9 38

2.3.3 SbNd and Sb_3Nd_4 interactions with HT9 45

2.3.4 Understanding Fe and SbNd interactions using electronic structure calculations 49

2.4 Conclusion 50

Chapter 3 Evaluation of Tellurium as a Fuel Additive in Neodymium-Containing U-Zr Metallic Fuel 55

3.1 Introduction 56

3.2 Results and Discussion 57

3.2.1 Microstructural and compositional analysis of U-10Zr with Te additive 58

3.2.3 Computational prediction of phases 72

3.3 Conclusions 74

3.4 Methodology 75

3.4.1 Experimental methods 75

3.4.2 Computational methods 77

Chapter 4 Evaluation of Sb-Nd and Te-Nd Phases within the U-Zr Fuel Matrix and Their Interactions with HT9 83

4.1 Introduction 84
4.2 Materials and Methodology 85
4.2.1 Materials 85
4.2.2 Experimental methods 86
4.2.3 Characterization methods 87
4.2.4 Ab initio calculation methods 88
4.3 Results and Discussion 89
4.3.1 As-cast and annealed structures of the Sb-Nd alloy 89
4.3.2 Annealed structure of the Te-Nd alloy 93
4.3.3 Diffusion interactions of Nd/HT9 96
4.3.4 Diffusion interactions of Sb-Nd/HT9 101
4.3.5 Diffusion interactions of Te-Nd/HT9 105
4.3.6 Interactions based on DFT calculations 108
4.3.7 Comparison of annealed structures 110
4.3.8 Comparison of diffusion interactions 111
4.4 Conclusion 113
Chapter 5 Evaluation of Arsenic as a Fuel-Based Additive in the U-Zr Fuel System and its Interactions with Neodymium 118
5.1 Introduction 118
5.2 Methodology 120
5.2.1 Experiment methodology 120
5.2.2 Characterization methodology 122
5.3 Results and Discussion 123
5.3.1 As-cast and annealed structure 123
5.3.2 Interactions with HT9 128

5.5 Conclusion 135

Concluding Remarks 138

Future Work and Recommendations 142

Appendices 145

Appendix A Chapter 4 Supplemental Information 145

Appendix B Experimental Validation of Arsenic and Selenium as Additives 148

Appendix C List of Journal Publications and Conference Presentations 161

Table of Figures

Figure 1.1. Optical micrograph of U-Pu-Zr fuel pin after 1.9 at.% burnup 7

Figure 1.2. A schematic showing the general construction of an EBR-II fuel element 8

Figure 1.3. Scanning electron microscopy (SEM) analysis of U-Zr fuel with HT9 cladding. (a) Shows a backscatter electron (BSE) micrograph of a region of high FCCI and parts (b)–(f) contain energy dispersive X-ray spectroscopy (EDS) elemental maps of Fe, Cr, U, Zr and Ce, respectively, of the region indicated in (a) 9

Figure 1.4. Regions of high FCCI form between metallic fuels and cladding alloys after irradiation: (a) Interactions between the fuel U-19Pu-10Zr (wt.%) and the austenitic cladding alloy D9. (b) Interactions between the fuel U-10Zr (wt.%) and the ferritic-martensitic cladding alloy HT9 10

Figure 1.5. Agglomeration of a lanthanide-rich fission product layer at the fuel-cladding interface 10

Figure 1.6. Radial composition profiles by EPMA where (a) shows elemental compositions of fission product elements and (b) shows elemental compositions of cladding elements 13

Figure 1.7. FCCI layers observed at the fuel-cladding interface of irradiated U-10Zr (wt.%) fuel with HT9 cladding. Grain boundary (i.e. GB) attack by lanthanides (i.e. Ln) is shown in section B within the cladding 14

Figure 1.8. (a) U-Fe binary phase diagram and (b) Pu-Fe binary phase diagram 15

Figure 1.9. ((a) BSE micrograph of U-15Zr-1.16Pd-2.15Ln (wt.%) alloy, where Ln is an alloy of 53Nd-25Ce-16Pr-6La, wt.%. (b) BSE micrograph of irradiated U-10Zr (wt.%) where Pd-Ln precipitates were observed to form 23

Figure 2.1. (a) Fe-Nd binary phase diagram and (b) Nd-Sb binary phase diagram 33

Figure 2.2. Diagram of the diffusion couple jig and the internal components used for the isothermal diffusion experiments in the present study 35

Figure 2.3. BSE SEM micrographs of the Sb-Nd cast alloy revealing its two-phase morphology. (a) shows the matrix microstructure at a lower magnification (250x) and (b)

shows the matrix microstructure at a higher magnification (750x). The SbNd phase appears in grey contrast and the Sb_3Nd_4 phase in light contrast 37

Figure 2.4. XRD plots of the Nd and Sb-Nd alloy specimens in the as-received and as-cast conditions, respectively 38

Figure 2.5. The Nd/HT9 diffusion couple interaction region. (a) A BSE SEM micrograph displaying the EDS line-scan analysis location, (b) the plot of the line-scan results, and (c) EDS elemental mapping results of the interaction region of the diffusion couple 41

Figure 2.6. A section of the Nd/HT9 diffusion couple showing a larger interaction region. (a) A BSE SEM micrograph showing both the EDS line-scan analysis location and point analysis locations. (b) The plot of the line-scan results across the interaction region 42

Figure 2.7. XRD plot of the diffusion interaction region in the Nd/HT9 diffusion couple.... 44

Figure 2.8. (a) A SE SEM micrograph of indentations made within the interaction region. (b) Micro-indentation plot across the Nd/HT9 diffusion interaction region 45

Figure 2.9. The diffusion interface of the Sb-Nd/HT9 diffusion couple. (a) A BSE SEM micrograph indicating the locations of both the EDS line-scan analysis and elemental mapping analysis. (b) The plot of the line-scan analysis results, and (c) shows the elemental mapping results of the diffusion interface 46

Figure 2.10. BSE SEM micrographs of two different sections of the diffusion interface showing EDS analysis locations. (a) Corresponds to the analysis location of Figure 2.9, and (b) corresponds to a new analysis location 48

Figure 2.11. Orbital resolved DOS of Fe substituted SbNd system. The vertical dashed line represents the Fermi level. The positive and negative vertical axis represent up and down spin components, respectively 50

Figure 3.1. BSE SEM images of (a1) the 2Te alloy and (b1) the 4Te alloy; (a2) and (b2) are the magnified BSE SEM images of the 'red' rectangular inset regions in (a1) and (b1), respectively 59

Figure 3.2. Elemental EDS maps of the 2Te alloy. Analysis location aligns with the area imaged in Figure 3.1 (a1) 60

Figure 3.3. XRD patterns of the 2Te and 4Te alloys 61

Figure 3.4. BSE images of (a) the 2Te-2Nd and (b) the 4Te-4Nd alloys 63

Figure 3.5. Elemental EDS maps of the 2Te-2Nd alloy. Analysis location aligns with the area imaged in Figure 3.4 (a) 64

Figure 3.6. Elemental EDS X-ray maps of the 4Te-4Nd alloy. Analysis location aligns with the area marked in Figure 3.4 (b) 65

Figure 3.7. TEM analysis results of precipitates in the 4Te-4Nd alloy. (a) SEM image of the TEM lamella, and HAADF micrographs of (b) U-Te-Nd, Zr-Te, and Zr precipitates; (c) U-Te-Nd precipitate; and (d) Zr-Te precipitate. Single zone-axis SAED patterns from (e) grain *A* along the [011] zone axis, (f) grain *B* along the [012] zone axis, and (g) grain *C* along the [351] zone axis 67

Figure 3.8. XRD patterns of (a) the 2Te-2Nd alloy and (b) the 4Te-4Nd alloy 70

Figure 3.9. The charge density difference (CDD) between (a) U-Zr-Te and U and (b) U-Nd-Zr-Te and U systems; the yellow isosurface represents excess charge, and the blue isosurface represents a charge deficit or the negative value of charge density 72

Figure 3.10. Orbital resolved DOS for (a) U-Zr-Te-Nd and (b) U-Te-Nd. The vertical dashed lines represent the Fermi level, the energy states up to which states are occupied. The states in the negative and positive vertical axis represent down and up spin components, respectively. U-DOS remain more or less similar in all systems 73

Figure 3.11. DFT optimized configuration of U-Zr-Te-Nd system 76

Figure 4.1. (a)–(d) BSE micrographs of the Sb-Nd alloy in the as-cast condition at different magnifications. EDS point analysis results can be found in Table 4.3. (e) EDS elemental maps of the area imaged in (b) 89

Figure 4.2. XRD patterns of the Sb-Nd alloy in both the as-cast and annealed condition. Crystallographic details of the phases can be found in Table 4.4 90

Figure 4.3. (a) and (b) BSE micrographs of the Sb-Nd alloy in the annealed condition at different magnifications. EDS point analysis results can be found in Table 4.3. (c) EDS elemental maps of the area shown in (a), which overlaps with that imaged in (b) 92

Figure 4.4. (a) and (b) BSE micrographs of the Te-Nd alloy in the annealed condition. EDS results are found in Table 4.5. (c) EDS elemental map results of the area depicted in (b) 94

Figure 4.5. XRD results of Te-Nd alloy in the annealed condition. Crystallographic details of the identified phases are listed in Table 4.4 95

Figure 4.6. Interaction region of the Nd/HT9 diffusion couple. (a) and (b) BSE micrographs of the interaction region at different magnifications. EDS point analysis results can be found in Table 4.6. (c) EDS elemental maps of the region in (a). (d) EDS elemental maps of the region in (b). (e) Results of elemental line analysis of location depicted in (b) 97

Figure 4.7. Interaction region of the Nd/HT9 diffusion couple displaying an Nd precipitate at the diffusing interface. (a) and (b) BSE micrographs of the interaction region at different magnifications. EDS point analysis results are listed in Table 4.7. (c) EDS elemental line scan results of the location depicted in (b). (d) EDS elemental maps of the region depicted in (a) 100

Figure 4.8. (a) and (b) SEM BSE micrographs of the diffusing interface of the Sb-Nd/HT9 diffusion couple. EDS point analysis results are listed in Table 4.8. (c) EDS elemental maps of the area imaged in (b) 102

Figure 4.9. (a) and (b) SEM BSE micrographs of the diffusing interface of the Sb-Nd/HT9 diffusion couple. EDS point analysis results are listed in Table 4.8. (c) EDS elemental line scan results of the area depicted in (b). (d) EDS elemental maps of the area imaged in (b) 103

Figure 4.10. (a) and (b) BSE micrographs of the diffusing interface of the Te-Nd/HT9 diffusion couple. EDS point analysis results are listed in Table 4.9. (c) EDS elemental line scan results of the area depicted in (b). (d) EDS elemental maps of the area imaged in (b) 105

Figure 5.1. Plots of the enthalpy of mixing values of different additives and lanthanides correlated with various additives (a) electronegativity and (b) covalent radius 119

Figure 5.2. (a) Muffle furnace used within the glovebox for fuel-based diffusion experiments. (b) An assembled diffusion jig before the final outer tantalum foil wrapping. (c) Diagram of the diffusion couple jig and the internal components used for the isothermal diffusion experiments 120

Figure 5.3. SEM/EDS characterization of the U-10Zr-2.6As-4Nd alloy in the as-cast condition. (a) BSE micrograph of different precipitate formations within the alloy. (b) high magnification BSE micrograph of the area indicated in (a). (c) EDS elemental map results of the area imaged in (a). (d) high magnification BSE micrograph of the area indicated in (a). EDS point analysis of the locations indicated in (b) and (d) are listed in Table 5.2 123

Figure 5.4. SEM/EDS characterization of the U-10Zr-2.6AS-4Nd alloy in the annealed condition. (a) and (b) BSE micrographs of different precipitate formations within the alloy. (c) EDS elemental map results of the area imaged in (a). (d) EDS elemental map results of the area imaged in (b). EDS point analysis of locations indicated in (b) are listed in Table 5.2 124

Figure 5.5. Nd-As binary phase diagram 126

Figure 5.6. XRD results of the U-Zr-As-Nd alloy in its (a) as-cast condition and (b) annealed condition 127

Figure 5.7. SEM/EDS characterization of the U-10Zr-2.6As-4Nd/HT9 diffusion couple. (a) and (b) BSE micrographs of the interaction region at varying magnifications. (c) EDS elemental line scan plot of the location indicated in (a). (d) EDS elemental map results of the region imaged in (b). EDS point analysis of the locations indicated in (b) are listed in Table 5.4 128

Figure 5.8. SEM/EDS characterization of a separate section of the U-10Zr-2.6As-4Nd/HT9 diffusion couple. (a) BSE micrograph of the diffusion couple interface. (b) EDS elemental line scan plot of the location indicated in (a). (c) EDS elemental map results of the region imaged in (a). EDS point analysis of the locations indicated in part (a) are summarized in Table 5.4 129

Figure 5.9. U-Zr-Fe ternary isotherm at 680°C (953K) showing the phase layers observed through the interaction region in Figure 5.7 131

Figure A.1. (a) and (b) BSE micrographs of the large precipitate found in the as-cast Sb-Nd alloy. EDS point analysis results can be found in Table A.1 144

Figure A.2. XRD results of the Sb-Nd alloy in a region near the large precipitate imaged in Figure A.1 145

Figure A.3. (a) BSE micrograph of the Nd/HT9 diffusion couple in the annealed section of the U-10Zr-4Nd (wt.%) alloy well away from the diffusion interface. (b) EDS elemental maps of the region in (a) 146

Figure B.1. Backscattered electron SEM image indicating locations of EDS point analysis (a) alloy1 (92U4Nd-4As, wt.%) (b) alloy2 (94U-4Nd-2As, wt.%). XRD patterns of (c) alloy1 and (d) alloy2 samples..... 150

Figure B.2. BSE SEM image of the 2Se alloy, (a), with elemental maps, (b)–(d). Elemental map analysis was conducted at higher magnification on a portion of the grey-contrast region of (a). Corresponding EDS point data listed in Table B-2 152

Figure B.3. X-ray diffraction pattern of the light grey-contrast region in the 2Se alloy confirming the formation of NdSe phase within α-U matrix 153

Figure B.4. Backscatter SEM image of the 3As alloy, (a), with elemental maps, (b)–(d). Corresponding EDS point data listed in Table B-3 154

Figure B.5. XRD diffraction plots of the 3As alloy shown in Figure B.4 confirming the formation of CeAs and Ce_4As_3 phases within the α-U matrix 155

Figure B.6. (a) BSE SEM micrograph of U-10Zr-2.6As-4Nd alloy showing precipitate formation. (b) BSE SEM micrograph of precipitate from section (a) inlay. (c) EDS elemental map of area imaged in section (a)..... 157

Figure B.7. Plot of XRD data collected on U-10Zr-2.6As-4Nd alloy 158

Table of Tables

Table 1.1. Select design parameters (nominal) of EBR-II metal driver fuel elements 6

Table 1.2. Lanthanide element diffusivity in liquid sodium metallic system at various temperatures 11

Table 1.3. Nominal compositions, in wt.%, of typical cladding alloys used historically in SFR systems 18

Table 2.1. Chemical composition in wt.% of the HT9 cladding alloy used in this study 34

Table 2.2. Crystallographic information of phases indexed through XRD analysis 39

Table 2.3. EDS analysis data in at.% correlating to locations in Figure 2.6 (a) 43

Table 2.4. Hardness analysis results of the Nd/HT9 diffusion couple 45

Table 2.5. EDS analysis data in at.% correlating to locations displayed in Figure 2.10 48

Table 3.1. Alloys evaluated in this study 58

Table 3.2. SEM EDS elemental data results of analysis points depicted in Figure 3.1 (at.%) 60

Table 3.3. Crystallographic information for all phases indexed through XRD analysis 62

Table 3.4. SEM EDS elemental data results of analysis points depicted in Figure 3.4 (a) and (b) (in at.%) 66

Table 3.5. TEM EDS elemental data results (in at%) of analysis points depicted in Figure 3.7 (b), (c), and (d) 68

Table 3.6. Crystallographic details from determined phases from SAED patterns presented in Figure 3.7 (d), (e), and (f) 70

Table 3.7. Enthalpy of mixing values (as predicted by DFT) for different elements in various systems. A negative enthalpy indicates ease of formation of the stable compound 71

Table 4.1. Chemical composition in wt.% of the HT9 cladding alloy used in this study 84

Table 4.2. Samples analyzed in this study and their experimental condition 85

Table 4.3. EDS points analysis results, in at.%, of the as-cast and annealed Sb-Nd alloy for locations depicted in Figure 4.1 (b) and Figure 4.3 (b) 91

Table 4.4. Crystallographic information of phases identified through XRD analysis in Figure 4.2 and Figure 4.5 93

Table 4.5. EDS point analysis results, in at.%, of the Te-Nd alloy. Points correlate with locations identified in Figure 4.4 (b) 94

Table 4.6. EDS point analysis results, in at.%, of the Nd/HT9 diffusion couple for the locations depicted in Figure 4.6 (a) and (b) 98

Table 4.7. EDS point analysis results, in at.%, of the Nd/HT9 diffusion couple for the locations depicted in Figure 4.7 (b) 101

Table 4.8. EDS point analysis results, in at.%, of the Sb-Nd/HT9 diffusion couple for the locations depicted in Figures 4.8 (b) and 4.9 (b) 104

Table 4.9. EDS point analysis results, in at.%, of the Te-Nd/HT9 diffusion couple for the locations depicted in Figure 4.10 (b) 106

Table 4.10. Enthalpy of mixing values for different elements in fuel and cladding matrices 108

Table 4.11. Enthalpy of mixing values of different fuel-based compounds with Nd 109

Table 5.1. Intrinsic properties of select additive and lanthanide elements 118

Table 5.2. EDS point analysis results, in at.%, corresponding to locations indicated in Figure 5.3 (b) and (d) and in Figure 5.4 (b) 125

Table 5.3. Crystallographic information of phases identified through XRD analysis shown in Figure 5.6 127

Table 5.4. EDS point analysis results, in at.%, corresponding to locations indicated in Figure 5.7 (b) and Figure 5.8 (a) 132

Table A.1. EDS points analysis results, in at.%, of the locations depicted in Figure A.1 (b) 144

Table A.2. Crystallographic information of phases identified through XRD analysis in Figure A.2 145

Table B.1. EDS point analysis compositions of precipitates (at.%) in reference to Fig. B.1 (a) alloy1 (92U-4Nd-4As, wt.%) and (b) alloy2 (94U-4Nd-2As, wt.%) 150

Table B.2. EDS point (Pt.) analysis compositions of locations (atom %) identified in the BSE image shown in Figure B.2 (a) 152

Table B.3. EDS point (Pt.) analysis compositions of locations (atom %) identified in the BSE images of Figure B.4 (a) 154

Table B.4. EDS point analysis results of Figure B-6 (b) in at.% 157

CHAPTER 1
INTRODUCTION

1.1 Research Motivation and Objectives

Metallic fuels, such as the U-Zr and U-Pu-Zr fuel systems, are attractive for use in the advanced sodium-cooled fast reactor (SFR), a next-generation advanced reactor concept [1,2]. Research and development of the SFR systems over the past 55 years has led to a large knowledgebase on its safe operation. Furthermore, the extensive research already completed on the U-Zr and U-Pu-Zr fuel systems, has yielded a solid foundation of their irradiation behavior. Historically, after prolonged burnup within the reactor such fuel systems have been found to chemically interact with the inner surface of the cladding tubes used to contain the fuel, limiting their overall performance potential. This interaction phenomenon, known as fuel-cladding chemical interaction (FCCI), has been found to be a complex, multi-component, multi-mechanism interaction between solid fission products, fuel components and cladding material constituents. In particular, lanthanide fission products, e.g. lanthanum (La), cerium (Ce), neodymium (Nd), praseodymium (Pr) and samarium (Sm), are of greatest concern due to their propensity to form low-melting, brittle intermetallic phases with cladding constituents. Further, lanthanide fission products are observed to migrate to the fuel-cladding interface making them readily available to interact with the cladding constituents. In-pile experiments, such as those conducted at the Experimental Breeder Reactor II (EBR-II), showed that beyond 10 at.% burnup the onset of FCCI leads to deleterious effects, drastically affecting the performance of the fuel-cladding system and limiting its burnup potential within the reactor system [3–6]. Therefore, as new reactor concepts and more advanced versions of the SFR, are being contemplated, extending the burnup capabilities of the fuel is one way to increase the fuel economy. However, in order to increase the burnup of the metallic fuel systems, methods to mitigate and limit the effects of FCCI must be employed. Alloying fuels with additives that preferentially bind with lanthanides within the fuel meat is one method that has been proposed [7]. Both tellurium (Te) and antimony (Sb) have been proposed as potential additives to bind with lanthanide fission products within the fuel, but a focused study has not yet been undertaken. The goal of the proposed research is to evaluate the effectiveness of these additives

to bind with lanthanide elements and mitigate their interaction with cladding constituents. An additional goal of this research is to evaluate alternative elements, which may demonstrate a propensity to also bind with the lanthanides of interest. Specific research objectives covered in this dissertation are:

1. Carry out isothermal diffusion couple experiments between lanthanide (Ln) elements of interest and iron (Fe) and the cladding alloy HT9. Such experiments will provide a baseline understanding of the interaction characteristics between lanthanides and the primary cladding constituents.
2. Fabricate additive-based fuel alloys, i.e. U-Zr-X ('X' denotes the additive), and evaluate the interactions of the additive within the fuel alloy. Then fabricate additive-lanthanide fuel alloys, i.e. U-Zr-X-Ln ('Ln' denotes the lanthanide), and evaluate the additive-lanthanide interactions within the fuel alloy. Characterize the phases that form in the fuel alloy due to both the additive and lanthanide additions.
3. Carry out isothermal diffusion couple experiments between U-Zr-Ln and U-Zr-X-Ln alloys and the cladding alloy HT9 to evaluate the effectiveness of the additive to bind with the lanthanides and mitigate its interaction with the cladding alloy HT9.
4. Experimentally evaluate elements that are identified through first principle-based calculations to exhibit a high tendency to bind with lanthanide elements.

1.1.1 Dissertation arrangement

In the organization of this dissertation, it was important to arrange chapters in a manner that would make the research more comprehensible. To that end, chapter 1 provides an introduction to metal fuels, their historical use within SFR systems, phenomenological effects they have encountered, and methods that have been proposed to counter such effects. Chapter 2 directly evaluates the effectiveness of Sb as an additive for Nd experimentally and outside of the normal U-Zr fuel structure. This work aims to isolate the direct diffusion interactions of Nd metal and that of an Sb-Nd alloy against HT9, an important step before progressing onto more complex diffusion experiments which involve additional alloy constituents. In a way, the experiments carried out in chapter 2 can be viewed as a "separate effects" evaluation of the Sb

additive. Before progressing directly into the more complex fuel-based diffusion experiments, it was important to characterize additive and additive-lanthanide interactions once alloyed within the fuel matrix. Chapter 3 initially details the interaction of Te within the U-Zr matrix, i.e. U-Zr-Te alloy, simulating the condition of the alloy at the beginning of an irradiation cycle and before fission products form. This is then followed with detailing the interactions of Te and Nd within the U-Zr matrix, i.e. U-Zr-Te-Nd alloy, which simulates a fuel that has been irradiated and thus lanthanides have formed. Regarding the characterization of Sb within the U-Zr matrix, i.e. U-Zr-Sb alloy, this has been previously published by a separate research group and therefore was not carried out in depth in this research. However, the interaction of Sb and Nd within the U-Zr matrix is detailed within chapter 4, both in the as-cast and annealed conditions. Chapter 4 further evaluates the U-Zr-Te-Nd system in an annealed condition, complimenting the work described in chapter 3. Chapter 4 further details the more complex diffusion experiments of U-Zr alloys against HT9, which include U-Zr-Nd/HT9, U-Zr-Sb-Nd/HT9 and U-Zr-Te-Nd/HT9. Chapter 5 deviates from Sb and Te as additives, but instead evaluates the alternative additive arsenic (As). Both As and Se were identified as alternative additives through computational-based research carried out by others within the research group. Initial experimental work carried out to aid in validating the computational work on both alternative additives can be found in Appendix B, which provides additional context on the progression to the work that is documented in chapter 5. Within chapter 5, the interaction of As and Nd is evaluated initially within the U-Zr system, i.e. U-Zr-As-Nd alloy, both in an as-cast and annealed condition. This is followed by detailing observations made of the initial diffusion experiments between a U-Zr-As-Nd alloy and HT9. Finally, chapter 6 provides a conclusions section for the entire dissertation along with a section discussing some of the limitations of this research as well as recommendations for follow-on research.

1.2 Sodium-Cooled Fast Reactors

An attractive Generation-IV reactor concept is the sodium-cooled fast reactor (SFR). Such a reactor relies on liquid sodium as the primary coolant and gains much of its advantages from the thermo-physical properties exhibited by sodium, such as its high thermal conductivity, vaporization point, boiling point and heat capacity, yielding a coolant with a high degree of thermal inertia. Another major advantage of the SFR concept is the long history of

practical research that has been conducted. Over the past 60 years major advancements in its functionality has already been completed [1]. The fast reactor concept in general is attractive for various reasons, in particular it can address concerns regarding the proliferation of plutonium through its use as a fuel, as well as the management of spent nuclear fuel. Furthermore, such a reactor system presents a viable path forward for addressing the long-term management of minor actinides and that of other long-lived fission products with its ability to fission or burn such constituents [8]. One potential fuel form proposed by the Technology Roadmap Update for Gen-IV Nuclear Energy Systems for the SFR concept is the metal-alloy class of fuels [1]. Metallic fuels offer some distinct advantages over ceramic fuels, such as ease of fabrication and reprocessing, high thermal conductivity, good compatibility with the sodium coolant, and an ability to contain high densities of fissile and fertile materials. Combined, these reactor characteristics lead to a decreased core size (i.e. a more compact core) [2,9,10]. However, the use of such metallic fuel systems has led to the discovery of irradiation-induced phenomenon such as fuel-cladding mechanical interaction (FCMI) and fuel-cladding chemical interaction (FCCI), which have limited such fuel systems from achieving high burnups. FCMI is a physical interaction experienced between the fuel and cladding, a result of fuel swelling. Initially, FCMI limited burnup to only a few at.% and with changes in the fuel pin design such issues were resolved. FCCI is now considered the primary limiting factor for metallic fuel systems and is the result of chemical interactions between fuel constituents and fission products with the cladding constituents. The FCCI phenomenon, at its core, is a complex, multi-component diffusion problem but understanding such mechanisms as fission product transport within the fuel, the inter-diffusion between the fuel and cladding constituents and finally ways to mitigate such interactions will be key in overcoming it [5].

1.2.1 Metallic fuels for SFRs

Over the development years of fast reactor technology, several alloy concepts have been evaluated and this discussion will be primarily based on such research conducted by the subsequent metallic fuel R&D program in the United States. The primary US reactor system where the majority of its fast reactor research took place was that of the Experimental Breeder Reactor II (EBR-II) a research-based, sodium-cooled fast reactor. EBR-II is located at, what is now, the Materials and Fuels Complex (MFC) of the Idaho National Laboratory (INL), a

facility where much of the research into SFR's and metallic fuel systems has been carried out to date. Beyond just expanding the knowledge base on the operation of fast reactors and their respective fuels, research at the EBR-II facility included closing the fuel cycle, which led to the investigation of pyroprocessing and refining techniques to reprocess metallic fuels. For this reason, metallic fuels used and developed at EBR-II contained a certain percentage of metals that would be carried over through the melt-refining process. The first two driver fuel concepts for EBR-II, the Mk-I and Mk-II fuel concepts, were a metallic alloy of U-5 wt.% Fs (Fs stands for fissium, a mixture of 2.46% Mo, 1.96% Ru, 0.28% Rh, 0.19% Pd, 0.1% Zr, and 0.01% Nb, wt.%, which were carry-over, metal-based fission products) [9,10]. Through the development of metallic fuels, interactions between the fuel and cladding were observed and it was found alloying metallic uranium with zirconium aided in not only limiting the fuel-cladding interactions but also served to increase the solidus temperature of the fuel. Ultimately, this led to the development of the current metallic fuel form, U-10Zr wt.% (U-23Zr at.%). Table 1.1 shows the progression and characteristics of the EBR-II driver fuel elements over its operational lifetime.

1.3 Metallic Fuel Performance

1.3.1 Irradiation of metal fuels

Metal fuel, such as U-Zr and U-Pu-Zr, in their *as-cast* form exhibit a relative homogeneous distribution of their fuel constituents at their beginning-of-life (BOL) in the reactor. Very early during irradiation, however, the fuel constituents tend to segregate to form phase structures stable at temperatures attained within the respective radial regions of the fuel slug. Zirconium tends to be the primary constituent observed to migrate. Temperatures at the hot region (i.e. the fuel centerline) can lead to the formation of the γ phase, which is a high temperature, U-Zr solid solution phase. The formation of the γ phase, having high solubility of Zr, promotes its migration out of the middle band region towards the center region, where Zr concentrations have been documented to reach 33 wt.%. Temperatures at the cold region (i.e. the fuel periphery) tend to lead to the formation of a two phase, αU and δZr_2U, structure. The composition within this exterior region tends to match the nominal fuel composition (i.e. U-10Zr wt.%). Because of Zr migration, the middle band region has been documented to exhibit a Zr concentration down to 4 wt.%, which in turn leads to a high U concentration that

deviates from that of the nominal fuel composition. It should be noted that the Zr concentration within this middle band region is observed to fluctuate and be dependent on the temperature and thus phase attained at the center region of the fuel. In the case of the U-Pu-Zr fuel system, the uranium and zirconium segregates in a similar manner where plutonium tends to exhibit little to no migration. Due to the presence of Pu, alternative phases, such as the U-Pu ζ phase, may also form. Ultimately, the phase structures within a U-Pu-Zr fuel slug becomes dependent on the total Pu concentration within the alloy [9,11]. Figure 1.1 shows an optical micrograph of a cross-section of a U-Pu-Zr fuel pin, as well as an overlay of the elemental concentration of the fuel elements moving from the fuel centerline to the fuel periphery.

Table 1.1. Select design parameters (nominal) of EBR-II metal driver fuel elements [10].

Campaign	**Mk-I/-IA**	**Mk-II/-IIC/-IICS**	**Mk-III/-IIIA**	**Mk-IV**	**Mk-V/-VA[a]**
Fuel alloy (wt.%)	U-5Fs	U-5Fs & U-10Zr	U-10Zr	U-10Zr	U-10Pu-10Zr
^{235}U enrichment (%)	52	67-78	66.9	69.6	Variable
Slug diameter (mm)	3.66	3.30	4.39	4.27	4.27-4.39
Fuel smear density (%)	85	75	75	75	75
Burn up limit (at.%)	2.6	8.9	10	N/A	TBD
Plenum/fuel vol. ratio	0.18	0.68-1.01	1.45	1.45	1.45
Plenum gas	Inert	Inert	Inert	Inert	Argon
Cladding material	304L	304L & 316	CW 316 & CW D9	HT9	HT9 & CW 316

[a] Conversion to the Mark-V/-VA fuel types was not started before EBR-II was terminally shutdown in 1994

Through irradiation, metal fuels have been observed to exhibit unique characteristics in comparison with ceramic-based fuel. Metallic fuels tend to hold more fission gas atoms and thus exhibit a higher rate of gas swelling in the early stages of irradiation. In turn, metal fuel tends to show a higher rate of creep leading to an expansion of the fuel slug and upon making contact with the cladding, experiences compressive stresses. Further, metal fuel tends to exhibit fission product generation and subsequent transport to and agglomeration at the fuel peripheral [9]. Early development of metal fuel concepts found that their initial expansion was a major limiting factor. Such fuel designs were only able to reliably achieve 1–2 at.% burnup before the potential for failure would rise. It was found that these failures were the result of stresses

that would occur from the mechanical interaction of the fuel and cladding, i.e. FCMI, and such interactions were directly related to the expansion of the fuel and fission gas generation. With continued fuel expansion, the stresses on the internal cladding surface would increase and the probability of cladding breach would rise [5].

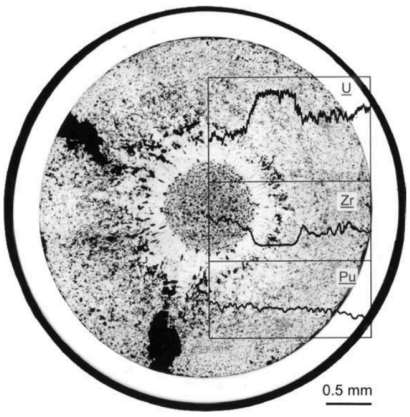

Figure 1.1. Optical micrograph of U-Pu-Zr fuel pin after 1.9 at.% burnup [12].

Continued development to achieve greater burnups in metal fuels led to a decrease of the fuel smear density and an increase in the plenum-to-fuel volume ratio, i.e. the gas plenum size was increased, to accommodate the greater generation of fission gases. Further, to maintain thermal contact and to facilitate the dissipation of heat generation, sodium is used to *bond* the fuel slug to the inner cladding wall. Figure 1.2 shows a general schematic of a typical fuel element used in EBR-II. It was determined by decreasing the smear density down to ~75%, the fuel-cladding gap would allow the fuel to adequately expand to a point where the porosity within the fuel would become interconnected and thus allow fission gas to be released to the gas plenum. Although contact between the fuel and cladding still occurred, the mechanical force was greatly reduced and thus limiting the effects of FCMI. As summarized in Table 1.1, such design evolutions were made in the EBR-II fuel structure, progressing from the Mk-I to the Mk-II series and the burnup capabilities were indeed increased between the two fuel designs. By overcoming the phenomenon of FCMI and with longer fuel burnups (~8 at.% burnup for Mk-II fuel) being attainable, a new problem became evident; chemical interactions at the fuel-cladding interface, i.e. FCCI. Such chemical interactions are a phenomenon where fuel constituents and fission products, that have migrated to the fuel-cladding interface, chemically interact with the cladding constituents. Such interactions were not previously

experienced in the Mk-I fuel because burnup was limited to 1–2 at.% due to FCMI and irradiation time was not sufficient for the effects of FCCI to fully manifest. FCCI only becomes a factor at higher burnups.

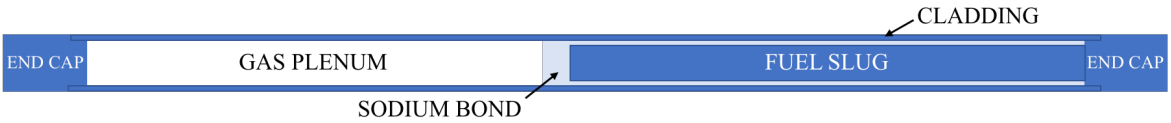

Figure 1.2. A schematic showing the general construction of an EBR-II fuel element.

As previously mentioned during the first 1–2 at. % burnup of the fuel, fission gas formation and subsequent fuel swelling leads the fuel slug to make intimate contact with the internal surface of the cladding at numerous locations within the fuel pin. It is at these contact points where brittle and low-melting phases can form. Such chemical interactions at the fuel-cladding interface are problematic because these regions can promote the inter-diffusion of primary cladding constituents into the fuel, and fuel constituents and fission products into the cladding, which in turn leads to a breakdown of the cladding integrity. Analysis of reactor-irradiated fuels has indicated FCCI tends to be most severe at locations correlating to higher inner cladding temperatures. For EBR-II fuel this condition was typically observed towards the top of the fuel slug [13]. Figure 1.3 shows a region of high FCCI that formed between U-10 wt.% Zr fuel and the ferritic/martensitic cladding alloy HT9, irradiated to an average peak burnup of 12.4 at.%. In particular the interaction between Fe and Ce is evident by their co-location in the elemental maps shown is parts (b) and (f).

The loss of primary alloying elements, the growth of interaction zones and the physical thinning of the cladding is commonly referred to as cladding wastage, i.e. regions of the cladding that do not contribute to the overall cladding strength. The continued increase of cladding wastage further decreases the cladding integrity until breach of the cladding wall occurs. Figure 1.4 shows regions of high FCCI of irradiated metallic fuels with different claddings. FCCI observed between U-Pu-Zr fuel and D9 cladding (Figure 1.4 (a)) shows the depletion of nickel from the inner cladding region. Conversely, decaburization has been observed to occur between U-Pu-Zr fuel and the ferritic/martensitic cladding alloy HT9. In both instances, such depletion leads to the formation of a soft ferrite phase in the inner region of the cladding and in turn contributes to cladding wastage [5,9,12,13]. It should be noted that the level of ferrite formation in HT9 is lower than that in D9 [6]. Additionally, Figure 1.4 (b)

shows an area exhibiting a high degree of FCCI between the binary fuel alloy U-Zr and HT9 and in this instance the interaction depth was measured to be ~150 µm [13].

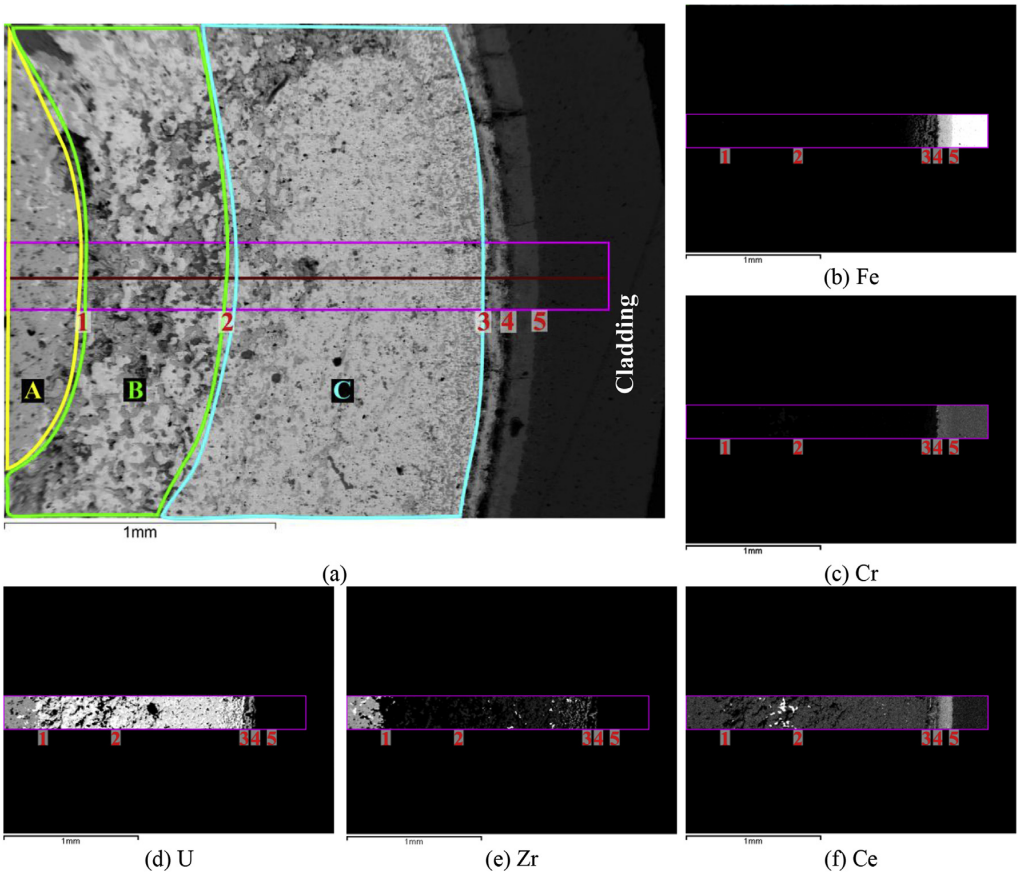

Figure 1.3. Scanning electron microscopy (SEM) analysis of U-Zr fuel with HT9 cladding. (a) Shows a backscatter electron (BSE) micrograph of a region of high FCCI and parts (b)–(f) contain energy dispersive X-ray spectroscopy (EDS) elemental maps of Fe, Cr, U, Zr and Ce, respectively, of the region indicated in (a) [11].

Analysis of regions of high FCCI between metallic fuel alloys and claddings indicate the primary problematic fission products that appear to both agglomerate at the fuel-cladding interface and more readily participate in the inter-diffusion process are those of the lanthanide series of elements. An analysis by Mariani *et al.* [7] of a U-10 wt.% Zr fuel pin irradiated in EBR-II up to ~ 8 at.% burnup showed the presence of neodymium (Nd), cerium (Ce), lanthanum (La), and praseodymium (Pr) as fission products making up the majority of the lanthanide elements present in irradiated fuel having concentrations of 0.90%, 0.53%, 0.27% and 0.26% wt.% (1.17%, 0.71%, 0.37% and 0.35% at.%), respectively. Furthermore,

lanthanide elements in general tend to make up nearly 45% of the fission product yield in metallic fuels of fast reactors [14].

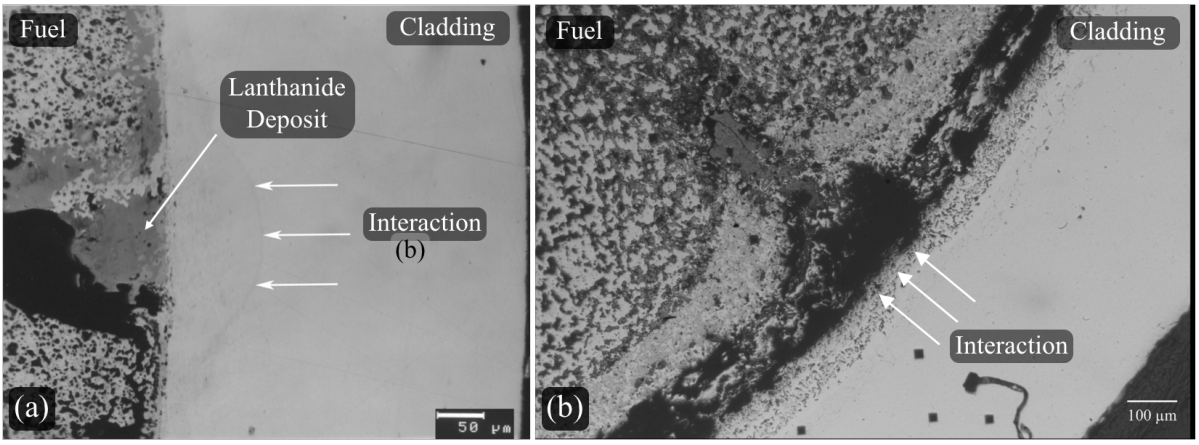

Figure 1.4. Regions of high FCCI form between metallic fuels and cladding alloys after irradiation. (a) Interactions between the fuel U-19Pu-10Zr (wt.%) and the austenitic cladding alloy D9 [15]. (b) Interactions between the fuel U-10Zr (wt.%) and the ferritic/martensitic cladding alloy HT9 [13].

1.3.2 Lanthanide migration

It is apparent that lanthanide elements play a major role in the FCCI phenomenon of metallic fuels and it is important to understand the method to which such elements transport to the fuel-cladding interface. Lanthanide elements tend to be immiscible in the U-Zr and U-Pu-Zr matrices and thus are more readily available to transport to the fuel periphery. The formation of such a lanthanide-rich layer at the fuel-cladding interface is indicated in Figure 1.5.

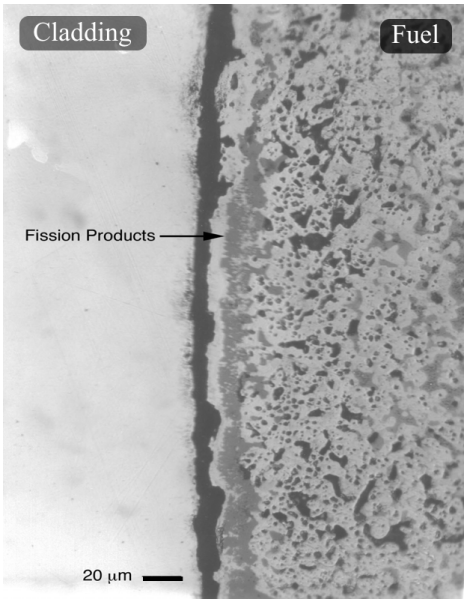

Figure 1.5. Agglomeration of a lanthanide-rich fission product layer at the fuel-cladding interface [15].

Such transport appears to be strongly tied to temperature gradients present between the fuel centerline and fuel periphery a diffusion process known as thermophoresis or the Soret effect [5,6,15,16]. Recent research in this area has shown that the transport mechanisms of the lanthanides tends to be liquid-like. When the fuel undergoes swelling in the first few at.% burnup due to porosity formation, liquefied sodium becomes displaced and backfills into the interconnected network of pores (sodium is present within the fuel pin as depicted in Figure 1.2). Further, cesium, which forms as a fission product, is also believed to liquefy and concentrate within pores of the fuel. It is through these interconnected cesium-filled and sodium-filled pores lanthanide elements are believed to diffuse as solutes to the fuel periphery [16]. Molecular dynamic models have been used to determine the diffusivity of the primary lanthanide elements, i.e. Ce, Nd and Pr, in liquid sodium. The results showed the diffusion coefficients of the lanthanides in liquid sodium were estimated to be in the order of 10^{-5} cm^2/s, which correlates with liquid-like transport mechanisms [16]. Table 1.2 shows the tabulated diffusivities of the lanthanide elements of interest in liquid sodium at various temperatures. It is largely believed that such elements readily dissolve into liquid sodium/cesium. Experimental results indicated the solubility of Ce, Pr and Nd in liquid sodium varied from 2×10^{-5} to 5×10^{-5} at.% between 450 to 550°C. Further, results showed the solubility limit is reached within ~30min, suggesting lanthanide transport in such liquid systems is not limited by their dissolution but rather on their diffusion once in solution [16]. The previous discussion is a common proposed mechanism for lanthanide transport, and although lanthanide transport is occurring on timescales beyond that of solid-state diffusion, the exact mechanisms for their transport to the fuel periphery is not yet fully known.

Table 1.2. Lanthanide element diffusivity in liquid sodium metallic system at various temperatures [17].

System	**Temperature [K]**	**Diffusivity ($\times10^{-5}$) [cm^2/s]**
Ce in Na	523	1.04±0.07
	723	1.97±0.14
	1000	5.34±0.13
Pr in Na	723	4.53±0.29
	923	6.01±0.34
Nd in Na	723	4.00±0.27
	923	4.63±0.28

1.4 FCCI in Metallic Fuels

The early stages of fuel development included performing isothermal diffusion studies between fuel alloys and potential cladding alloys. It was found that the 300 series of austenitic stainless steels showed limited chemical interactions with the U-Fs fuels. However, austenitic alloys would eventually be replaced by the ferritic/martensitic class of alloys due to their improved swelling characteristics [18]. In transitioning to the U-10Zr fuel system, the addition of zirconium yielded a marked improvement in the chemical interactions between the fuel and cladding. With the addition of zirconium, the development of a Zr-rich layer, or Zr-rind, at the fuel periphery was observed. It was found that the Zr-rind provides an inherent barrier which limits the inter-diffusion of fuel and cladding constituents. As a result, FCCI is typically observed to be most severe only at locations where there is a breakdown of this barrier [5,6]. Continued advancement of metallic fuels lies primarily in overcoming the FCCI phenomenon as it is a major factor preventing metallic fuels from consistently achieving higher burnups [4].

The interaction zones between the fuel and cladding alloys have been observed to be quite extensive and complex. As previously noted, FCCI appears to be primarily based on multi-component diffusion and the active mechanisms that appear to take place are numerous. Although migration of the lanthanides to the fuel-cladding interface is believed to follow a liquid-like transport mechanism, the FCCI phenomenon, under normal operating conditions, is considered to be based on solid-state diffusion mechanisms [5]. An in-depth historical account of FCCI experimentations and investigation is provided by Keiser [19], where Matthews *et al.* [4] provides an in-depth discussion on the FCCI phenomenon, breaking it down into its unique parts. The following section is a summary of FCCI while providing details on the role fission products, fuel components and cladding constituents play in the overall phenomenon.

1.4.1 Role of fission products in FCCI

The transport of lanthanides to the fuel-cladding interface leads to a build-up of lanthanides, as shown in Figure 1.5, which readily promotes lanthanide interactions with the cladding. In general, the presence of lanthanides in the fuel has been found to enhance interactions between the fuel and cladding. Detailed analysis was conducted using electron probe microanalysis (EPMA) on a FCCI region between U-10Zr (wt.%) and HT9 cladding that

was irradiated in EBR-II. The results of the analysis are shown in Figure 1.6. This analysis shows the presence of Nd, Ce, La, Pr and Sm in the cladding. Of the fission products formed, Nd and Ce tend to diffuse the farthest into the cladding.

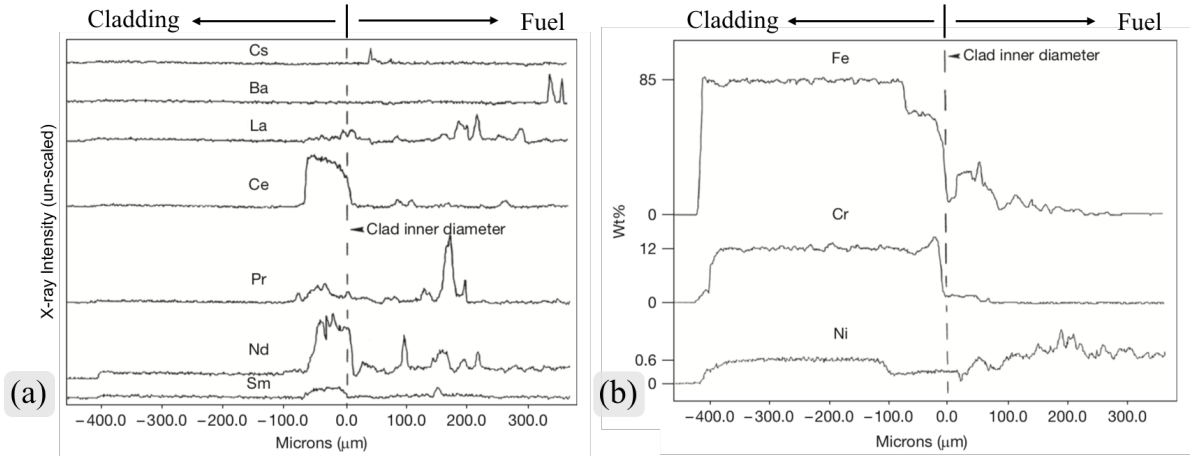

Figure 1.6. Radial composition profiles by EPMA where (a) shows elemental compositions of fission product elements and (b) shows elemental compositions of cladding elements [6].

Some of the primary concerns associated with FCCI are the intermetallic phases that form within the cladding. Such intermetallic compounds can be brittle and can contribute to a weakened cladding. On the cladding side of the interaction zone the formation of $(Fe,Cr)_{17}Ln_2$ and $(Fe,Cr)_3Ln$ have been observed, where Ln denotes lanthanide elements in general [6,11,15,20]. Additionally, the intermetallic compounds that form can have relatively low-melting points with the primary cladding constituents (e.g. Fe, Ni, and Cr). For example, such binary compounds as Fe-Nd, Fe-Pr and Ni-Ce exhibit eutectic melting temperatures of 682ºC, 667ºC and 477 ºC, respectively. If formed, such compounds could be problematic. Although some experiments have indicated peak inner cladding temperatures up to 648ºC [13], typical operating conditions should not lead to liquid phase formations, with the exception being the Ni-Ce binary compound. However, temperatures could evolve through off-normal or transient conditions that could induce liquid phases. Such liquefaction reactions can, in turn, exacerbate cladding wastage issues at the fuel-cladding interface and again lead to quick cladding failure. Further, the formation of such low-melting phases may likely be why greater interaction is observed when lanthanides are present. This is because as the operational temperatures approach the eutectic temperature of these phases, the diffusivity of the components is increased leading to greater interaction [4].

Overall, lanthanides interact with the different cladding materials in different ways and their level of interaction is dependent on the alloying constituents of the cladding alloy. For example, lanthanides were observed to more readily diffuse through the grain boundaries of the cladding alloy HT9, which has not been observed in other cladding alloys [5,11]. SEM analysis was performed on a high-temperature section of an irradiated U-10Zr (wt.%) fuel with HT9 cladding, revealing the complexity of the interactions that occur at the fuel-cladding interface. Evaluation at the cladding resolved what appeared to be preferential lanthanide attack of the cladding grain boundaries (Figure 1.7) which could indicate a weaker layer in the cladding than originally believed [11]. This preferential grain boundary attack by lanthanides of HT9 claddings is not fully understood but demonstrates the variability of lanthanide interactions within the fuel-cladding system.

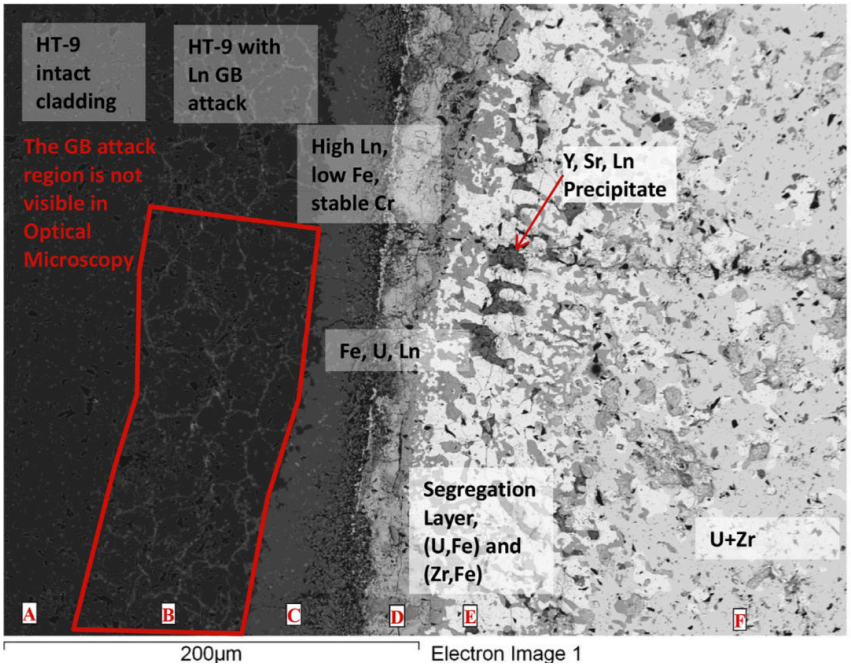

Figure 1.7. FCCI layers observed at the fuel-cladding interface of irradiated U-10Zr (wt.%) fuel with HT9 cladding. Grain boundary (i.e. GB) attack by lanthanides (i.e. Ln) is shown in section B within the cladding [11].

1.4.2 Role of fuel constituents in FCCI

Contrary to the level of interaction observed by lanthanides, fuel components e.g. U, Zr and Pu, tend to only interact with the cladding within a short distance of the fuel-cladding interface. In particular both U and Pu have been found to primarily interact with Fe to form, UFe_2 and U_6Fe, or $PuFe_2$ and Pu_6Fe phases, respectively [6]. Further, for U-Pu containing fuels

$(U,Pu)Fe_2$ and $(U,Pu)_6Fe$ are likely to form within the interaction region [21]. The UFe_2 phase is typically found to form on the cladding side of the fuel-cladding interface, where the U_6Fe phase forms on the fuel-side of the UFe_2 phase. In more simplistic diffusion couple experiments between U and Fe, the U_6Fe phase was found to form faster and thicker than the UFe_2 phase, where growth of the latter phase was restricted by the growth of the former [22]. In comparing the depth of penetration of the primary fuel components, Pu tends to penetrate the furthest into the cladding compared to U [15]. Of primary concern from U,Pu-Fe interaction is the potential for eutectic reactions, where the binary systems U-Fe and Pu-Fe, experience such reactions at 725ºC and 410ºC, respectively. The binary phase diagrams of the U-Fe and Pu-Fe systems are shown in Figure 1.8. The U-Fe eutectic temperature is above that of normal reactor temperatures, whereas the Pu-Fe eutectic temperature is problematic as it is well below normal operating temperatures. Although a discreet Pu_6Fe phase is not expected to form, given Pu is typically alloyed into U-Pu-Zr fuels, localized liquefaction has been observed in diffusion couple experiments on the fuel side of the diffusion interface when the Pu concentration in the $(U,Pu)_6Fe$ phase reaches its solubility limit, believed to be ~16 at.% [21,23].

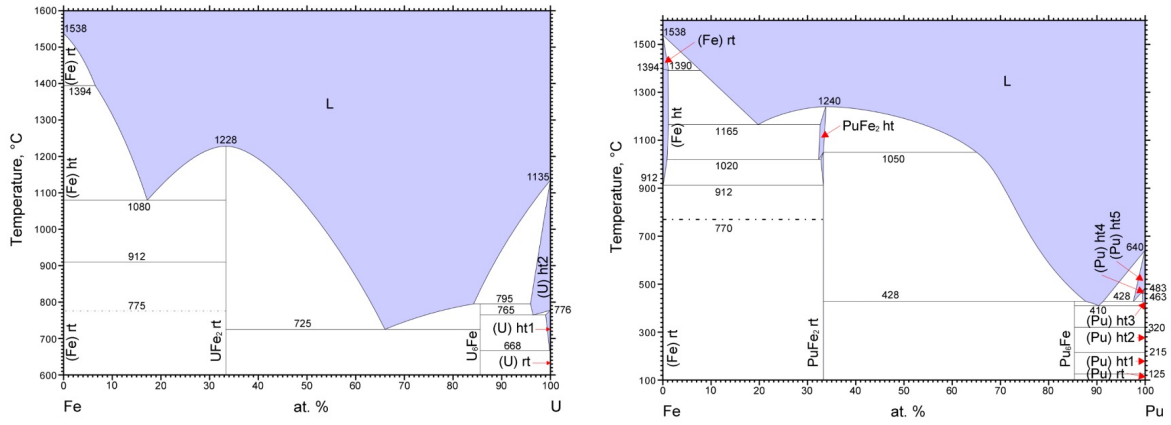

(a) (b)

Figure 1.8. (a) U-Fe binary phase diagram [24] and (b) Pu-Fe binary phase diagram [25].

To evaluate the susceptibility of fuels to FCCI under off-normal reactor conditions Ogata *et al.* [26] performed a series of diffusion couple experiments between U-Zr alloys and elemental Fe to evaluate the growth of their interaction layer at 730ºC (1003K), which is just above the U-Fe eutectic temperature. To simulate steady-state fuel-cladding interaction at normal reactor temperatures, they first exposed several diffusion couples to long-term annealing at 650ºC (923K) and then exposed them to short term annealing at the elevated

temperature of 730ºC (1003K). Not surprisingly, they found evidence of liquefaction occurring at regions where the U_6Fe phase formed after annealing at the higher temperature. However, the diffusion couples that experienced initial annealing at lower temperatures experienced smaller reaction layers overall compared to those directly exposed to the higher annealing temperatures. It was believed at the lower temperatures the UFe_2 is more favored to form compared to the U_6Fe phase. Then at the higher annealing temperatures the U_6Fe phase preferentially forms over the UFe_2 phase, as discussed previously. It is believed the initial formation of the UFe_2 phase actually limits the formation of the U_6Fe phase at the higher temperatures, i.e. the phase that undergoes eutectic liquefaction, and thus limits the overall amount of interaction between the diffusing elements.

Regarding the role of Zr in the fuel, its alloying with U was found to improve the interactions between the fuel and cladding materials. This was attributed to a Zr-rich layer, i.e. Zr-rind, that formed at the fuel periphery, which appeared to inhibit major interactions from occurring between the fuel and cladding constituents. There are a few conjectures on the processes that drive the formation of the Zr-rind at the fuel surface. It was initially speculated that the Zr-rind formation was the result of the injection casting process used to fabricate fuel pins for EBR-II, where a ZrO_2 powder was placed within the mold to facilitate the fuels removal from the mold [4]. However, fuels fabricated using alternative processes without the ZrO_2 powder, e.g. arc-melting, still exhibited the formation of a Zr-rind. Therefore, the formation of the Zr-rind appears to not be dependent on the fabrication process. It is now largely accepted that the presence of the Zr-rind is the result of interstitial impurities, such as oxygen, nitrogen and carbon, which stabilize its formation. Amongst these, nitrogen is believed to be the primary impurity that leads to a stable Zr-rind. In addition to the introduction of impurities from the fabrication process, claddings having different concentrations of nitrogen can also affect the characteristics of the Zr-rind in the fuel. For example, claddings that exhibit a greater concentration of dissolved nitrogen tend to promote a larger Zr-rind, i.e. 316 stainless steel with 600 ppm compared to HT9 and D9 stainless steels with 40–50 ppm [5,27]. Further, it is also speculated that the formation of the Zr-rind is driven by the decomposition of the δ-Zr_2U phase within the fuel. At the fuel-cladding interface the δ-Zr_2U phase is believed to decompose in the presence of nitrogen, promoting the formation of the Zr-rind. In turn, this results in the formation of a layer within the fuel and next to the Zr-rind which tends to be

deficient in Zr i.e. a Zr-depleted zone [28–30]. Even with the formation of the Zr-rind, fuel components such as U are still found to interact with the cladding leading to the formation of the UFe_2 phase, or some variation of this phase depending on the constituents present, i.e. $(U,Pu)Fe_2$, $(U,Zr)(Fe,Cr)_2$, etc. Furthermore, cladding constituents such as Fe, are still observed to diffuse into the fuel. But all diffusion-based experiments appear to agree that the formation of the Zr-rind drastically reduces the level of interaction that occurs between the fuel and cladding. As for the continued interaction after the Zr-rind forms, some believe the components are able to diffuse through this interface formation, but likely at a reduced rate leading to a more limited interaction region [28,29]. However, Lee *et al.* [30] observed the formation of cracks in the Zr-rind after carrying out high temperature diffusion couple experiments between U-10Zr (wt.%) and HT9. They believed that these cracks provided a diffusion pathway for U to interact with the cladding forming a $(U,Zr)(Fe,Cr)_2$ phase. They further observed these cracks allowed Fe to diffuse into the fuel where it was observed to preferentially interact with Zr-rich precipitates. Additionally, it should be noted that in-pile experiments found that the areas exhibiting the greatest amount of FCCI in a fuel pin tend to correspond to areas where the Zr-rind was found to have cracked or otherwise had been compromised. However, it is difficult to state that cracks in the Zr-rind are the only pathway for U and Fe to diffuse through the Zr-rind because not every diffusion couple experiment observed such cracks when clearly observing U-Fe and Zr-rich layer formations as well as the diffusion of Fe and subsequent interaction with the fuel. Overall, the use of Zr greatly improves the FCCI performance between U-10Zr (wt.%) fuels and cladding alloys as long as the Zr-rind remains intact.

1.4.3 Role of cladding constituents in FCCI

Cladding constituents also play a major role in FCCI. The EPMA analysis detailed in Figure 1.6 (b) shows not only the diffusion of Fe and Ni into the fuel but also their level of depletion from the inside region of the cladding. Further, the Cr concentration is observed to be elevated in the cladding at the fuel-cladding interface, which is likely the result of the other cladding constituents diffusing out of the cladding. Over the development history of improving fuel performance, several alloys have been evaluated to be used as cladding, each showing a varying degree of interaction. Early fuel development utilized the austenitic, 300 series

stainless steels, e.g. 304L and 316. This was followed by the incorporation of the alloy D9, a titanium-modified, cold-worked austenitic stainless steel, and the alloy HT9, a ferritic/martensitic stainless steel, each of which showed a marked improvement in overall performance within the reactor compared to the 300 series alloys [31]. However, although these claddings showed improvement in performance, they still exhibited FCCI at elevated burnups, but in different ways, and largely dependent on their primary alloying constituents. For reference, Table 1.3 displays the nominal compositions of these cladding alloys. For D9 the primary alloying elements are Fe, Ni, and Cr whereas for HT9 they are Fe and Cr. It was previously discussed above in section 1.3.1 and observed in Figure 1.4 that the loss of alloying constituents in the cladding led to the formation of a ferrite phase in D9 and HT9. Although the ferrite formation occurred as the result of different processes, collectively such a phase formation contributes to cladding wastage or a loss of cladding strength. Further, it was previously discussed above (section 1.4.2) that the diffusion of Fe into the fuel can potentially lead to the formation of low melting phases in the fuel. Both of these two aspects of FCCI are problematic. Therefore, understanding how these claddings participate in FCCI becomes dependent on understanding the role of their primary alloying elements.

Table 1.3. Nominal compositions, in wt.%, of typical cladding alloys used historically in SFR systems [32].

Alloy	**Fe[a]**	**C**	**Si**	**Mn**	**Ni**	**Cr**	**Mo**	**Ti**	**W**	**V**	**Al**
316	Bal.	0.08	1.00	2.00	12.0	17.0	2.50	n/a	n/a	n/a	n/a
D9	Bal.	0.05	1.00	2.00	15.5	13.5	1.50	0.25	n/a	n/a	n/a
HT9	Bal.	0.20	0.25	0.55	0.55	11.8	1.00	n/a	0.50	0.30	n/a

[a]These are ferrous-based alloys and thus Fe makes up the remaining concentration of the alloy composition

Out-of-pile diffusion couple experiments performed by Keiser *et al.* [28] evaluated U-10Zr (wt.%) fuel against different alloy combinations of Fe, Ni and Cr to elucidate the level of interaction that occurs from each cladding component. Overall, their research determined that cladding alloys containing Ni exhibited the greatest amount of interactions, observing numerous phase formations within the fuel and the greatest depth of diffusion into the fuel. Further, in comparing diffusion couple experiments between U-10Zr (wt.%) and elemental Fe and a Fe-19Cr (wt.%) alloy, their research found that Cr-containing alloys showed slightly

more interaction compared to elemental Fe but both were considerably less than any of the Ni-containing alloys. They reason that Ni experiences greater interaction due to the greater number of potential phases it can form with both U and Zr compared to Fe and Cr. The observation of Fe-Cr alloys exhibiting slightly greater chemical interactions in comparison to elemental Fe was also an observation made by Nakamura *et al.* [33]. However, it should be noted that although Fe-Cr alloys may exhibit slightly increased levels of chemical interaction, Fe-12Cr wt.% cladding alloys such as HT9 are preferred due to other factors impacting their performance as a cladding, such as their resistance to irradiation-induced swelling.

Research has been performed by Nakumura *et al.* [34] to characterize the U-Zr-Fe ternary system and then in follow-on research by Nakumura *et al.* [33] shows the formation of such ternary phases experimentally through diffusion couple experiments between U-10Zr (wt.%) and a Fe and Fe-Cr alloy. Their research details the formation of three U-Zr-Fe ternary phases ε, λ, and χ; the compositions of which are U-(33–50)Zr-33Fe, U-(21–25)Zr-6Fe, and U-32Zr-50Fe (at.%), respectively [34]. Through their diffusion couple experiments they were able to identify all of these ternary phases forming within the fuel due to Fe diffusion from the cladding. Further, they observed Cr being dissolved within several of the phases at or near the diffusion interface, but Cr was not found to dissolve far into the fuel [33]. Additionally, observations made by Harp *et al.* [11] found that Fe and Ni diffusion into the fuel had the additional effect of promoting segregation of the U-Zr matrix.

Research has shown that Fe is considered to be an ultra-fast diffusing solute in Ce, Pr and Nd. This is attributed to the ability of solute atoms to enter into interstitial positions, which appears to be more easily attained due to the open structure of the rare-earths, i.e. lanthanide elements. The research also noted that other transition metals, such as Ni, exhibits fast diffusing mechanisms as well [35]. This was further observed by Inagaki *et al.* [20] where diffusion couple experiments were carried out between a lanthanide alloy, 13La-24Ce-12Pr-39Nd-12Sm (wt.%), and a Fe-12Cr (wt.%) alloy. They observed Fe had diffused up to 400 μm into the Ln alloy, where Ln elements had only diffused 100 μm into the Fe-Cr alloy.

Overall, interstitial diffusion likely explains why cladding elements, such as Fe and Ni, diffuse so readily into the fuel matrix. Furthermore, the build-up of lanthanide elements at the fuel periphery, as shown in Figure 1.5, could possibly give an avenue for Fe and Ni to easily diffuse into the fuel matrix. This does not completely account for all Fe and Ni diffusion into

the fuel as it has been observed to occur in non-lanthanide containing fuels as well. Instead the lanthanide-buildup at the fuel-cladding interface may act to enhance the diffusion of Fe and Ni into the fuel. Additionally, by observing the EPMA results of an FCCI region in Figure 1.6, it is noted that lanthanide elements, i.e. Ce, Nd, Sm, etc., are not found to diffuse farther into the cladding than the region depleted in Fe and Ni. In Figure 1.6 this is observed to be just short of 100 μm. It could be that lanthanide diffusion into the fuel is limited by Fe and Ni diffusion out of the cladding, thus the lanthanide movement into the cladding is likely based on substitutional diffusion. Further, the diffusion of lanthanides into the cladding may also be limited by each elements self-diffusion through the $(Fe,Cr)_{17}Ln_2$ layer that forms just inside the cladding.

1.4.4 Additional diffusion mechanisms

In addition to the more traditional diffusion mechanisms, radiation enhanced diffusion (RED) adds additional complexity to the kinetics of the FCCI phenomenon [6]. Through irradiation, the formation of defects, such as vacancies, within a matrix can lead to a system that components can more readily diffuse through. Understanding the diffusion of lattice atoms by the vacancy mechanism can be determined by:

$$D_a^V = f_V D_V C_V \tag{1.1}$$

where D_V is the vacancy diffusion coefficient, C_V is the vacancy concentration and f_V is the correlation coefficient. From this equation, it can be interpreted that with an increase in the vacancy concentration (C_V) due to irradiation damage, the diffusion rate of atoms via vacancy exchange ($\sim D_a^V$) will also increase. It is also worth noting that radiation-induced defects can include both the formation of interstitial and di-vacancy defects. Such defects, in addition to monovacancy formations, can contribute to the overall diffusion of atoms [36]. An increase in the vacancy concentration, for example in the cladding, due to irradiation may contribute to the diffusion of both the lanthanides and fuel constituents into the cladding via vacancy-based diffusion. That and the depletion of Fe and Ni from within the cladding likely facilitates the infiltration from the fuel. Furthermore, as previously discussed, lanthanides such as Nd, have recently been observed to infiltrate the cladding through grain boundaries and such surface-based diffusion mechanisms tends to exhibit diffusivities with lower activation energies

compared to lattice-based diffusion mechanisms. Thus, constituents that exhibit such surface-based diffusion mechanisms has the potential to more easily diffuse into the cladding or fuel.

1.5 Controlling FCCI

1.5.1 Diffusion barriers

Countering such inter-diffusion, it was previously noted that the formation of the Zr-rind acted as a natural diffusion barrier to FCCI. It was further determined the formation of a Zr-rind in the presence of claddings with interstitial impurities, i.e. N, C, or O, would in turn more readily stabilize the Zr-rich layers further impeding the inter-diffusion process [5,16]. This is likely because the interstitial diffusion mechanism, previously discussed as a potential mechanism for Fe and Ni to diffuse into the fuel, is being limited due to the occupation of interstitial sites within the Zr-rind by nitrogen, for example. Therefore, research by Khatkhatay *et al.* [37] evaluated the effectiveness of ZrN and TiN coatings as diffusion barriers. Through diffusion couple experiments, both coatings proved to be effective in mitigating interaction between Fe and Ce. Additional research was performed by Kim *et al.* [38] to evaluate the effectiveness of deposited layers of zirconium, chromium and titanium to act as diffusion barriers. Their research evaluated diffusion couple experiments between U-10Zr (wt.%) and HT9, experimenting with various combinations of the barrier coatings. They found that only the pure zirconium coating remained intact through the experiment while the multi-element coatings broke down through the experiment. However, in all experiments Fe and Cr were still found within the fuel, *al beit* to a lesser extent compared to the experiment where no coating was employed, indicating their diffusion through the barriers. This aligns with previous discussions on the Zr-rind and how cladding components were still observed to diffuse through. This would also appear to indicate an effective barrier must block interstitial-based diffusion. Other research on the effectiveness of coatings and the use of other coatings, such as TiO_2 and yttrium-stabilized ZrO_2 (YSZ), have also been carried out [39–41]. However, it should be noted that the deployment and robustness of such coatings is of concern. Whether applied to the internal surface of the claddings or to the exterior surface of the fuel, it is difficult to know if the coatings will be maintained through normal fuel loading procedures.

In addition to coatings the use of foils has also been evaluated. Foils of pure metals, such as Zr, niobium (Nb), titanium (Ti), vanadium (V), and Cr, to name a few, have also been

proposed [42,43]. The use of pure Zr foils ended up dissolving through the diffusion experiments due to the solubility of Zr in U. This was also observed with both Nb and Ti foils. The use of Cr and V foils proved to be successful in mitigating interactions between U-10Zr (wt.%) and HT9 [42]. Research by Lee *et al.* [43] also found that the use of a Zr foil was not effective in limiting interaction between lanthanide elements and HT9, but interestingly they found that when Zr foils are paired with a deposited Zr coating the interactions are mitigated. They attributed this change to the belief that the Zr coating was likely covering defects in the Zr foil that would otherwise have promoted interaction.

1.5.2 Fuel-based additives

Another method proposed to mitigate lanthanide interactions with cladding constituents is through the utilization of additives alloyed into the fuel. The use of additives is not to necessarily immobilize the fission products within the fuel matrix but rather to form high-temperature, stable intermetallic compounds with the lanthanide elements so that they no longer interact with the cladding constituents. It should be noted that the use of additives is not expected to alleviate all FCCI, such as that of cladding components diffusing into the fuel, but instead to limit the detrimental effects of lanthanide-based intermetallic phase formations within the cladding that contribute to cladding wastage. Thus, through the use of additives, a significant portion of the FCCI phenomenon may be mitigated or at the very least limited so that the fuel can achieve greater burn-up without major cladding issues. Research conducted by Mariani *et al.* [7] proposed intentionally alloying metal fuel with palladium (Pd) due to its high propensity to form compounds with lanthanide elements. Through their research they documented Pd-Ln formations through the fabrication of U-Zr-Pd-Ln alloys. Further, in the analysis of irradiated U-10Zr (wt.%) fuel, Harp *et al.* [11] observed Pd, which evolves in small concentrations as a fission product within metallic fuel, binding with lanthanide elements to form stable Pd-Ln precipitates within the fuel. Figure 1.9 details Pd-Ln precipitate formations observed in the research conducted by both Mariani *et al.* [7] and Harp *et al.* [11].

Beyond Pd, Mariani *et al.* [7], also proposed additional elements that may serve as potential fuel-based additives. Based on thermodynamic and other considerations, tin (Sn), antimony (Sb) and tellurium (Te) were also proposed as potential additives. Other work by Kim *et al.* [44] proposed thallium (Tl), gallium (Ga) and indium (In) as potential additives,

primarily based on enthalpy of formation calculations between potential additives and lanthanide elements. Research in the area of fuel-based additives is ongoing and prior to the research effort discussed in this dissertation the main focus has been on both Pd and In. To date, the majority of research has been in the area of out-of-pile experiments, e.g. diffusion couple experiments, with favorable results indicating the viability of additives to mitigate FCCI. However, recent irradiation experiments carried out and characterized by Harp *et al.* [45] indicated mixed results on the effectiveness of alloying the U-Zr fuel with Pd. Favorable results were observed in the fuels having lower Pd concentrations of 1 and 2 wt.%, but when the Pd concentration was elevated to 4 wt.%, FCCI was observed even though the burnup was low; between 2–3% FIMA (fissions per initial metal atom), meaning very little lanthanide had formed. It was found that in alloying Pd with U-Zr, it initially forms compounds with Zr, but then preferentially binds with lanthanide elements as they form in the fuel. Thus, upon initial irradiation and before lanthanides form in the fuel, the Pd is bound to Zr removing it from the matrix [46,47]. In the work by Harp *et al.* [45], they observed in their irradiation experiments the alloys having a higher concentration of Pd resulted in a higher level of Pd-Zr interaction. This in turn left a higher concentration of un-alloyed U in the fuel and thus the FCCI that was observed was likely the result of U-Fe interactions. Due to such Pd-Zr interactions, a higher concentration of Zr is being evaluated for additive-containing fuel alloys to negate such adverse effects [48,49].

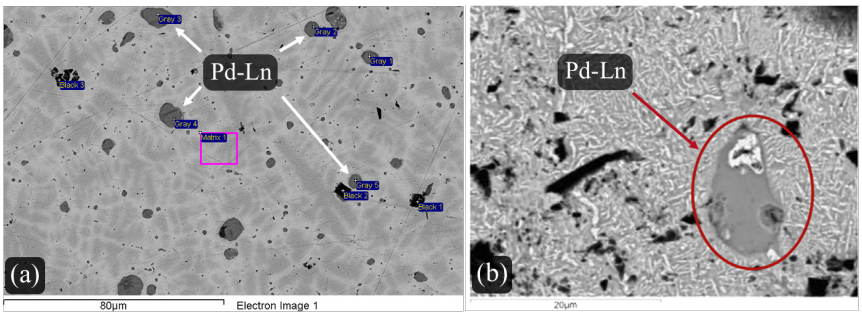

Figure 1.9. (a) BSE micrograph of U-15Zr-1.16Pd-2.15Ln (wt.%) alloy, where Ln is an alloy of 53Nd-25Ce-16Pr-6La, wt.% [7]. (b) BSE micrograph of irradiated U-10Zr (wt.%) where Pd-Ln precipitates were observed to form [11].

In addition to Pd and In additives, to date research has been carried out evaluating the viability of Sn [50], Sb [51–53], Sn + Sb [54], and Te [55,56] as additives. Discussions on the additives Sb and Te are provided at length in later chapters of this dissertation. An evaluation

of Sn is provided by Benson *et al.*[50]. They observed Sn also tends to bind with Zr, forming Zr_5Sn_3 precipitates in U-Zr-Sn alloys. It was noted that the Zr_5Sn_3 intermetallic has an additive-zirconium ratio that is less, compared to that of the additive Pd, which was observed to form Zr_2Pd precipitates. This indicates the Sn additive would remove less Zr from the U-Zr matrix. Benson further evaluated the interactions of Sn in the presence of lanthanides by evaluating a U-Zr-Sn-Ln alloy (Ln = 53Nd-25Ce-16Pr-6La wt.%). It was found that Sn left Zr and preferentially bound to the lanthanide elements. However, they found that Zr was still contained within the Sn-Ln precipitates forming either a Ln_5Sn_3 or $(Ln,Zr)_5Sn_3$ precipitate. They were unable to conclude if the Zr was dissolved within the precipitates or if Zr atoms were substituting for Ln atoms within the Ln_5Sn_3 lattice. The latter is supported by the fact that the crystal structures of Zr_5Sn_3 and Nd_5Sn_3, along with high temperature crystal structures of Ce_5Sn_3, Pr_5Sn_3 and La_5Sn_3 are of the same space group and crystal prototype. The continued engagement of Zr within Sn-Ln precipitates may be problematic, however, the decreased concentration of Zr being removed from the U-Zr matrix in its BOL condition is promising. Given additives may exhibit varying reactivities with different lanthanides, a multi-additive alloy has also been explored using both Sn and Sb. Research by Benson *et al.* [54] fabricated and characterized the interactions observed within U-10Zr-2Sn-2Sb (wt.%) and U-10Zr-2Sn-2Sb-4Ln (wt.%) alloys. In the former alloy, as previously observed in other additives, the additives were preferentially binding with Zr to form $Zr_5(Sn,Sb)_3$ precipitates. This was the same precipitate observed to form in the U-Zr-Sn alloy [50] and although this is a stable Zr-Sb phase, deviates from Zr_2Sb precipitates observed to form in a U-Zr-Sb alloy by Xie *et al.* [53]. Within the U-Zr-Sn-Sb-Ln alloy both $Ln_5(Sn,Sb)_4$ and $Zr_5(Sn,Sb)_3$ compounds were observed to form. It was noted that the alloy was fabricated to be slightly additive-rich, thus the formation of the Zr-(Sn,Sb) precipitates was not surprising. However, it was noted that Sb was forming in greater concentrations within the $Ln_5(Sn,Sb)_4$ compounds where Sn was forming in greater concentrations within the $Zr_5(Sn,Sb)_3$ compounds. The authors were unable to conclude if the results were due to greater Sn-Zr or Sb-Ln attraction. Initially the multi-additive approach was to evaluate if the additives experience varying reactivities with different lanthanides, but instead this research reveals competing additive reactivities between Zr and Ln elements. However, one conclusion that should be noted is that with the introduction of lanthanide elements into the U-Zr-Sn-Sb alloy, Sb was observed to leave the Zr-(Sn,Sb) precipitates to

preferentially bind with Ln precipitates, where Sn preferentially remains with Zr precipitates. This result still indicates favorability of these additives to bind with lanthanide elements. It is likely due to these favorable results that Pd, Sn, and Sb are being continued to be evaluated in irradiation-based experiments, where U-Zr-Pd, U-Zr-Sn and U-Zr-Sb alloys are being included in the Advanced Fuels Campaign (AFC) Fission Accelerated Steady-State Test (FAST) series of irradiation experiments to take place in INL's Advanced Test Reactor (ATR).

Modeling methods, such as atomistic-based models, have also been developed to evaluate the interactions of other elements with lanthanides and have determined a list of other viable additives. These additives include arsenic (As) [57,58], selenium (Se) [58], and bismuth (Bi) [59], which have undergone limited research thus far. In addition to the references cited, the initial experimental carried out to validate models predicting both As and Se is provided in Appendix B of this dissertation.

The following research described in this doctoral dissertation will detail the investigation of both Te and Sb as potential additives and their propensity to interact and bind with Nd, being a major lanthanide element involved in FCCI. Additionally, initial experimental work evaluating the viability of As will also be discussed.

References

[1] OECD Nuclear Energy Agency, Technology Roadmap Update for Generation IV Nuclear Energy Systems, 2014. https://www.gen-4.org/gif/upload/docs/application/pdf/2014-03/gif-tru2014.pdf.

[2] D.C. Crawford, D.L. Porter, S.L. Hayes, Fuels for sodium-cooled fast reactors: US perspective, Journal of Nuclear Materials. 371 (2007) 202–231. https://doi.org/10.1016/j.jnucmat.2007.05.010.

[3] D.D. Keiser Jr., M.C. Petri, Interdiffusion behavior in U-Pu-Zr fuel versus stainless steel couples, Journal of Nuclear Materials. 240 (1996) 51–61. https://doi.org/10.1016/S0022-3115(96)00476-X.

[4] C. Matthews, C. Unal, J. Galloway, D.D. Keiser, S.L. Hayes, Fuel-cladding chemical interaction in U-Pu-Zr metallic fuels: A critical review, Nuclear Technology. 198 (2017) 231–259. https://doi.org/10.1080/00295450.2017.1323535.

[5] G.L. Hofman, L.C. Walters, T.H. Bauer, Metallic fast reactor fuels, Progress in Nuclear Energy. 31 (1997) 83–110. https://doi.org/10.1016/0149-1970(96)00005-4.

[6] D.D. Keiser Jr., Metal fuel-cladding interaction, Comprehensive Nuclear Materials. 3 (2012) 423–441. https://doi.org/10.1016/B978-0-08-056033-5.00067-7.

[7] R.D. Mariani, D.L. Porter, T.P. O'Holleran, S.L. Hayes, J.R. Kennedy, Lanthanides in metallic nuclear fuels: Their behavior and methods for their control, Journal of Nuclear Materials. 419 (2011) 263–271. https://doi.org/10.1016/j.jnucmat.2011.08.036.

[8] D.E. Burkes, R.S. Fielding, D.L. Porter, D.C. Crawford, M.K. Meyer, A US perspective on fast reactor fuel fabrication technology and experience part I: metal fuels and assembly design, Journal of Nuclear Materials. 389 (2009) 458–469. https://doi.org/10.1016/j.jnucmat.2009.02.035.

[9] T. Ogata, Metal Fuel, in: Comprehensive Nuclear Materials, Elsevier, 2012: pp. 1–40. https://doi.org/10.1016/B978-0-08-056033-5.00049-5.

[10] W.J. Carmack, D.L. Porter, Y.I. Chang, S.L. Hayes, M.K. Meyer, D.E. Burkes, C.B. Lee, T. Mizuno, F. Delage, J. Somers, Metallic fuels for advanced reactors, Journal of Nuclear Materials. 392 (2009) 139–150. https://doi.org/10.1016/j.jnucmat.2009.03.007.

[11] J.M. Harp, D.L. Porter, B.D. Miller, T.L. Trowbridge, W.J. Carmack, Scanning electron microscopy examination of a Fast Flux Test Facility irradiated U-10Zr fuel cross section clad with HT-9, Journal of Nuclear Materials. 494 (2017) 227–239. https://doi.org/10.1016/j.jnucmat.2017.07.040.

[12] Y.S. Kim, G.L. Hofman, S.L. Hayes, Y.H. Sohn, Constituent redistribution in U-Pu-Zr fuel during irradiation, Journal of Nuclear Materials. 327 (2004) 27–36. https://doi.org/10.1016/j.jnucmat.2004.01.012.

[13] W.J. Carmack, Temperature and Burnup Correlated FCCI in U- 10Zr Metallic Fuel Metallic Fuel, 2012.

[14] T. Ogata, T. Yokoo, Development and Validation of ALFUS: An Irradiation Behavior Analysis Code for Metallic Fast Reactor Fuels, Nuclear Technology. 128 (1999) 113–123. https://doi.org/10.13182/NT99-A3018.

[15] D.D. Keiser, Fuel-Cladding Interaction Layers in Irradiated U-Zr and U-Pu-Zr Fuel Elements, 2006. http://www.osti.gov/bridge/product.biblio.jsp?osti_id=885496 (accessed October 6, 2016).

[16] C. Unal, C. Matthews, L. Xiang, J. Isler, J. Zhang, J. Galloway, A Potential Mechanism for Lanthanide Transport in Metallic Fuels, Transaction of the American Nuclear Society. 116 (2017) 501–503.

[17] X. Li, A. Samin, J. Zhang, C. Unal, R.D. Mariani, Ab-initio molecular dynamics study of lanthanides in liquid sodium, Journal of Nuclear Materials. 484 (2017) 98–102. https://doi.org/10.1016/j.jnucmat.2016.11.028.

[18] L.C. Walters, Thirty years of fuels and materials information from EBR-II, Journal of Nuclear Materials. 270 (1999) 39–48. https://doi.org/10.1016/S0022-3115(98)00760-0.

[19] D.D. Keiser Jr., Fuel cladding chemical interaction in metallic sodium fast reactor fuels: A historical perspective, Journal of Nuclear Materials. 514 (2019) 393–398. https://doi.org/10.1016/j.jnucmat.2018.09.045.

[20] K. Inagaki, T. Ogata, Reaction of lanthanide elements with Fe-Cr alloy, Journal of Nuclear Materials. 441 (2013) 574–578. https://doi.org/10.1016/j.jnucmat.2013.04.046.

[21] K. Nakamura, T. Ogata, M. Kurata, T. Yokoo, M. a. Mignanelli, Reactions of Uranium-Plutonium Alloys with Iron, Journal of Nuclear Science and Technology. 38 (2001) 112–119. https://doi.org/10.1080/18811248.2001.9715013.

[22] K. Huang, Y. Park, A. Ewh, B.H. Sencer, J.R. Kennedy, K.R. Coffey, Y.H. Sohn, Interdiffusion and reaction between uranium and iron, Journal of Nuclear Materials. 424 (2012) 82–88. https://doi.org/10.1016/j.jnucmat.2012.02.004.

[23] T. Ogata, K. Nakamura, M. Kurata, T. Yokoo, M.A. Mignanelli, Reactions between U-Pu-Zr Alloys and Fe at 923 K, Journal of Nuclear Science and Technology. 37 (2000) 244–252. https://doi.org/10.1080/18811248.2000.9714890.

[24] H. Okamoto, Fe-U (Iron - Uranium), in: T.B. Massalski, H. Okamoto, P.R. Subramanian, L. Kacprzak (Eds.), Binary Alloy Phase Diagrams, II, ASM International, 1990.

[25] H. Okamoto, Fe-Pu (Iron-Plutonium), in: T.B. Massalski, H. Okamoto, P.R. Subramanian, L. Kacprzak (Eds.), Binary Alloy Phase Diagrams, II, ASM International, 1990.

[26] T. Ogata, K. Nakamura, A. Itoh, M. Akabori, Reactions between U–Zr alloys and Fe at 1003 K, Journal of Nuclear Materials. 441 (2013) 579–582. https://doi.org/10.1016/J.JNUCMAT.2012.09.038.

[27] G.L. Hofman, A.G. Hins, D.L. Porter, L. Leibowitz, E.L. Wood, Chemical Interaction of Metallic Fuel with Austenitic and Ferritic Stainless Steel Cladding, in: International Conference on Reliable Fuels for Liquid Metal Reactors, Tucson, Ar, 1986.

[28] D.D. Keiser, M.A. Dayananda, Interdiffusion between U-Zr fuel and selected Fe-Ni-Cr alloys, Journal of Nuclear Materials. 200 (1993) 229–243. https://doi.org/10.1016/0022-3115(93)90334-U.

[29] S. Kaity, J. Banerjee, S.C. Parida, A. Laik, C.B. Basak, V. Bhasin, Studies on fuel-cladding chemical interaction between U−10 wt%Zr alloy and T91 steel, Journal of Nuclear Materials. 513 (2019) 16–32. https://doi.org/10.1016/j.jnucmat.2018.10.041.

[30] C.T. Lee, H. Kim, T.K. Kim, C.B. Lee, Diffusion behavior in an interface between U–10Zr alloy and HT-9 steel, Journal of Nuclear Materials. 395 (2009) 140–144. https://doi.org/10.1016/j.jnucmat.2009.10.044.

[31] R.G. Pahl, D.L. Porter, D.C. Crawford, L.C. Walters, Irradiation behavior of metallic fast reactor fuels, Journal of Nuclear Materials. 188 (1992) 3–9. https://doi.org/10.1016/0022-3115(92)90447-S.

[32] J.H. Kittel, B.R.T. Frost, J.P. Mustelier, K.Q. Bagley, G.C. Crittenden, J. van Dievoet, History of fast reactor fuel development, Journal of Nuclear Materials. 204 (1993) 1–13. https://doi.org/10.1016/0022-3115(93)90193-3.

[33] K. Nakamura, T. Ogata, M. Kurata, A. Itoh, M. Akabori, Reactions of U–Zr alloy with Fe and Fe–Cr alloy, Journal of Nuclear Materials. 275 (1999) 246–254. https://doi.org/10.1016/S0022-3115(99)00227-5.

[34] K. Nakamura, M. Kurata, T. Ogata, A. Itoh, M. Akabori, Equilibrium phase relations in the U–Zr–Fe ternary system, Journal of Nuclear Materials. 275 (1999) 151–157. https://doi.org/10.1016/S0022-3115(99)00116-6.

[35] M.P. Dariel, The Solute Diffusion of Iron in the Light Rare-Earth Metals Cerium, Praseodymium and Neodymium., Acta Metallurgica. 23 (1975).

[36] G.S. Was, Radiation-Enhanced Diffusion and Defect Reaction Rate Theory, in: Fundamentals of Radiation Materials Science, Springer US, 2007: pp. 191–221.

[37] F. Khatkhatay, J. Jian, L. Jiao, Q. Su, J. Gan, J. Cole, H. Wanga, Diffusion barrier properties of nitride-based coatings on fuel cladding, Journal of Alloys and Compounds. 580 (2013) 442–448. https://doi.org/10.1016/j.jallcom.2013.06.108.

[38] J.H. Kim, H.J. Ryu, J.H. Baek, S.J. Oh, B.O. Lee, C.B. Lee, Y.S. Yoon, Performance of a diffusion barrier under a fuel-clad chemical interaction (FCCI), Journal of Nuclear Materials. 394 (2009) 144–150. https://doi.org/10.1016/j.jnucmat.2009.08.018.

[39] V. Firouzdor, J. Brechtl, B. Hauch, K. Sridharan, T. Allen, Electrophoretic deposition of diffusion barrier titanium oxide coatings for nuclear reactor cladding applications, Applied Surface Science. 282 (2013) 798–808. https://doi.org/10.1016/j.apsusc.2013.06.058.

[40] V. Firouzdor, J. Brechtl, L. Wilson, B. Semerau, K. Sridharan, T. Allen, Development of titanium diffusion barrier coatings for mitigation of fuel-cladding chemical interactions, Surface and Coatings Technology. 219 (2013) 59–68. https://doi.org/10.1016/j.surfcoat.2013.01.005.

[41] V. Firouzdor, J. Brechtl, L. Wilson, B. Semerau, K. Sridharan, T. Allen, Development of Yttrium Stabilized Zirconia (YSZ) diffusion barrier coatings for mitigation of Fuel-Cladding Chemical Interactions, Journal of Nuclear Materials. 438 (2013) 268–277. https://doi.org/10.1016/j.jnucmat.2013.02.032.

[42] H.J. Ryu, B.O. Lee, S.J. Oh, J.H. Kim, C.B. Lee, Performance of FCCI barrier foils for U-Zr-X metallic fuel, Journal of Nuclear Materials. 392 (2009) 206–212. https://doi.org/10.1016/j.jnucmat.2009.03.011.

[43] K.S. Lee, I.Y. Kim, W. Lee, Y.S. Yoon, Effect of Zr thin film on Zr foil as a FCCI barrier between lanthanide (La-Ce) and clad material, Metals and Materials International. 21 (2015) 498–503. https://doi.org/10.1007/s12540-015-4433-7.

[44] Y.S. Kim, G.L. Hofman, A.M. Yacout, Migration of minor actinides and lanthanides in fast reactor metallic fuel, Journal of Nuclear Materials. 392 (2009) 164–170. https://doi.org/10.1016/j.jnucmat.2009.03.043.

[45] J.M. Harp, H.J.M. Chichester, L. Capriotti, Postirradiation examination results of several metallic fuel alloys and forms from low burnup AFC irradiations, Journal of Nuclear Materials. 509 (2018) 377–391. https://doi.org/10.1016/J.JNUCMAT.2018.07.003.

[46] M.T. Benson, L. He, J.A. King, R.D. Mariani, Microstructural characterization of annealed U-12Zr-4Pd and U-12Zr-4Pd-5Ln: Investigating Pd as a metallic fuel additive, Journal of Nuclear Materials. 502 (2018) 106–112. https://doi.org/10.1016/j.jnucmat.2018.02.012.

[47] M.T. Benson, L. He, J.A. King, R.D. Mariani, A.J. Winston, J.W. Madden, Microstructural characterization of as-cast U-20Pu-10Zr-3.86Pd and U-20Pu-10Zr-3.86Pd-4.3Ln, Journal of Nuclear Materials. 508 (2018) 310–318. https://doi.org/10.1016/J.JNUCMAT.2018.05.062.

[48] J.M. Harp, L. Capriotti, F. Cappia, Baseline Postirradiation Examination of the AFC-3C, AFC-3D, and AFC-4A Experiments, 2018. https://doi.org/10.2172/1498255.

[49] F.G. di Lemma, T.L. Trowbridge, L. Capriotti, J.M. Harp, M.T. Benson, R.D. Mariani, Palladium influence on fuel performance in irradiated metallic fuel, Journal of Nuclear Materials. SUBMITTED (2021).

[50] M.T. Benson, J.A. King, R.D. Mariani, M.C. Marshall, SEM characterization of two advanced fuel alloys: U-10Zr-4.3Sn and U-10Zr-4.3Sn-4.7Ln, Journal of Nuclear Materials. 494 (2017) 334–341. https://doi.org/10.1016/j.jnucmat.2017.07.057.

[51] Y. Xie, J. Zhang, M.T. Benson, R.D. Mariani, Diffusion behavior of lanthanide-additive compounds (Ce 4 Sb 3 , Ce 2 Sb, and CeTe) against HT9 and Fe, Materials Characterization. 150 (2019) 107–117. https://doi.org/10.1016/j.matchar.2019.02.012.

[52] Y. Xie, J. Zhang, M.T. Benson, R.D. Mariani, Thermodynamic stability studies of Ce-Sb compounds with Fe, Journal of Nuclear Materials. 499 (2018) 440–445. https://doi.org/10.1016/j.jnucmat.2017.12.008.

[53] Y. Xie, M.T. Benson, J.A. King, R.D. Mariani, J. Zhang, Characterization of U-Zr fuel with alloying additive Sb for immobilizing fission product lanthanides, Journal of Nuclear Materials. 498 (2018) 332–340. https://doi.org/10.1016/j.jnucmat.2017.10.039.

[54] M.T. Benson, Y. Xie, J.A. King, R.D. Mariani, I. Charit, J. Zhang, M.P. Short, S. Choudhury, R. Khanal, N. Jerred, Characterization of U-10Zr-2Sn-2Sb and U-10Zr-2Sn-2Sb-4Ln to assess Sn+Sb as a mixed additive system to bind lanthanides, Journal of Nuclear Materials. 510 (2018) 210–218. https://doi.org/10.1016/j.jnucmat.2018.08.017.

[55] N.D. Jerred, R. Khanal, M.T. Benson, E. Perez, J.A. King, M. Dubey, J. Burns, I. Charit, S. Choudhury, R.D. Mariani, Evaluation of Tellurium as a Fuel Additive in Neodymium-Containing U-Zr Metallic Fuel, Scientific Reports. 9 (2019) 1–14. https://doi.org/10.1038/s41598-019-51852-z.

[56] Y. Xie, J. Zhang, M.T. Benson, J.A. King, R.D. Mariani, Assessment of Te as a U-Zr fuel additive to mitigate fuel-cladding chemical interactions, Journal of Nuclear Materials. 513 (2019) 175–184. https://doi.org/10.1016/j.jnucmat.2018.10.050.

[57] R. Khanal, N. Jerred, M.T. Benson, D.A. Andersson, R.D. Mariani, I. Charit, S. Choudhury, A novel approach to selection of dopant to immobilize neodymium in uranium-based metallic fuels, Journal of Nuclear Materials. 529 (2020) 151922. https://doi.org/10.1016/j.jnucmat.2019.151922.

[58] R. Khanal, N. Jerred, M.T. Benson, Y. Xie, R.D. Mariani, Interactions and immobilization of lanthanides with dopants in uranium-based metallic fuels, Journal of Nuclear Materials. 540 (2020) 152372. https://doi.org/10.1016/j.jnucmat.2020.152372.

[59] C. Jiang, Y. Xie, M.T. Benson, Efficient computational search for lanthanide-binding additive dopants for advanced U-Zr based fuels, Materialia. 10 (2020) 100653. https://doi.org/10.1016/j.mtla.2020.100653.

CHAPTER 2
Nd, SbNd AND Sb_3Nd_4 AND THEIR INTERACTIONS WITH THE CLADDING ALLOY HT9

Published in the Journal of Nuclear Materials in December 2020.
"Nd, SbNd and Sb_3Nd_4 and their interactions with the cladding alloy HT9." *J. Nucl. Mater.* 541:152387 (2020). https://doi.org/10.1016/j.jnucmat.2020.152387

Abstract. Lanthanide fission products, such as neodymium, formed during the irradiation of metallic fuels are known to cause deleterious effects from chemical interactions occurring at the fuel-cladding interface; a phenomenon known as fuel-cladding chemical interaction (FCCI). The use of fuel-based additives that bind with the lanthanide elements within the fuel meat, alleviating their interactions at the fuel-cladding interface, is one potential method proposed to mitigate the FCCI phenomenon and extend the burnup potential of such metallic fuel systems. In this study, antimony (Sb) is evaluated as one such additive, and neodymium (Nd) is used to represent the lanthanides. A Sb-Nd alloy is fabricated, which consists of two intermetallic phases, SbNd and Sb_3Nd_4. Isothermal diffusion couple experiments are carried out at 675 °C for 24 h between Nd and the Fe-12Cr based HT9 cladding alloy. The results are compared against similar diffusion couple experiments carried out between the Sb-Nd alloy and also HT9. Inter-diffusion between Nd/HT9 diffusion couple is characterized and the phases $Fe_{17}Nd_5$ and $Fe_{17}Nd_2$ were found to form whereas no interactions were observed in the Sb-Nd/HT9 diffusion couple. The lack of compound forming tendencies between Fe, the primary alloying constituent of HT9, and SbNd is elucidated through density functional theory (DFT) calculations on enthalpy of mixing, aligning well with the experimental observations. The strong binding of Nd with Sb appears to be favorable, alleviating Nd interactions with HT9 constituent elements.

2.1 Introduction

Metallic fuel systems, e.g. U-Zr and U-Pu-Zr, continue to be attractive for advanced nuclear reactor concepts, such as the advanced sodium-cooled fast reactor (SFR) [1–3]. However, the tendency of chemical interactions between fuel, fission product and cladding constituents occurring at the fuel-cladding interface greatly limits their burnup potential. Particularly, the lanthanide elements, e.g. neodymium (Nd), cerium (Ce), lanthanum (La) and praseodymium (Pr), have been found to be a major driver of chemical interactions at this interface, generally termed fuel-cladding chemical interaction (FCCI). The lanthanides form in the fuel as fission products and tend to migrate to the fuel-cladding interface, driven primarily by temperature gradients [4–6]. The onset of FCCI can lead to the formation of interaction regions where brittle and low-melting phases form, exacerbating cladding wastage, which can eventually lead to cladding breach [4]. The use of alloying additives to the fuel matrix is one approach being evaluated toward mitigating the negative effects of FCCI. This is accomplished by using additives that bind with and form high temperature, stable compounds with the lanthanide elements as they form within the fuel matrix. In turn, the formation of such stable lanthanide-additive compounds restricts their participation in FCCI. An evaluation of potential additives to bind with the lanthanides has been presented by Mariani *et al.* [6] and several additives have thus far been studied—palladium (Pd) [6,7], tin (Sn) [8], antimony (Sb) [9,10], Sn+Sb [11], tellurium (Te) [12,13], arsenic (As) [14–16], selenium (Se) [16], and bismuth (Bi) [17]. Mariani *et al.* [6], further detailed that the total concentration of lanthanides to form as fission products within U-10wt.%Zr fuel at 8 at.% burnup is ~2.6 at.%. Furthermore, they promoted utilizing an additive concentration that matches the expected formation of lanthanides within the fuel at a 1:1 atomic ratio. The same concept of utilizing a 1:1 atomic ratio (additive:lanthanide) was carried into this research.

In this study, Nd is used as the lanthanide element as it forms in the highest concentration of all the lanthanide fission products within irradiated U-Zr fuel [6]. The, effectiveness of Sb as an additive to stabilize Nd and prevent its interaction with the Fe-12Cr based cladding alloy HT9 is evaluated. Isothermal diffusion couple experiments are carried out for Nd/HT9 and Sb-Nd/HT9 in order to understand their interactions and to reveal the efficacy of Sb to limit FCCI. Previous research on Sb as an additive [9–11] focused on characterizing the phase formations observed between Sb and different lanthanide elements. In that study, Sb

was found to effectively bind with lanthanide elements within the U-Zr matrix. More recent research carried out by Zhuo *et al.* [18] evaluated the behavior of Sb in U-metal and then in the presence of the lanthanide cerium (Ce). They found that in the U-Sb alloy, intermetallics formed between Sb and U, whereas in the U-Sb-Ce alloy, Sb showed more favorable interactions with Ce. Additionally, previous diffusion couple experiments performed by Xie *et al.* [19] found that Sb was effective in limiting the interaction of Ce with both Fe and HT9. Furthermore, isothermal diffusion experiments carried out by Egeland *et al.* [20] showed a high level of interaction between Nd/Fe and this research will expand upon that work carrying out similar experiments between Nd and HT9 and characterizing their interactions. It should be noted, in evaluating the Fe-Nd binary phase diagram, shown in Figure 2.1 (a), this system experiences a low-melting eutectic reaction at 685 °C (985 K) [21]. The eutectic reaction is the combination of the $Fe_{17}Nd_5$ phase and elemental Nd. Given the Fe-Nd reaction is an Nd-rich reaction such a liquid phase formation could occur at the fuel periphery. Thus, if a reactor system experiences an off-normal event and the fuel-cladding interface exceeds 685 °C (985 K) the formation of a liquid phase of the Fe and Nd interactions would be possible and thus exacerbate adverse chemical interactions.

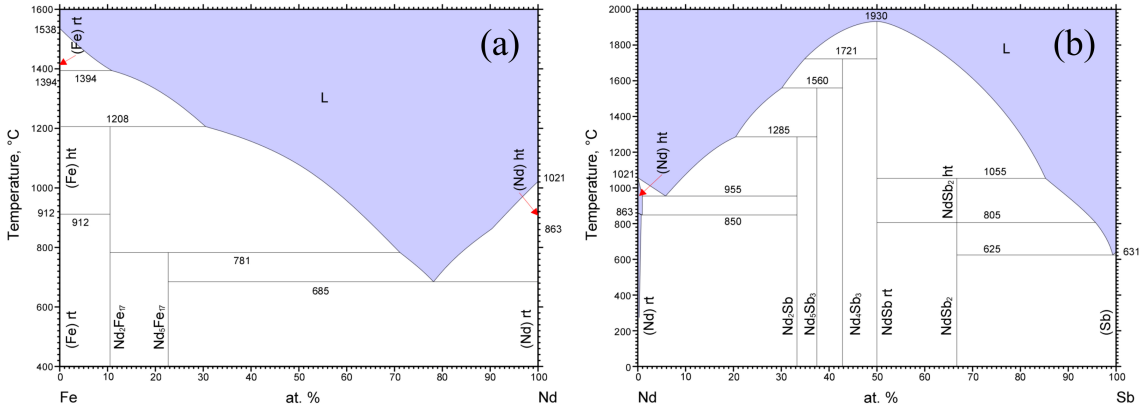

Figure 2.1. (a) Fe-Nd binary phase diagram [20] and (b) Nd-Sb binary phase diagram [22].

2.2 Materials and Methods

2.2.1 Materials

Materials used in experiments were the cladding alloy HT9, an Sb-Nd alloy and elemental Nd. The HT9 alloy was received from Idaho National Laboratory in rod form under an annealed condition. The chemical composition of the HT9 alloy is listed in Table 2.1. The

Sb-Nd alloy was fabricated at a 1:1 atom ratio using arc melting. The elemental Sb and Nd feedstock materials were both procured from Alfa Aesar. The Sb was received in shot form exceeding 99.9% purity, and the Nd was received as a rod ~6.35mm in diameter with a 99.5% purity. The arc melting of the Sb-Nd alloy was conducted inside an argon atmosphere glovebox, where the alloys were melted and flipped three times and then drop cast into a ~5mm diameter pin.

Table 2.1. Chemical composition in wt.% of the HT9 cladding alloy used in this study.

Element	**C**	**Si**	**Mn**	**Cr**	**Ni**	**Mo**	**W**	**V**	**Fe**
Concentration	0.17	0.29	0.58	11.73	.58	1.03	0.5	0.29	Bal.

2.2.2 Experimental details

To evaluate the different alloy interactions isothermal diffusion experiments were carried out between two alloys to create a diffusion couple. Isothermal diffusion couple experiments are typically carried out to study the FCCI phenomena *out-of-pile* [4] and are further used to evaluate the effectiveness of additives to mitigate lanthanide interactions with cladding alloys [18–20]. Experiments were performed inside a muffle furnace contained in an inert argon glovebox. The glovebox atmosphere was maintained at 1–5 ppm oxygen, while a continuous flow of high purity argon cover gas was maintained into the furnace at a rate of 0.25 ft^3/h (1.97 cm^3/s) for the length of the experiment. To achieve a high purity, the argon cover gas is initially passed through an oxygen getter furnace reducing its oxygen content down to 10^{-10}–10^{-11} ppb oxygen. The diffusing materials were sectioned into discs approximately 2.5 mm thick and polished to a 1 μm finish within the glovebox to alleviate any oxide layer formations. The discs were directly wrapped in a layer of tantalum foil (~0.025mm) and placed inside a jig made of Kovar™ steel, an iron-nickel-cobalt alloy that exhibits low thermal expansion. Alumina discs were placed directly between the diffusion couple and jig contact points to avoid adverse interactions during the experiment. A diagram of the experimental diffusion couple jig setup is shown in Figure 2.2. The entire jig was then wrapped in tantalum foil and placed into the furnace. The flow of high purity argon into the furnace chamber was maintained for 30 m prior to turning on the furnace and initiating the diffusion experiments. The furnace was heated at a rate of 1,000 °C/h (0.28 K/s) up to the experiment temperature.

Upon completion of the diffusion experiment, the jig was immediately removed from the furnace chamber and allowed to cool in the open glovebox environment. The cooling rate of the jig was measured to be 22 °C/m (0.37 K/s). For this study, diffusion experiments were carried out at 675 °C (948 K) for 24 h (86,400 s).

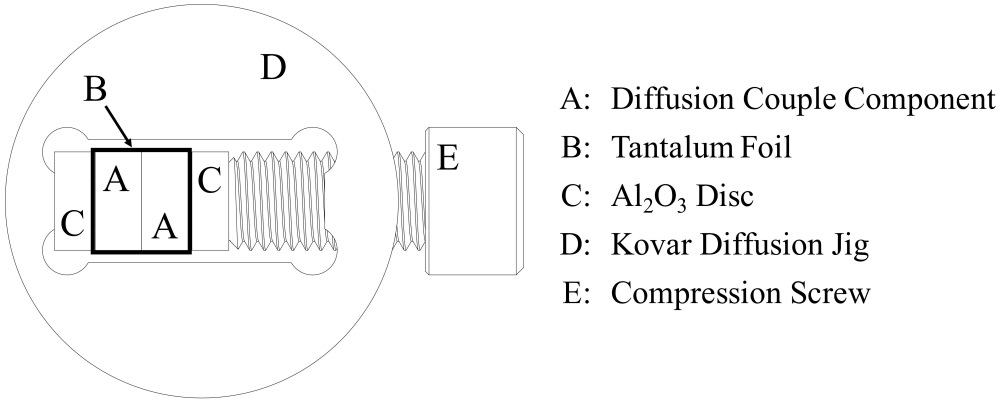

Figure 2.2. Diagram of the diffusion couple jig and the internal components used for the isothermal diffusion experiments in the present study.

2.2.3 Characterization details

At the conclusion of an experiment the diffusion couple was sectioned and mounted in epoxy for microstructural characterization. Samples were prepared by grinding using sequential grits of SiC papers followed by polishing down to a 1 μm finish using diamond-based suspensions. All sample preparation steps were performed within an inert argon glovebox to avoid surface oxidation on the analysis surface. The polished surfaces were then coated with a thin layer of gold to control charging of the metallographic mount during electron microscopy.

Scanning electron microscopy (SEM) was performed using a JEOL JSM-6610LV operated at an accelerating voltage of 20 kV. Imaging was primarily conducted in backscatter electron (BSE) imaging mode to get better contrast of phase formations, while secondary electron (SE) imaging was performed intermittingly. Energy dispersive X-ray spectroscopy (EDS) was conducted using an EDAX Apollo X silicon drift detector (SDD) and EDAX TEAM v4.4 (2016) software. The amp time was adjusted for each analysis to generate a dead time of between 20% to 30%. In conducting point analysis, elemental spectra were collected for 50 live seconds per analysis location. For elemental spectra mapping a dwell time of 200 μs was used. Elemental data collected from EDS was quantified based on the standardless ZAF

method using the EDAX TEAM library of spectra standards. X-ray diffraction (XRD) was performed using a Rigaku SmartLab X-Ray Diffractometer paired with SmartLab Guidance software (v 2.0.4.7). XRD was conducted using a parallel beam (PB) optics configuration, Cu Kα radiation at a tube current of 44 mA, and a D/tex Ultra 250 1D silicon strip detector. Focused XRD $\theta/2\theta$ scans were performed using a 0.04° step size and a 5°/m scan speed. Data was analyzed and indexed using Rigaku's PDXL 2 software (v2.3.1.0) and the International Centre for Diffraction Data (ICDD) (PDF-2 Release 2016) database.

Microhardness indentation was performed using a LECO LM247 AT automatic micro-indentation apparatus equipped with a Vickers indenter. Recorded values are reported in units of hardness Vickers number (HVN). To verify the integrity of the indenter and system, five indentations were made on a calibration block using the calibration load of 4903.3 mN (500 g_f). The measured values were found to fall within tolerance of the calibration block. To evaluate the load effects on the material hardness values of the diffusion couple materials, a series of five indents were performed at each of the following loads; 4903.3 mN (500 g_f), 980.7 mN (100 g_f), 490.3 mN (50 g_f), 245.2 mN (25 g_f), and 98.1 mN (10 g_f). These indents were made in the base material areas of the diffusion couple, away from the interaction region. Additionally, several loads were used within the interaction region. No major fluctuations in hardness were observed. Thus, the reported hardness values in this study are based on indentations made using a load of 245.2 mN (25 g_f) and a dwell time of 13 s. Indentation spacing was maintained at a minimum of 2.5 times the indent mean diagonal length, adhering to ASTM E384 specifications.

2.2.4 Electronic structure calculations

Electronic structure calculations using Density Functional Theory (DFT) [23,24] were performed to further evaluate the compound forming behavior of Fe inside the SbNd phase, in the Vienna *Ab initio* Simulation Package (VASP) [25,26]. The calculations used a 2× 2 × 2 supercell with 64 atoms of the SbNd phase (space group $Fm\bar{3}m$, 225 ICSD [27] ID 165728) with the 4 × 4 × 4 Monkhorst Pack k-point grid. Further details of the simulation method used can be found in previous publications [13–15].

2.3 Results and Discussion

2.3.1 Initial conditions of Nd and Sb-Nd alloy

SEM and XRD characterization were initially performed on the as-received Nd and as-cast Sb-Nd materials. SEM analysis of the Sb-Nd alloy revealed a two-phase morphology, as shown in the SEM micrographs in Figure 2.3 (a) and (b).

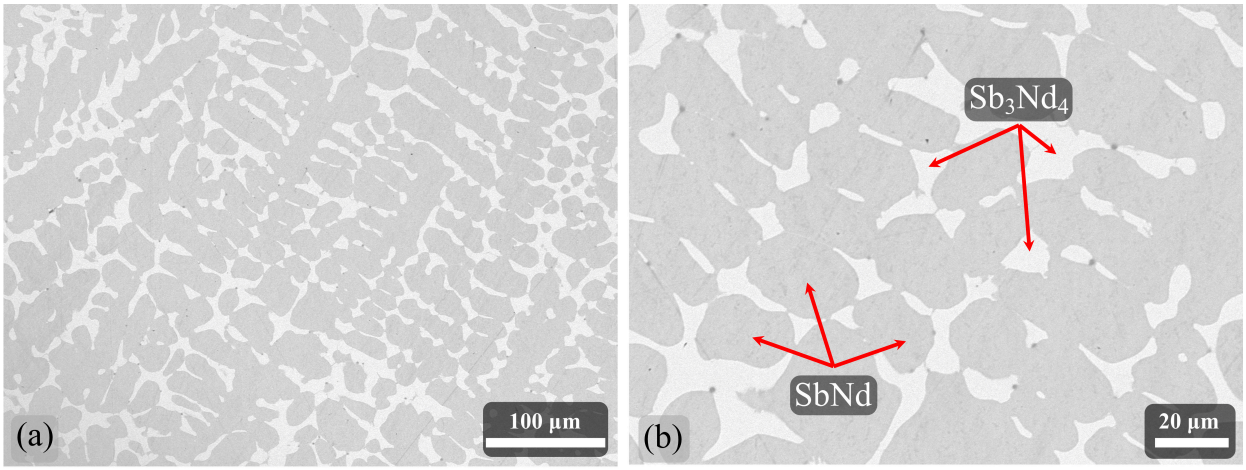

Figure 2.3. BSE SEM micrographs of the Sb-Nd cast alloy revealing its two-phase morphology. (a) shows the matrix microstructure at a lower magnification (250x) and (b) shows the matrix microstructure at a higher magnification (750x). The SbNd phase appears in grey contrast and the Sb_3Nd_4 phase in light contrast.

Through EDS characterization, these phases were initially assessed to be SbNd and Sb_3Nd_4 based on their atomic mixing ratios. Results of the XRD analysis on the Nd rod and Sb-Nd alloy are shown in Figure 2.4, and the crystallographic information can be found in Table 2.2. The Nd rod material was found to be in its primary room temperature allotrope, a double hexagonal structure. Further, the Sb-Nd alloy was confirmed to consist of a two-phase morphology with the SbNd and Sb_3Nd_4 phases identified. The formation of the SbNd and Sb_3Nd_4 phases are favorable as they are stable up to temperatures substantially greater than normal reactor operational temperatures as shown in the Sb-Nd binary phase diagram in Figure 2.1 (b).

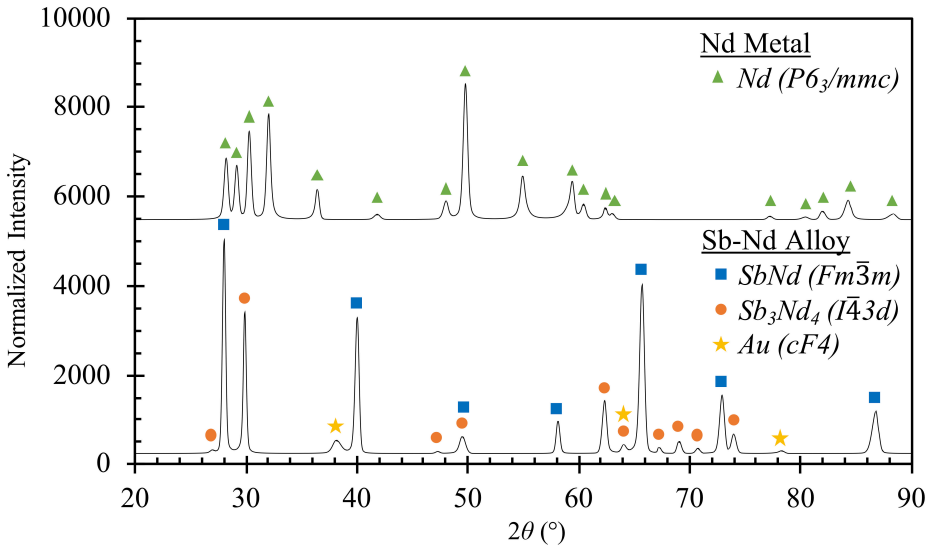

Figure 2.4. XRD plots of the Nd and Sb-Nd alloy specimens in the as-received and as-cast conditions, respectively. **the presence of gold is due to its application as a surface coating to accommodate the SEM analysis.*

2.3.2 Nd interaction with HT9

Analysis of the Nd/HT9 diffusion couple shows the formation of two primary regions within the interaction region; one that is of light grey contrast (*Region A*) and another that is of medium grey contrast (*Region B*). As shown in Figure 2.5 (a) and Figure 2.6 (a) the entire interaction region fluctuates in size from between 35 µm and 50 µm in thickness. This size fluctuation is also seen to occur in Region A and Region B with each unique phase region fluctuating from between 10 µm and 25 µm in size. Previous research performed by K. Inagaki *et al.* [35], where diffusion reactions were evaluated between an alloy comprised of La, Nd, Ce, Pr, and Sm and a Fe-12Cr alloy, led to the development of the following correlating equation for the thickness formation of the interaction region:

$$\delta^2 = Kt \tag{2.1}$$

where δ (m) is the interaction layer thickness, K (m^2/s) is the reaction rate coefficient, and t (s) is the isothermal experiment time. Further, they found K followed an inverse temperature ($1/T$) Arrhenius formulation defined by:

$$K = 1.93 \times (10)^{-8} \times exp\left(-\frac{94{,}500}{RT}\right) \tag{2.2}$$

where R ($JK^{-1}mol^{-1}$) is the gas constant and T (K) is the isothermal temperature of the experiment. Based on these equations, the thickness of the interaction region for the Nd/HT9

diffusion couple should be ~100 μm, nearly double the thickness of that observed in this study. It should be noted that the isothermal condition in the present study slightly exceeds the range studied by Inagaki, which evaluated a maximum isothermal temperature of 923 K. Further, Inagaki only mentioned the use of a Fe-12Cr alloy. Although HT9 is considered a Fe-12Cr-based alloy, it contains additional alloying constituents, such as, Mn, Mo, W, V, etc., and it is not entirely clear how they would affect the intrinsic diffusion mechanisms. Additionally, the current study is evaluating only the diffusion of Nd into HT9, whereas the additional lanthanide elements of Inagaki's research would lead to a varying degree of diffusion into the Fe-12Cr alloy.

Table 2.2. Crystallographic information of phases indexed through XRD analysis.

Compound	**Space Group (Space Group No.)**	**Cell Parameters**	**Alloy Conditions**
Nd [28]	$P6_3/mmc$ (194), hexagonal	a=b=0.366, c=1.180 (nm) $\alpha=\beta=90°$, $\gamma=120°$	As-received/ Diffusion Couple
SbNd [29]	$Fm\bar{3}m$ (225), cubic	a=b=c=0.634 (nm) $\alpha=\beta=\gamma=90°$	As-cast
Sb_3Nd_4 [30]	$I\bar{4}3d$ (220), cubic	a=b=c=0.941 (nm) $\alpha=\beta=\gamma=90°$	As-cast
Au [31]	$Fm\bar{3}m$ (225), cubic	a=b=c=0.408 (nm) $\alpha=\beta=\gamma=90°$	Sputter coating
α-Fe [32]	$Im\bar{3}m$ (229), cubic	a=b=c=0.287 (nm) $\alpha=\beta=\gamma=90°$	Diffusion Couple
$Fe_{17}Nd_2$ [33]	$R\bar{3}m$ (166), trigonal	a=b=0.858, c=1.246 (nm) $\alpha=\beta=90°$, $\gamma=120°$	Diffusion Couple
$Fe_{17}Nd_5$ [34]	$P6_3/mcm$ (193), hexagonal	a=b=2.021, c=1.233 (nm) $\alpha=\beta=90°$, $\gamma=120°$	Diffusion Couple

To evaluate the primary elemental interactions occurring through the interaction region seen in Figure 2.5 (a), an elemental line-scan analysis was performed from the Nd to the HT9 section of the diffusion couple. The line-scan analysis location is shown in Figure 2.5 (a), and a plot of the results are shown in Figure 2.5 (b). Further, elemental mapping was also conducted on the area imaged in Figure 2.5 (a) to evaluate the presence of Fe, Nd, and Cr; the results are shown in Figure 2.5 (c). Evaluating the results of both Figure 2.5 (b) and (c) it can be seen that

Region A contains Fe and Nd whereas Region B contains Fe, Nd and Cr. Further, as indicated through the line-scan plot of Figure 2.5 (b), Region A and Region B appear to be comprised of differing Fe and Nd concentrations. It has been previously found that Cr does not typically diffuse out of an Fe-Cr alloy, i.e. HT9, or tends to be fairly sluggish [35,36]; therefore, in this study the initial interface is presumed to be near the transition plane between Regions A and B. Further, Region B shows a slight increase in the Cr concentration compared to the HT9 base material. This Cr increase is the result of a decrease in the Fe concentration indicating the diffusion of Fe out of the HT9 alloy. Thus, the formation of Region A is the likely result of Fe diffusing into Nd and the formation of Region B is that of Nd diffusing into the cladding alloy. It should be noted the presence of Fe globules seen 50–100 μm into the Nd side is not considered to be the result of diffusion but instead the displacement of Fe during sample preparation steps, which then embedded within the soft Nd metal. To better refine the interactions occurring in each unique region, a line-scan analysis was conducted at a higher magnification using a 0.1 μm step size on a new section of the interaction region; shown in Figure 2.6. Here the interaction region is again seen to be primarily the interaction of Fe and Nd. Region A is better defined, and the Fe and Nd concentration appears to be relatively steady. Additionally, Region B is better defined as well and it can more clearly be seen that the Fe and Nd concentration appears to change through the region. The Fe concentration is seen to be highest near the HT9 and is then seen to decrease linearly to Region A, where the Nd concentration is vice versa. Again, an elevation in the Cr concentration is seen in Region B due to the loss of Fe to Region A.

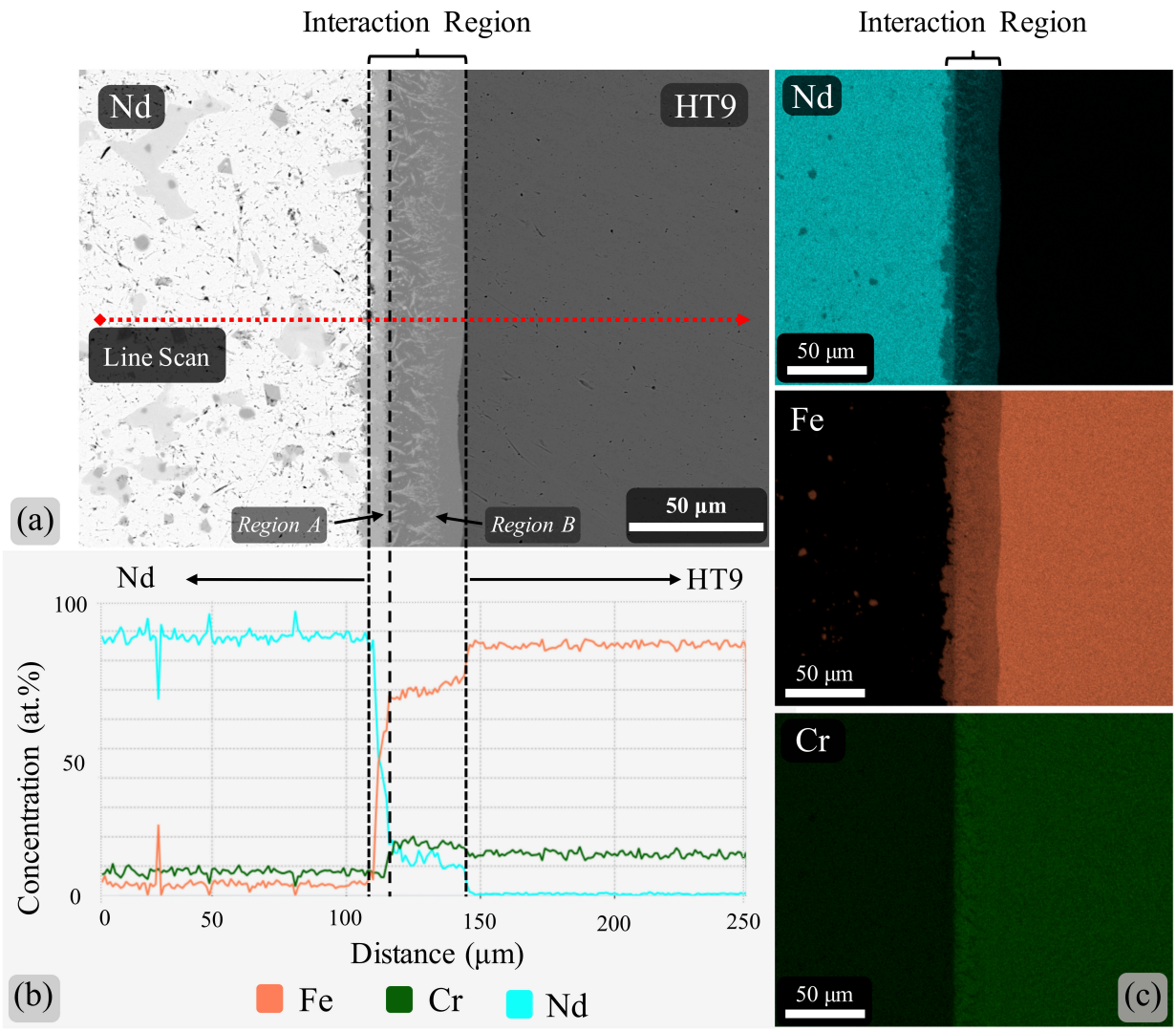

Figure 2.5. The Nd/HT9 diffusion couple interaction region. (a) A BSE SEM micrograph displaying the EDS line-scan analysis location, (b) the plot of the line-scan results, and (c) EDS elemental mapping results of the interaction region of the diffusion couple.

To get a better understanding of the elemental composition of the different phases observed across the interaction region, high magnification EDS point analysis was conducted on the diffusion couple section imaged in Figure 2.6, with the analysis locations shown in Figure 2.6 (a). The compositional results of Nd, Fe and Cr concentrations from the EDS point analysis are reported in Table 2.3.

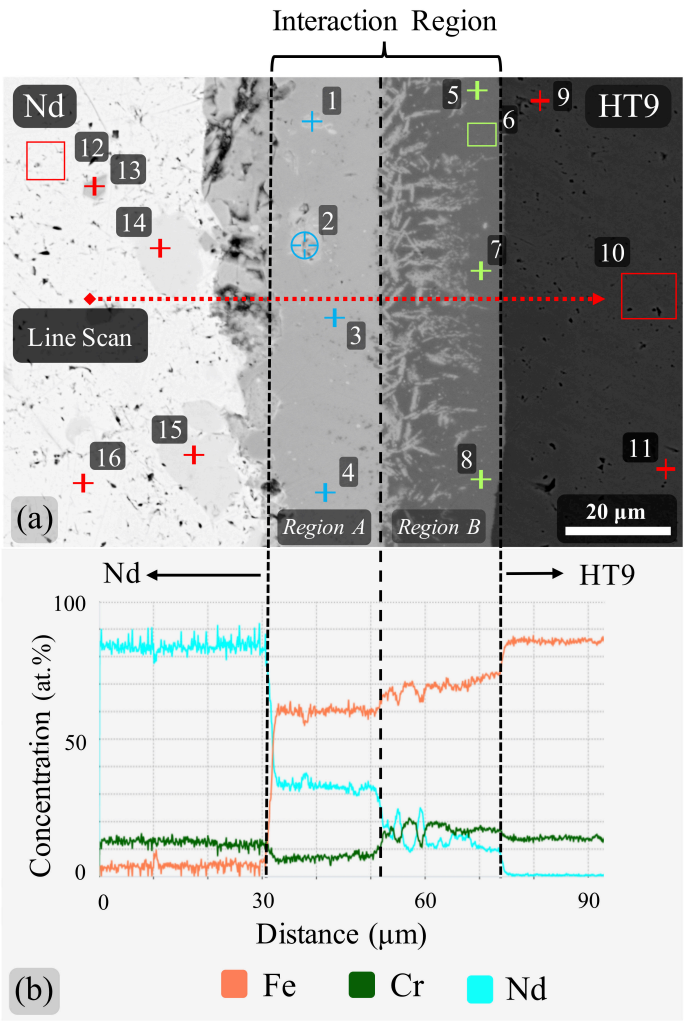

Figure 2.6. A section of the Nd/HT9 diffusion couple showing a larger interaction region. (a) A BSE SEM micrograph showing both the EDS line-scan analysis location and point analysis locations. (b) The plot of the line-scan results across the interaction region. **Point analysis results are reported in Table 2.3.*

Results from EDS point analysis appear to further support that the interaction region is the primary result of Fe and Nd interaction (pts. 1–8). However, there is a variation in the composition of the two distinct phases seen within the interaction region. Region A (pts. 1–4) shows a consistent atomic ratio of Fe:Nd to be ~1.8:1–2.2:1, which does not align with a thermodynamically stable Fe-Nd phase. However, the Fe and Nd concentration correlates closely to the atomic ratio of the stable $Fe_{17}Nd_5$ phase (atomic ratio Fe:Nd 3.4:1). It should be noted, the detection of Cr in this region is not likely as Cr is not expected to diffuse out of HT9. Its presence and thus its detection may likely be the result of smearing from sample preparation.

Region B (pts. 5–8) shows an atomic ratio of Fe:Nd to be 10.4:1–10.7:1. Again, this ratio does not align with a thermodynamically stable Fe-Nd phase, but correlates closely with the stable $Fe_{17}Nd_2$ phase (atomic ratio Fe:Nd 8.5:1). It's worth noting that the section of Region B where data for pts. 5–8 was collected correlates with the higher Fe and lower Nd concentration previously seen in the line-scan of Figure 2.6 (b). It is feasible that a portion of Region B, closer to the transition plane to Region A, may have a Fe and Nd atomic ratio that is much closer to that of the $Fe_{17}Nd_2$ phase. Further, it can be seen that dendrite-like formations of Region A are seen expanding into Region B. In the line-scan analysis of Figure 2.6 (b) these formations can be seen as having an elevated Nd concentration, similar to that of Region A, when compared to Region B.

Table 2.3. EDS analysis data in at.% correlating to locations in Figure 2.6 (a).

	Nd	Fe	Cr	Phase[a]		Nd	Fe	Cr	Phase[a]
		Region A					*HT9 Alloy Matrix*		
1	27	59	6	*$Fe_{17}Nd_5$*	**9**	0	85	12	*HT9*
2	30	55	5	*$Fe_{17}Nd_5$*	**10**	0	86	12	*HT9*
3	27	59	5	*$Fe_{17}Nd_5$*	**11**	0	87	11	*HT9*
4	27	59	6	*$Fe_{17}Nd_5$*			*Neodymium Matrix*		
		Region B			**12**	77	2	8	*Nd*
5	7	73	17	*$Fe_{17}Nd_2$*	**13**	78	2	7	*Nd*
6	7	75	17	*$Fe_{17}Nd_2$*	**14**	78	1	8	*Nd*
7	7	74	17	*$Fe_{17}Nd_2$*	**15**	77	2	8	*Nd*
8	7	73	16	*$Fe_{17}Nd_2$*	**16**	77	2	8	*Nd*

[a]Suggested phase based on EDS analysis.

Analysis of the HT9 matrix (pts. 9–11) show the primary constituents of the alloy are present and no degradation has occurred outside of the interaction region. Analysis of the Nd base material away from the interaction region (pts. 12–15) shows it to be primarily Nd. There is a trace concentration of Fe which falls within the error of EDS analysis. There is also a concentration of Cr detected, however, as previously discussed above its presence is likely due to smearing and subsequent embedding during polishing. To confirm phase formations within the Nd/HT9 diffusion couple, micro-XRD analysis was performed focusing on the interaction region and the results are shown in Figure 2.7. Based on the XRD results, both the $Fe_{17}Nd_5$

phase and $Fe_{17}Nd_2$ phase were detected confirming their formation within the interaction region. Further, it can be seen that both the α-Fe and Nd phases are also detected. It is important to note that although considered a micro-analysis technique, the expected incident beam area is ~400 µm in diameter. Therefore, given that its resolution far exceeds the width of the interaction region, phases of the base materials of the diffusion couple were expected.

Based on both the EDS and XRD results, Region A is the $Fe_{17}Nd_5$ phase whereas Region B is the $Fe_{17}Nd_2$ phase. These results appear to correlate well with those reported by Egeland *et al.* [20], who evaluated the diffusion interaction directly between Fe and Nd. In that study, the $Fe_{17}Nd_5$ phase was found to have formed nearest to the Nd side of the diffusion couple and the $Fe_{17}Nd_2$ phase nearest the Fe side of the diffusion couple. Additionally, similar unpublished diffusion experiments conducted by the author of this study between Fe and Nd under similar experimental conditions showed similar phase formations within the interaction region. Based on the phase formations it can be seen that Nd, when in intimate contact with the cladding alloy HT9, begins to diffuse into the alloy while Fe diffuses into Nd.

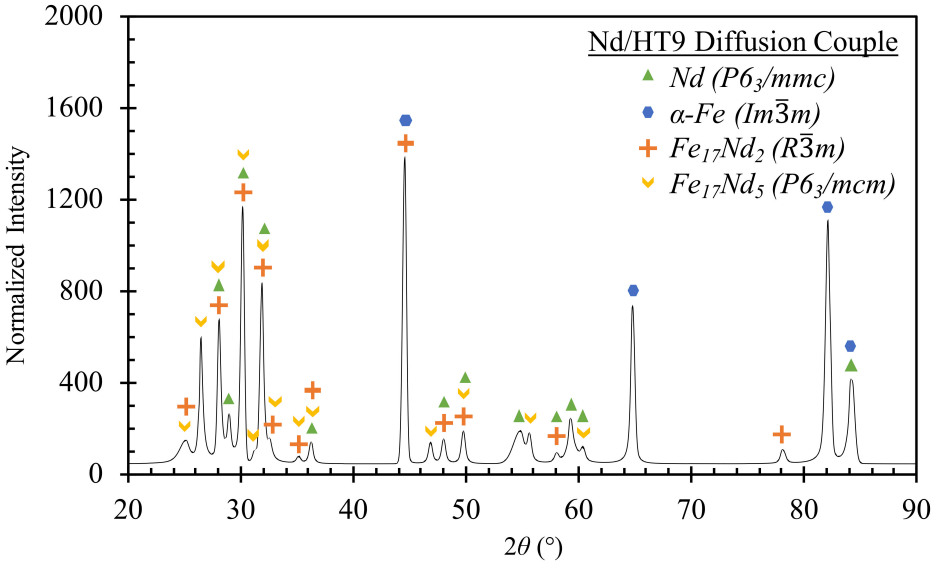

Figure 2.7. XRD plot of the diffusion interaction region in the Nd/HT9 diffusion couple.

The deformation tendencies of the intermetallic phases formed within the interaction region were mechanically probed using Vickers microhardness analysis technique. Single line indentations were performed across the diffusion couple and multiple single indentations were performed within the phase formations of the interaction region. A SE SEM micrograph of the

indents made through the interaction region are shown in Figure 2.8 (a) where the hardness change of the different phases can be visualized by the change in indent sizes. Further, the plot of the results of the single line indentation is shown in Figure 2.8 (b). Table 2.4 contains the hardness results of each phase of the diffusion couple. The Nd and HT9 base materials were found to have an average hardness of 57 HVN and 274 HVN, respectively. In comparison, the interaction region exhibits an elevated hardness with respect to that of the diffusion couple base materials. Further probing of the individual phase formations of the interaction region indicates the average hardness of the $Fe_{17}Nd_5$ (Region A) phase to be 563 HVN and that of the $Fe_{17}Nd_2$ (Region B) phase to be 973 HVN.

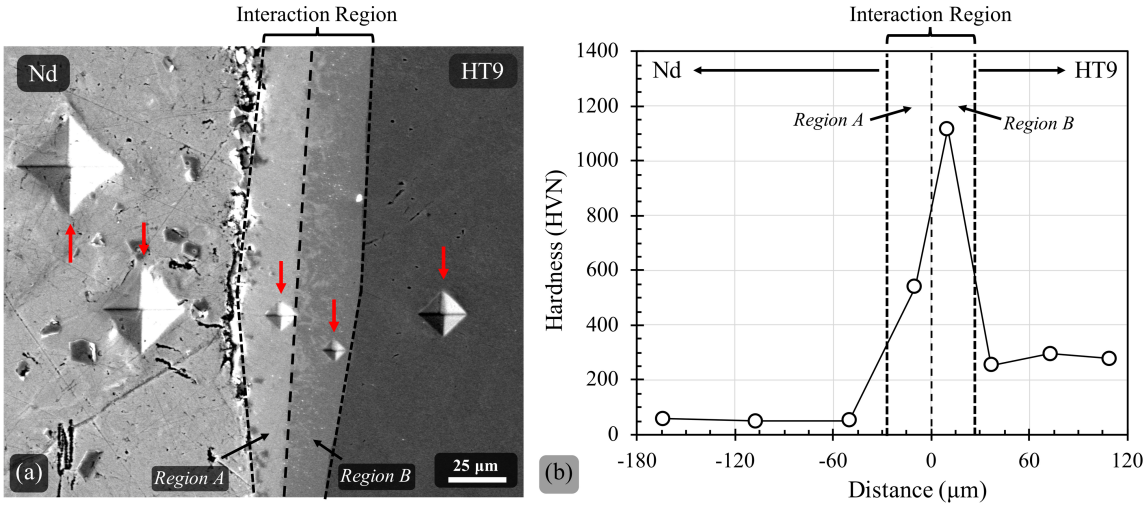

Figure 2.8. (a) A SE SEM micrograph of indentations made within the interaction region. (b) Micro-indentation plot across the Nd/HT9 diffusion interaction region.

Table 2.4. Hardness analysis results of the Nd/HT9 diffusion couple.

Material/Phase	**Hardness, HVN[a]**	**Mean Diagonal Length, µm[a]**
Nd	57	30
$Fe_{17}Nd_5$ (Region A)	563	9
$Fe_{17}Nd_2$ (Region B)	973	7
HT9	274	13

[a]An average value comprised of three or more indents

2.3.3 SbNd and Sb_3Nd_4 interactions with HT9

The Sb-Nd/HT9 diffusion couple was analyzed to evaluate the effects alloying Sb with Nd has on the interactions of Nd with HT9 through an isothermal diffusion experiment.

Previously, it was observed that the Sb-Nd alloy developed a two-phase morphology where the SbNd and Sb_3Nd_4 phases were identified (Figures 2.3 and 2.4). An evaluation of the Sb-Nd matrix after the isothermal experiment, away from the diffusion interface, revealed no change in the two-phase morphology. EDS analysis indicated the atomic ratios of the two phases to be consistent with SbNd and Sb_3Nd_4 stoichiometry. Upon initial evaluation of the diffusion interface it was apparent there was significant cracking, primarily in the Sb-Nd alloy at or near the original interface; such cracking can be seen in the SEM micrographs of Figures 2.8 and 2.9.

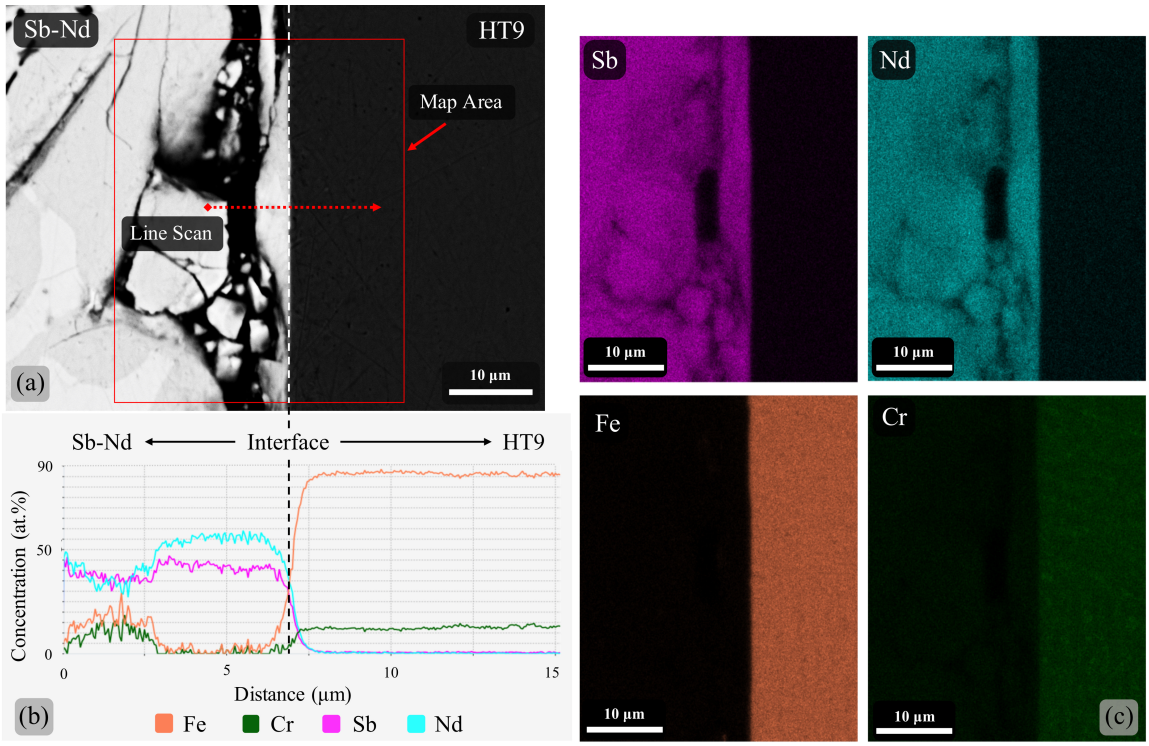

Figure 2.9. The diffusion interface of the Sb-Nd/HT9 diffusion couple. (a) A BSE SEM micrograph indicating the locations of both the EDS line-scan analysis and elemental mapping analysis. (b) The plot of the line-scan analysis results, and (c) shows the elemental mapping results of the diffusion interface.

The Sb-Nd intermetallic alloy was observed to be brittle after casting and it is possible the cracking in the diffusion couple was the result of cooling while being constrained within the diffusion jig after the experiment. Further, the potential thermal expansion mismatch between the HT9 alloy and the Sb-Nd intermetallic may explain why the cracking occurred at or near the diffusion boundary. Because of the cracking, analysis of potential diffusion

interactions was primarily concentrated on areas where intimate contact was still observed between each alloy. One such location can be seen in Figure 2.9. The different EDS analysis locations are shown in the high magnification BSE SEM micrograph of Figure 2.9 (a), where the EDS line-scan results are plotted in Figure 2.9 (b). Visually, the BSE micrograph of Figure 2.9 (a) does not appear to show the formation of different phases or that of an interaction region at the diffusion interface. The line-scan results appear to concur showing no interaction between the two alloys, as the alloying constituents of each alloy quickly drop off at the interface. There is a slight increase in the Fe and Cr concentration on the line-profile about 12 μm away from the interface into the Sb-Nd alloy; however, this appears to correlate with the location of the crack. It is likely that these elements collected within the crevice of the crack during sample preparation. To further evaluate the potential of Fe and Cr interacting with the Sb-Nd alloy, high magnification elemental mapping was conducted at the exact area where the prior line-scan analysis was performed. The results of the elemental mapping and the presence of Sb, Nd, Fe, and Cr are shown in Figure 2.9 (c), which correlates to the area shown in the SEM micrograph of Figure 2.9 (a). Based on the mapping results, Fe and Cr is not observed within the Sb-Nd alloy and neither is Sb and Nd observed within the HT9 alloy; each element is confined to its base material location. Elemental point analysis was conducted in two separate sections of the diffusion couple that showed intimate contact between the two alloys. The point analysis locations are shown in Figure 2.10 where (a) corresponds to the location shown in Figure 2.9 and Figure 2.10 (b) corresponds to a new analysis location; the elemental data is listed in Table 2.5.

First in evaluating the area closest to the bond line in Figure 2.10 (a) (pts. 1–4) there is no significant concentration of Fe or Cr detected. The small amount of Fe present in these four points (4–5 at. %) is difficult to state as being conclusive due to the inherent limitations of EDS. Furthermore, the proximity of these points to the HT9 alloy, the detection of Fe could be the outcome of volume-based interactions of the electron beam. Further, it can be noted that the Sb and Nd ratios of pts. 1–4 along with the point analysis of the Sb-Nd alloy away from the diffusion interface (pts. 5–8) correlate closely with SbNd and Sb_3Nd_4, the phases observed in the base alloy.

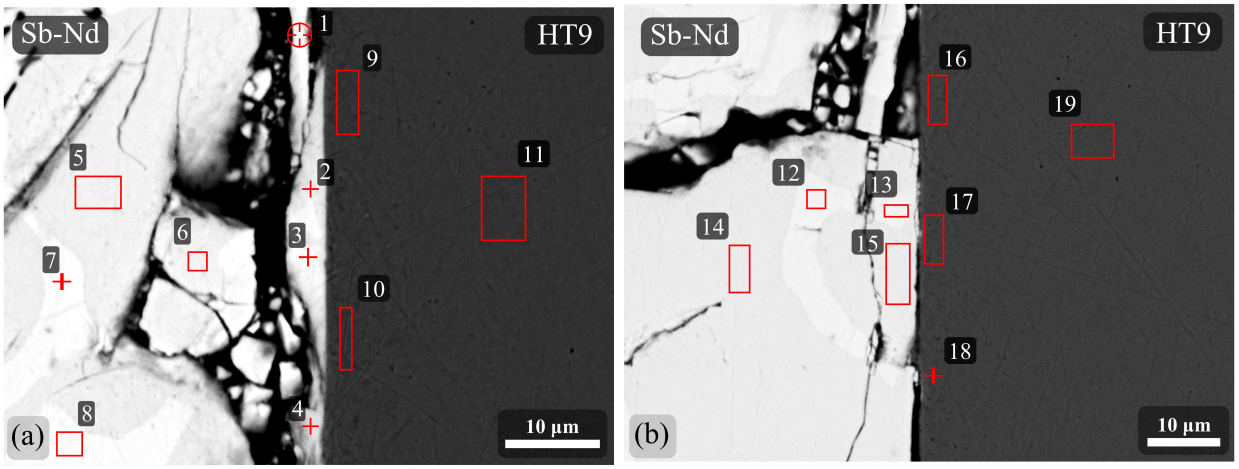

Figure 2.10. BSE SEM micrographs of two different sections of the diffusion interface showing EDS analysis locations. (a) Corresponds to the analysis location of Figure 2.9, and (b) corresponds to a new analysis location. **Point analysis results are reported in Table 2.5.*

Table 2.5. EDS analysis data in at.% correlating to locations displayed in Figure 2.10.

	Figure 2.10 (a)						*Figure 2.10 (b)*				
	Sb	**Nd**	**Fe**	**Cr**	**Phase[a]**		***Sb***	**Nd**	**Fe**	**Cr**	**Phase[a]**
1	36	52	4	1	Sb_3Nd_4	**12**	38	54	1	1	Sb_3Nd_4
2	42	45	5	2	*SbNd*	**13**	37	52	2	1	Sb_3Nd_4
3	36	52	4	1	Sb_3Nd_4	**14**	45	48	1	0	*SbNd*
4	35	39	4	1	*SbNd*	**15**	44	47	1	0	*SbNd*
5	45	47	1	1	*SbNd*	**16**	0	0	83	13	*HT9*
6	44	48	1	1	*SbNd*	**17**	0	0	85	12	*HT9*
7	38	54	1	1	Sb_3Nd_4	**18**	0	0	83	13	*HT9*
8	38	54	1	1	Sb_3Nd_4	**19**	0	0	84	12	*HT9*
9	0	0	84	12	*HT9*						
10	0	0	85	11	*HT9*						
11	0	0	84	13	*HT9*						

[a]Suggested phase based on EDS analysis.

On the HT9 side of the diffusion interface, pts. 9 and 10 are area scans taken next to the diffusion interface and they show no trace of the Sb and Nd elements. Further, their elemental concentrations are consistent with pt. 11, taken in the HT9 some distance away from the diffusion interface. Similar results of elemental concentrations are observed in Figure 2.10 (b). Pts. 13 and 15, taken nearest to the diffusion interface, indicate that they are likely the Sb_3Nd_4 and SbNd phases, respectively, with little to no trace of Fe and Cr. Further, this aligns

with the analysis taken in the general Sb-Nd section, pts. 12 and 14, respectively. On the HT9 side of the interface, pts. 16–18 again are found to match with that of the HT9 base material (pt. 19), showing no trace of Nd or Sb. It is apparent that the intermetallic phases, SbNd and Sb_3Nd_4, remain stable when in contact with HT9 at elevated temperatures and are not found to interact.

2.3.4 Understanding Fe and SbNd interactions using electronic structure calculations

Total energy obtained from DFT calculations can help to examine the compound forming tendency between various elements and phases from a thermodynamic point of view. Therefore, to better substantiate the experimental observations, DFT-based electronic structure calculations were carried out between Fe and the SbNd phase to elucidate their potential interactions. The mixing enthalpy of Fe within the SbNd phase was analyzed in addition to the orbital resolved density of states (DOS). The mixing enthalpy was calculated by:

$$\Delta E_{\text{mixing}} = E(\text{Sb}_{m-1}\text{Nd}_m\text{Fe}) + E(\text{Sb}) - E(\text{Sb}_m\text{Nd}_m) - E(\text{Fe}), \quad (2.3)$$

where $E(\text{Sb}_{m-1}\text{Nd}_m\text{Fe})$ is the total energy of the SbNd supercell, with one Sb atom replaced by one Fe atom in a simulation cell of $2m$ sites; $E(\text{Sb}_m\text{Nd}_m)$ is the total energy of the SbNd supercell in a simulation cell with m atom of each Sb and Nd; and E(Sb) and E(Fe) are the total energy per atom for Sb and Fe, respectively. The calculated enthalpy of mixing of Fe on the SbNd system at the Sb site is +4.75 eV. Similar calculations performed by replacing one Nd atom within SbNd by a Fe atom revealed an enthalpy of mixing significantly greater than +4.75 eV. Highly positive mixing enthalpies of Fe on the SbNd system indicates the phase-separating tendency or absence of stable compounds [37] between Fe and SbNd. It should be noted that a Fe-Sb-Nd ternary compound has been observed in literature [38,39], but such phases were not observed in this study. It appears that once the SbNd phase forms its interaction with Fe becomes unfavorable.

The DOS of Fe substituted in the SbNd system is shown in Figure 2.11. Here the mixing of the Nd *d-orbitals* with the Sb *p-orbitals* can be seen at 3.75 eV below the Fermi level (0 eV). Such overlapping of orbitals indicates the stability of the SbNd compound. Further, the Fe *d-orbitals* shows two peaks, one at the Fermi level and one at about -2 eV, along with its *s-orbitals* the Fe valence orbitals stand out from the Sb and Nd orbitals; indicating a lack of bonding. The stability of the SbNd compound and non-interacting nature with Fe is in

agreement with the experimental observations that Fe does not interact with the SbNd phase. Given these results, it is believed a similar outcome is expected if Fe is analyzed within the Sb_3Nd_4 phase.

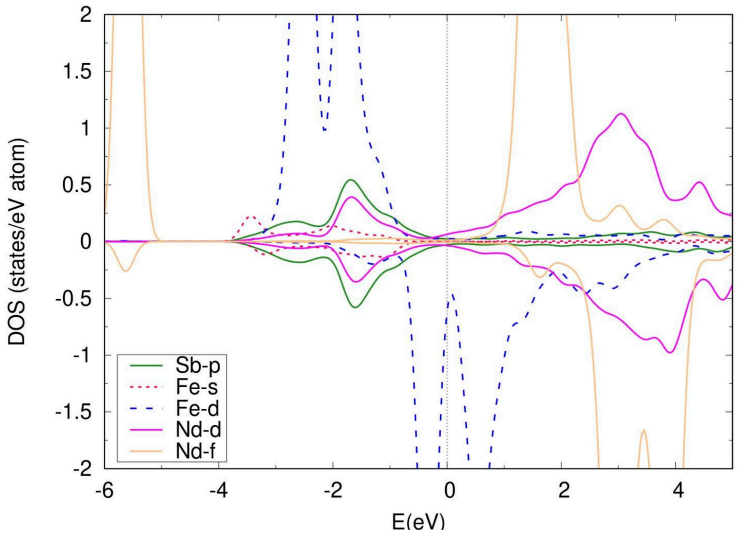

Figure 2.11. Orbital resolved DOS of Fe substituted SbNd system. The vertical dashed line represents the Fermi level. The positive and negative vertical axis represent up and down spin components, respectively.

2.4 Conclusion

When Nd is placed in contact with the HT9 cladding under elevated temperatures interdiffusion between Nd and Fe occurs leading to the formation of a multi-phase interaction region. Through EDS and XRD analysis the $Fe_{17}Nd_2$ and $Fe_{17}Nd_5$ phases were found to have formed within the interaction region and micro-indentation analysis alludes to their potentially brittle nature.

To mitigate Nd and Fe interactions, the utilization of Sb as a dopant that binds with Nd was proposed. By alloying Nd with Sb at a roughly 1:1 atomic ratio, the SbNd and Sb_3Nd_4 phases were found to form. Isothermal diffusion couple experiments carried out between the multi-phase Sb-Nd alloy and the cladding alloy HT9 at temperatures and timescales similar to those performed between Nd and HT9, no adverse interactions were observed between the Sb-Nd phases and HT9. Additionally, DFT calculations indicated that incorporation of Fe within the SbNd phase would be highly unfavorable.

It is apparent that the binding of Nd with Sb clearly retards the interactions experienced between Nd and Fe. Thus, Sb appears to be an effective additive for arresting the lanthanide

Nd. This research is a first step in evaluating the effectiveness of Sb as an additive in metallic fuel systems, as longer timescale isothermal diffusion experiments should be explored. Additionally, it is difficult to duplicate all mechanisms induced during irradiation in *out-of-pile* experiments. Therefore, to truly test Sb as an effective additive, irradiation-based experiments will be needed to more effectively represent the environment in which FCCI occurs. However, the favorable results reported here indicate the potential of Sb and therefore it should be further explored as an additive to mitigate FCCI in more complex experiments.

Acknowledgments

This work is being supported by the U.S. Dept. of Energy's Nuclear Energy University Programs (NEUP) under contract DE-NE0008557. This research made use of resources located at the Center for Advanced Energy Studies (CAES) and that of the High-Performance Computing Center of the Idaho National Laboratory which is supported by the Office of Nuclear Energy of the U.S. Dept. of Energy under Contract No. DE-AC07-05ID14517.

References

[1] D. C. Crawford, D. L. Porter, S. L. Hayes, Fuels for sodium-cooled fast reactor: US perspective, *J. Nucl. Mater.* 371(1–3): 202–231, 2007. https://doi.org/10.1016/j.jnucmat.2007.05.010

[2] T. Ogata, Metal Fuel, *Compr. Nucl. Mater.* Vol. 3: 1–40, 2012. https://doi.org/10.1016/B978-0-08-056033-5.00049-5

[3] W. J. Carmack, D. L. Porter, Y. I. Chang, S. L. Hayes, M. K. Meyer, D. E. Burkes, C. B. Lee, T. Mizuno, F. Delage, J. Somers, Metallic fuels for advanced reactors, *J. Nucl. Mater.* 392(2): 139–150, 2009. http://dx.doi.org/10.1016/j.jnucmat.2009.03.007

[4] D. D. Keiser, Metal fuel-cladding interaction, *Compr. Nucl. Mater.* Vol. 3: 423–441, 2012. http://dx.doi.org/10.1016/B978-0-08-056033-5.00067-7

[5] C. W. Arnold, J. Galloway, C. Unal, Towards understanding FCCI: modeling cerium solid transport in metal fuels, *Trans. American Nucl. Society* 112:269–270, June 2015

[6] R. D. Mariani, D. L. Porter, T. P. O'Holleran, S. L. Hayes, J. R. Kennedy, Lanthanides in metallic nuclear fuels: Their behavior and methods for their control, *J. Nucl. Mater.* 419(1–3): 263–271, 2011. http://dx.doi.org/10.1016/j.jnucmat.2011.08.036

[7] M. T. Benson, L. He, J. A. King, R. D. Mariani, Microstructural characterization of annealed U-12Zr-4Pd and U-12Zr-4Pd-5Ln: Investigating Pd as a metallic fuel

additive, *J. Nucl. Mater.* 502: 106–112, 2018. https://doi.org/10.1016/j.jnucmat.2018.02.012

[8] M. T. Benson, J. A. King, R. D. Mariani, M. C. Marshall, SEM characterization of two advanced fuel alloys: U-10Zr-4.3Sn and U-10Zr-4.3Sn-4.7Ln. *J. Nucl. Mater.* 494: 334–341, 2017. http://dx.doi.org/10.1016/j.jnucmat.2017.07.057

[9] Y. Xie, M. T. Benson, J. A. King, R. D. Mariani, J. Zhang, Characterization of U-Zr fuel with alloying additive Sb for immobilizing fission product lanthanides, *J. Nucl. Mater.* 498: 332–340, 2018. https://doi.org/10.1016/j.jnucmat.2017.10.039

[10] Y. S. Kim, T. Wieneck, E. O'Hare, J. Fortner, Effectiveness of a dopant in U-Zr metallic fuel to prevent lanthanide migration, *Proc. of GLOBAL 2013,* 1118–1125, Sep. 2013.

[11] M. T. Benson, Y. Xie, J. A. King, K. R. Tolman, R. D. Mariani, I. Charit, J. Zhang, M. P. Short, S. Choudhury, R. Khanal N. D. Jerred, Characterization of U-10Zr-2Sn-2Sb and U-10Zr-2Sn-2Sb-4Ln to assess Sn+Sb as a mixed additive system to bind lanthanides, *J. Nucl. Mater.* 510: 210–218, 2018. https://doi.org/10.1016/j.jnucmat.2018.08.017

[12] Y. Xie, J. Zhang, M. T. Benson, J. A. King, R. D. Mariani, Assessment of Te as a U-Zr fuel additive to mitigate fuel-cladding chemical interactions, *J. Nucl. Mater.* 513: 175–184, 2019. https://doi.org/10.1016/j.jnucmat.2018.10.050

[13] N. D. Jerred, R. Khanal, M. T. Benson, E. Perez, J. A. King, M. Dubey, J. Burns, I. Charit, S. Choudhury, R. D. Mariani, Evaluation of tellurium as a fuel additive in neodymium-containing U-Zr metallic fuel, *Sci. Rep.* 9(16043), 2019. https://doi.org/10.1038/s41598-019-51852-z

[14] R. Khanal, N. Jerred, M. Benson, D. A. Andersson, R. Mariani, I. Charit, S. Choudhury, A novel approach to selection of dopant to immobilize neodymium in uranium-based metallic fuels, *J. Nucl. Mater.* 529(151922), 2020. https://doi.org/10.1016/j.jnucmat.2019.151922

[15] R. Khanal, N. Ayers, N. Jerred, M. T. Benson, R. D. Mariani, I. Charit, S. Choudhury, Role of Zr in lanthanide-dopant interactions within uranium-based metallic fuels, *J. Nucl. Mater.* 2020. UNDER REVIEW.

[16] R. Khanal, N. D. Jerred, M. T. Benson, Y. Xie, R. D. Mariani, I. Charit, S. Choudhury, Interactions and immobilization of lanthanides with dopants in uranium-based metallic fuels, *J. Nucl. Mater.* 2020. IN-PRESS. https://doi.org/10.1016/j.jnucmat.2020.152372

[17] C. Jiang, Y. Xie, M. T. Benson, Efficient computational search for lanthanide-binding additive dopants for advanced U-Zr based fuels, *Materialia* 2020. https://doi.org/10.1016/j.mtla.2020.100653

[18] W. Zhuo, Y. Xie, M. Benson, H. Wu, R. Mariani, J. Zhang, Experimental assessment of antimony (Sb) in pure uranium for immobilizing fission product lanthanides, *J. Nucl. Mater.* 534: 152135, 2020. https://doi.org/10.1016/j.jnucmat.2020.152135

[19] Y. Xie, J. Zhang, M. T. Benson, R. D. Mariani, Diffusion behavior of lanthanide-additive compounds (Ce_4Sb_3, Ce_2Sb, and CeTe) against HT9 and Fe, *Mater. Charact.* 150: 107–117, 2019. https://doi.org/10.1016/j.matchar.2019.02.012

[20] G. W. Egeland, R. D. Mariani, T. Hartmann, D. L. Porter, S. L. Hayes, J. R. Kennedy, Reducing fuel-cladding chemical interaction: the effect of palladium on the reactivity of neodymium on iron in diffusion couples, *J. Nucl. Mater.* 432: 539–544, 2013. https://doi.org/10.1016/j.jnucmat.2012.07.028

[21] H. Okamoto, Fe-Nd (Iron-Neodymium), *J. Phase Equilib.* 18(1): 106, 1997. https://doi.org/10.1361/105497102770331244

[22] Abulkhaev V.D., Physicochemical analysis of inorganic systems—neodimium-antimony system, *Russ. J. Inorg. Chem.* Vol. 44, 2: 264–267, 1999.

[23] W. Kohn, L. J. Sham, Self-consistent equations including exchange and correlation effects, *Phys. Rev.* 140: A1133–A1138, 1965. https://doi.org/10.1103/PhysRev.140.A1133

[24] P. Hohenberg, W. Kohn. Inhomogeneous electron gas, *Phys. Rev.* 136: B864–B871, 1964. https://doi.org/10.1103/PhysRev.136.B864

[25] G. Kresse, J. Furthmüller, Efficient iterative schemes for *ab initio* total-energy calculations using a plane-wave basis set, *Phys. Rev. B* 54: 11169–11186, 1996. https://doi.org/10.1103/PhysRevB.54.11169

[26] G. Kresse, J. Furthmüller, Efficiency of *ab-initio* total energy calculations for metals and semiconductors using a plane-wave basis set, *Comput. Mater. Sci.* 6: 15–50, 1996. https://doi.org/10.1016/0927-0256(96)00008-0

[27] M. Hellenbrandt, The inorganic crystal structure database (icsd)—present and future, *Crystallogr. Rev*. Vol. 10, no. 1, 17–22, 2004.

[28] K. W. Hermann, A. H. Daane, F. H. Spedding, The crystal structures and lattice parameters of high-purity scandium, yttrium and the rare earth metals, *Acta Crystallogr.* 9:559–563, 1956. https://doi.org/10.1107/S0365110X5600156X

[29] P. Manfrinetti, A. Provino, A. V. Morozkin, O. Isnard, Magnetic structure of the NaCl-type NdSb compound, *J. Alloys Compd.* 487(1–2): L28–L29, 2009. https://doi.org/10.1016/j.jallcom.2009.08.038

[30] D. Hohnke, E. Parthe, The anti-Th_3P_4 structure type for rare earth germanides, antimonides and bismuthides, *Acta Crystallogr.* 21: 435–437, 1966. https://doi.org/10.1107/S0365110X66003098

[31] H. E. Swanson, E. Tatge, Standard X-ray diffraction powder patterns, *Natl. Bur. Stand*. (U.S.) Circ. 539, I: 33 (June 1953).

[32] O. Crisan, A. D. Crisan, Phase transformation and exchange bias effects in mechanically alloyed Fe/magnetite powders, *J. Alloys Cmpd.* 509: 6522–6527, 2011. https://doi.org/10.1016/j.jallcom.2011.03.147

[33] T. Kajitani, Y. Morii, S. Funahashi, T. Iriyama, K. Kobayashi, H. Kato, Y. Nakagawa, K. Hiraya, High-resolution neutron powder diffraction study on nitrogenated Nd_2Fe_{17}, *J. Appl. Phys.* 73: 6032, 1993. https://doi.org/10.1063/1.353460

[34] J. Moreau, L. Paccard, J. P. Nozieres, F. P. Missell, G. Schneider, V. Villas-Boas, A new phase in the Nd-Fe system: Crystal structure of Nd_5Fe_{17}, *J. Less-Common Met.* 163: 245, 1990. https://doi.org/10.1016/0022-5088(90)90590-G

[35] K. Inagaki, T. Ogata, Reaction of lanthanide elements with Fe-Cr alloy, *J. Nucl. Mater.* 441: 574–578, 2013. https://doi.org/10.1016/j.jnucmat.2013.04.046

[36] K. Nakamura, T. Ogata, M. Kurata, A. Itoh, M. Akabori, Reactions of U-Zr alloy with Fe and Fe-Cr alloy, *J. Nucl. Mater.* 275: 246-254, 1999. https://doi.org/10.1016/S0022-3115(99)00227-5

[37] C. Jiang, First-principles study of ternary bcc alloys using special quasi-random structures, *Acta Mater.* 57: 4716–4726, 2009. https://doi.org/10.1016/j.actamat.2009.06.026

[38] L. Zeng, P. Qin, L. Nong, J. Zhang, J. Liao, The 773 K isothermal section of the Nd-Fe-Sb ternary system, *J. Alloys Compd.* 437: 84-86, 2007. https://doi.org/10.1016/j.jallcom.2006.07.066

[39] W. Wang, T. Liu, H. Song, S. Xue, W. Zhang, H. Zhang, L. Zhang, Y. Jia, N. Wang, X. Cheng, C. Zeng, A thermodynamic modeling of the Fe-Nd-Sb system, *Mater. Trans.* Vol. 57, 2: 103–111, 2016. https://doi.org/10.2320/matertrans.M2015333

CHAPTER 3
EVALUATION OF TELLURIUM AS A FUEL ADDITIVE IN NEODYMIUM-CONTAINING U-ZR METALLIC FUEL

Published in Springer Nature's journal of Scientific Reports in November 2019.
"Evaluation of Tellurium as a Fuel Additive in Neodymium-Containing U-Zr Metallic Fuel." *Sci. Reports*, 9:16043 (2019). https://doi.org/10.1038/s41598-019-51852-z

Abstract. Phase-stability in a U-Zr-Te-Nd multi-component metallic fuel for advanced nuclear reactors is systematically investigated by taking into account binary, ternary and quaternary interactions between elements involved. Historically, the onset of fuel-cladding chemical interactions (FCCI) greatly limits the burnup potential of U-Zr fuels primarily due to interactions between lanthanide fission products and cladding constituents. Tellurium (Te) is evaluated as a potential additive for U-Zr fuels to bind with lanthanide fission products, e.g. neodymium (Nd), negating or mitigating the FCCI effect. Potential fresh fuel alloy compositions with the Te additive, U-Zr-Te, are characterized. Te is found to completely bind with Zr within the U-Zr matrix. Alloys simulating the formation of the lanthanide element Nd within U-Zr-Te are also evaluated, where the Te-Nd binary interaction dominates and NdTe is found to form as a high temperature stable compound. The experimental observations agree well with the trends obtained from density functional theory calculations. According to the calculated enthalpy of mixing, Zr-Te compound formation is favored in the U-Zr-Te alloy whereas NdTe compound formation is favored in the U-Zr-Te-Nd alloy. Further, the calculated charge density distribution and density of states provide sound understanding of the mutual chemical interactions between elements and phase-stability within the multi-component fuel.

3.1 Introduction

Phase stability in a multi-component alloy is determined by a complex set of mutual chemical, elastic and other energetic interactions between elements of the alloy. Such binary, ternary, and quaternary interactions between two or more elements lead to the minimization of the total energy of the alloy. Understanding such interactions is critical to the design of alloy chemistry for a targeted application. In this study, experimental and theoretical efforts are combined to understand such mutual interactions between elements to investigate the overall phase stability in a U-Zr-Te-Nd multi-component alloy. The binary U-Zr metallic nuclear fuels have largely been used in fast-spectrum reactors, such as the Experimental Breeder Reactor II (EBR-II), and they continue to be attractive for advanced nuclear reactor concepts, such as the advanced sodium-cooled fast reactor (SFR). Some major advantages of such fuel systems are their ease of fabrication and reprocessing, high thermal conductivity, good compatibility with the sodium coolant, and their ability to contain high densities of fissile and fertile materials [1-3]. However, the onset of chemical interactions between fission products and fuel components with cladding constituents greatly limits the burnup potential of U-Zr fuels.

The lanthanide elements have been found to be a major cause of chemical interactions at the fuel-cladding interface, also known as fuel-cladding chemical interaction (FCCI). Such lanthanides form in the fuel as fission products and tend to migrate to the fuel periphery; being primarily driven by temperature gradients via 'liquid-like' transport [4-6]. Metallic fuels tend to swell due to fission gas formations within the first 1 – 2 at.% burnup leading to intimate contact to be made between the fuel and cladding components [2,7]. With prolonged reactor operation, such fuel – cladding contact leads to the initiation of FCCI. Lanthanide elements (Nd, Ce, La and Pr), being primarily immiscible in the U-Zr system, along with fuel constituents tend to interact with cladding constituents at the fuel – cladding interface. Such interactions can lead to the formation of brittle, low-melting phases exacerbating cladding wastage, which can eventually lead to cladding breach [4]. Therefore, to increase metallic fuel longevity and achieve greater fuel burnups, an effective method to mitigate FCCI is needed.

Several methods have been proposed to control FCCI, including internal cladding liners [8], internal cladding coatings [9] and fuel additives [6]. As opposed to acting as a diffusion barrier, i.e. liners and coatings, fuel additives are alloyed with the fuel to form high-temperature, stable compounds with lanthanide fission products as they form within the fuel

during irradiation, stabilizing them within the fuel meat and limiting their interaction with cladding constituents at the fuel – cladding interface. Criteria for potential additives have previously been developed by Mariani *et al.* [6], several of which have been studied – Pd [6**,** 10], Sn [11], Sb [12, 13], Sn+Sb [14], and In [13, 15], and have demonstrated additives as a promising approach to counter FCCI. Additionally, As and Se have been identified as potential additives based on density functional theory (DFT) calculations and experimental observations [16].

Tellurium (Te) was initially identified as a potential additive for metallic nuclear fuels by Mariani *et al.* [6] but detailed experimental work has been limited in this area. The focus of the present study is an evaluation of Te's effectiveness to bind with neodymium (Nd). First principles studies carried out by Khanal *et al.* [16] show agreement in the potential of Te to bind with Nd in an α-U matrix. Recent research conducted by Xie *et al.* [17] characterized the interactions of Te with another lanthanide element, cerium (Ce), in a U-10Zr alloy. In their evaluation of the U-10Zr-Te alloy, they were unable to obtain direct evidence of the formation of a Zr-Te phase; instead they postulated the formation of a Te-Zr-U ternary phase. Interestingly, the current research confirms the formation of a non-equilibrium phase Zr_2Te in a similar alloy composition. Furthermore, it is worth noting that in their characterization of the U-10Zr-Te-Ce alloy, their results indicate Te and Ce primarily form the stable compound CeTe.

In the present study, the microstructure of potential fuel compositions that may be resistant to FCCI are characterized, followed by a characterization of fuel compositions that contain Nd to simulate the formation of lanthanide fission products through fuel burnup. Nd was chosen for this study due to its identification as a predominant lanthanide to form within U-10Zr fuel irradiated in a liquid breeder fast reactor EBR-II [6] and has been observed to readily diffuse into the cladding [4]. Furthermore, this research focuses on the mutual interactions between elements in the U-Zr-Te and U-Zr-Te-Nd multi-component alloys, which lead to stable phase formations within the U-Zr matrix.

3.2 Results and Discussion

Four alloys evaluated in the current work are listed in Table 3.1. The 2Te and 4Te alloys represent potential fresh U-Zr fuels containing Te as an additive. The 2Te-2Nd and 4Te-

4Nd alloys represent simplified fuel compositions that simulate the formation of lanthanide fission products within the fuel through irradiation, where Nd represents the lanthanide fission product. The Te addition is based on the anticipated amount needed to bind all of the lanthanides that form in the fuel at the respective concentrations. The concentration of neodymium in the alloys represents the anticipated total lanthanide amount to form within the fuel at both 8 and 16 at.% burnups based on fission product concentrations reported by Mariani *et al.* [6]. Essentially, the additive – lanthanide atomic ratio is targeted to be 1:1; however, the alloys are in essence slightly additive-rich to counter possible volatilization loss of tellurium during casting.

Table 3.1. Alloys evaluated in this study

Alloy	**Composition in wt.%**	**Composition in at.%**
2Te	U-10Zr-2Te	U-22.2Zr-3.17Te
4Te	U-10Zr-4Te	U-21.8Zr-6.24Te
2Te-2Nd	U-10Zr-2.16Te-2Nd	U-21.9Zr-3.4Te-2.8Nd
4Te-4Nd	U-10Zr-4.3Te-4Nd	U-21.3Zr-6.6Te-5.4Nd

During initial arc-melting and subsequent drop casting of the alloys, some loss of Te was observed. Tellurium is considered a metalloid and has a relatively low melting temperature of 723 K (450 °C) and boiling point of 1263 K (990 °C), which leads to a narrow temperature range where the element can remain in a liquid state. Loss of Te primarily occurred during its addition to the U-10Zr (wt.%) button, which requires an increased amount of energy to fully liquefy having a solidus temperature of approximately 1521 K (1248 °C) and liquidus temperature between 1628 K – 1633 K (1355 °C – 1360 °C) [18]. Once Te was homogenized into the U-10Zr (wt.%) alloy, it became stabilized by the formation of Zr-Te precipitates (further discussed in later sections).

3.2.1 Microstructural and compositional analysis of U-10Zr with Te additive

The microstructures of the 2Te and 4Te alloys are shown in the scanning electron microscopy (SEM) backscatter electron (BSE) images in Figure 3.1. Round grey-contrast precipitates are observed within the matrix of both alloys ranging in size from sub-micron to

approximately 20 μm across. It should be noted that the matrix, a combination of a primary light phase with a dispersed light-grey phase, is the expected phase formation of the U-Zr system in the as-cast condition. Extensive work has been done on U-Zr alloys, and in particular the U-10Zr (wt.%) [18-24]. Furthermore, the phase formations between U and Zr in the as-cast condition, specifically the co-formation of the α-U and δ-UZr_2 phases, have been discussed elsewhere [19, 23]. A more recent study by Irukuvarghula *et al.* [24] concluded the phase formations for the majority of U-Zr alloys, including the U-10Zr alloy, in the as-cast condition are likely α-U phase and a disordered, metastable ω phase. Even though the ω and δ phases have the same chemical composition, the δ phase is partially ordered. Given the extensive knowledge base on the U-Zr binary system, the present study focuses on the observed ternary interactions of Te, U, and Zr and how the addition of Nd changes such mutual interactions.

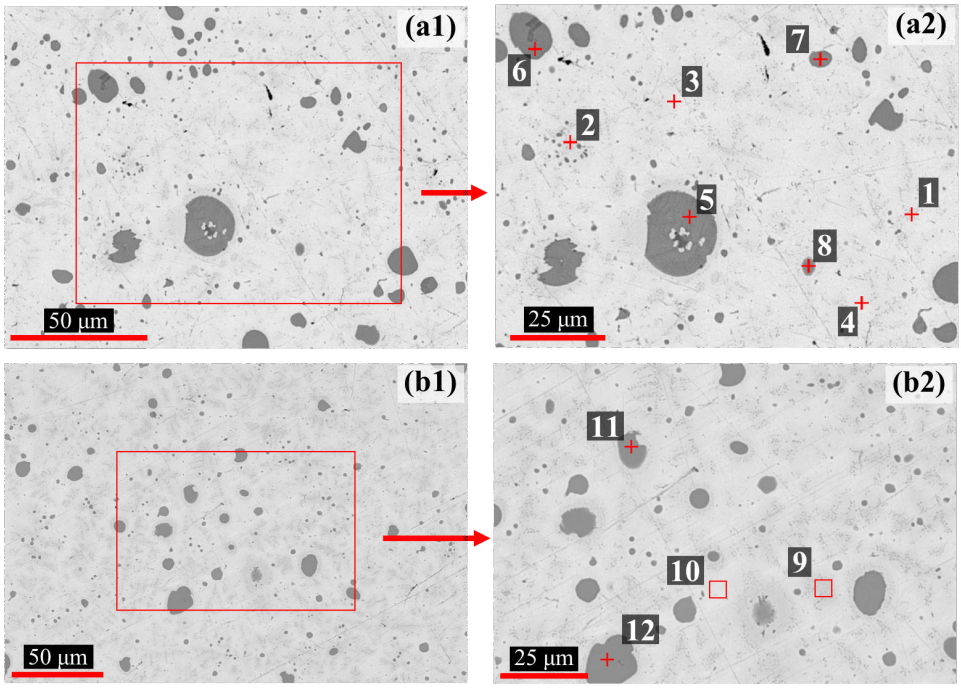

Figure 3.1. BSE SEM images of (a1) the 2Te alloy and (b1) the 4Te alloy; (a2) and (b2) are the magnified BSE SEM images of the 'red' rectangular inset regions in (a1) and (b1), respectively.

Elemental maps of U, Zr and Te, as obtained from energy dispersive X-ray spectroscopy (EDS) studies of the 2Te alloy for the location displayed in Figure 3.1 (a1), are shown in Figure 3.2. The maps reveal that the precipitates are the combination of Zr and Te contained within a primarily U matrix. Elemental compositions of areas designated in Figure 3.1 (a2) and (b2) are listed in Table 3.2. Based on EDS point analysis, the precipitates (points

5 – 8, 11, 12) exhibit a ratio range of 2:1 to 2.4:1 (Zr:Te), indicating that they are likely the Zr_2Te compound. Small white inclusions are also detected in the larger spherical precipitates (Figure 3.1 (a1)). Such inclusions are likely trapped matrix material. Xie *et al.* also made similar observations in their analysis of a U-10Zr-Te alloy [17].

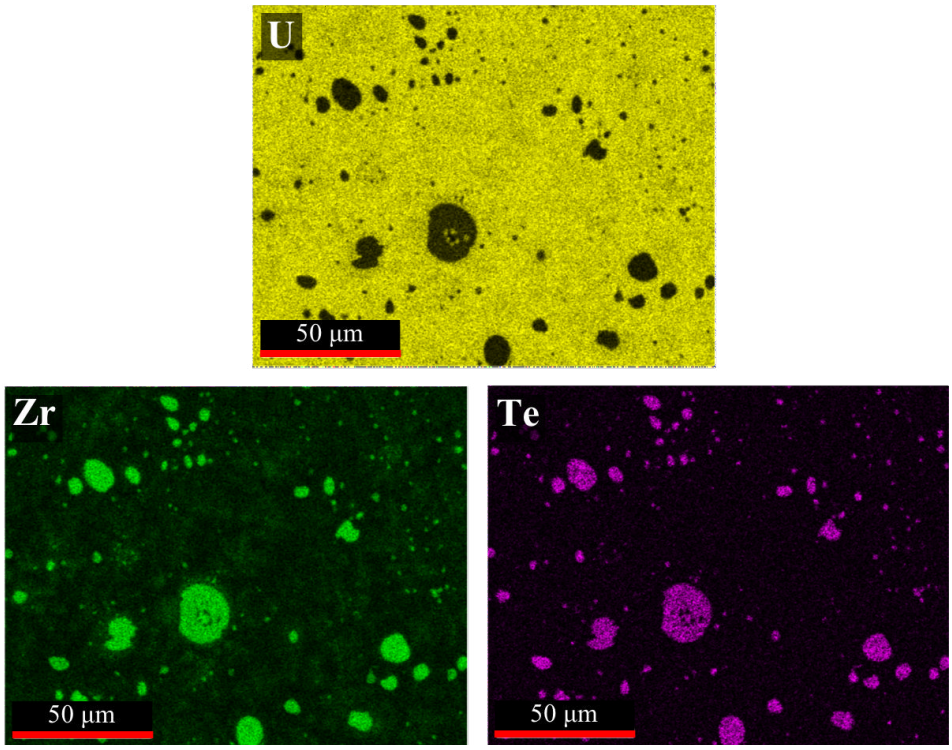

Figure 3.2. Elemental EDS maps of the 2Te alloy. Analysis location aligns with the area imaged in Figure 3.1 (a1).

Table 3.2. SEM EDS elemental data results of analysis points depicted in Figure 3.1 (at.%).

	Figure 3.1 (a2)					*Figure 3.1 (b2)*			
	U	**Zr**	**Te**	**Phase[a]**		**U**	**Zr**	**Te**	**Phase[a]**
1	62	31	7	U-Zr[b]	**9**	59	40	2	U-Zr[b]
2	60	38	2	U-Zr[b]	**10**	83	16	1	U-Zr[b]
3	84	14	2	U-Zr[b]	**11**	6	67	27	Zr_2Te
4	77	21	2	U-Zr[b]	**12**	5	67	28	Zr_2Te
5	9	64	27	Zr_2Te					
6	6	67	27	Zr_2Te					
7	7	62	31	Zr_2Te					
8	11	63	26	Zr_2Te					

[a] *suggested phase based on EDS analysis*
[b] *matrix phase of the as-cast U-Zr alloy*

Focused X-ray diffraction (XRD) analyses of alloys 2Te and 4Te alloys are presented in the form of XRD patterns in Figure 3.3, and the corresponding crystallographic information listed in Table 3.3. The XRD pattern shows that the alloys are primarily comprised of the α-U based solid solution phase. The presence of UO_2 was also seen and its formation is likely due to the specimen exposure to air during analysis. The Zr_2Te compound was also detected confirming the EDS elemental data obtained on the precipitates in the alloy. The Zr_2Te phase is not depicted as an equilibrium phase on the Zr-Te binary phase diagram by Okamoto [25]. However, more recent work by Örlygsson and Harbrecht [26] detailed the existence of the Zr_2Te phase. Their study detected the Zr_2Te phase in an as-cast specimen using EDS analysis and powder-based XRD. Further, they suggested that the Zr_2Te phase is formed through a peritectic reaction near the incongruent melting point of the Zr_3Te phase. It is plausible that Zr_2Te is a metastable phase, which may decompose to stable Zr_5Te_4 and Zr_3Te compounds [25].

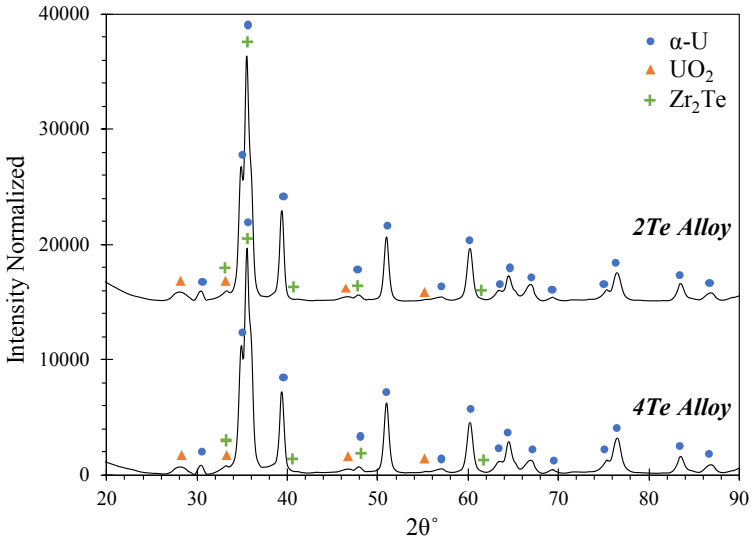

Figure 3.3. XRD patterns of the 2Te and 4Te alloys

In analyzing U-10Zr-Te alloys, it is important to note that no free Te was observed within the alloys; instead it is clear that Te is primarily binding with Zr to form precipitates. Similar observations have been made in other additives-based research in U-10Zr matrix [11, 12, 15, 17]. Such Zr-Te phase formation is deemed beneficial as they would stabilize the additive within the fresh fuel alloy. Here the precipitates were found to primarily consist of the Zr_2Te phase, which implies that the fuel composition, i.e. U-10Zr, is not being maintained

when Te is added to the fuel. As Zr is added to increase the solidus temperature of the alloy, the loss of Zr from the matrix solid solution may decrease the overall solidus temperature of the fuel matrix. To counter such outcome, additional Zr may be needed to maintain the necessary solidus temperature when additives are employed.

Table 3.3. Crystallographic information for all phases indexed through XRD analysis.

Compound	**Pearson Symbol**	**Space Group**	**Cell parameters**	**Alloy ID[a]**			
				2Te	*4Te*	*2Te-2Nd*	*4Te-4Nd*
α-U [27]	oS4	Cmcm (63)	a=0.286, b=0.585, c=0.498 [nm] $\alpha=\beta=\gamma=90°$	x	x	x	x
UO_2 [28]	cF12	$Fm\bar{3}m$ (225)	a=b=c=0.547 [nm] $\alpha=\beta=\gamma=90°$	x	x	x	x
Zr_2Te [26]	oP36	Pnma (62)	a=1.995, b=0.382, c=1.065 [nm] $\alpha=\beta=\gamma=90°$	x	x		
Zr_3Te [29]	tI32	$I\bar{4}$ (82)	a=b=1.134, c=0.563 [nm] $\alpha=\beta=\gamma=90°$				x
NdTe [30]	cF8	$Fm\bar{3}m$ (225)	a=*b*=*c*=0.627 [nm] $\alpha=\beta=\gamma=90°$			x	x
Nd_2O_3 [31]	cI80	$Ia\bar{3}$ (206)	a=b=c=1.110 [nm] $\alpha=\beta=\gamma=90°$			x	x
Au [32]	cF4	$Fm\bar{3}m$ (225)	a=b=c=0.408 [nm] $\alpha=\beta=\gamma=90°$			x	x

[a]*Denotes the alloy in which the particular phase was detected through XRD analysis*

3.2.2 Microstructural and compositional analysis of U-10Zr-2Te-2Nd and U-10Zr-4Te-4Nd alloys

To evaluate the effectiveness of the Te additive to bind with potential lanthanide fission products, Nd was added into the fuel alloys. Here two such alloys listed in Table 3.1 were evaluated. The Te addition of 2.16 wt.% and 4.3 wt.% corresponds to a targeted 1:1 atomic ratio of additive to lanthanide at the respective burnups. It is important to note that Nd was added to a U-Zr-Te alloy, and therefore the microstructure of the pre-alloy can be presumed to be similar to the previously discussed U-Zr-Te alloys. Therefore, in order for the additive (Te) to bind with the lanthanide (Nd), the Zr_2Te precipitates would need to decompose. As

previously mentioned, in casting Nd into the U-Zr-Te alloy, the Te is stabilized by the formation of Zr_2Te. Based on the research of Örlygsson and Harbrecht [26] it can be inferred that Zr_2Te has a melting temperature sufficiently higher than the melting temperature of Nd (T_{melt} = 1021 °C), therefore loss of Te was not likely when Nd was added.

Representative optical micrographs of the 2Te-2Nd and 4Te-4Nd alloys are shown in the SEM-BSE images of Figures 3.4 (a) and 1.4 (b), respectively. Both alloys have multiple precipitated phases within the U-Zr matrix. Both show a combination of larger grey-contrast precipitates (approximately 25 µm in size) along with various sized, smaller grey-contrast precipitates. Furthermore, dendritic and small, round black precipitates are observed to form throughout the matrix, with instances of the latter precipitates forming around the large grey-contrast precipitates. Both alloys exhibit the light- and light-grey matrix phases of the U-Zr as-cast structure as previously observed in the U-Zr-Te alloys. The primary difference between the two U-Zr-Te-Nd alloys is the presence of small, round black precipitate clusters that have formed within sections of the light-grey matrix in the 4Te-4Nd alloy (Figure 3.4 (b)).

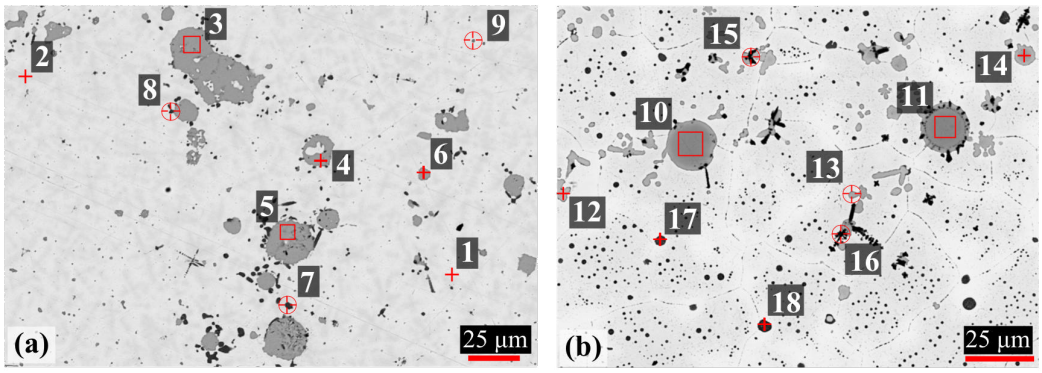

Figure 3.4. BSE images of (a) the 2Te-2Nd and (b) the 4Te-4Nd alloys.

Elemental EDS maps for the 2Te-2Nd and 4Te-4Nd alloys, which correspond to the locations imaged in Figure 3.4, are shown in Figures 3.5 and 3.6, respectively. The EDS maps in Figure 3.5 show that the larger grey-contrast precipitates observed in the 2Te-2Nd alloy consist of Te and Nd, whereas the small black and grey-contrast precipitates are found to primarily contain Zr and Nd, respectively. In the 2Te-2Nd alloy, the Te appears to be contained in all of the same precipitates as Nd and no longer appears to be contained with any Zr-containing precipitates. The EDS maps in Figure 3.6 show that the grey-contrast precipitates and the dendritic precipitates observed in the 4Te-4Nd alloy also consist of Te and Nd, and Zr,

respectively. However, the round black clustered precipitates are found to be primarily Zr with several containing Te. Furthermore, there does not appear to be precipitates that contain only Nd.

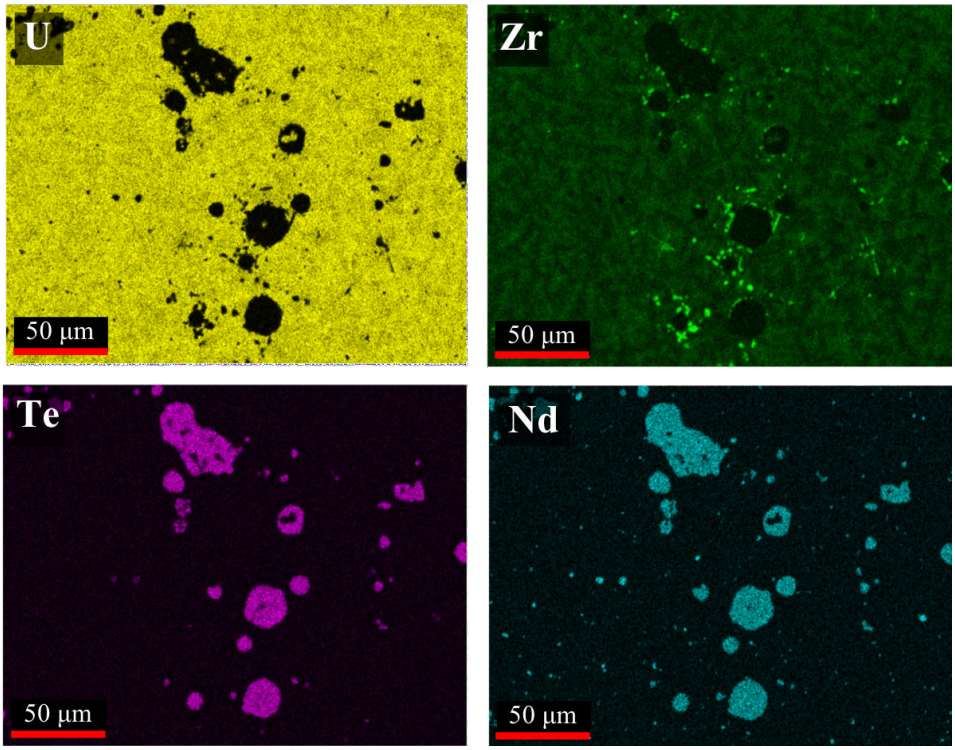

Figure 3.5. Elemental EDS maps of the 2Te-2Nd alloy. Analysis location aligns with the area imaged in Figure 3.4 (a).

EDS point analysis conducted on various precipitates in each alloy is tabulated in Table 3.4 based on locations indicated in Figures 3.4 (a) and (b). The elemental composition of the grey-contrast precipitates, depicted by points 3-6, 10 and 11, indicates that they are likely the NdTe compounds. Analysis of the smaller grey-contrast precipitates in the 4Te-4Nd alloy (depicted by points 12-14) indicates that they are more Te-rich than the NdTe (1:1) compound but also contain appreciable amounts of U (20 at.%, 12 at.%, and 14 at.%). Given the small size of the precipitates, some of the U detected could be from the alloy matrix due to the interaction volume of the electron beam. These Te-rich Nd-Te phases could either have uranium dissolved within or be the formation of a ternary U-Te-Nd phase. To resolve the exact nature of the precipitate, higher resolution characterization via transmission electron microscopy (TEM) was carried out on similar precipitates from the 4Te-4Nd alloy, which is discussed in detail below. Analysis of the very small (approximately 1-2 μm) grey-contrast

precipitates (point 9) in the 2Te-2Nd alloy were found to primarily consist of Nd. The presence of pure Nd inclusions indicates the Nd concentration is in excess to that of Te within the alloy. This is further confirmed because no Zr-Te containing compound phases were observed in the alloy and therefore all the Te available bound with the Nd.

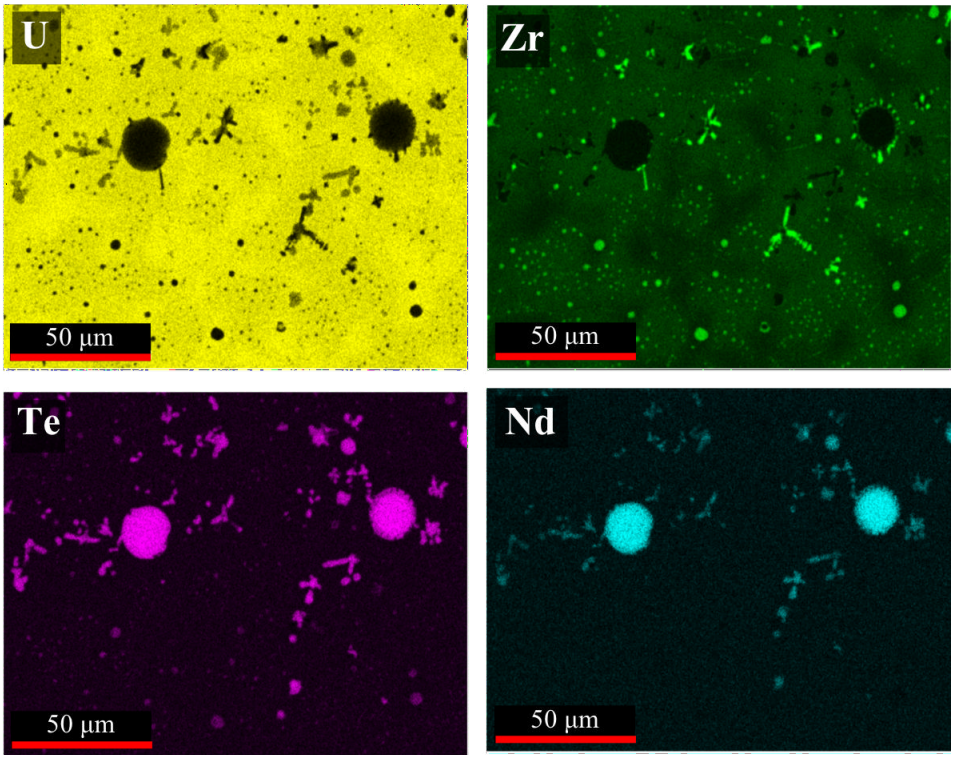

Figure 3.6. Elemental EDS X-ray maps of the 4Te-4Nd alloy. Analysis location aligns with the area marked in Figure 3.4 (b).

The small, dendritic black precipitates observed in both alloys are found to consist of high concentrations of Zr (points 7, 8, 15, and 16 in Figure 3.4). Such Zr-rich phases were not expected within the alloy. However, Janney and O'Halleran [33] observed similar Zr-rich phases in an as-cast structure of U-Zr with actinide and lanthanide additions. They found that the Zr-rich precipitates tend to form near lanthanide-containing precipitates, similar to what was observed here. They also suggested that such Zr-rich precipitates might get stabilized during casting and subsequent cooling due to trace impurities of C, N and O.

Evaluation of the larger round black precipitates (approximately 4-5 μm) within the clusters (points 17 and 18 in Figure 3.4 (b)) in the 4Te-4Nd alloy indicate that they may be Zr_3Te compound; a more Zr-rich compound than the Zr_2Te phases previously observed in the U-Zr-Te alloys. It should also be noted that points 17 and 18 indicate a higher Zr concentration

than what would be expected in the Zr_3Te compound. Given the size of the Zr-Te precipitates and the fact that they are clustered within a Zr-rich region of the U-Zr matrix, the higher Zr content and presence of U may be due to the beam interactions with the surrounding matrix. Because of the small size (submicron) of the clustered black precipitates, their accurate elemental composition could not be reliably assessed via SEM equipment used in this study.

Table 3.4. SEM EDS elemental data results of analysis points depicted in Figure 3.4 (a) and (b) (in at.%).

	Figure 3.4 (a)						*Figure 3.4 (b)*				
	U	**Zr**	**Te**	**Nd**	**Phase[a]**		**U**	**Zr**	**Te**	**Nd**	**Phase[a]**
1	75	22	2	1	*U-Zr[b]*	**10**	1	3	50	46	*NdTe*
2	57	42	0	1	*U-Zr[b]*	**11**	1	4	50	46	*NdTe*
3	0	6	45	49	*NdTe*	**12**	20	4	56	21	*U-Te-Nd*
4	0	6	45	48	*NdTe*	**13**	12	3	53	32	*U-Te-Nd*
5	1	7	44	47	*NdTe*	**14**	14	4	54	28	*U-Te-Nd*
6	0	6	46	48	*NdTe*	**15**	3	91	6	0	*Zr*
7	1	99	0	0	*Zr*	**16**	7	93	1	0	*Zr*
8	4	95	0	1	*Zr*	**17**	3	74	23	0	*Zr_3Te*
9	5	11	0	84	*Nd*	**18**	3	75	22	0	*Zr_3Te*

[a]*suggested phase based on EDS analysis*
[b]*matrix phase of the as-cast U-Zr alloy*

To positively identify the phases of the smaller precipitates previously observed in the 4Te-4Nd alloy, TEM analysis was performed. The TEM specimen, shown in Figure 3.7 (a), was made using a focused ion-beam (FIB) lift-off technique targeting a similar precipitate to that observed between points 12 and 14 in Figure 3.4 (b). The fabricated TEM specimen included a Zr-Te precipitate similar to that at point 16. High-angle annular dark field (HAADF) images and selected area electron diffraction (SAED) patterns of the precipitates are presented in Figure 3.7. SAED patterns were collected using multiple zone-axes of a single grain within the phase of interest. A SAED pattern from each analysis area is shown in Figures 3.7 (e), (f) and (g). The location of the grains used to generate SAED patterns are denoted by circles in the HAADF images of Figures 3.7 (b), (c), and (d). EDS analysis was also performed on the TEM specimen to determine the elemental concentrations of the various precipitates. The

analysis areas are denoted in the HAADF images of Figure 3.7 (b), (c), and (d); the results are listed in Table 3.5.

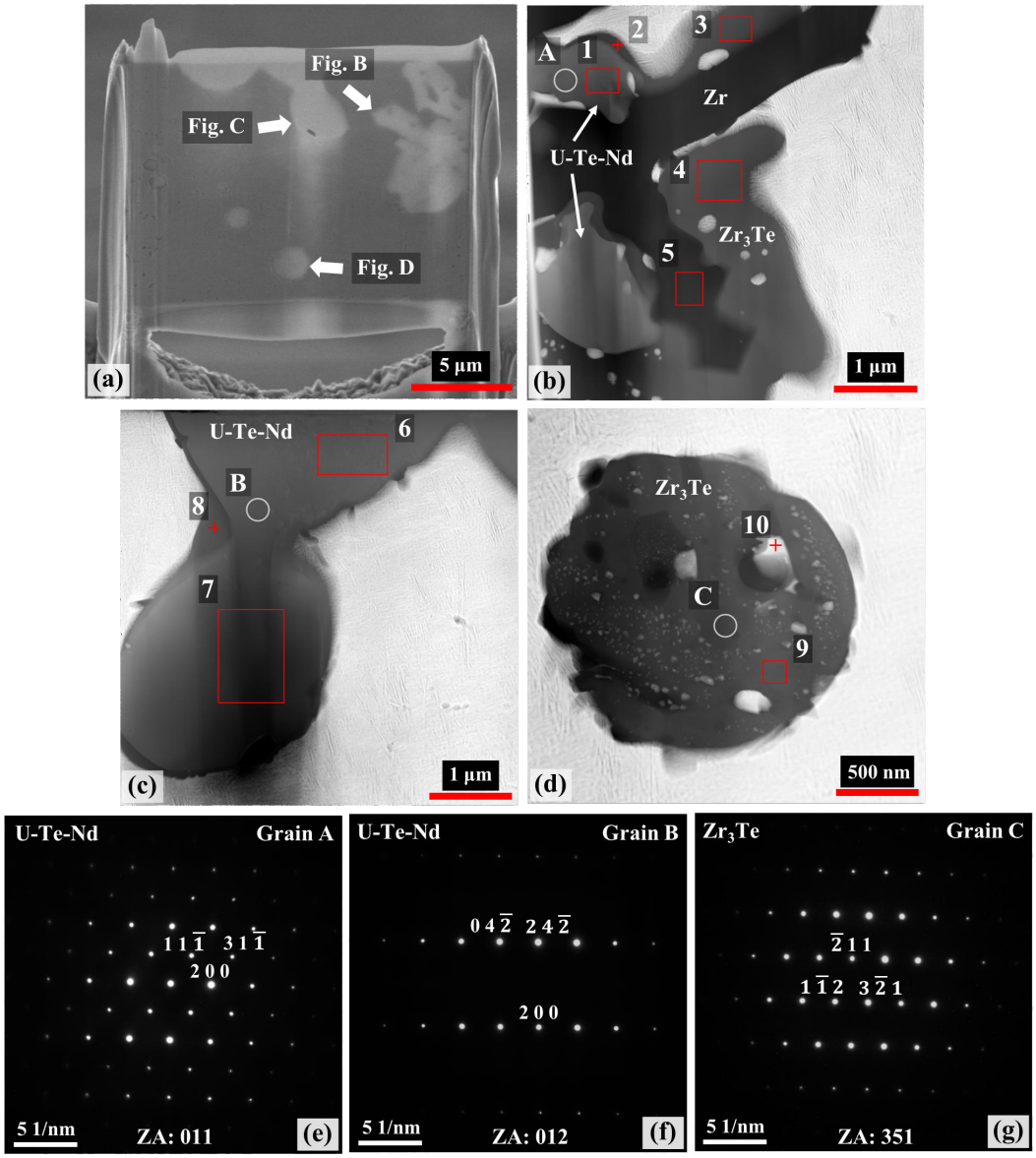

Figure 3.7. TEM analysis results of precipitates in the 4Te-4Nd alloy. (a) SEM image of the TEM lamella, and HAADF micrographs of (b) U-Te-Nd, Zr-Te, and Zr precipitates; (c) U-Te-Nd precipitate; and (d) Zr-Te precipitate. Single zone-axis SAED patterns from (e) grain *A* along the [011] zone axis, (f) grain *B* along the [012] zone axis, and (g) grain *C* along the [351] zone axis.

The HAADF micrographs shown in Figure 3.7 (b), (c) and (d) exhibit different types of precipitates. Elemental analysis of the lighter grey-contrast phases, depicted by points 1, 6 and 7, indicates that they are the combination of Nd, Te and U; similar to points 12-14 in Table 3.4. SAED patterns, obtained from locations *A* and *B* in Figures 3.7 (b) and (c) respectively,

are both found to index with the NdTe and UTe compounds, both of which are cubic and have similar crystallographic characteristics (Table 3.6). The formation of UTe precipitates within an alloy containing both Zr and Nd is not likely based on the thermodynamic characteristics of U-Te, Zr-Te and Nd-Te; as discussed further in the computational section later. Other potential binary compounds were considered – Nd_2Te_3, $NdTe_2$, Nd_2Te_5, and $NdTe_3$ – albeit none were found to match with the SAED patterns of a given grain. The few U-Nd-Te ternary compounds noted in literature were considered – UTe_4Nd_2, UTe_5Nd_2, and UTe_6Nd – but none could be indexed with the SAED patterns. The existence of stable U-Te-Nd compounds indicates that the formation of such a ternary phase is possible. It is worth noting that the U-Te-Nd phases documented in literature are Te-rich, which is a similar scenario to those precipitates analyzed in Figure 3.7 (b) and (c). Hence, due to the lack of a U-Te-Nd ternary phase diagram, the possibility that U-Te-Nd precipitates analyzed in this study being an undocumented ternary phase cannot be ruled out.

Table 3.5. TEM EDS elemental data results (in at%) of analysis points depicted in Figure 3.7 (b), (c), and (d).

	Figure 3.7 (b)						*Figure 3.7 (c) and (d)*				
	U	**Zr**	**Te**	**Nd**	**Phase[a]**		**U**	**Zr**	**Te**	**Nd**	**Phase[a]**
1	42.1	2.3	42.8	12.9	*U-Te-Nd*	**6**	38.1	0.9	39.6	21.3	*U-Te-Nd*
2	7.1	78.5	14.4	0	*Zr_3Te*	**7**	40.7	0	44	15.3	*U-Te-Nd*
3	3.4	77.6	18.8	0.2	*Zr_3Te*	**8**	1.7	75.4	21.5	1.5	*Zr_3Te*
4	4.0	76.5	19.4	0.1	*Zr_3Te*	**9**	3.0	76.5	19.2	1.4	*Zr_3Te*
5	0.3	99.6	0.1	0	*Zr*	**10**	83.2	16.3	0.3	0.2	*U-Zr[b]*

[a]*suggested phase based on EDS analysis*
[b]*matrix phase of the as-cast U-Zr alloy*

A medium grey-contrast phase is also found to be present in the HAADF images of Figure 3.7. This phase is observed to occupy a large portion of the precipitate phases formed in Figure 3.7 (b), in addition to forming as a layer surrounding the U-Te-Nd containing precipitates (Figure 3.7 (b) and (c)). It also appears to be the primary phase present in the globular precipitate of Figure 3.7 (d). Analysis of this phase (points 2 – 4, 8 and 9) indicates that it is a Zr-Te containing phase and based on the atomic ratio of the various points it appears to be the Zr_3Te compound. Diffraction analysis performed on location *C* (Figure 3.7 (d))

confirms this phase to be Zr_3Te. The Zr_3Te precipitates are observed to contain small white inclusions of varying sizes. EDS analysis of these inclusions observed in both Figures 3.7 (b) and (d), point 10, indicates these inclusions are in fact U-Zr precipitates matching that of the U-Zr matrix. Higher magnification of the Zr_3Te precipitates showed a fine dispersion of such inclusions measuring 10 – 50 nm in width. The presence of such inclusions would explain why the precipitates appear to be more Zr-rich than the Zr_3Te compound as well as explain the presence of U contained within the Zr_3Te precipitates. The middle of the precipitate in Figure 3.7 (b) contains a dark phase and as indicated by point 5, is found to be a Zr-rich inclusion, similar to those previously observed through SEM analysis (points 7, 8, 15, and 16 in Table 3.4).

Focused XRD analysis was also performed on the 2Te-2Nd and 4Te-4Nd alloys, the plots of which are presented in Figure 3.8 (a) and (b), respectively. The corresponding crystallographic information of the indexed phases are listed in Table 3.3. The diffraction patterns for both alloys indicate that each is comprised primarily of the α-U phase. Both alloys also exhibit peaks for the sputtered coating of Au, which was not removed prior to XRD analysis. Both diffraction plots confirm the presence of the NdTe compound, albeit with limited peak intensities. However, such limited intensities would be expected given the compound is only present in the alloy as dispersed precipitates, which were observed to be no larger than 25 μm. As with SAED, no U-Te-Nd ternary phase could be indexed in the XRD patterns. The Zr_3Te phase is indexed in the XRD pattern of the 4Te-4Nd alloy, further confirming its presence in the alloy. Traces of both UO_2 and Nd_2O_3 were found in both diffraction patterns, and the formation of UO_2 is, again, likely the result of surface oxidation. The formation of Nd_2O_3 can likely be attributed to the combination of surface oxidation and trace amounts of residual oxidation on the Nd feedstock materials that got mixed into the alloy.

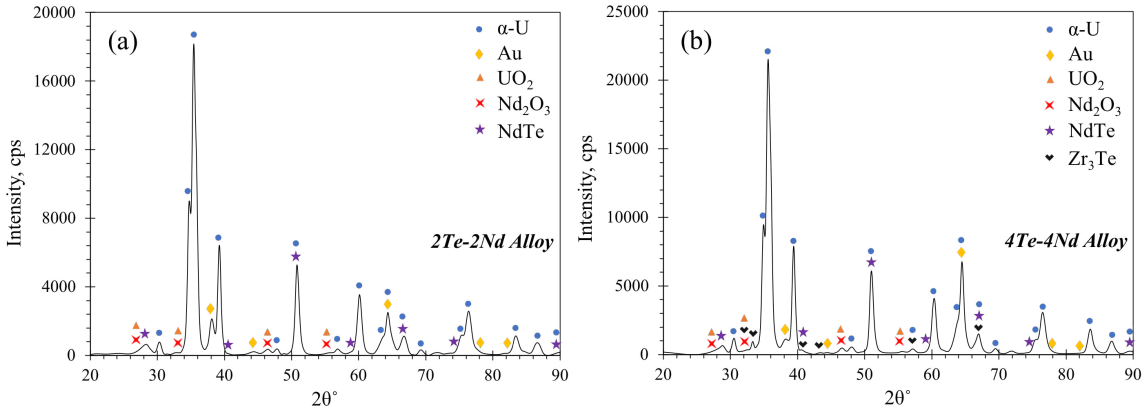

Figure 3.8. XRD patterns of (a) the 2Te-2Nd alloy and (b) the 4Te-4Nd alloy.

Table 3.6. Crystallographic details from determined phases from SAED patterns presented in Figure 3.7 (d), (e), and (f).

Compound	Pearson Symbol	Space Group	Cell Parameters
NdTe [34]	cF8	Fm$\bar{3}$m (225)	a = *b* = *c* =0.627 [nm] $\alpha = \beta = \gamma = 90°$
UTe [35]	cF8	Fm$\bar{3}$m (225)	*a* = *b* = *c* = 0.615 [nm] $\alpha = \beta = \gamma = 90°$
Zr_3Te [36]	tl32	I$\bar{4}$ (82)	*a* = *b* = 1.134, *c*=0.563 [nm] $\alpha = \beta = \gamma = 90°$

In the 2Te-2Nd alloy, all the precipitate phases observed were of NdTe type. This points toward the fact that during the final casting step, when Nd was added to the U-Zr-Te alloy, the existing Zr_2Te precipitates decomposed, releasing Te to form new precipitates with Nd. The formation of the NdTe compound is favorable, and according to the Nd-Te binary phase diagram it exhibits high temperature stability (T_{melt} = 2025 °C [37]), which can aid in mitigating availability of Nd to participate in processes leading to FCCI. Characterization of the 4Te-4Nd alloy revealed the formation of several compounds – NdTe and Zr_3Te as well as a possible U-Te-Nd ternary phase. However, it is important to note that no free Nd was observed in the alloy. This indicates that all available Nd was bound with Te. Therefore, the formation of other Te-based compounds, Zr-Te and U-Te-Nd, would indicate the alloy was Te-rich at this particular analysis plane and the 1:1 additive – lanthanide ratio was not maintained. It is worth recalling that the initial alloys were cast slightly additive-rich and thus the formation of other Te-based compounds beyond Nd-Te could be an indication that less Te

may have been lost during casting than what was initially assumed. Regardless, the presence of Nd-Te precipitates demonstrates their propensity to form preferably over Zr-Te compounds.

3.2.3 Computational prediction of phases

Formation of different compounds observed experimentally as well as the mutual interactions between Te, Nd and Zr can be understood from first principles calculations based on density functional theory (DFT) [16]. DFT calculated enthalpy of mixing (Table 3.7) for different elements was used as a guidance to predict preferred compound formation tendencies. For each composition in Table 3.7 the element at the end is the one for which enthalpy of mixing was calculated within a matrix containing all the previous element(s).

Table 3.7. Enthalpy of mixing values (as predicted by DFT) for different elements in various systems. A negative enthalpy indicates ease of formation of the stable compound.

Composition	**Enthalpy of mixing**
U-Te	0.16 eV
U-Zr-Te	-0.28 eV
U-Zr-Nd	2.54 eV
U-Nd-Te	-3.23 eV
U-Zr-Nd-Te	-1.48 eV

The enthalpy of mixing of Te inside the α-U matrix is slightly positive, i.e., 0.16 eV, whereas that of Te in the U-Zr system is negative, -0.28 eV. This indicates that Te will bind with the Zr within the U-matrix. Indeed, formation of the Zr_2Te phase was observed in the U-Zr-Te alloys, as shown in Figure 3.1. Further, the enthalpy of mixing of Nd inside the U-Zr matrix is 2.54 eV. This positive enthalpy of mixing indicates a phase-separating tendency of Nd in the U-Zr matrix and thus it is understandable why no Nd containing compound was observed within the U-Zr system. On the other hand, the enthalpy of mixing for Te in the U-Zr-Nd system is -1.48 eV and that in U-Nd is -3.23 eV, suggesting a strong compound forming tendency of Te with Nd regardless of presence or absence of Zr within the U-matrix. With the enthalpy of mixing of Te being more negative in both U-Zr-Nd (-1.48eV) and U-Nd (-3.23 eV)

compared to the enthalpy of mixing of Te in U-Zr (-0.28eV), the interactions between Nd and Te are expected to be stronger than the interactions between Zr and Te. Thus, it can be concluded that the phase stability in the ternary and in quaternary U-Zr-Nd-Te system can be inferred based on binary interactions between the elements involved (e.g.: Zr-Te interactions vs. Nd-Te interactions).

Furthermore, to understand the interactions between the elements the charge density differences (CDD) have been calculated, as depicted in Figure 3.9. The CDD is calculated by taking the difference in the calculated charge densities between final configurations and a pristine U-matrix at each atomic position. From Figure 3.9 (a), the charge transfer (indicated by a yellow isosurface) observed from Zr to Te indicates a potential interaction mechanism between the elements and therefore is one of the reasons for the negative enthalpy of mixing that was calculated for Te in the U-Zr matrix. Also, when there is Nd and Te in the system together with Zr, as shown in Figure 3.9 (b), the charge is noted to transfer from both Nd and Zr towards Te. The excess charge on Te (yellow isosurface) and the charge deficient region on both Nd and Zr (blue isosurface) indicate the attractive interaction of Te with Zr and Nd, which may lead to the formation of a stable compound. A similar interaction was observed between Nd and Te in the system when Zr was absent in the U-matrix [16].

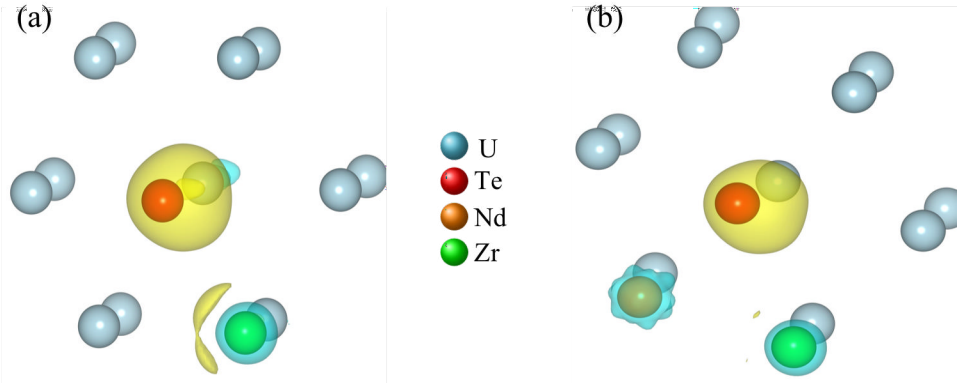

Figure 3.9. The charge density difference (CDD) between (a) U-Zr-Te and U and (b) U-Nd-Zr-Te and U systems; the yellow isosurface represents excess charge, and the blue isosurface represents a charge deficit or the negative value of charge density. Note that the figures were created by VESTA 3.0 software, https://onlinelibrary.wiley.com/iucr/doi/10.1107/S0021889811038970.

To gain a detailed understanding of the interactions between Nd, Te, and Zr, the partial density of states (DOS) have been plotted for Te and Nd in U-Zr-Te-Nd and U-Te-Nd systems, as shown in Figure 3.10 (a) and (b), respectively. The occupied 4*f* states of Nd lies below the

Fermi level and is localized between -5 to -4 eV, while the unoccupied 4*f* states are above the Fermi level. Furthermore, Figure 3.10 shows that localized Nd 4*f* orbitals (solid magenta lines) located between -5 to -4 eV interact with Te (solid green lines) via valence electrons (orbital hybridization), namely, *p* electrons of Te (indicated by the shaded region). The overlapping of the valence orbitals of the additive Te with the Nd *f* orbitals, as shown in Figure 3.10 (b), was also found to be the key indication for other additives such as Se and As, which were shown to be effective in binding with Nd inside the U-matrix [16]. Hence, from the comparison of both the enthalpy of mixing for Te in U-Zr-Nd and U-Nd matrices as well as the density of states shown in Figure 3.10 (a) and (b), it can be argued that Te is an effective candidate additive to bind with Nd inside the fuel matrix (U-Zr system).

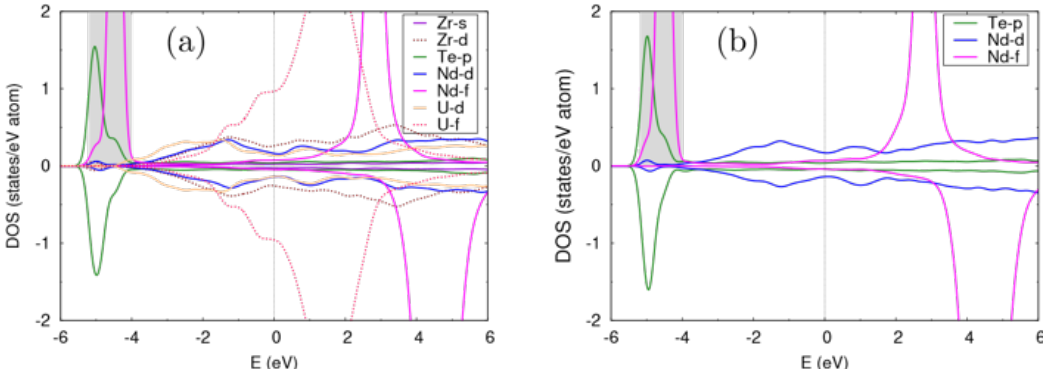

Figure 3.10. Orbital resolved DOS for (a) U-Zr-Te-Nd and (b) U-Te-Nd. The vertical dashed lines represent the Fermi level, the energy states up to which states are occupied. The states in the negative and positive vertical axis represent down and up spin components, respectively. U-DOS remain more or less similar in all systems.

Results from DFT calculations support the observations made in the characterization of the alloys of interest. The calculations show that the Zr-Te interaction is favorable within the U-Zr-Te alloys. On the other hand, the Nd-Te interactions appear to be even more favorable than Zr-Te, and thus as the fission product Nd forms within the U-Zr-Te alloys, Te is expected to leave Zr in order to bind with Nd.

3.3 Conclusions

To summarize, both experimental and DFT calculations confirm that binary interactions of Te with both Zr and Nd dominates the phase formations within the multi-component U-Zr-Te and U-Zr-Te-Nd alloys. In the ternary U-Zr-Te alloys, the binary interaction between Te and Zr was observed to be dominant through the formation of Zr_2Te

precipitates. In the quaternary U-Zr-Te-Nd alloys the binary interactions of Te with Nd and Zr were both observed through the formation of NdTe and Zr_3Te compounds, where the latter phase likely formed due to a Te concentration that exceeded the available Nd. Further, it was concluded that ternary interactions could be plausible through the formation of an unconfirmed U-Te-Nd compound.

It is apparent that Te can be an effective additive to bind with Nd within the U-Zr matrix. Furthermore, the formation of stable, high-melting point, Nd-Te compounds has the potential to stabilize the lanthanide within the fuel, and thus counteract its participation in the FCCI phenomenon. However, further work is necessary to evaluate the stability of the Nd-Te interactions in the non-equilibrium state experienced within an irradiation environment. Additionally, the FCCI phenomenon is driven by diffusion-based mechanisms and therefore further studies on the diffusion interactions of U-Zr-Te-Nd alloys with potential claddings alloys, such as HT-9, are being conducted to further examine the effectiveness of Te as a fuel additive to mitigate FCCI.

3.4 Methodology

3.4.1 Experimental methods

Raw materials, such as zirconium, tellurium and neodymium, were acquired from Alfa Aesar company. Neodymium was received as a rod packaged in mylar under argon. Uranium, depleted in the ^{235}U isotope to 0.22%, was initially cleaned by submersion in nitric acid, followed by a water wash and a subsequent ethanol wash.

Alloys were cast using an arc-melter, with high purity argon as a cover gas, contained within an argon glovebox. To achieve a homogeneous alloy, the button was melted and flipped three times after each element addition. The U-10Zr-Te alloys were cast using a two-step process, whereas the U-10Zr-Te-Nd alloys were cast using a three-step process. Initially, the uranium and zirconium were added to create a pre-alloy of U-10Zr (wt%). For all four alloys tellurium was added to the U-10Zr buttons in the second step at the appropriate concentration; the button was only flipped and re-melted twice in this step to limit loss of the additive. For the U-10Zr-Te-Nd alloys, neodymium was added to the U-10Zr-Te buttons in the third step at the appropriate concentrations to generate the simulated fuel alloys of interest. The alloys were then drop-cast to form pins with a diameter of approximately 5 mm.

A sample of each alloy pin was sectioned and mounted in a phenolic resin ring and epoxy for microstructural characterization. Samples were prepared by grinding using 320 grit SiC papers to achieve a uniform plane on the sample surface followed by sequential polishing steps with 9 μm, 3 μm and 1 μm polycrystalline diamonds suspended in an ethylene glycol solution. Final polishing steps of the samples were performed within an argon glovebox to limit surface oxidation. The polished surfaces were then sputtered with a 9 nm layer of gold to control charging of the metallographic mount within scanning electron microscope.

Scanning electron microscopy (SEM) was performed using a JEOL JSM-6610LV operated at an accelerating voltage of 20 kV. Imaging of the sample was primarily conducted using the backscatter electron imaging mode (BSE) to provide better contrast of the different phase formations. Energy dispersive x-ray spectroscopy (EDS) was conducted on the SEM in secondary electron (SE) mode using an EDAX Apollo X silicon drift detector (SDD) and the EDAX TEAM v4.4 (2016) software. The *amp time*, which is the time interval that x-ray energy absorption is processed at the detector, was adjusted for each analysis to generate a dead time of approximately 30%. In conducting point analysis, elemental spectra were collected for 50 live seconds per analysis location. In generating elemental X-ray maps a dwell time of 200 μs was used. Elemental data from EDS was quantified based on the standardless ZAF method, which relies on the EDAX TEAM library of stored spectra of standards. Furthermore, it is largely understood that such quantification can have a statistical error of between 2 – 5%. Transmission electron microscope (TEM) specimens were prepared on a FEI Quanta 3D FEG dual-beam microscope using a focused ion beam (FIB) lift-off technique. The TEM study was conducted using a Tecnai G2 F30 at an accelerating voltage of 300 kV. Both selected area electron diffraction (SAED) patterns and EDS data were collected using bright-field (BF) and high-angle annular dark field (HAADF) detectors. X-ray diffraction (XRD) was performed using a Rigaku SmartLab X-Ray Diffractometer paired with SmartLab Guidance software (v 2.0.4.7). The diffractometer was operated at a set tube current of 44 mA using Cu Kα radiation. Analysis was conducted with the optics set in the medium focus, parallel beam (PB) mode paired with a D/tex Ultra 250 1D silicon strip detector. Focused XRD $\theta/2\theta$ scans were conducted at several locations on the sample surface using a 0.04° step size and a scan speed of 2°/min. Data was analyzed and indexed using Rigaku's PDXL 2 software (v2.3.1.0) utilizing

the International Centre for Diffraction Data (ICDD) (PDF-2 Release 2016) database for XRD pattern indexing.

3.4.2 Computational methods

All calculations were performed using the density functional theory (DFT) as implemented in the Vienna *Ab initio* Simulation Package (VASP) [38, 39]. Computational details including the choice of *U* for GGA+*U* can be found in the work of Khanal *et al.* [16]. The following procedure was adopted in adding elements within the supercell. First a U atom was substituted with atom A (either Nd, Zr or Te atom) on a fully optimized 3 × 3 × 3 supercell of α-U, *Cmcm* (orthorhombic) structure [27], followed by a re-optimization of the atomic coordinates. After obtaining a newly DFT-optimized atom substituted system, another U-atom at the first nearest neighbor position to atom A was substituted with atom B, and the internal coordinates of the final structure at a fixed volume were optimized again. It is notable that for the quaternary U-Zr-Te-Nd system, several atomic configurations are possible among elements. For finding the most stable configuration of the U-Zr-Te-Nd system, sixteen different possible configurations were created by considering all nearest neighbor non-equivalent arrangements of the third element by fixing two elemental pairs at a time, i.e. Nd-Te, Zr-Te or Nd-Zr. Atomic positions for each configuration were optimized, and the most stable, i.e. minimum energy, configuration among all potential sixteen configurations was chosen for further study. Figure 3.11 shows an optimized structure of Nd and Te substituted within the U-Zr matrix.

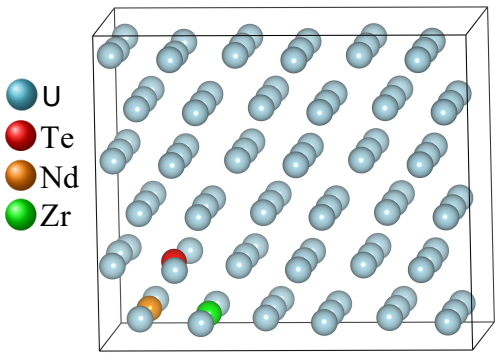

Figure 3.11. DFT optimized configuration of U-Zr-Te-Nd system. Note that the figure was created by VESTA 3.0 software, https://onlinelibrary.wiley.com/iucr/doi/10.1107/S0021889811038970.

Equation (3.1) shows a typical equation used to calculate the enthalpy of mixing of an element B in an U-A matrix (Table 3.7) [40, 41]:

$$\Delta E_{\text{mixing}} = E(U_{n-2}NdTe) + E(U) - E(U_{n-1}Nd) - E(Te), \quad (3.1)$$

in which $E(U_{n-2}AB)$ is the total energy of $(n-2)$ U atoms, one A and one B atom in a simulation cell of n sites; $E(U_{n-1}A)$ is the total energy of $(n-1)$ U atoms and one A atom in a simulation cell of n sites; and $E(B)$ and $E(U)$ are the total energy per atom for B and U, respectively. Here, negative enthalpy indicates ease of formation of the stable compounds whereas positive enthalpy, or a higher value, represents less tendency for the formation of a stable compound. The concept of mixing enthalpy in the formation of intermetallic compounds has been previously used in studying the stability of high entropy alloys (HEA) [42, 43].

Acknowledgments

Funding to support this research was provided by the Department of Energy's Nuclear Energy University Program (NEUP) grant under contract number DE-NE0008557. Furthermore, the authors gratefully acknowledge the Department of Energy, under DOE-NE Idaho Operations Office Contract DEAC07-05ID14517. The support from staff was instrumental at both Idaho National Laboratory (INL) and the Center for Advanced Energy Studies (CAES), where the research activities were performed. In particular, the Advanced Materials Laboratory (AML) and Microscopy and Characterization Suite (MaCS) located at CAES were used extensively for their radiological sample handling and sample preparation capabilities, as well as for their microscopy and data analysis tools. The authors would like to thank Wayne Poole of INL, as well as Kristi Moser-McIntire, Mason Jaussi, and Joanna Taylor of CAES for their support in the logistics of shipping and handling of the radiological materials. A special thank you to Bryan Forsmann of CAES for his hands-on support in the radiological work. Computational power for this study was provided by the High-Performance Computing (HPC) Center at INL. Publication of this article was funded by the University of Idaho – Open Access Publishing Fund.

References

[1] D. C. Crawford, D. L. Porter, and S. L. Hayes. Fuels for sodium-cooled fast reactor: US perspective. *J. Nucl. Mater.,* 371(1-3): 202-231, 2007. https://doi.org/10.1016/j.jnucmat.2007.05.010

[2] T. Ogata. Metal Fuel. *Compr. Nucl. Mater.,* Vol. 3: 1-40, 2012. https://doi.org/10.1016/B978-0-08-056033-5.00049-5

[3] W. J. Carmack, D. L. Porter, Y. I. Chang, S. L. Hayes, M. K. Meyer, D. E. Burkes, C. B. Lee, T. Mizuno, F. Delage, and J. Somers. Metallic fuels for advanced reactors. *J. Nucl. Mater.,* 392(2): 139-150, 2009. http://dx.doi.org/10.1016/j.jnucmat.2009.03.007

[4] D. D. Keiser. Metal fuel-cladding interaction. *Compr. Nucl. Mater.,* Vol. 3: 423-441, 2012. http://dx.doi.org/10.1016/B978-0-08-056033-5.00067-7

[5] C. W. Arnold, J. Galloway, and C. Unal. Towards understanding FCCI: modeling cerium solid transport in metal fuels. *Trans. American Nucl. Society,* 112:269-270, June 2015

[6] R. D. Mariani, D. L. Porter, T. P. O'Holleran, S. L. Hayes, and J. R. Kennedy. Lanthanides in metallic nuclear fuels: Their behavior and methods for their control. *J. Nucl. Mater.*, 419(1-3): 263-271, 2011. http://dx.doi.org/10.1016/j.jnucmat.2011.08.036

[7] G. L. Hofman, L. C. Walters, and T. H. Bauer. Metallic fast reactor fuels. *Progress in Nucl. Energy,* 31(1): 83-110, 1997.

[8] D. D. Keiser and J. I. Cole. An evaluation of potential liner materials for eliminating FCCI in irradiated metallic nuclear fuel elements. *Proc. of GLOBAL 2007*, 569-604, Sep. 2007.

[9] F. Khatkhatagy, J. Jian, L. Jiao, Q. Su, J. Gan, J. I. Cole, and H. Wang. Diffusion barrier properties of nitride-based coatings on fuel cladding. *J. Alloys Compds.,* 580: 442-448, 2013. http://dx.doi.org/10.1016/j.jallcom.2013.06.108

[10] M. T. Benson, L. He, J. A. King, and R. D. Mariani. Microstructural characterization of annealed U-12Zr-4Pd and U-12Zr-4Pd-5Ln: Investigating Pd as a metallic fuel additive. *J. Nucl. Mater.*, 502: 106-112, 2018. https://doi.org/10.1016/j.jnucmat.2018.02.012

[11] M. T. Benson, J. A. King, R. D. Mariani, and M. C. Marshall. SEM characterization of two advanced fuel alloys: U-10Zr-4.3Sn and U-10Zr-4.3Sn-4.7Ln. *J. Nucl. Mater.,* 494: 334-341, 2017. http://dx.doi.org/10.1016/j.jnucmat.2017.07.057

[12] Y. Xie, M. T. Benson, J. A. King, R. D. Mariani, and J. Zhang. Characterization of U-Zr fuel with alloying additive Sb for immobilizing fission product lanthanides. *J. Nucl. Mater.,* 498: 332-340, 2018. https://doi.org/10.1016/j.jnucmat.2017.10.039

[13] Y. S. Kim, T. Wieneck, E. O'Hare, and J. Fortner. Effectiveness of a dopant in U-Zr metallic fuel to prevent lanthanide migration. *Proc. of GLOBAL 2013,* 1118-1125, Sep. 2013.

[14] M. T. Benson, Y. Xie, J. A. King, K. R. Tolman, R. D. Mariani, I. Charit, J. Zhang, M. P. Short, S. Choudhury, R. Khanal and N. D. Jerred. Characterization of U-10Zr-2Sn-2Sb and U-10Zr-2Sn-2Sb-4Ln to assess Sn+Sb as a mixed additive system to bind lanthanides. *J. Nucl. Mater.*, 510: 210-218, 2018. https://doi.org/10.1016/j.jnucmat.2018.08.017

[15] Y. S. Kim, T. Wieneck, E. O'Hare, J. Fortner, A. Wright, J. S. Cheon, and B. O. Lee. Effect of indium addition in U-Zr metallic fuel on lanthanide migration. *J. Nucl. Mater.*, 484: 297-306, 2017. https://doi.org/10.1016/j.jnucmat.2016.11.012

[16] R. Khanal, N. Jerred, M. Benson, D. A. Andersson, R. Mariani, I. Charit, and S. Choudhury. A novel approach to selection of dopant to immobilize neodymium in uranium-based metallic fuels. *Sci. Rep.,* under review (2019).

[17] Y. Xie, J. Zhang, M. T. Benson, J. A. King, and R. D. Mariani. Assessment of Te as a U-Zr fuel additive to mitigate fuel-cladding chemical interactions. *J. Nucl. Mater.,* 513: 175-184, 2019. https://doi.org/10.1016/j.jnucmat.2018.10.050

[18] D. Janney and S. Hayes. Experimentally known properties of U-10Zr alloys: A critical review. *Nucl. Tech.,* 203(2): 109-128, 2018. https://doi.org/10.1080/00295450.2018.1435137

[19] Y. Zhang, X. Wang, G. Zeng, H. Wang, J. Jia, L. Sheng, and P. Zhang. Microstructural investigation of as-cast uranium rich U-Zr alloys. *J. Nucl. Mater.,* 471: 59-64, 2016. http://dx.doi.org/10.1016/j.jnucmat.2016.01.005

[20] L. Leibowitz, R. A. Blomquist and A. D. Pelton. Thermodynamics of the uranium-zirconium system. *J. Nucl. Mater.,* 167: 76-81, 1989. https://doi.org/10.1016/0022-3115(89)90426-1

[21] W. Xiong, W. Xie, C. Shen, and D. Morgan. Thermodynamic modeling of the U-Zr system – A revisit. *J. Nucl. Mater.,* 443(1-3): 331-341, 2013. http://dx.doi.org/10.1016/j.jnucmat.2013.07.034

[22] A. P. Moore, B. Beeler, C. Deo, M. I. Baskes, and M. A. Okuniewski. Atomistic modeling of high temperature uranium-zirconium alloy structure and thermodynamics. *J. Nucl. Mater.* 467: 802-819, 2015. https://doi.org/10.1016/j.jnucmat.2015.10.016

[23] J. T. McKeown S. Irukuvarghula, S. Ahn, M. A. Wall, L. L. Hsiung, S. M. McDeavitt, and P. E. A. Turchi. Coexistence of the α and δ phases in an as-cast uranium-rich U-Zr alloy. *J. Nucl. Mater.,* 436(1-3): 100-104, 2013. http://dx.doi.org/10.1016/j.jnucmat.2013.01.313

[24] S. Irukuvarghula, S. Ahn, and S. M. McDeavitt. Decomposition of the γ phase in as-cast and quenched U-Zr alloy. *J. Nucl. Mater.,* 473: 206-217, 2016. http://dx.doi.org/10.1016/j.jnucmat.2016.02.028

[25] H. Okamoto. Te-Zr (tellurium-zirconium). *J. Phase Equilib.,* 20: 168, 1999.

[26] G. Örlygsson and B. Harbrecht. Synthesis and crystal structure of Zr_2Te. Distinctions in bonding to isotypic Sc_2Te and the relationship to the structure of congeneric Hf_2Te and Zr_2Se. *Inorg. Chem.,* 38(14): 3377-3383, 1999. http://dx.doi.org/10.1021/ic990024a

[27] W. T. Eeles and A. L. Sutton. X-ray determination of the atomic positions in *α*-uranium at 22°C and 600°C. *Acta. Cryst.*, 16(6): 575, June 1963. https://doi.org/10.1107/S0365110X63001511

[28] L. Desgranges, G. Baldinozzi, G. Rousseau, J. C. Nièpce, and G. Calvarin. Neutron diffraction study of the in-situ oxidation of UO_2. *Inorg. Chem.,* 48(16): 7585-7592, July 2009. https://doi.org/10.1021/ic9000889

[29] B. Harbrecht and R. Leersch. Synthesis and crystal structure of Zr_3Te. *J. Alloys Compd.*, 238(1-2): 13-17, May 1996. https://doi.org/10.1016/0925-8388(95)02078-0

[30] W. Lin, H. Steinfink, and E. J. Weiss. The phase equilibria and crystal chemistry of the rare earth group VI systems. III. neodymium-tellurium. *Inorg. Chem.*, 4(6): 877-881, June 1965. https://doi.org/10.1021/ic50028a024

[31] C. Artini, M. Pani, J. R. Plaisier, and G. A. Costa. Structural study of Nd oxidation by means of in-situ synchrotron X-ray diffraction ($400 \leq T \leq 700$ ºC). *Solid State Ionics*, 257: 38-41, April 2014. https://doi.org/10.1016/j.ssi.2014.01.034

[32] H. E. Swanson and E. Tatge. Standard X-ray diffraction powder patterns. *Natl. Bur. Stand. (U.S.) Circ. 539*, I: 33, June 1953.

[33] D. E. Janney and T. P. O'Holleran. Zr inclusion in actinide-Zr alloys: New data and ideas about how they form. *J. Nucl. Mater.* 460: 13-15, 2015. http://dx.doi.org/10.1016/j.jnucmat.2015.01.065

[34] S. S. Batsanov, V. P. Bokarev, and G. V. Dorogova. Shock synthesis of solid solutions of neodymium and samarium chalcogenides. *Russ. J. Inorg. Chem.*, 30 (138-139): 246-248, 1985.

[35] T. Herrmannsdörfer, P. Fischer, K. mattenberger, and O. Vogt. Temperature dependences of rhombohedral lattice distortion and of ferromagnetic uranium ordering in the uranium monochalcogenides. *J. Alloys Compd.*, 414(1-2): 14-19, 2006. https://doi.org/10.1016/j.jallcom.2005.07.022

[36] R. de Boer, E. H. P. Cordfunke, P. van Vlaanderen, D. J. W. IJdo, and J. R. Plaisier. The crystal stuctures of Zr_5Te_4 and Zr_3Te. *J. Solid State Chem.*, 139: 213-219, 1998.

[37] H. Okamoto. Nd-Te (neodymium-tellurium). *Binary Alloy Phase Diagram,* 2nd Ed., Ed. T. B. Massalski*,* 1990.

[38] G. Kresse and J. Furthmüller. Efficient iterative schemes for ab initio total-energy calculations using a plane-wave basis set. *Phys. Rev. B*, 54(16): 11169–11186, October 1996. https://doi.org/10.1103/PhysRevB.54.11169

[39] G. Kresse and J. Furthmüller. Efficiency of ab-initio total energy calculations for metals and semiconductors using a plane-wave basis set. *Comput. Mater. Sci.*, 6(1): 15–50, July 1996. https://doi.org/10.1016/0927-0256(96)00008-0

[40] A. E. Shields, S. E. Ruiz Hernandez, and N. H. de Leeuw. Theoretical analysis of uranium-doped thorium dioxide: Introduction of a thoria force field with explicit polarization. *AIP Adv.*, 5(8):087118, August 2015. https://doi.org/10.1063/1.4928438

[41] Chao Jiang. First-principles study of ternary bcc alloys using special quasi-random structures. *Acta Mater.*, 57(16): 4716–4726, September 2009. http://dx.doi.org/10.1016/j.actamat.2009.06.026

[42] O. N. Senkov, G. B. Wilks, D. B. Miracle, C. P. Chuang, and P. K. Liaw. Refractory high-entropy alloys. *Intermetallics*, 18(9): 1758–1765, September 2010. https://doi.org/10.1016/j.intermet.2010.05.014

[43] S. Singh, N. Wanderka, B. S. Murty, U. Glatzel, and J. Banhart. Decomposition in multi-component AlCoCrCuFeNi high-entropy alloy. *Acta Mater.*, 59(1): 182–190, January 2011. https://doi.org/10.1016/j.actamat.2010.09.023

CHAPTER 4
EVALUATION OF Sb-Nd AND Te-Nd PHASES WITHIN THE U-Zr FUEL MATRIX AND THEIR INTERACTIONS WITH HT9

Prepared for publication in the Journal of Nuclear Materials
"Evaluation of Sb-Nd and Te-Nd Phases within the U-Zr Fuel Matrix and their Interactions with HT9" *J. Nucl. Mater.*, (2021) TO BE SUBMITTED.

Abstract. Antimony (Sb) and tellurium (Te) are investigated as potential additives for U-10Zr (wt.%) metallic fuel to limit the fuel-cladding chemical interaction (FCCI) phenomena. Neodymium (Nd) is utilized to simulate the formation of lanthanide-based solid fission products which have been found to play a detrimental role in FCCI. Fuel alloys of U-Zr-Sb-Nd and U-Zr-Te-Nd are evaluated in their annealed condition and compared against their as-cast conditions. Isothermal diffusion couple experiments are carried out between U-Zr-Nd, U-Zr-Sb-Nd, and U-Zr-Te-Nd against the cladding alloy HT9 to evaluate the effectiveness of the additives to stabilize Nd within the fuel alloys, as well as investigate the interaction regions that form between the different fuel alloys and HT9. SbNd, Sb_3Nd_4, and TeNd were found to be the primary lanthanide-based phases to form within the U-Zr-Sb-Nd and U-Zr-Te-Nd alloys, respectively. The zirconium-based phase, Zr_2Sb, was also found to form within the former alloy. All phases were found to remain stable through the diffusion experiments and exhibited no interaction with cladding alloy constituents.

4.1 Introduction

The U-Zr metallic fuel system begins to experience deleterious effects due to chemical interactions at the fuel-cladding interface under increasing burnup conditions, commonly referred to as fuel-cladding chemical interactions (FCCI) [1–4]. The U-Zr alloy has been extensively used in historical sodium cooled fast reactors (SFR), e.g. Experimental Breeder Reactor II (EBR-II), [5,6] and is a primary fuel option for more advanced SFR concepts [7,8]. However, the onset of FCCI greatly limits the burnup potential of U-Zr fuels. In particular lanthanides, e.g. Nd, Ce, La, and Pr, which form as solid fission products (FPs), have been found to interact aggressively with cladding-based constituents. Such interactions can lead to the formation of brittle, low-melting phases that diminish cladding strength and can eventually lead to cladding breach [1]. The use of alloying additives in the fuel matrix is being evaluated to mitigate the negative effects of FCCI. This is accomplished by using additives that bind with and form high temperature, stable compounds with the lanthanide elements as they form or burn-in to the fuel matrix. In turn, the formation of such stable additive-lanthanide compounds reduces their chemical reactivity with cladding constituents. An evaluation of potential additives to bind with the lanthanides has been presented by Mariani *et al.* [9] and several additives have thus far been studied: Pd [9–12], Sn [13], Sb [14–17], Sn+Sb [18], Te [17,19,20], As [21–23], Se [23], and Bi [24].

In this study both Sb and Te are evaluated as additives and Nd is used to represent lanthanide FP formation. Each additive is alloyed into the U-10Zr (wt.%) fuel followed by the addition of Nd, to evaluate the additive-lanthanide interactions within the matrix. Sb is attractive as an additive as it has already demonstrated its propensity to bind with Ce, as well as mitigate its interactions with Fe and the Fe-12Cr (wt.%) cladding alloy HT9 [14,17,25]. In the authors' previous research [16], it was demonstrated that alloying Sb with Nd, at roughly a 1:1 atomic ratio, leads to the formation of the SbNd and Sb_3Nd_4 phases, which in turn mitigates the interactions of Nd with HT9. The interaction tendencies of Sb within the U-Zr matrix, i.e. a U-Zr-Sb alloy, have been previously characterized and the Zr_2Sb phase was found to be the primary intermetallic compound formed [14]. The diffusion interactions of U-Zr-Sb alloys against HT9 has also been carried out and is characterized by Zhuo *et al.* [25]. Te is also attractive as an additive as it has been found to preferentially bind with Nd. In the work of Jerred *et al.* [20], which is also reported in Chapter 3 of this dissertation, it was found that Te

binds with Zr to primarily form the Zr_2Te intermetallic compound. Then when Nd was alloyed into the U-Zr-Te alloy, Te was found to primarily form the high-temperature, stable TeNd compound. It should be noted that in Xie *et al*. [17], which evaluated the diffusion behavior of the CeTe phase with Fe and HT9, found that the CeTe phase did not remain stable after 72 h at 853 K and Ce was found to bind with Cr whereas Te was found to bind with Cr and Fe forming Cr_3Te_4 and TeFe phases. However, an evaluation of Sb and Te (as additives) and Nd (as the lanthanide) and their interactions with HT9 has not been carried out within the U-Zr matrix. This study will evaluate the thermal stability of the Sb-Nd and Te-Nd formations through the characterization of a U-Zr-Sb-Nd alloy in both the as-cast and annealed conditions, as well as a U-Zr-Te-Nd alloy in the annealed condition. Finally, the efficacy of Sb and Te as additives are examined using isothermal diffusion couple experiments between U-Zr-Nd, U-Zr-Sb-Nd, and U-Zr-Te-Nd alloys against HT9. Such an experimentation method is typical in studying the FCCI phenomena out-of-pile [1] and has been used extensively to evaluate the effectiveness of additives to mitigate lanthanide interactions with cladding alloys [11,12,16,17].

4.2 Materials and Methodology

4.2.1 Materials

To synthesize the alloys, raw materials, such as Zr, Sb, Te and Nd, were acquired from Alfa Aesar company. The Sb was received in shot form exceeding 99.9% purity, and the Nd was received as a rod having a purity of 99.5%. Uranium, depleted in the ^{235}U isotope to 0.22%, used for alloying was initially cleaned by submersion in nitric acid, followed by a water wash and a subsequent ethanol wash. The chemical composition of the HT9 alloy used is listed in Table 4.1

Table 4.1. Chemical composition in wt.% of the HT9 cladding alloy used in this study.

Element	**C**	**Si**	**Mn**	**Cr**	**Ni**	**Mo**	**W**	**V**	**Fe**
Concentration	0.17	0.29	0.58	11.73	.58	1.03	0.5	0.29	Bal.

All alloys were fabricated using an arc-melter, with high purity argon as a cover gas, contained within an argon glovebox. To achieve a homogeneous alloy, the button alloy was

melted and flipped three times after each element addition. The button was then melted and cast into a rod ~5mm diameter. Disks were then sectioned from the rod for either alloy characterization or isothermal diffusion experiments. A U-10Zr (wt.%) pre-alloy was initially fabricated. For the U-10Zr-4Nd (wt.%) alloy, the Nd was added to the U-Zr button. For the U-10Zr-3.6Sb-4Nd (wt.%) alloy, Sb was first added to the U-Zr button to achieve a U-Zr-Sb alloy and then Nd was added to create the final alloy composition. For the U-10Zr-4.3Te-4Nd (wt.%) alloy, the button was only melted and flipped twice after the Te addition to limit evaporation loss due to its low boiling temperature of 988 °C (1261 K). Nd was then added to the U-Zr-Te alloy. The Nd concentration used matches the total lanthanide concentration that can potentially form within U-10Zr (wt.%) fuel up to 16 at.% burnup, which is based on the chemical analysis of a U-10Zr (wt.%) fuel irradiated in EBR-II [9]. The alloyed concentration of Sb and Te targets a ~1:1 atomic ratio to that of the Nd concentration in order to promote the formation of the high temperature SbNd and TeNd intermetallic compounds. Although both alloys were fabricated slightly additive-rich, the concentration of Te was slightly greater to compensate for its loss during arc melting. Table 4.2 provides more details on the different specimens being evaluated in this study and experimental conditions.

Table 4.2. Samples analyzed in this study and their experimental condition.

Sample ID	**Alloy Composition (wt.%)**	**Alloy Composition (at.%)**	**Sample Condition[a]**
Sb-Nd	U-10Zr-3.6Sb-4Nd	U-23.4Zr-5.8Sb-5.4Nd	as-cast and annealed, 675 °C (948 K), 96 h
Te-Nd	U-10Zr-4.3Te-4Nd	U-21.32Zr-6.6Te-5.4Nd	annealed, 675 °C (948 K), 96 h
Nd/HT9	U-10Zr-4Nd/HT9	U-22Zr-5.6Nd/HT9	diffusion couple against HT9, 675 °C (948 K), 96 h
Sb-Nd/HT9	U-10Zr-3.6Sb-4Nd/HT9	U-23.4Zr-5.8Sb-5.4Nd/HT9	diffusion couple against HT9, 675 °C (948 K), 96 h
Te-Nd/HT9	U-10Zr-4.3Te-4Nd/HT9	U-21.32Zr-6.6Te-5.4Nd/HT9	diffusion couple against HT9, 675 °C (948 K), 96 h

[a]refers to the condition of the sample when analyzed, i.e. as-cast or annealed (at stated furnace parameters) or as part of a diffusion couple experiment (at stated furnace parameters)

4.2.2 Experimental methods

Isothermal diffusion experiments were carried out to evaluate the interactions between fuel alloys and HT9. Diffusion couple experiments were performed inside a muffle furnace

contained in an inert argon glovebox. The diffusing materials for the experiments were initially sectioned into discs approximately 2.5 mm thick and the diffusing interfaces were polished to a 1 μm finish within the glovebox to alleviate any oxide layer formations. The discs were placed in contact with each other and then wrapped in a layer of tantalum foil (~0.025mm thick) and placed inside a jig made of Kovar™ steel, an iron-nickel-cobalt alloy that exhibits low thermal expansion. Alumina discs were placed directly between the diffusion couple and jig contact points to avoid adverse interactions through the experiment. The entire jig was then wrapped in additional layers of tantalum foil and placed into the furnace. The glovebox atmosphere was maintained at 1–5 ppm oxygen, while a continuous flow of high purity argon cover gas was maintained into the furnace at a rate of 0.25 ft^3/h (1.97 cm^3/s) for the length of the experiment. To achieve a high purity, the argon cover gas was initially passed through an oxygen getter furnace, reducing its oxygen content down to 10^{-10}–10^{-11} ppb. The flow of high purity argon into the furnace chamber was maintained for 30 m prior to initiating the diffusion experiments. The furnace was then heated at a rate of 1,000 °C/h (0.28 K/s) up to the experiment temperature of 675 °C (948 K) and held for 96 h. Upon completion of the diffusion experiment, the jig was immediately removed from the furnace chamber and allowed to cool in the open glovebox environment. The experiment temperature, although exceeding the normal reactor steady-state temperature for such fuel, was chosen to align with other diffusion couple research investigating cladding alloys but to not exceed the Fe-Nd eutectic temperature of 685 °C (958 K).

4.2.3 Characterization methods

For microstructural characterization, samples were mounted in epoxy and prepared by grinding using sequential grits of SiC papers followed by polishing down to a 1 μm finish using diamond-based suspensions. A section of the Sb-Nd alloy, in the as-cast condition, was separated directly from the cast pin and then mounted. The diffusion couples were each cross-sectioned to expose the interaction regions and then mounted. To analyze the Sb-Nd and Te-Nd alloys in their annealed conditions, analysis was performed on their respective diffusion couples focusing on an area of the fuel alloy away from the diffusing interface. All sample preparation steps were performed within an inert argon glovebox to avoid surface oxidation on

the analysis surface. The polished surfaces were then coated with a thin layer of gold to control charging of the metallographic mount during electron microscopy analysis.

Scanning electron microscopy (SEM) was performed using a JEOL JSM-6610LV operated at an accelerating voltage of 20 kV. Imaging was conducted in the backscatter electron (BSE) imaging mode to get better contrast of phase formations. Energy dispersive X-ray spectroscopy (EDS) was conducted using an EDAX Apollo X silicon drift detector (SDD) and EDAX TEAM v4.4 (2016) software. The amp time was adjusted for each analysis to generate a dead time of between 20% to 30%. Elemental spectra were collected for 50 live seconds for point analysis per location, and a dwell time of 200 µs was used for elemental mapping. EDS datasets were quantified based on the standardless ZAF method using the EDAX TEAM library of spectra standards. X-ray diffraction (XRD) was performed using a Rigaku SmartLab X-Ray Diffractometer paired with SmartLab Guidance software (v 2.0.4.7). XRD was conducted using a parallel beam (PB) optics configuration, Cu Kα radiation at a tube current of 44 mA, and a D/tex Ultra 250 1D silicon strip detector. Focused XRD $\theta/2\theta$ scans were performed using a 0.04° step size and a 5°/min scan speed. Datasets were analyzed and indexed using Rigaku's PDXL 2 software (v2.3.1.0) and the International Centre for Diffraction Data (ICDD) (PDF-2 Release 2016) database.

4.2.4 Ab initio calculation methods

Calculations were performed using the density functional theory (DFT) method as implemented in the Vienna *Ab initio* Simulation Package (VASP) [26,27]. Mixing enthalpy calculations of additives and lanthanides in (i) Fe, (ii) Fe-Cr, (iii) U, (iv) U-Zr, and (v) U-Nd matrices were carried out to further understand the thermodynamics and compound forming tendencies of these systems. Both Fe and Cr were chosen in systems (i) and (ii) as they are the primary cladding constituents of concern in the HT9 cladding alloy. Systems (iii) and (iv) are representative of the fuel, where system (v) represents the fuel after fission, i.e. once Nd forms as a solid FP. To calculate the enthalpy of mixing of element B within the U-A-B system, first, a U atom was substituted for an A atom (A=Nd or Zr) in a fully optimized 3 x 3 x 3 supercell of α-U, *Cmcm* (orthorhombic) structure. The atomic coordinates were then re-optimized. Within the U-A system a U atom, at the first nearest neighbor position to the A atom, was substituted for a B atom (B=Te or Sb or Fe or Cr). Internal coordinates of the final structure

(U-A-B) were also optimized at a fixed volume. The enthalpy of mixing of element B in the U-A system was then calculated as follows:

$$\Delta E_{\text{mixing}} = E(U_{n-2}AB) + E(U) - E(U_{n-1}A) - E(B) \quad (4.1)$$

$E(U_{n-2}AB)$ is the total energy of $(n-2)$U atoms in a simulation cell of n sites with one atom of both A and B as the first nearest neighbor. $E(U_{n-1}A)$ is the total energy of (n − 1)U atoms in a simulation cell of n sites. E(B) and E(U) are the total energy per atom for B and U, respectively. A similar approach was adopted to calculate the enthalpy of mixing within the (i) Fe and (ii) Fe-Cr systems. Additional details of this computational approach, including the choice of U for GGA+U, has been reported elsewhere [21–23].

4.3 Results and Discussion

4.3.1 As-cast and annealed structures of the Sb-Nd alloy

An evaluation of the Sb-Nd alloy in its as-cast condition found that the primary precipitate formations were observed to form in two different morphologies. One formation was needle-like and was noted to be dispersed throughout the alloy, while the other was globular and was observed to be distributed in clusters throughout the alloy. SEM images of the Sb-Nd as-cast alloy are shown in Figure 4.1 (a)–(d). The needle shaped precipitates were thin, being only a few microns wide and were 10–20 μm in length. The globular precipitates (shown in Figure 4.1 (b) and (d)) vary in size from between 5 μm up to 20 μm in diameter. EDS analysis, both point and elemental mapping, was performed on the section of the alloy shown in Figure 4.1 (b). Elemental map results are shown in Figure 4.1 (e), and the corresponding point analysis results are listed in Table 4.3.

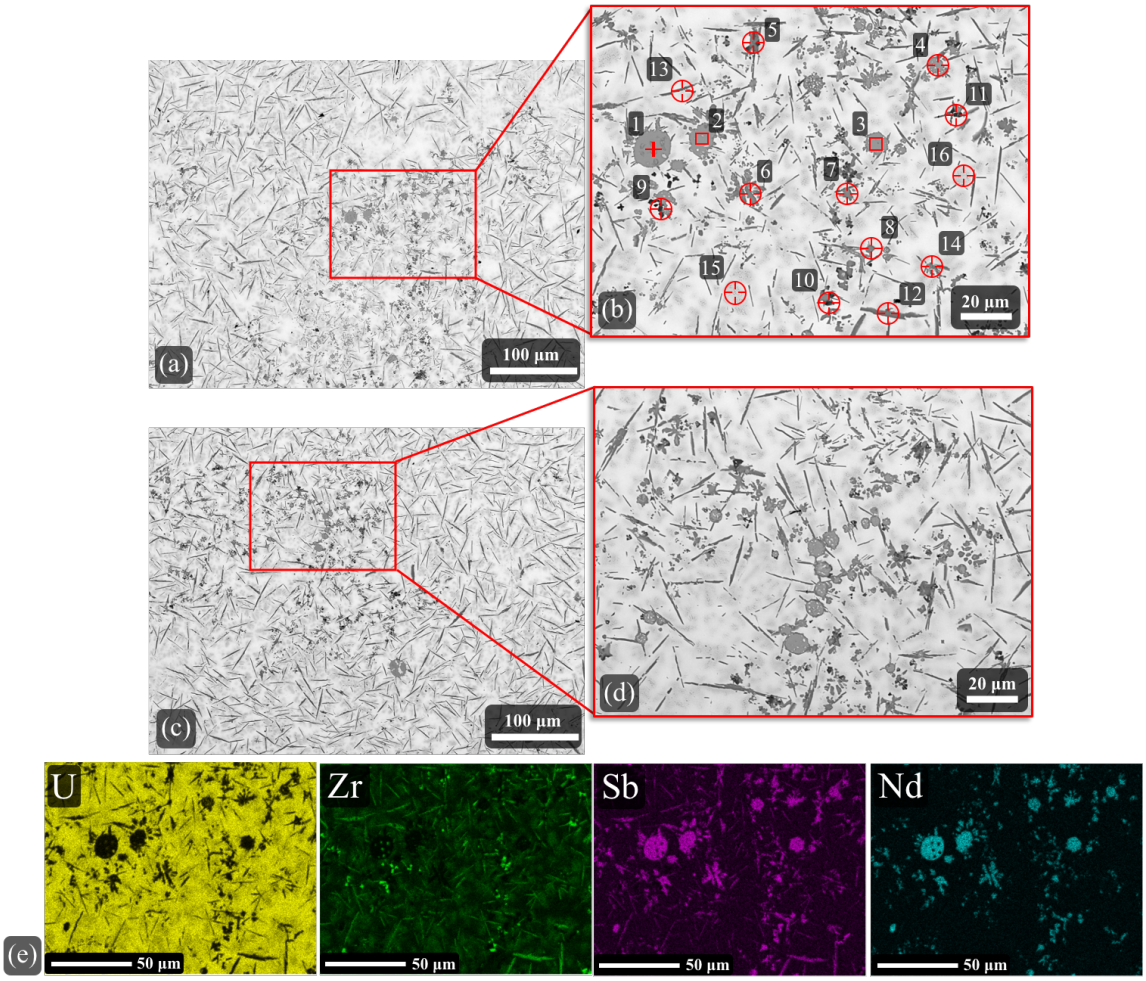

Figure 4.1. (a)–(d) BSE micrographs of the Sb-Nd alloy in the as-cast condition at different magnifications. EDS point analysis results can be found in Table 4.3. (e) EDS elemental maps of the area imaged in (b).

From the elemental maps in Figure 4.1 (e), the needle-like precipitates appear to contain Zr and Sb, whereas the globular precipitates contain Sb and Nd. From location-specific EDS analysis listed in Table 4.3, the larger globular precipitates (pts. 1–4) appear to be the Sb_3Nd_4 phase, where the smaller globular precipitates (pts. 5–8) appear to be the SbNd phase. The needle-like precipitates (pts. 11–13) appear to be Zr_2Sb. The detection of U at these analysis locations are likely the result of volume interaction of the electron beam with the surrounding matrix due to how thin the needle precipitates are. Zr-based inclusions are also observed (pts. 9 and 10), primarily forming in proximity of the Sb-Nd precipitates. The preferential formation of Zr-containing second phases near Nd-based precipitates was also previously observed in the U-Zr-Te-Nd alloy [20]. Additionally, from Figure 4.1 (e) the matrix is observed to primarily

consist of U with Zr clustered throughout in solid-solution, which is shown as the light-grey areas in the SEM micrographs (pts. 14 and 15). This matrix characteristic appears to be typical of an as-cast U-Zr-based alloy. Figure 4.2 shows the diffraction patterns obtained from XRD analysis performed on the Sb-Nd alloy in both the as-cast and annealed condition; the latter condition is discussed further below. For the as-cast alloy the α-U, Sb_3Nd_4, SbNd, and Zr_2Sb phases were identified. The UO_2 phase was also identified, which is likely due to an oxide layer forming during analysis. Additional crystallographic details on the phases identified through XRD analysis are listed in Table 4.4.

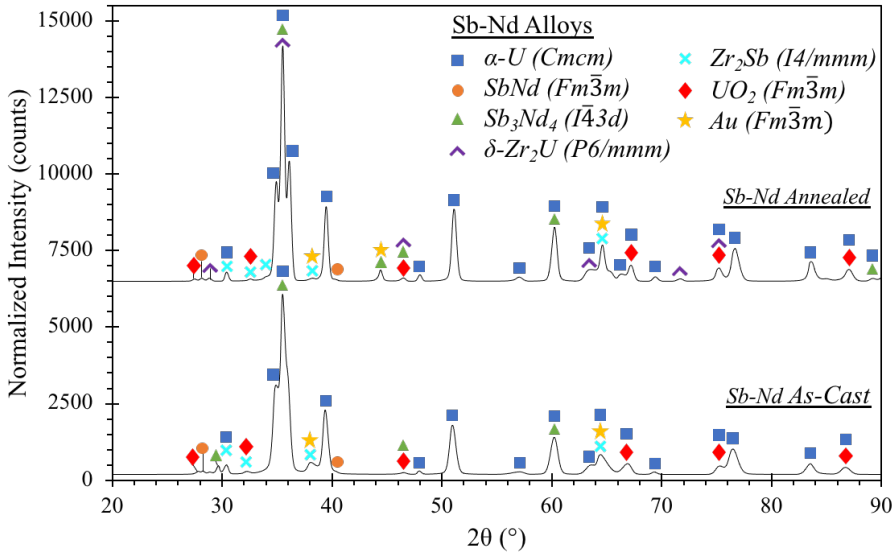

Figure 4.2. XRD patterns of the Sb-Nd alloy in both the as-cast and annealed condition. Crystallographic details of the phases can be found in Table 4.4.

A large precipitate was also observed to form in the Sb-Nd alloy measuring 0.5 mm to 1 mm across. The precipitate is visible in the SEM micrographs in Figure A.1 of the supplemental information section found in Appendix A. This large precipitate appears to be $SbNd_2$, a more Nd-rich phase compared to the globular precipitates that were observed throughout the matrix. The $SbNd_2$ phase is confirmed in Figure A-2, also in the supplemental information section, which displays the XRD pattern from analysis focused on the large precipitate. It is likely that a large concentration of the Nd added to the alloy is contained within the large precipitate and is likely why there was only a limited number of Sb-Nd precipitate clusters observed throughout the alloy. However, it is important to note that there was no

detection of an elemental Nd phase, indicating Nd was completely bound with Sb within the U-Zr matrix.

Table 4.3. EDS points analysis results, in at.%, of the as-cast and annealed Sb-Nd alloy for locations depicted in Figure 4.1 (b) and Figure 4.3 (b).

Pt.	U	Zr	Sb	Nd	Phase[a]	Pt.	U	Zr	Sb	Nd	Phase[a]
Figure 4.1 (b)						*Figure 4.3 (b)*					
1	0.3	4	39	56.5	Sb_3Nd_4	**1**	0.5	6	38	55	Sb_3Nd_4
2	0.5	5	39	55	Sb_3Nd_4	**2**	0.7	6	39	54	Sb_3Nd_4
3	1	7.5	39	52.5	Sb_3Nd_4	**3**	0.4	6	39	55	Sb_3Nd_4
4	1	4	40	54	Sb_3Nd_4	**4**	0.5	8	38	54	Sb_3Nd_4
5	1	6	45	47	*SbNd*	**5**	0.7	7	45	47	*SbNd*
6	4	4	45	47	*SbNd*	**6**	1	6	46	47	*SbNd*
7	1	4	46	49	*SbNd*	**7**	0.8	6	45	48	*SbNd*
8	3	5	45	48	*SbNd*	**8**	0.7	6	46	48	*SbNd*
9	5	91	1	2	*Zr incl.*	**9**	1	7	46	47	*SbNd*
10	5	79	8	8	*Zr incl.*	**10**	3	65	31	1	Zr_2Sb
11	17	54	25	3.5	Zr_2Sb	**11**	5	62	30	3	Zr_2Sb
12	17	51	27	4	Zr_2Sb	**12**	85	10	4	2	*α-U*
13	17	52	27.5	3	Zr_2Sb	**13**	86	9	4	1	*α-U*
14	52	41	5	0.7	*U-Zr*[b]	**14**	34	63	3	1	δ-Zr_2U
15	53	42	4	0.8	*U-Zr*[b]	**15**	34	63	2	1	δ-Zr_2U

[a] *suggested phase based on EDS results*
[b] *matrix phase of the as-cast U-Zr alloy*

After annealing, both globular clusters and needle-like precipitate formations were observed in the Sb-Nd alloy, shown in the BSE images in Figure 4.3 (a) and (b). EDS elemental mapping and point analysis was performed in the same vicinity as shown in Figure 4.3 (b); the results of which can be found in Figure 4.3 (c) and Table 4.3, respectively. The globular and needle-like precipitates were again found to consist of Sb and Nd, and Zr and Sb, respectively. In the annealed alloy, the larger globular precipitates appear to consist of two different phases. Based on the elemental ratios from EDS point analysis, the center of the precipitates (pts. 1–4) appear to be the Sb_3Nd_4 phase, while the darker outer section of the precipitates (pts. 5–7) appear to be the SbNd phase. Additionally, the smaller globular precipitates observed in the matrix appears to be the SbNd phase (pts. 8 and 9). The needle-like precipitates (pts. 10 and 11) appear to be largely unchanged from the as-cast alloy, and again are likely the Zr_2Sb phase.

A distinct change is observed in the matrix of the annealed alloy, which has separated into two distinct phases. The white phase (pts. 12 and 13) is primarily U, likely the α-U phase, whereas the dispersed light grey phase (pts. 14 and 15) appears to be the δ-Zr_2U phase. These phases were confirmed through XRD analysis of the annealed alloy, which is plotted in Figure 4.2. It is apparent in comparing the as-cast and annealed alloys, that the Sb-Nd and Zr-Sb phases remain relatively stable. The only major variation observed was that of the matrix, where the α-U and δ-Zr_2U phases became much more defined compared to the solid-solution observed in the as-cast alloy .

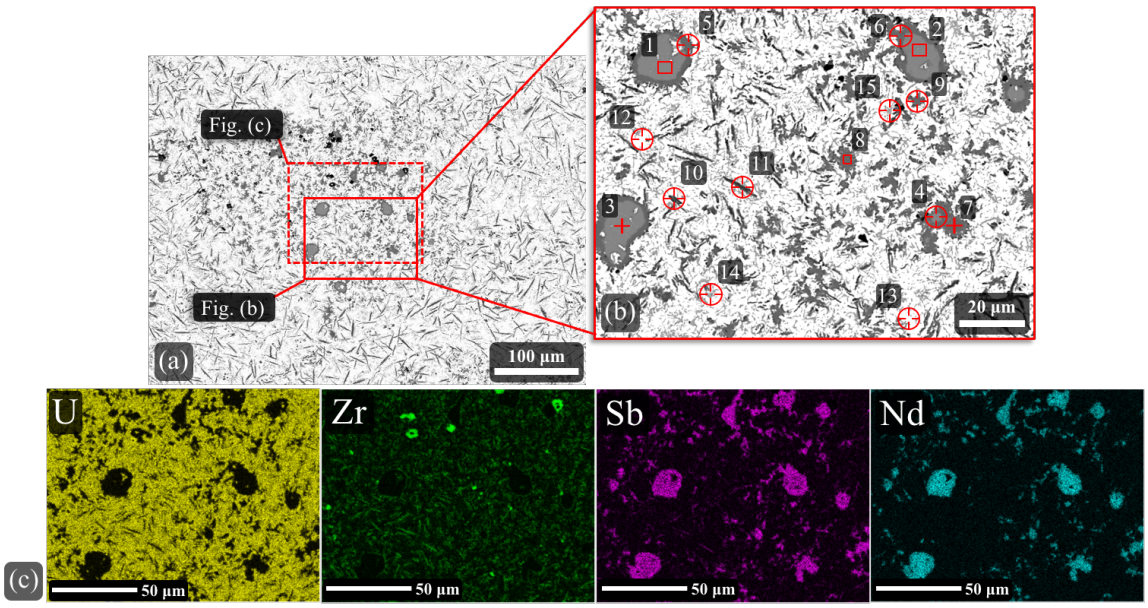

Figure 4.3. (a) and (b) BSE micrographs of the Sb-Nd alloy in the annealed condition at different magnifications. EDS point analysis results can be found in Table 4.3. (c) EDS elemental maps of the area shown in (a), which overlaps with that imaged in (b).

4.3.2 Annealed structure of the Te-Nd alloy

Prior to discussing the Te-Nd alloy in its annealed condition, a brief description of the alloy in its as-cast condition is included here. In the work by Jerred *et al.* [20], which is Chapter 3 of this dissertation, a detailed analysis of a similar alloy composition was made in the as-cast condition. Through EDS, XRD and transmission electron microscopy (TEM) analysis, the TeNd phase was confirmed to form within the alloy. Additionally, the Zr_3Te phase was also found to form. However, no elemental Nd was observed within the alloy, implying that the alloy was likely Nd-poor and excess Te was bound with Zr to form the Zr-rich telluride compound. Further, there was formation of what appeared to be a U-Te-Nd ternary phase that

formed near pure Zr inclusions. Through TEM analysis it was determined that these precipitates were indeed the TeNd phase, confirmed through electron diffraction, with uranium likely dissolved within. The matrix of the as-cast alloy was also observed to be primarily α-U with Zr-rich regions clustered throughout in solid-solution; similar to that of the Sb-Nd as-cast alloy.

Table 4.4. Crystallographic information of phases identified through XRD analysis in Figure 4.2 and Figure 4.5.

Compound	**Space Group (Space Group No.)**	**Cell parameters**	**Alloy[a]**		
			Sb-Nd As-cast	*Sb-Nd Annealed*	*Te-Nd Annealed*
α-U [28]	Cmcm (63), orthorhombic	a = 0.286, b = 0.586, c = 0.496 [nm] $\alpha = \beta = \gamma = 90°$	x	x	x
SbNd [29]	$Fm\bar{3}m$ (225), cubic	a = b = c = 0.632 [nm] $\alpha = \beta = \gamma = 90°$	x	x	
Sb_3Nd_4 [30]	$I\bar{4}3d$ (220), cubic	a = b = c = 0.941 [nm] $\alpha = \beta = \gamma = 90°$	x	x	
TeNd [31]	$Fm\bar{3}m$ (225), cubic	a = b = c = 0.626 [nm] $\alpha = \beta = \gamma = 90°$			x
δ-Zr_2U [32]	P6/mmm (191), hexagonal	a = b = 0.503, c = 0.308 [nm] $\alpha = \beta = 90°, \gamma = 120°$		x	x
Zr_2Sb [33]	I4/mmm (139), tetragonal	a = b = 0.412, c = 1.58 [nm] $\alpha = \beta = \gamma = 90°$	x	x	
UO_2 [34]	$Fm\bar{3}m$ (225), cubic	a = b = c = 0.548 [nm] $\alpha = \beta = \gamma = 90°$	x	x	x
Au [35]	$Fm\bar{3}m$ (225), cubic	a = b = c = 0.408 [nm] $\alpha = \beta = \gamma = 90°$	x	x	x

[a]*denotes the alloy the phase was identified in*

In its annealed condition, the Te-Nd alloy exhibits large, light grey globular precipitate formations within the matrix, each measuring between 5 to 20 μm in size. These precipitates are shown in the BSE micrographs of Figure 4.4 (a) and (b). There also appears to be a fine dispersion of dark grey precipitates, whereas the matrix is comprised of a two-phase morphology, a bright and light grey phase. The results of EDS mapping of the area shown in Figure 4.4 (b) can be found in Figure 4.4 (c). Here the large light grey precipitates appear to be Te-Nd containing phases and the fine dispersion of dark grey precipitates are Zr containing.

Point-specific EDS elemental analysis was conducted at locations depicted in Figure 4.4 (b) with the results listed in Table 4.5. The larger light grey globular precipitates (pts. 1–4) are likely that of the TeNd phase whereas the fine dark grey dispersion (pts. 5–7) are likely Zr inclusions. As for the matrix phases (pts. 8–13), they are likely both α-U and δ-Zr_2U as the bright and light grey phases, respectively.

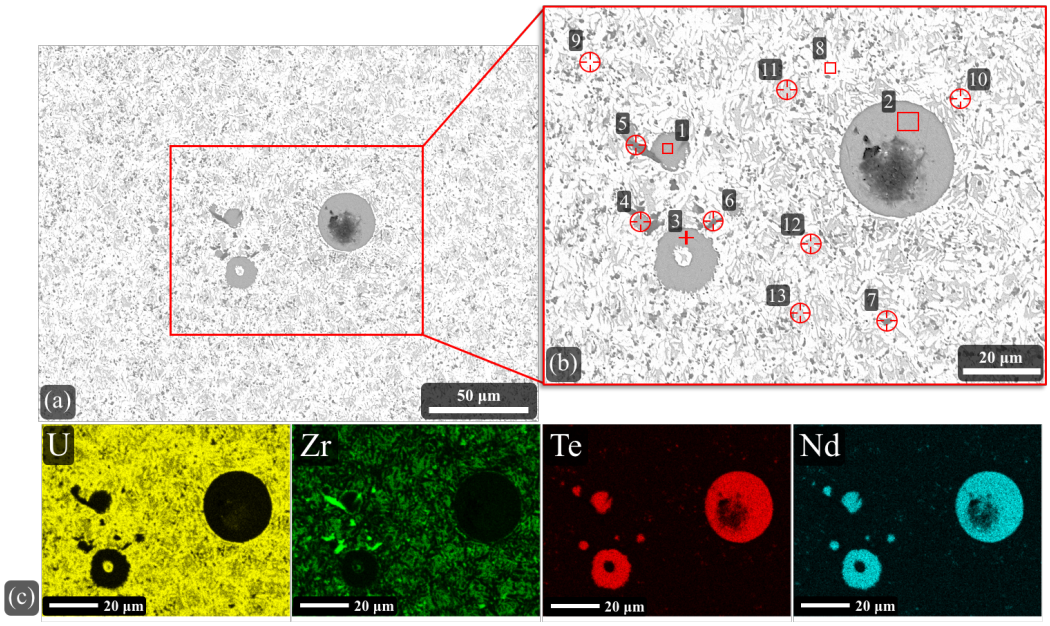

Figure 4.4. (a) and (b) BSE micrographs of the Te-Nd alloy in the annealed condition. EDS results are found in Table 4.5. (c) EDS elemental map results of the area depicted in (b).

Table 4.5. EDS point analysis results, in at.%, of the Te-Nd alloy. Points correlate with locations identified in Figure 4.4 (b).

Pt.	U	Zr	Te	Nd	Phase[a]	Pt.	U	Zr	Te	Nd	Phase[a]
1	0.3	5	47	47	*TeNd*	**8**	86	8	2	0.9	*α-U*
2	0.7	6	45	46	*TeNd*	**9**	87	9	2	0.5	*α-U*
3	0.5	6	46	46	*TeNd*	**10**	86	9	2	0.7	*α-U*
4	0.5	6	46	47	*TeNd*	**11**	35	61	1	0.5	*δ-Zr_2U*
5	3	96	0.1	0.3	*Zr incl.*	**12**	35	63	0.8	0.7	*δ-Zr_2U*
6	4	94	0.3	0.2	*Zr incl.*	**13**	35	63	1	0.4	*δ-Zr_2U*
7	7	91	0.6	0.3	*Zr incl.*						

[a]*suggested phase based on EDS results*

Through XRD analysis of the Te-Nd annealed alloy (plotted in Figure 4.5), the presence of TeNd, α-U and δ-Zr_2U phases are confirmed, with crystallographic details of the identified phases reported in Table 4.4. In comparing the results of the annealed alloy to the results of a

similar alloy in its as-cast condition reported by Jerred *et al.* [20] (Chapter 3), it is apparent the TeNd phase remains stable through annealing. Further, there is no indication of a formation of any Zr-Te phase, plausibly due to this section not being Nd-poor. It is again important to note that an elemental Nd phase was not observed, an indication that Nd is fully bound with Te. Additionally, there is no evidence of U-Te-Nd phase formations as was also observed by Jerred [20] and the TeNd precipitates that were observed to form alongside Zr inclusions in the annealed alloy (pts. 1 and 4), exhibit no appreciable concentration of U.

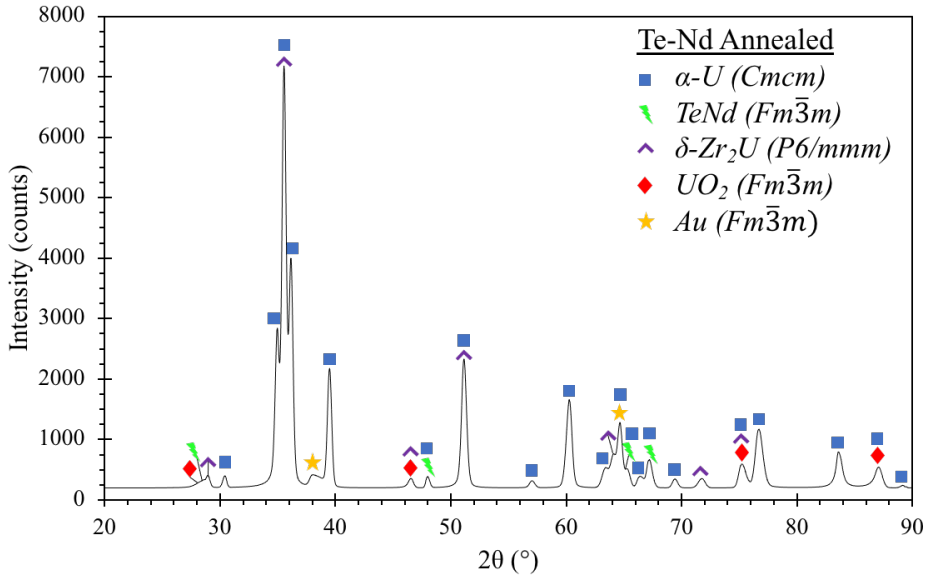

Figure 4.5. XRD results of Te-Nd alloy in the annealed condition. Crystallographic details of the identified phases are listed in Table 4.4.

4.3.3 Diffusion interactions of Nd/HT9

The Nd/HT9 diffusion couple is used to demonstrate the anticipated interaction of the U-Zr alloy with the cladding alloy HT9 once Nd has formed within the fuel. Further, it is important to characterize the interaction between these two base alloys before comparing the results to that of fuel alloys containing additives. It should be noted that this is an isothermal experiment and does not fully represent the thermal conditions within a reactor but can still be used to evaluate interactions driven by the thermodynamics of the system. Discussion on phase formation from the diffusion experiment will largely be based on EDS results, as XRD analysis performed at the interface resulted in only identification of the α-U phase; being the most dominant phase in the U-10Zr (wt.%) alloy. Phases formed within the interaction regions were likely too small or too low in concentration to be detectable above background of the XRD

plots. To that end, formations are only identified as being a certain phase only when the EDS data is consistent across multiple locations. Analysis of the Nd/HT9 diffusion couple shows considerable interaction has occurred between the U-10Zr-4Nd (wt.%) fuel alloy and HT9 cladding alloy. The interaction region shows two distinct layer formations between the two alloys as observed in the BSE micrographs in Figure 4.6 (a) and (b). One layer consists of a light grey phase measuring 3 to 7 μm wide Figure 4.6 (b)), followed by a separate layer, having a morphology that deviates from that of the fuel alloy and measures ~60 μm wide (Figure 4.6 (a)). EDS analysis was performed throughout the interaction region to determine the composition of the various formations and the results are listed in Table 4.6. Results of EDS elemental mapping of the different analysis areas are shown in Figure 4.6 (c) and (d), where Figure 4.6 (c) corresponds to the area imaged in Figure 4.6 (a) and the elemental maps in Figure 4.6 (d) correspond to the area imaged in Figure 4.6 (b). The results of an EDS elemental line scan is plotted in Figure 4.6 (e), which corresponds to the location depicted in Figure 4.6 (b). For comparison SEM and EDS analysis of the U-Zr-Nd fuel alloy in an annealed condition, away from the diffusing interface, can be found in the supplemental information section of this chapter (Figure A.3 of Appendix A). From the analysis shown in Figure 4.6, the general fuel alloy was found to contain α-U and δ-Zr_2U phases (pts. 12,13 and 9–11, respectively). In comparing the fuel alloy to that of the large interaction region, the α-U phase is noted to be present (pts. 3 and 4), but the δ-Zr_2U phase is not observed. Instead, a U-Zr-Fe ternary phase appears to form (pts. 1 and 2), an indication of the diffusion of Fe into the fuel. It is likely this ternary phase is the λ-phase that has been characterized by Nakamura *et al*. [36], and characterized by Fabrichnaya [37] as the τ_2-phase; having a composition of U-(21–25)Zr-6Fe (at.%). Additionally, both elemental Nd precipitates (pts. 5 and 6) and Zr-based inclusions (pts. 7 and 8) are observed throughout the interaction region. The light grey phase observed to form at the interface in Figure 4.6 (b) is found to primarily contain U and Fe (Figure 4.6 (d)) and is likely the UFe_2 phase (pts. 16–18).

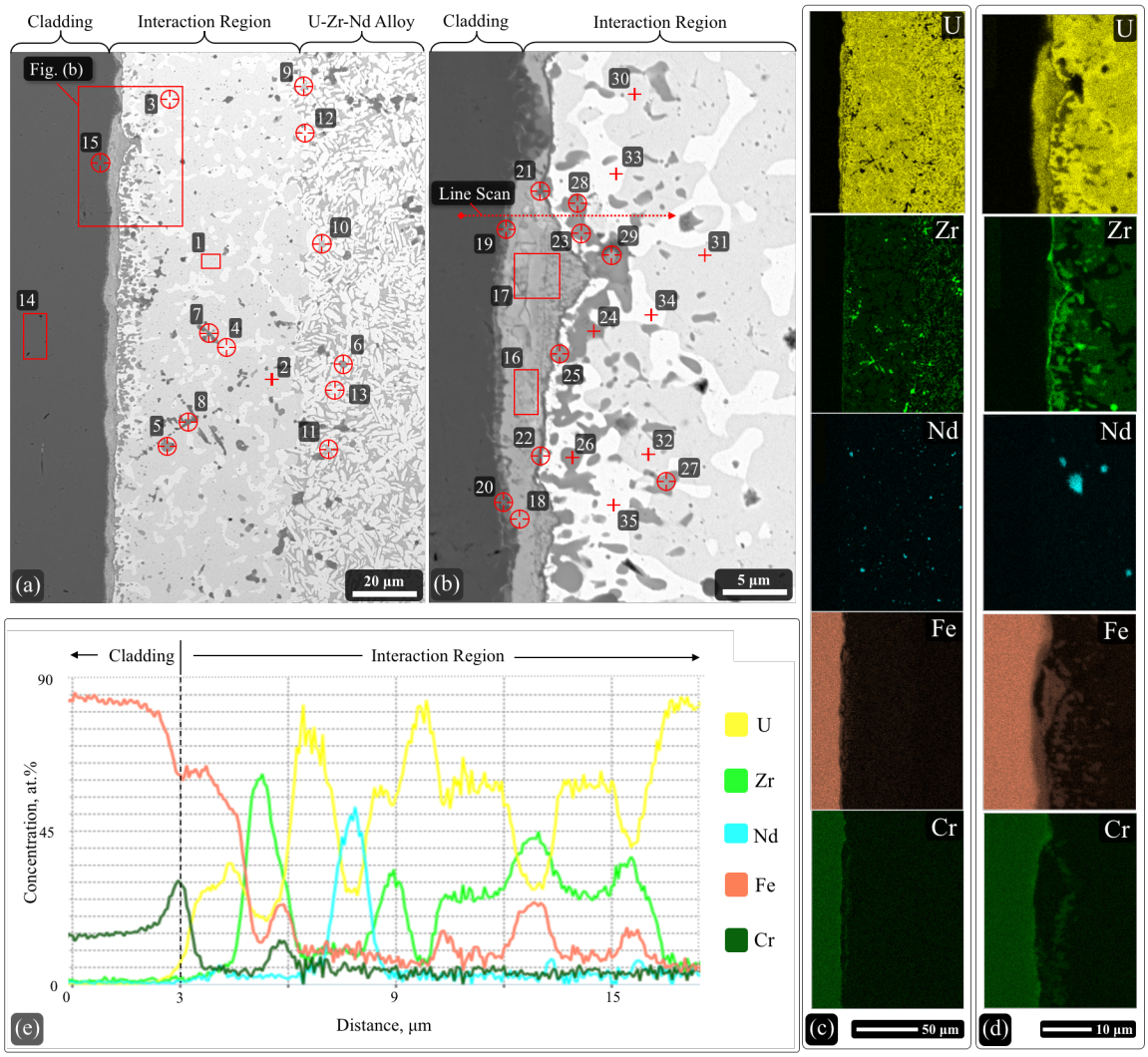

Figure 4.6. Interaction region of the Nd/HT9 diffusion couple. (a) and (b) BSE micrographs of the interaction region at different magnifications. EDS point analysis results can be found in Table 4.6. (c) EDS elemental maps of the region in (a). (d) EDS elemental maps of the region in (b). (e) Results of elemental line analysis of location depicted in (b).

A Cr-rich layer is noted to form on the cladding side of the UFe_2 layer, while a Zr-rich layer is found to form on the fuel-side of this phase. These thin layer formations can be more easily discerned from the EDS line scan results in Figure 4.6 (e), but the elevated Cr and Zr concentrations in these layers are clear from pts. 14 and 15 and pts. 20 and 21, respectively. Beyond the Zr-rich layer, a non-continuous dark grey phase is observed to form, which appears to be a combination of U, Zr, Fe, and Cr. This phase, depicted by points 23–27, aligns with the ε-phase, a U-Zr-Fe ternary phase also identified by Nakumura [36] (identified by Fabrichnaya [37] as the τ_1-phase), having a composition of U-(33–50)Zr-33Fe (at.%). A few Nd precipitates are also observed in close proximity to the interface (pts. 28 and 29), but they only contain a

small concentration of Fe (3–6 at.%). Further analysis of the phase formations within the larger section of the interaction region (Figure 4.6 (b)) confirm the likely formation of the λ-phase (pts. 30–32) and that of the α-U phase (pts. 33–35). Overall, the composition change of these various layers and phases throughout the interaction region can be further visualized through the EDS line scan results shown in Figure 4.6 (e).

Table 4.6. EDS point analysis results, in at.%, of the Nd/HT9 diffusion couple for the locations depicted in Figure 4.6 (a) and (b).

Pt.	**U**	**Zr**	**Nd**	**Fe**	**Cr**	**Phase[a]**	**Pt.**	**U**	**Zr**	**Nd**	**Fe**	**Cr**	**Phase[a]**
Figure 4.6 (a)							*Figure 4.6 (b)*						
1	60	27	1	7	0.7	λ	**16**	29	4	0.9	61	2	UFe_2
2	58	28	0.5	7	0.7	λ	**17**	29	10	0.5	55	2	UFe_2
3	84	8	0.6	2	0.4	α-U	**18**	22	9	0.9	59	7	UFe_2
4	84	7	0.7	2	0.5	α-U	**19**	7	1	0.1	65	23	Cr-rich layer
5	0.1	6	89	1	0.8	Nd prec.	**20**	2	1	0	68	26	Cr-rich layer
6	2	7	85	1	1	Nd prec.	**21**	16	62	0.4	15	3	Zr-rich layer
7	4	91	1	0.3	0.2	Zr incl.	**22**	24	61	0.5	10	2	Zr-rich layer
8	3	93	0.3	0.3	0.3	Zr incl.	**23**	12	32	0.3	34	18	ε
9	34	61	0.5	0.8	0.3	δ-Zr_2U	**24**	13	32	0.2	34	18	ε
10	33	60	1	1	0.3	δ-Zr_2U	**25**	13	32	0.2	33	20	ε
11	34	61	0.7	0.6	0.4	δ-Zr_2U	**26**	15	31	0.3	36	14	ε
12	84	7	0.9	2	0.6	α-U	**27**	23	42	0.9	27	0.8	ε
13	85	7	0.3	1	0.5	α-U	**28**	14	12	60	6	3	Nd prec.
14	0	1	0.2	85	12	HT9	**29**	2	9	82	3	1	Nd prec.
15	0	0.8	0.1	84	14	HT9	**30**	58	27	1	7	2	λ
							31	59	27	0.5	7	2	λ
							32	59	27	0.7	8	2	λ
							33	83	7	0.6	2	0.7	α-U
							34	82	7	1	2	1	α-U
							35	83	7	0.7	2	0.9	α-U

[a]*suggested phase based on EDS results*

For a more in-depth discussion on the formation of U-Zr-Fe ternary phases and the interaction layers that form in diffusion experiments between a standard U-10Zr (wt.%) fuel alloy and a Fe-Cr alloy, the reader is directed to references 36–39, whereas only a brief summary is provided here. It has been observed that cladding alloys containing Cr tend to exhibit a greater level of inter-diffusion with uranium-based fuels in comparison to pure Fe, however Fe-Cr alloys tend to exhibit far less interaction compared to Fe-Cr-Ni alloys, e.g. austenitic stainless steels [38,39]. The formation of the Cr-rich layer observed on the cladding side of the interface in Figure 4.6 (a) and (b) is largely attributed to the sluggish diffusion of Cr from the cladding compared to Fe, which has diffused into the fuel [38]. The formation of the Zr-rich layer on the fuel alloy side of the interface is believed to be the result of a breakdown of the δ-Zr_2U phase, and in turn becomes stabilized by impurities, such as nitrogen, oxygen, and carbon, dissolved within the fuel or cladding alloys. The formation of the U-Fe layer is believed to occur on the cladding side of the interface and is likely due to the diffusion of U through the Zr-rich layer [39–44]. This would further explain the observation that the interaction region lacks any formation of the δ-Zr_2U phase.

Another section of the interaction region of the Nd/HT9 diffusion couple is shown in Figure 4.7 with the corresponding EDS point analysis results reported in Table 4.7. A Nd precipitate is observed at the fuel-cladding interface (Figure 4.7 (b)). EDS elemental maps of the area denoted in Figure 4.7 (a) are shown in Figure 4.7 (c). The interaction region, extending 20 to 40 μm away from the interface, is shown in Figure 4.7 (a) and exhibits similar phase formations to those observed in Figure 4.6. The Nd precipitate (pts. 1 and 2) shows limited concentration of Fe and Cr, 3–6 at.% and 5 at.%, respectively. Further, Nd appears to have also diffused slightly into the HT9 alloy, exhibiting a concentration of 5 at.% and 9 at.% at points 3 and 4, respectively. However, it does not appear that an exact Fe-Nd phase has stabilized as neither point aligns with a stoichiometric Fe-Nd compound, $Fe_{17}Nd_2$ or $Fe_{17}Nd_5$. Previous research on the direct interaction of Nd and HT9 [16], which is also contained in Chapter 2 of this dissertation, found that the phase formation on the HT9 side of the diffusing interface was the $Fe_{17}Nd_2$ compound, whereas the $Fe_{17}Nd_5$ compound was found to form on the fuel side. From points 5 and 6 of Figure 4.7 (b), the interaction layer along the diffusing interface is observed to decrease in its Nd concentration, whereas the U concentration increases. However, this region does not align with a stoichiometric U-Fe compound, such as UFe_2 which was

previously observed in Figure 4.6. At this analysis location Zr inclusions (pts. 7–9), the λ-phase (pts. 10 and 11), and the α-U phase (pt. 12) were again observed to form. Interestingly, the ε-phase was not detected and the UFe_2 phase was only found to form near the bottom of the BSE micrograph of Figure 4.7 (a).

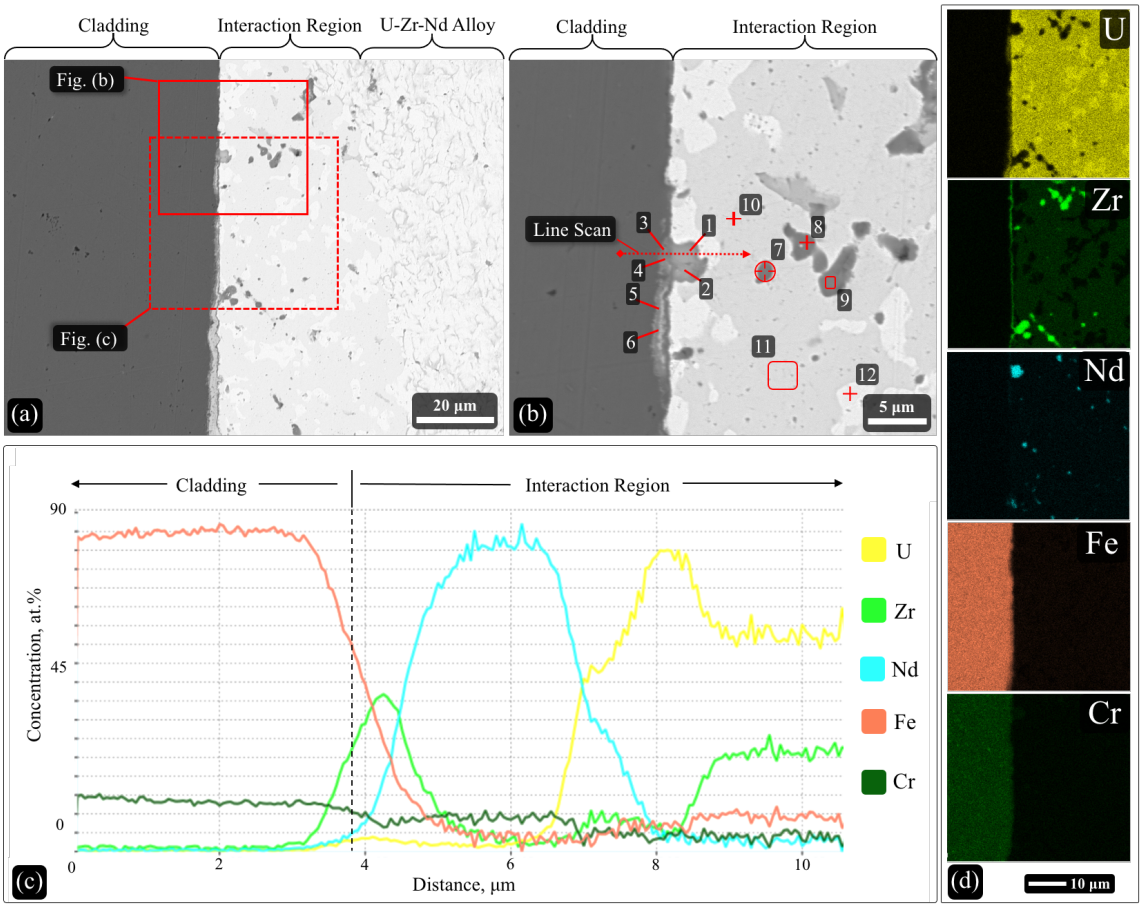

Figure 4.7. Interaction region of the Nd/HT9 diffusion couple displaying an Nd precipitate at the diffusing interface. (a) and (b) BSE micrographs of the interaction region at different magnifications. EDS point analysis results are listed in Table 4.7. (c) EDS elemental line scan results of the location depicted in (b). (d) EDS elemental maps of the region depicted in (a).

4.3.4 Diffusion interactions of Sb-Nd/HT9

SEM micrographs of one section of the Sb-Nd/HT9 diffusion couple interface is shown in Figure 4.8 (a) and (b). EDS elemental maps of Figure 4.8 (b) are shown in Figure 4.8 (c) and the corresponding point analysis results is reported in Table 4.8. Visually, the interface indicates some layer formation, and upon evaluation of the EDS maps (Figure 4.8 (c)), there appears to be primarily a Zr-rich layer. Needle-like precipitates, as previously observed in the Sb-Nd alloy, were found to form alongside a large globular precipitate near the interface. The

globular precipitate, measuring ~10 μm across, appears to be comprised of Sb and Nd and is likely the SbNd phase (pts. 1 and 2). The needle-like phases, measuring a few microns in width and ~10 μm long, are primarily comprised of Zr and Sb and are likely the Zr_2Sb phase (pts. 3 and 4). Other needle-like precipitates in the analysis area (pts. 7–10) were also found to align with the Zr_2Sb phase.

Table 4.7. EDS point analysis results, in at.%, of the Nd/HT9 diffusion couple for the locations depicted in Figure 4.7 (b).

Pt.	U	Zr	Nd	Fe	Cr	Phase[a]
1	0.2	5	87	3	5	*Nd prec.*
2	3	13	73	6	5	*Nd prec.*
3	2	10	5	70	13	*Fe-Nd*
4	5	20	9	53	13	*Fe-Nd*
5	8	3	0.9	75	14	*U in HT9*
6	10	5	1	71	13	*U in HT9*
7	8	89	1	1	0.5	*Zr incl.*
8	5	93	1	1	0.3	*Zr incl.*
9	4	92	2	1	0.5	*Zr incl.*
10	59	32	2	6	1	*λ*
11	60	31	2	6	2	*λ*
12	86	8	3	2	1	*α-U*

[a]*suggested phase based on EDS results*

A separate section of the Sb-Nd/HT9 diffusion couple was analyzed showing a mix of precipitates directly at the interface. SEM micrographs of the analysis area are shown in Figure 4.9 (a) and (b). EDS analysis was performed within the region imaged in part (b), where the EDS elemental line scan and map results are shown in Figure 4.9 (c) and (d), respectively. Results from the EDS point analysis of locations depicted in Figure 4.9 (b) are listed in Table 4.8. Several smaller globular precipitates are observed at this interface location and these are also likely the SbNd phase (pts. 22–26). The small globular precipitate directly at the diffusing interface (pt. 26), although indicating both Zr and Fe, is found to have a 1:1 atomic ratio of Sb and Nd and is likely the SbNd phase as well. The presence of these other elements is likely due to both the small size of the precipitate and its close proximity to the Zr-rich layer and cladding

alloy. There are also a few dark globular phases (pts. 27 and 28), which appear to be pure Zr inclusions, whereas the needle-shaped phase formations observed throughout the region are again likely the Zr_2Sb phase (pts. 29 and 30).

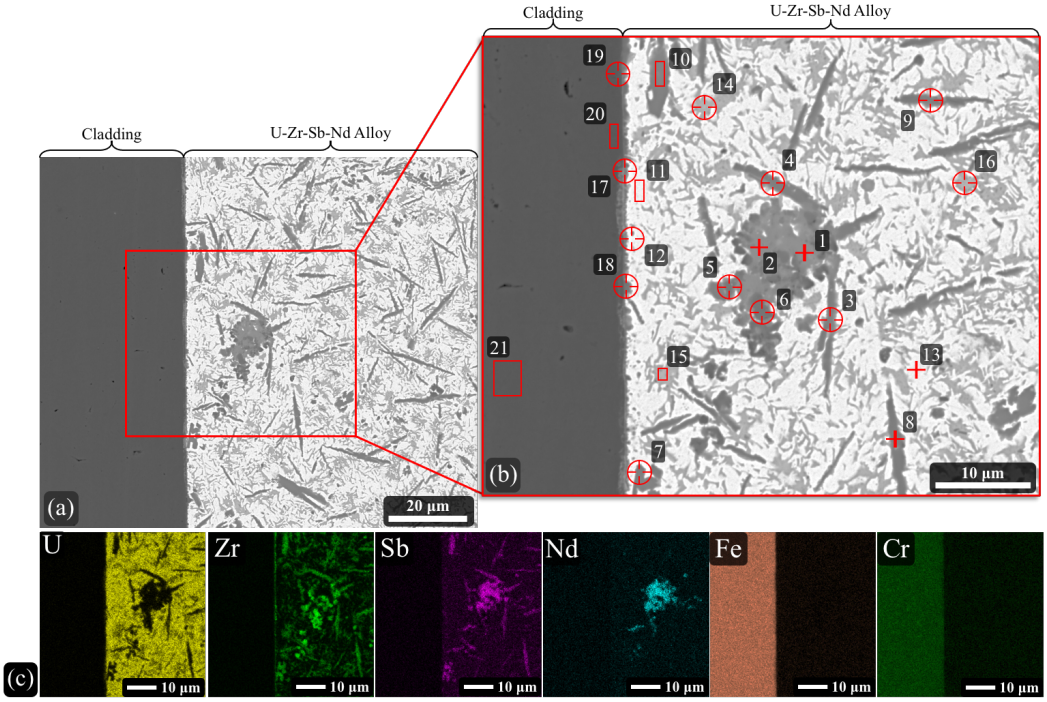

Figure 4.8. (a) and (b) SEM BSE micrographs of the diffusing interface of the Sb-Nd/HT9 diffusion couple. EDS point analysis results are listed in Table 4.8. (c) EDS elemental maps of the area imaged in (b).

The matrix of the Sb-Nd/HT9 diffusion couple appears to show no variations up to the diffusing interface unlike that of the Nd/HT9 diffusion couple where an interaction region was clearly observed to form, the result of Fe diffusing into the fuel. However, the diffusion of Fe into the U-Zr-Sb-Nd alloy is still suspected to have occurred but at a far lower degree. This is evident from EDS point analysis data of the matrix phase. At or near the interface, the α-U phase is found to contain 4–9 at.% Fe (pts. 11, 12 and 31) whereas locations some distance away from the interface do not (pts. 13, 32 and 33). The lack of gross interaction in the Sb-Nd/HT9 diffusion couple is further evident by the presence of a δ-Zr_2U phase within the fuel alloy up to the interface (pts. 14–16, 34 and 35). This phase was not observed within the interaction region of the Nd/HT9 diffusion couple as it had likely broken down and led to the formation of U-Zr-Fe compounds from the diffusion of Fe into the fuel. A Zr-rich layer is again observed to have formed at the interface of the Sb-Nd/HT9 diffusion couple, which is evident from Figure 4.8 (c) and Figure 4.9 (c) and (d). EDS point analysis of the Zr-rich layer is found

to contain U and Fe, but the composition of U, Zr and Fe is not consistent (pts. 17, 18 and 36–39). Further, the compositions do not align with any known U-Zr-Fe ternary phase. Given the size of the layer, the U and Fe concentrations may be attributed to the interaction volume from EDS analysis given the close proximity of the layer to both the fuel and cladding matrix phases. Another notable difference from the Nd/HT9 diffusion couple is the lack of interaction between U and Fe. Previously, the UFe_2 phase, was observed to have likely formed on the cladding side of the interface. However, here analysis of the HT9 matrix, both right next to the interface (pts. 19, 20 and 40) and at locations away from it (pts. 21 and 41), indicates there is little to no variation in the composition and no fuel-based constituents are present.

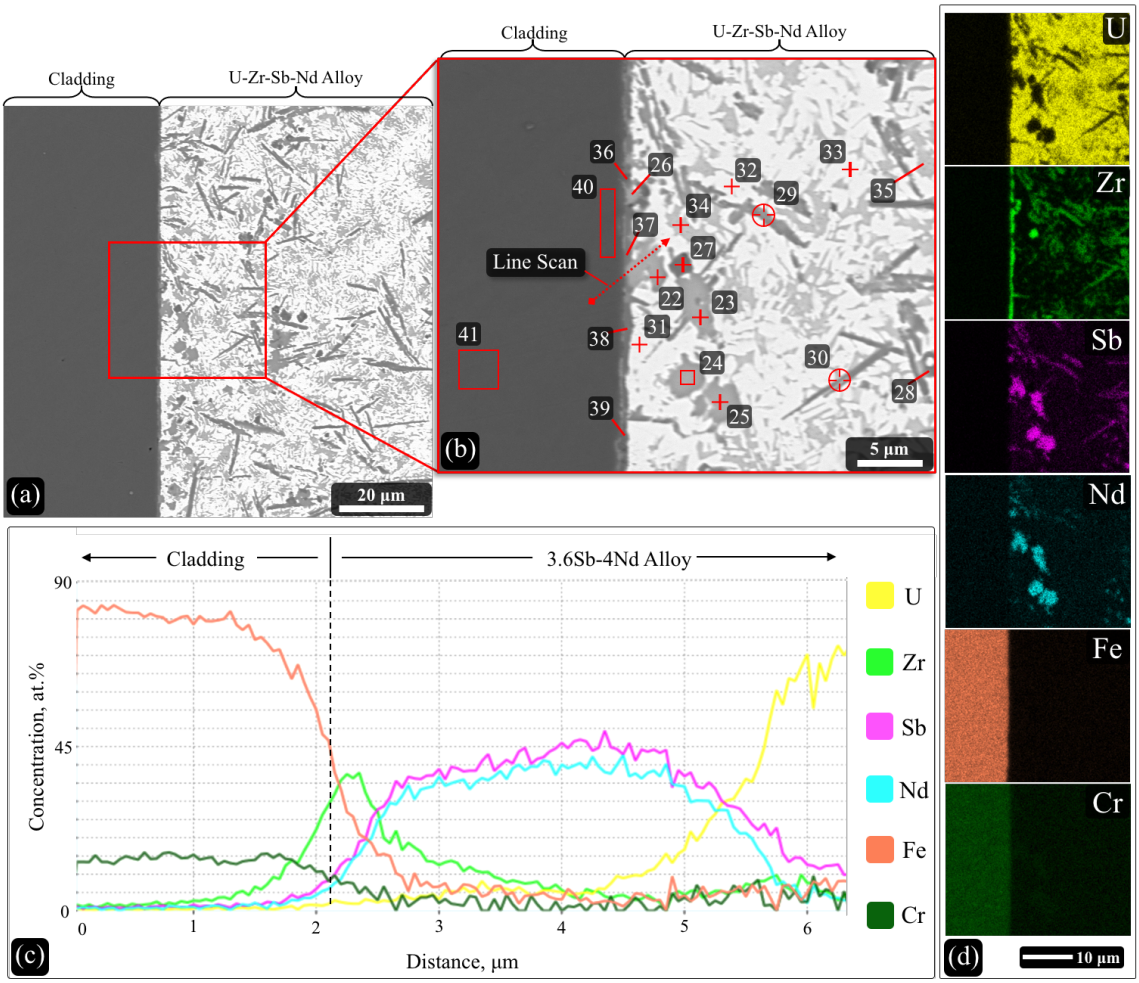

Figure 4.9. (a) and (b) SEM BSE micrographs of the diffusing interface of the Sb-Nd/HT9 diffusion couple. EDS point analysis results are listed in Table 4.8. (c) EDS elemental line scan results of the area depicted in (b). (d) EDS elemental maps of the area imaged in (b).

Table 4.8. EDS point analysis results, in at.%, of the Sb-Nd/HT9 diffusion couple for the locations depicted in Figures 4.8 (b) and 4.9 (b).

Pt.	U	Zr	Sb	Nd	Fe	Cr	Phase[a]	Pt.	U	Zr	Sb	Nd	Fe	Cr	Phase[a]
			Figure 4.8 (b)								*Figure 4.9 (b)*				
1	1	8	44	45	0.5	1	*SbNd*	**22**	5	4	43	42	2	4	*SbNd*
2	1	8	44	45	1	1	*SbNd*	**23**	6	7	43	40	1	3	*SbNd*
3	12	56	27	5	1	0.5	*Zr_2Sb*	**24**	1	3	46	45	1	3	*SbNd*
4	5	58	31	6	0.5	0.6	*Zr_2Sb*	**25**	1	3	46	46	0.9	4	*SbNd*
5	9	83	6	1	0.7	0.2	*Zr incl.*	**26**	5	31	27	26	7	4	*SbNd*
6	3	90	2	2	0.5	0.4	*Zr incl.*	**27**	7	90	1	0.8	0.7	0.3	*Zr incl.*
7	7	59	31	1	2	0.2	*Zr_2Sb*	**28**	18	78	2	1	0.8	0.5	*Zr incl.*
8	7	60	29	4	0.6	0.1	*Zr_2Sb*	**29**	14	51	26	6	1	1	*Zr_2Sb*
9	12	56	26	4	1	0.5	*Zr_2Sb*	**30**	32	43	21	2	1	0.3	*Zr_2Sb*
10	3	62	32	1	0.7	0.2	*Zr_2Sb*	**31**	83	4	6	0.7	5	1	*α-U*
11	82	9	4	0.8	4	0.7	*α-U*	**32**	85	5	6	0.9	2	1	*α-U*
12	72	13	3	1	9	3	*α-U*	**33**	86	5	6	0.7	2	2	*α-U*
13	84	9	4	1	1	1	*α-U*	**34**	34	59	4	0.3	2	0.6	*δ-Zr_2U*
14	32	63	3	0.4	1	0.5	*δ-Zr_2U*	**35**	33	60	4	0.7	1	0.7	*δ-Zr_2U*
15	31	61	4	0.6	2	0.8	*δ-Zr_2U*	**36**	5	60	9	7	15	4	*Zr-rich layer*
16	32	63	3	0.3	1	0.3	*δ-Zr_2U*	**37**	6	68	5	3	15	3	*Zr-rich layer*
17	27	50	0.6	0.4	19	3	*Zr-rich layer*	**38**	4	41	1	0.9	45	8	*Zr-rich layer*
18	15	63	0.2	0.3	18	4	*Zr-rich layer*	**39**	8	59	1	0.2	27	7	*Zr-rich layer*
19	0	2	0	0.1	11	87	*HT9*	**40**	0	0.9	0	0.1	87	12	*HT9*
20	0.5	3.4	0	0.1	10	85	*HT9*	**41**	0	0.4	0.1	0.2	87	12	*HT9*
21	0	1	0	0.3	12	86	*HT9*								

[a]*suggested phase based on EDS results*

4.3.5 Diffusion interactions of Te-Nd/HT9

A light grey globular precipitate measuring ~10 μm in diameter, similar to the TeNd precipitates observed in the Te-Nd annealed alloy, was observed at the interface of the Te-Nd/HT9 diffusion couple. SEM micrographs of the analysis area are shown in Figure 4.10 (a) and (b). EDS analysis was performed at locations indicated in Figure 4.10 (b), with the results

listed in Table 4.9. The EDS line scan results are shown in Figure 4.10 (c) and EDS elemental maps of the area imaged in part (b) being shown in Figure 4.10 (d). The large globular precipitate (pts 1–3) is likely the TeNd phase, which was previously observed in the as-cast alloy as well [20]. Even with the precipitate being located directly at the interface, there does not appear to be any interaction with cladding constituents; an indication of the stabilizing effects Te has on Nd.

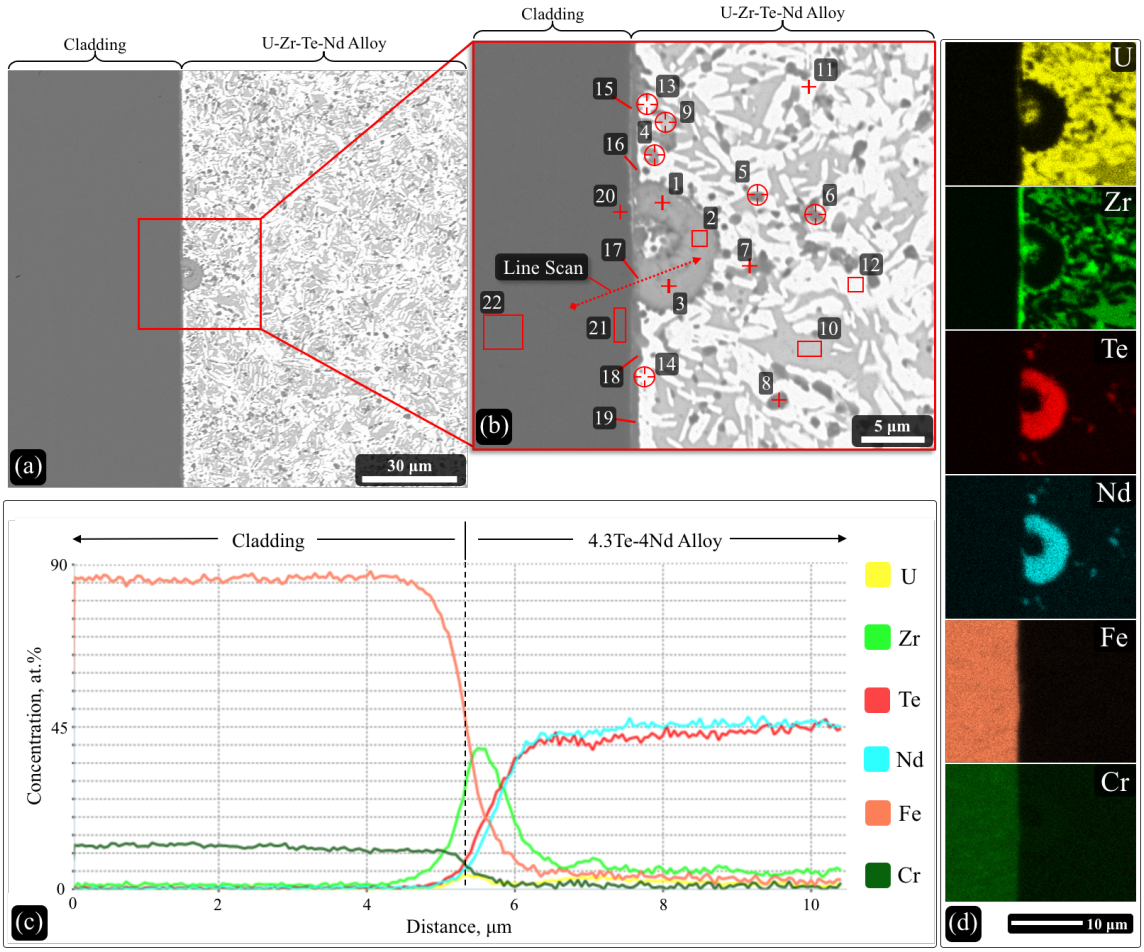

Figure 4.10. (a) and (b) BSE micrographs of the diffusing interface of the Te-Nd/HT9 diffusion couple. EDS point analysis results are listed in Table 4.9. (c) EDS elemental line scan results of the area depicted in (b). (d) EDS elemental maps of the area imaged in (b).

There is a Zr-rich layer formation observed at the interface (Figure 4.10 (c) and (d)), however, from the elemental maps this layer appears to be only somewhat continuous across the TeNd precipitate. Point analysis of the Zr-rich layer (pts. 15–19) again does not indicate much consistency in the composition except for being Zr-rich. However, the Fe and Cr ratio of the point data from the Zr-rich layer appears to be consistent with the atomic ratio of Fe and

Cr in the HT9 alloy being 7:1 (see Table 4.1). This would indicate volume interaction with the HT9 matrix during the EDS analysis. Additionally, point 17 shows a Te:Nd ratio close to 1:1, in addition to a high Zr concentration, which is due to its proximity to both the TeNd precipitate and Zr-rich layer. A dispersion of dark grey precipitates, measuring only a few microns in size, are also visible throughout the area (pts. 5–8) and they appear to be Zr-based inclusions. The fuel alloy matrix appears to be comprised of both the α-U (pts. 11–14) and δ-Zr_2U (pts. 9 and 10) phases. The δ-Zr_2U phase again appears be intact all the way up to the interface, similar to the observations of the Sb-Nd/HT9 diffusion couple and deviating from the observations of the Nd/HT9 diffusion couple.

Table 4.9. EDS point analysis results, in at.%, of the Te-Nd/HT9 diffusion couple for the locations depicted in Figure 4.10 (b).

Pt.	U	Zr	Te	Nd	Fe	Cr	Phase[a]	Pt.	U	Zr	Te	Nd	Fe	Cr	Phase[a]
1	0.7	7	45	45	2	0.8	*TeNd*	**12**	86	8	2	0.9	2	0.8	*α-U*
2	0.5	6	46	45	1	0.7	*TeNd*	**13**	74	13	2	1	8	2	*α-U*
3	0.7	6	47	45	1	0	*TeNd*	**14**	77	9	2	0.7	9	2	*α-U*
4	14	19	34	31	3	0.1	*TeNd*	**15**	4	44	0.3	0.7	44	7	*Zr-rich layer*
5	18	81	0.2	0.4	0.7	0.2	*Zr incl.*	**16**	10	76	0.6	0.5	11	2	*Zr-rich layer*
6	19	78	0.7	0.7	0.9	0.4	*Zr incl.*	**17**	1	36	23	20	17	3	*Zr-rich layer*
7	17	82	0.5	0.4	0.2	0	*Zr incl.*	**18**	13	73	0.6	0.3	11	3	*Zr-rich layer*
8	14	79	6	0.6	0.5	0	*Zr incl.*	**19**	12	65	0.5	0.4	18	4	*Zr-rich layer*
9	32	64	2	0.7	2	0	*δ-Zr_2U*	**20**	0.4	2	0	0.1	84	13	*HT9*
10	34	62	0.9	0.5	2	0.6	*δ-Zr_2U*	**21**	0	3	0	0.1	85	12	*HT9*
11	83	11	2	1	2	0.9	*α-U*	**22**	0	1	0.1	0.2	86	13	*HT9*

[a]*suggested phase based on EDS results*

Analysis of the α-U phase near the interface (pts. 13 and 14) does indicate elevated concentrations of both Fe and Cr (8–9 at.% and 2 at.%, respectively) compared to areas away from the interface (pts. 11 and 12). It is believed that the Fe concentration in the α-U phase is the result of Fe diffusion into the fuel alloy and not the result of volume interaction from EDS

analysis. If it were due to the latter, the Zr concentration would also likely be elevated given their proximity to the Zr-rich layer. However, the Zr concentration appears to be similar across all analysis locations that correspond to the α-U phase (pts. 11–14). Although Fe appears to have diffused into the fuel alloy, it is apparent that the level of diffusion is limited, and it is only co-located within the uranium phase. Additionally, there does not appear to be any formation of U-Zr-Fe ternary phases within the U-Zr-Te-Nd alloy, further indicating the level of Fe diffusion into the fuel alloy was low. On the cladding side of the interface, the HT9 appears to be unchanged exhibiting a consistent composition at several locations (points 20–22).

4.3.6 Interactions based on DFT calculations

DFT-based calculations can give a thermodynamic assessment of the tendency of different compounds to form. Here several systems are analyzed with the addition of Sb and Te to assess the tendency of such additive-based compounds to form. Systems are labeled in such a way that for compositions in the form of A-C and A-B-C, the enthalpy of mixing of C within each system is estimated by taking A and A-B as reference systems initially. For example, enthalpy of mixing for Cr in a first nearest neighbor position to Zr within a U-Zr reference system is 0.88eV. Additional mixing enthalpies of the various systems analyzed are listed in Table 4.10. The enthalpy of mixing of Te in the Fe matrix, system (i), and in the Fe-Cr matrix, system (ii), was calculated to be 0.96 eV and 1.02 eV, respectively. For the Sb additive, the enthalpy of mixing in systems (i) and (ii) was calculated to be 0.51 eV and 0.61 eV, respectively. The slightly positive enthalpy of mixing value of Te and Sb in the Fe matrix, with and without Cr, indicates both Te and Sb exhibit a decreased tendency to bind with these cladding constituents. It can then be further implied that both Te and Sb will exhibit a decreased tendency to interact with the HT9 cladding alloy in general. It should be noted that the lack of interaction between the additives and the cladding alloy is a critical metric for the selection of a suitable fuel additive. Further, the mixing enthalpies of Te and Sb in the U-matrix, system (iii), is also found to be positive being 0.52 eV and 0.99 eV, respectively. With the addition of Zr, i.e. U-Zr (system (iv)), the mixing enthalpies of Te and Sb change to negative values; -0.28 eV and -0.40 eV, respectively. This change in mixing enthalpy is an indication that Zr may help to stabilize both additives within the U-Zr matrix.

Table 4.10. Enthalpy of mixing values for different elements in fuel and cladding matrices.

Composition	Enthalpy of mixing (eV)	Composition	Enthalpy of mixing (eV)
Fe-Te	0.96	Fe-Cr-Te	1.02
Fe-Sb	0.51	Fe-Cr-Sb	0.61
U-Te	0.16	U-Zr-Te	-0.28
U-Sb	0.13	U-Zr-Sb	-0.4
U-Fe	0.52	U-Zr-Fe	0.41
U-Cr	0.99	U-Zr-Cr	0.88

In evaluating Fe and Cr in system (iii), the U-matrix without Zr, the enthalpies of mixing values are positive, 0.52 eV and 0.99 eV, respectively. With the addition of Zr into the matrix, i.e. system (iv), minimal change is observed in the enthalpies of mixing, 0.41eV and 0.88 eV for Fe and Cr, respectively. Therefore, based on the calculated negative enthalpy of mixing values in Table 4.10, only in the U-Zr-X systems, where X = Te or Sb, is the formation of Zr-X compounds predicted, aligning with experimental observations, where the Zr_2Sb [14] and Zr_2Te [20] compounds were observed to form in the U-Zr-Sb and U-Zr-Te alloys, respectively. In Table 4.11 the enthalpies of mixing is further evaluated for several systems in the presence of Nd. The enthalpy of mixing for Fe and Cr at the first nearest neighbor position to Nd within a U-Nd system are calculated to be -1.71 eV and -2 eV, respectively. The negative enthalpies of mixing of Cr and Fe in the system with Nd indicates that Nd would tend to stabilize Fe and Cr in the fuel matrix. Additionally, the mixing enthalpies of Te and Sb in the U-Nd system are -3.23 eV and -3.12 eV, respectively. Based on the significantly more negative enthalpy of mixing values for Te and Sb in the U-Nd system, compared to Fe and Cr, it can be inferred that there would be a higher tendency to form Nd-X precipitates, where X = Te or Sb, compared to Fe-Nd and Cr-Nd precipitates. This is confirmed experimentally by the observation of SbNd and Sb_3Nd_4 precipitates (Figure 4.3) and TeNd precipitates (Figure 4.4) in annealed U-Zr-Sb-Nd and U-Zr-Te-Nd alloys, respectively, and at or near the diffusion interface (Figure 4.9 and Figure 4.10) of the diffusion couples, respectively. It is notable that both Te and Sb retain strong negative enthalpies of mixing within the U-Nd matrix in the presence of Zr, calculated to be -1.46 eV and -1.5 eV for Te and Sb, respectively.

Overall, DFT calculated enthalpies of mixing supports the experimental observations that the primary constituents of HT9, i.e. Cr and Fe, can readily interact with the fuel matrix in

the presence of the lanthanide, Nd. However, when additives Te and Sb are present in the fuel matrix, their interactions with Nd should be thermodynamically the greatest of all, forming stable compounds with Nd.

Table 4.11. Enthalpy of mixing values of different fuel-based compounds with Nd.

Composition	**Enthalpy of mixing (eV)**	**Composition**	**Enthalpy of mixing (eV)**
U-Nd-Cr	-2	U-Nd-Zr-Te	-1.46
U-Nd-Fe	-1.71	U-Nd-Zr-Sb	-1.5
U-Nd-Te	-3.23		
U-Nd-Sb	-3.12		

4.3.7 Comparison of annealed structures

One major difference observed between the Te-Nd alloy and the Sb-Nd alloy appears to be in the additive-based phase formations within the fuel alloys. The Sb-Nd alloy, under both as-cast and annealed conditions, showed the formation of SbNd, Sb_3Nd_4 and Zr_2Sb precipitates, where the Te-Nd alloy showed the formation of only TeNd precipitates. Here it is important to note that elemental Nd was not observed to form in either alloy, thus the lanthanide element is fully binding with the additive element. Furthermore, the formation of the additive-Nd precipitates is also likely taking precedence over the formation of additive-Zr precipitates due to the former exhibiting more favorable formation energies with Te [20] and Sb [16]. Therefore, the formation of additive-Zr precipitates is likely because the additive-lanthanide atomic ratio of 1:1 is not being maintained in that analysis area and thus excess additive has led to the formation of additive-Zr precipitates. This is primarily evident in the Sb-containing alloys where the Zr_2Sb compound was observed to form. The formation of Zr-based intermetallic compounds, such as Zr_2Sb, removes Zr from the U-Zr matrix, which can have deleterious effects on fuel performance. For example, less Zr present will lower the solidus/liquidus temperatures of the fuel, and FCCI due to U-Fe interactions will increase. To negate this, a higher concentration of Zr has been added to fuel-additive alloys for irradiation [45,46]. However, additional Zr was not necessary in these *out-of-pile* experiments, though. Neither fuel melting or long term FCCI are concerns, and the optimal amount of Zr to include has not been determined and will likely be additive specific.

4.3.8 Comparison of diffusion interactions

In the Nd/HT9 diffusion couple experiment several interaction layers were observed to form, similar layer formations were also observed by Lee *et al.* [41] and Keiser *et al.* [39]. The presence of some U-Zr-Fe ternary phases were also observed in the Nd/HT9 diffusion couple, these phases have been previously detailed by Nakamura *et al.* [36,38]. Analysis of the Sb-Nd/HT9 and Te-Nd/HT9 diffusion couples found only a slight amount of interaction being observed between the additive-based fuel alloys and HT9. Furthermore, it appears the SbNd and TeNd phases remain unperturbed through the diffusion experiments, exhibiting no signs of interaction with cladding constituents even when these phases were observed to form directly at the interface. The observed stability of the SbNd phase in the presence of HT9 is consistent our previous research [16] (detailed in Chapter 2) that directly evaluated the diffusion interactions between SbNd and Sb_3Nd_4 with HT9. Additionally, the Zr_2Sb precipitates appear to also remain unperturbed, and although present at the interface, exhibit no interaction with cladding constituents as well. It is interesting that the Sb-Nd/HT9 and Te-Nd/HT9 diffusion couples show drastically different results at the diffusing interface compared to the Nd/HT9 diffusion couple as all three experiments were carried out under similar experimental conditions. In particular, the diffusion of Fe into the fuel was observed to be limited, being detected only within the α-U matrix phase near the interface in the additive-based fuels whereas the diffusion of Fe was very evident in the Nd/HT9 diffusion couple. This may be attributed to the formation of a thicker, more robust Zr-rich layer at the interface in the additive-containing fuel alloys, which in turn may be acting as a diffusion barrier. The formation of such a Zr-rich layer has been attributed to acting as a diffusion barrier in previous research [39,42]. Further, Kaity *et al.* [42] described that the more intact the Zr-rich layer, the more it acts as a diffusion barrier limiting cladding and fuel constituent interactions. However, it should be noted the Zr-rich layer was also observed to form at the interface of the Nd/HT9 diffusion couple, but it appears to be thinner compared to the layer formed in the additive-based fuel alloys, which appears to be several microns thicker. A breakdown or disruption in this layer has also been observed to result in an increase in the level of interaction between the cladding and fuel constituents [41]. The formation of the Zr-rich layer has previously been described as the result of the breakdown of the δ-Zr_2U phase within the fuel matrix. However, there does not appear to be a significant breakdown of the δ-Zr_2U phase within the additive-

based fuel alloys, at least not to the degree observed in the Nd/HT9 diffusion couple. Upon closer examination of the interface regions of the Sb-Nd/HT9 and Te-Nd/HT9 diffusion couples, a region directly adjacent to the Zr-rich layer on the fuel side of the interface may actually be devoid of the δ-Zr_2U phase, which may be an indication some breakdown had occurred promoting the formation of the Zr-layer. It is not fully understood at this time the level of δ-Zr_2U breakdown that is needed to facilitate a robust Zr-layer formation. Further, the Zr-layer is believed to be stabilized by impurities, such as nitrogen, and the amount of such impurities in either the fuel or cladding alloy is unknown. Even though all of the fuel alloys were fabricated under similar processes and the cladding alloy was the same for all experiments, a variation in impurities between the three fuel alloys cannot be ruled out as the concentration of such light elements were not measured directly. Upon an exhaustive literature search, there does not appear to be detailed research on exactly how the Zr-rich layer forms. Instead, most researchers explain its formation indirectly, based on observations made in their respective experiments, thus there are varying descriptions in the literature on its formation. The formation of this layer should be explored more directly through more targeted experiments.

The DFT calculations carried out may provide added insight on the diffusion-driven interactions observed experimentally. However, performing enthalpy of mixing calculations beyond a four-component system, e.g. U-Zr-Nd-Te-Fe or U-Zr-Nd-Sb-Fe, becomes much more difficult. Instead, insight can be gleaned from evaluating the different components within the U-Zr system alone. In the additive-containing fuel alloys the α-U matrix phase appears to contain appreciable concentrations of Sb and Te, depending on the alloy. The concentration is shown to be 3–6 at.% for Sb and ~2 at.% for Te (Table 4.8 and 4.9). Now comparing the enthalpies of mixing of the U-Zr-Sb and U-Zr-Te systems to that of U-Zr-Fe system, the former are shown to be more negative, i.e. more favorable. It should be noted that such DFT-based calculations provide an indication of the thermodynamics of the system and the tendency of a phase to form and does not provide an indication of the kinetics of the system, i.e. diffusion. However, the lower thermodynamics of the U-Zr-Fe system, compared to the U-Zr-Sb and U-Zr-Te systems, may lead to a lack of driving force for Fe to diffuse into the additive-containing fuel alloys.

In any case, one of the primary variations observed between the three diffusion experiments carried out in this research is the level of Fe and U diffusion and the subsequent phase formations. To review the interaction of the cladding alloy HT9 and U-10Zr (wt.%) fuel alloy more directly, the reader is directed to work by Lee *et al.* [41].

4.4 Conclusion

Both Sb and Te are potential additives proposed to mitigate the onset of FCCI and this research evaluated both within the U-10Zr (wt.%) matrix containing Nd to simulate the formation of solid FPs within the fuel. Further, the stability of the additive-lanthanide precipitates were evaluated through analysis of the alloys, i.e. U-10Zr-3.6Sb-4Nd and U-10Zr-4.3Te-4Nd (wt.%), in their annealed conditions. The diffusion experiment between U-10Zr-4Nd and HT9 provided a base line for the expected interactions between the fuel alloy and the cladding alloy. Similar isothermal diffusion experiments were carried out with the inclusion of Sb and Te additives, i.e. U-Zr-Sb-Nd/HT9 and U-Zr-Te-Nd/HT9, and the diffusion interaction between the fuel alloys and HT9 was found to change. Contrary to the Nd/HT9 diffusion couple, the additive-containing diffusion couples exhibited only limited Fe diffusion into the fuel alloy and the formation of a more distinct Zr-rich layer at the diffusion interface.

Overall, the experiments carried out in this work represent progress in the understanding of Sb and Te as additives to mitigating the onset of FCCI in the U-10Zr (wt.%) fuel alloy. Further, the diffusion experiments here were isothermal and thus does not fully represent the complete diffusion kinetics that the fuel and cladding system would undergo during normal reactor operation. However, the results presented in this research demonstrate that Sb and Te remain promising additives and should continue to be evaluated.

Acknowledgments

This work was supported by the U.S. Dept. of Energy's Nuclear Energy University Programs (NEUP) under contract DE-NE0008557. This research made use of resources located at the Center for Advanced Energy Studies (CAES) and Idaho National Laboratory (INL) which is supported by the Office of Nuclear Energy of the U.S. Department of Energy under Contract No. DE-AC07-05ID14517.

References

[1] D. D. Keiser, Metal fuel-cladding interaction, *Compr. Nucl. Mater.* Vol. 3: 423–441, 2012. http://dx.doi.org/10.1016/B978-0-08-056033-5.00067-7

[2] C. Matthews, C. Unal, J. Galloway, D. D. Keiser, S. L. Hayes, Fuel-cladding chemical interaction in U-Pu-Zr fuels: a critical review, *Nucl. Tech.* 198:3 231–259, 2017. https://doi.org/10.1080/00295450.2017.1323535

[3] D. D. Keiser, Fuel-cladding interaction layers in irradiated U-Zr and U-Pu-Zr fuel elements, Argonne National Laboratoy, *ANL-NT-240*, 2006. https://doi.org/10.2172/885496

[4] T. Ogata, Metal Fuel, *Compr. Nucl. Mater.* Vol. 3: 1–40, 2012. https://doi.org/10.1016/B978-0-08-056033-5.00049-5

[5] C. E. Lahm, J. F. Koenig, R. G. Pahl, D. L. Porter, D. C. Crawford, Experience with advanced driver fuels in EBR-II, *J. Nucl. Mater.* 204: 119–123, 1993. https://doi.org/10.1016/0022-3115(93)90207-F

[6] L. C. Walters, Thirty years of fuels and materials information from EBR-II, *J. Nucl. Mater.* 270: 39–48, 1999. https://doi.org/10.1016/S0022-3115(98)00760-0

[7] D. C. Crawford, D. L. Porter, S. L. Hayes, Fuels for sodium-cooled fast reactor: US perspective, *J. Nucl. Mater.* 371(1–3): 202–231, 2007. https://doi.org/10.1016/j.jnucmat.2007.05.010

[8] W. J. Carmack, D. L. Porter, Y. I. Chang, S. L. Hayes, M. K. Meyer, D. E. Burkes, C. B. Lee, T. Mizuno, F. Delage, J. Somers, Metallic fuels for advanced reactors, *J. Nucl. Mater.* 392(2): 139–150, 2009. http://dx.doi.org/10.1016/j.jnucmat.2009.03.007

[9] R. D. Mariani, D. L. Porter, T. P. O'Holleran, S. L. Hayes, J. R. Kennedy, Lanthanides in metallic nuclear fuels: Their behavior and methods for their control, *J. Nucl. Mater.* 419(1–3): 263–271, 2011. http://dx.doi.org/10.1016/j.jnucmat.2011.08.036

[10] M. T. Benson, L. He, J. A. King, R. D. Mariani, Microstructural characterization of annealed U-12Zr-4Pd and U-12Zr-4Pd-5Ln: Investigating Pd as a metallic fuel additive, *J. Nucl. Mater.* 502: 106–112, 2018. https://doi.org/10.1016/j.jnucmat.2018.02.012

[11] G. W. Egeland, R. D. Mariani, T. Hartmann, D. L. Porter, S. L. Hayes, J. R. Kennedy, Reducing fuel-cladding chemical interaction: the effect of palladium on the reactivity of neodymium on iron in diffusion couples, *J. Nucl. Mater.* 432: 539–544, 2013. https://doi.org/10.1016/j.jnucmat.2012.07.028

[12] G. W. Egeland, R. D. Mariani, T. Hartmann, D. L. Porter, S. L. Hayes, J. R. Kennedy, Reduction of FCCI effects in lanthanide–iron diffusion couples by doping with palladium, *J. Nucl. Mater.* 440: 178–192, 2013. http://dx.doi.org/10.1016/j.jnucmat.2013.04.060

[13] M. T. Benson, J. A. King, R. D. Mariani, M. C. Marshall, SEM characterization of two advanced fuel alloys: U-10Zr-4.3Sn and U-10Zr-4.3Sn-4.7Ln. *J. Nucl. Mater.* 494: 334–341, 2017. http://dx.doi.org/10.1016/j.jnucmat.2017.07.057

[14] Y. Xie, M. T. Benson, J. A. King, R. D. Mariani, J. Zhang, Characterization of U-Zr fuel with alloying additive Sb for immobilizing fission product lanthanides, *J. Nucl. Mater.* 498: 332–340, 2018. https://doi.org/10.1016/j.jnucmat.2017.10.039

[15] Y. S. Kim, T. Wieneck, E. O'Hare, J. Fortner, Effectiveness of a dopant in U-Zr metallic fuel to prevent lanthanide migration, *Proc. of GLOBAL 2013,* 1118–1125, Sep. 2013.

[16] N. D. Jerred, R. Khanal, M. T. Benson, R. D. Mariani, S. Choudhury, I. Charit, Nd, SbNd and Sb_3Nd_4 and their interactions with the cladding alloy HT9, *J. Nucl. Mater.* 541:152387, 2020. https://doi.org/10.1016/j.jnucmat.2020.152387

[17] Y. Xie, J. Zhang, M. T. Benson, R. D. Mariani, Diffusion behavior of lanthanide-additive compounds (Ce_4Sb_3, Ce_2Sb, and CeTe) against HT9 and Fe, *Mater. Charact.* 150: 107–117, 2019. https://doi.org/10.1016/j.matchar.2019.02.012

[18] M. T. Benson, Y. Xie, J. A. King, K. R. Tolman, R. D. Mariani, I. Charit, J. Zhang, M. P. Short, S. Choudhury, R. Khanal N. D. Jerred, Characterization of U-10Zr-2Sn-2Sb and U-10Zr-2Sn-2Sb-4Ln to assess Sn+Sb as a mixed additive system to bind lanthanides, *J. Nucl. Mater.* 510: 210–218, 2018. https://doi.org/10.1016/j.jnucmat.2018.08.017

[19] Y. Xie, J. Zhang, M. T. Benson, J. A. King, R. D. Mariani, Assessment of Te as a U-Zr fuel additive to mitigate fuel-cladding chemical interactions, *J. Nucl. Mater.* 513: 175–184, 2019. https://doi.org/10.1016/j.jnucmat.2018.10.050

[20] N. D. Jerred, R. Khanal, M. T. Benson, E. Perez, J. A. King, M. Dubey, J. Burns, I. Charit, S. Choudhury, R. D. Mariani, Evaluation of tellurium as a fuel additive in neodymium-containing U-Zr metallic fuel, *Sci. Rep.* 9(16043), 2019. https://doi.org/10.1038/s41598-019-51852-z

[21] R. Khanal, N. Jerred, M. Benson, D. A. Andersson, R. Mariani, I. Charit, S. Choudhury, A novel approach to selection of dopant to immobilize neodymium in uranium-based metallic fuels, *J. Nucl. Mater.* 529(151922), 2020. https://doi.org/10.1016/j.jnucmat.2019.151922

[22] R. Khanal, N. Ayers, N. Jerred, M. T. Benson, R. D. Mariani, I. Charit, S. Choudhury, Role of Zr in lanthanide-dopant interactions within uranium-based metallic fuels, *Nucl. Mater. Energy.* SUBMITTED. August 2020.

[23] R. Khanal, N. D. Jerred, M. T. Benson, Y. Xie, R. D. Mariani, I. Charit, S. Choudhury, Interactions and immobilization of lanthanides with dopants in uranium-based metallic fuels, *J. Nucl. Mater.* 540(152372), 2020. https://doi.org/10.1016/j.jnucmat.2020.152372

[24] C. Jiang, Y. Xie, M. T. Benson, Efficient computational search for lanthanide-binding additive dopants for advanced U-Zr based fuels, *Materialia* 2020. https://doi.org/10.1016/j.mtla.2020.100653

[25] W. Zhuo, Y. Xie, M. Benson, H. Wu, R. Mariani, J. Zhang, Experimental assessment of antimony (Sb) in pure uranium for immobilizing fission product lanthanides, *J. Nucl. Mater.* 534: 152135, 2020. https://doi.org/10.1016/j.jnucmat.2020.152135

[26] G. Kresse and J. Furthmu¨ller. Efficient iterative schemes for ab initio total-energy calculations using a plane-wave basis set. *Phys. Rev. B*, 54(16):11169–11186, October 1996.

[27] G. Kresse and J. Furthmu¨ller. Efficiency of ab-initio total energy calculations for metals and semiconductors using a plane-wave basis set. *Comput Mater Sci*, 6(1):15–50, July 1996.

[28] S. La Placa, ICDD, Polytechnic Inst. of Brooklyn, NY, USA, ICDD Grant-in-Aid, 1959.

[29] G. V. Samsonov, M. N. Abusalyamova, Kh. Shokirov, and S. A. Pryakhina, Physicochemical properties of the rare earth monoantimonides, *Inorg. Mater. (Engl. Transl.)* 10(11): 1672–1674, 1974.

[30] D. Honke and E. Parthe, The anti-Th_3P_4 structure type for rare earth germanides, antimonides and bismuthides, *Acta Cryst.* 21(3): 435–437, 1966. https://doi.org/10.1107/S0365110X66003098

[31] A. Iandelli, Monochalcogenides of lanthanum, cerium, praseodymium and neodymium, *Gazz. Chim. Ital.* 85: 881–887, 1955

[32] J. M. Silcock, Intermediate phase in the uranium-zirconium system, *J. Met. (Trans. AIME)* 209: 521, 1957.

[33] E. Garcia and J. D. Corbett, A synthetic and structural study of the zirconium-antimony system, *Solid State Chem.* 73(2):440–451, 1988. https://doi.org/10.1016/0022-4596(88)90130-2

[34] V. M. Goldschmidt and L. Thomassen, Geochemische Verteilungsgesetze der Elemente III Die Kristallstruktur Natürlicher und Synthetischer Oxyde von Uran, Thorium und Cerium, *Skr. Nor. Visensk.-Akad. Mat.-Nat.* 2:1–48, 1923.

[35] J. J. Couderc, G. Garigue, L. Lafourcade, and Q. T. Nguyen, Standard X-ray diffraction powder patterns, *Z. Metallkund.* 50:708–716, 1959.

[36] K. Nakamura, M. Kurata, T. Ogata, A. Itoh, M. Akabari, Equilibrium phase relations in the U-Zr-Fe ternary system, *J. Nucl. Mater.* 275(2): 151–157, 1999. https://doi.org/10.1016/S0022-3115(99)00116-6

[37] O. Fabrichnaya, Fe-U-Zr (Iron-Uranium-Zirconium), in: G. Effenberg and S. Ilyenko (Eds.), Non-Ferrous Metal Ternary Systems. Selected Nuclear Materials and Engineering Systems: Phase Diagrams, Crystallographic and Thermodynamic Data, *Non-Ferrous Metal Systems. Part 4* vol. 11C4: 320–327, 2007. Springer Materials, Berlin. https://doi.org/10.1007/978-3-540-48478-3_33

[38] K. Nakamura, T. Ogata, M. Kurata, A. Itoh, and M. Akabori, Reactions of U-Zr alloy with Fe and Fe-Cr alloy, *J. Nucl. Mater.* 275(3): 246–254, 1999. https://doi.org/10.1016/S0022-3115(99)00227-5

[39] D. D. Keiser, Jr. and M. A. Dayananda, Interdiffusion between U-Zr fuel and selected Fe-Ni-Cr alloys, *J. Nucl. Mater.* 200(2):229–243, 1993. https://doi.org/10.1016/0022-3115(93)90334-U

[40] G. L. Hofman and L. C. Walters, Metallic fast reactor fuels, in: B. R. T. Frost (Ed.), Nuclear Materials*, Materials Science and Technology* vol. 10A:1–44, 1994. VCH Publishers Inc., New York.

[41] C. T. Lee, H. Kim, T. K. Kim, and C. B. Lee, Diffusion behavior in an interface between U-10Zr alloy and HT-9 steel, *J. Nucl. Mater.* 395(1–3):140–144, 2009. https://doi.org/10.1016/j.jnucmat.2009.10.044

[42] S. Kaity, J. Banerjee, S. C. Parida, A. Laik, C. B. Basak, and V. Bhasin, Studies of fuel-cladding chemical interaction between U–10 wt%Zr alloy and T91 steel, *J. Nucl. Mater.* 513:16–32, 2019. https://doi.org/10.1016/j.jnucmat.2018.10.041

[43] G.L. Hofman, A.G. Hins, D.L. Porter, L. Leibowitz, E.L. Wood, Chemical interaction of metallic fuel with austenitic and ferritic stainless steel cladding, *Proc. of International Conference on Reliable Fuels for Liquid Metal Reactors*, Tucson, Ar, 1986.

[44] G.L. Hofman, L.C. Walters, T.H. Bauer, Metallic fast reactor fuels, *Progress in Nuclear Energy*, 31(1): 83–110, 1997. https://doi.org/10.1016/0149-1970(96)00005-4

[45] J. Harp, L. Capriotti, and F. Cappia, Baseline postirradiation examination of the AFC-3C, AFC-3D, and AFC-4A experiments report. (INL/EXT-18-51447), Idaho Falls, ID, 2018

[46] F.G. Di Lemma, T.L. Trowbridge, L. Capriotti, J.M. Harp, M.T. Benson, R.D. Mariani, Palladium influence on fuel performance in irradiated metallic fuel, *J. Nucl. Mater.*, 2021. SUBMITTED.

CHAPTER 5
EVALUATION OF ARSENIC AS A FUEL-BASED ADDITIVE IN THE U-Zr FUEL SYSTEM AND ITS INTERACTIONS WITH NEODYMIUM

Abstract. Arsenic (As) has been proposed through previous modeling-based research as a potential additive for the U-Zr metallic fuel system to mitigate fuel-cladding chemical interaction (FCCI). A U-10Zr-2.6As-4Nd (wt.%) alloy was fabricated to observe and characterize the interactions between As and the lanthanide Nd in a U-Zr matrix. The high temperature NdAs phase was observed to form as precipitates within the alloy, both in its as-cast and annealed conditions. No other As-based phases were observed to form indicating the tendency of As to bind with Nd. Both elemental Nd and Nd-rich precipitates were observed, a potential indication the fabricated alloy was additive-poor. To evaluate the effectiveness of As to bind with Nd and alleviate its interaction with the cladding alloy HT9, an isothermal diffusion couple experiment was carried out between the As-based fuel alloy and the HT9 alloy. An analysis of the diffusion couple interaction region showed the formation of a Zr-rich layer at the diffusing interface along with the diffusion of Fe from HT9 and into the fuel alloy. Several U-Zr-Fe ternary phases were observed to form within the interaction region, a result of Fe diffusion. Despite the diffusion of Fe into the fuel alloy, no interaction was observed to occur between NdAs precipitates and cladding-based constituents, an indication of the stabilizing effects As has on Nd. This research details the initial experimental work evaluating As as a fuel-based additive and the results indicate it has promise and should continue to be evaluated.

5.1 Introduction

Prior atomistic modeling and experimental studies conducted by our research group indicate that both As and Se have great potential as additives to bind with Nd and mitigate its participation in phenomenon known as fuel-cladding chemical interaction (FCCI) [1–3]. Initially, an evaluation of the intrinsic properties of both additive and lanthanide elements, such as, electronegativity, covalent radius and electron configuration, were found to be strong indicators of their propensity to form intermetallic compounds [1]. Such intrinsic properties of several additives and lanthanides of interested have been tabulated in Table 5.1. This was followed by models evaluating the enthalpy of mixing of additives (i.e. Tl, In, Ga, Sb, Te, Sn, Pd, As, and Se) with the primary lanthanide elements found to form as fission products in U-Zr fuel during burnup (i.e. Nd, Ce, Pr, and La). Calculations were performed evaluating the additive and lanthanide elements within the uranium matrix (i.e. U-Ln-X system, where 'Ln' denotes lanthanide elements and 'X' denotes additive elements) to give insight in to their compound forming tendencies. Figure 5.1 shows plots of the enthalpy of mixing of the additives calculated within the U-Ln matrix with respect to the additive's electronegativity (Figure 5.1 (a)) and the additive's covalent radius (Figure 5.1 (b)) [2]. From Figure 5.1 both As and Se are observed to exhibit a highly negative enthalpy of mixing with the lanthanide elements evaluated, i.e. exhibit a greater tendency to form compounds. Additional background on the experimental research carried out thus far evaluating both As and Se can be found in Appendix B.

Table 5.1. Intrinsic properties of select additive and lanthanide elements [4].

	Electronegativity [Pauling scale]	**Covalent Radius [pm]**	**Electron Configuration**
As	2.18	119	[Ar] $3d^{10}$ $4s^2$ $4p^3$
Se	2.55	116	[Ar] $3d^{10}$ $4s^2$ $4p^4$
In	1.78	144	[Kr] $4d^{10}$ $5s^2$ $5p^1$
Tl	1.62	148	[Xe] $4f^{14}$ $5d^{10}$ $6s^2$ $6p^1$
Nd	1.14	201	[Xe] $4f^4$ $6s^2$
Ce	1.12	204	[Xe] $4f^1$ $5d^1$ $6s^2$

Based on the atomistic modeling results, it was determined that As would be further evaluated within the U-10Zr (wt.%) alloy along with the addition of Nd to simulate solid fission product formation within the fuel. The fabrication of a U-Zr-As-Nd alloy would be used to experimentally evaluate the compound forming tendencies between As and Nd. This experimental fuel alloy was initially characterized in its as-cast condition. The alloy was then subjected to an isothermal diffusion couple experiment with the cladding alloy HT9. In addition to analyzing the diffusing interface to characterize the interaction region between the two alloys, the fuel section of the diffusion couple was further analyzed to characterize the fuel's microstructure as it resembles an annealed state.

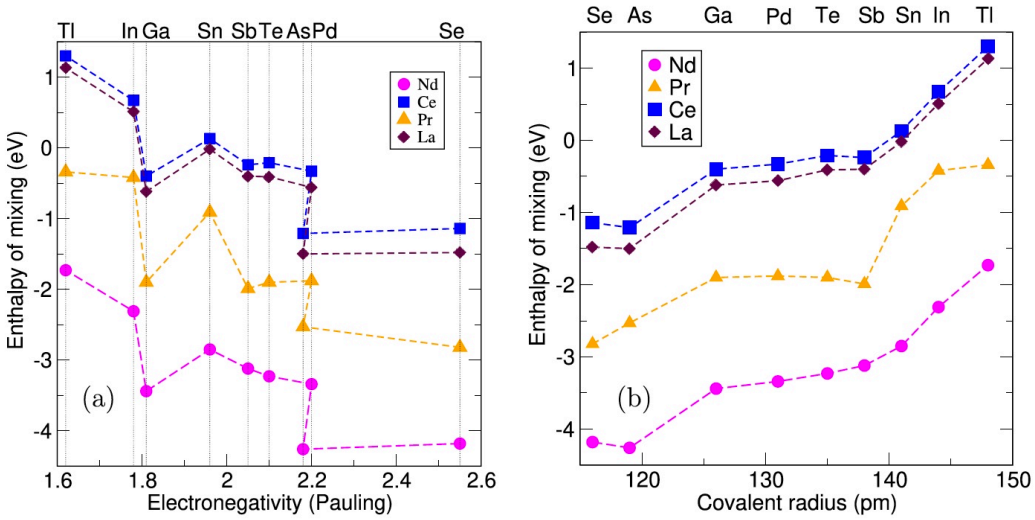

(a) (b)

Figure 5.1. Plots of the enthalpy of mixing values of different additives and lanthanides correlated with various additives (a) electronegativity and (b) covalent radius [2].

5.2 Methodology

5.2.1 Experiment methodology

A fuel composition of U-10Zr-2.6As-4Nd in wt.% (U-21Zr-6.6As-5.3Nd in at.%) was fabricated through arc-melting under an inert atmosphere glovebox. The lanthanide concentration in the alloy targeted the expected concentration of all lanthanides to form within the fuel at 16 at.% burnup as per data reported by Mariani *et al.* [5] for U-10Zr (wt.%) fuel irradiated within the Experimental Breeder Reactor (EBR) II. Further, the additive concentration in the alloy targeted an additive-lanthanide atomic ratio of 1:1, to target the formation of the high temperature NdAs phase. However, due to the propensity of As to

vaporize during arc-melting, the alloy was fabricated with a slightly greater additive concentration.

To evaluate the different alloy interactions, an isothermal diffusion experiment was carried out between the fuel alloy and cladding alloy HT9. Isothermal diffusion couple experiments are a typical *out-of-pile* experimental method used to study the FCCI phenomena [6] and have been extensively used to evaluate the effectiveness of additives to mitigate lanthanide interactions with cladding alloys [7–10]. The isothermal diffusion couple experiment was carried out at 948K (675°C) for 96 h. The diffusion experiment was performed inside a muffle furnace contained in an inert argon glovebox. The glovebox atmosphere was maintained at 1–5 ppm oxygen and a continuous flow of high purity argon cover gas was flowed directly into the furnace at a rate of 0.25 ft^3/hr (1.97 cm^3/s) for the length of the experiment. To achieve a high purity, the argon cover gas was initially passed through an oxygen getter furnace reducing its oxygen content down to 10^{-10}–10^{-11} ppb oxygen before being flowed into the furnace chamber. Figure 5.2 (a) shows the furnace used to carry out the isothermal diffusion experiment in this study.

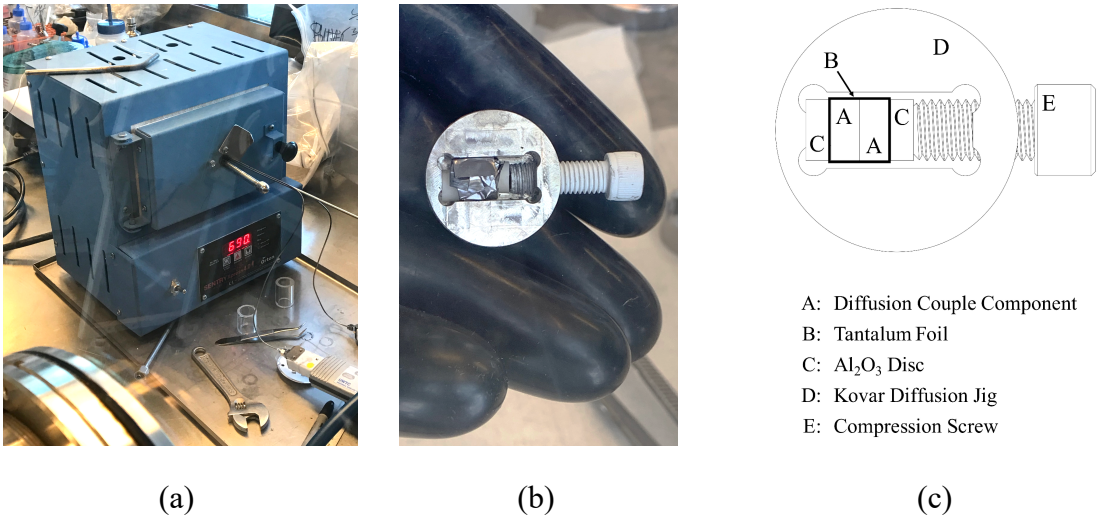

(a) (b) (c)

Figure 5.2 (a) Muffle furnace used within the glovebox for fuel-based diffusion experiments. (b) An assembled diffusion jig before the final outer tantalum foil wrapping. (c) Diagram of the diffusion couple jig and the internal components used for the isothermal diffusion experiments.

The diffusing materials were sectioned from rods into discs approximately 2.5 mm thick and polished to a 1 µm finish within the glovebox to prevent any oxide layer formation. The diffusing discs were placed in contact with each other and were directly wrapped in a layer

of tantalum foil (~0.025mm) and placed inside a jig made of Kovar™ steel, an iron-nickel-cobalt alloy that exhibits low thermal expansion. Alumina discs were placed directly between the diffusion couple and jig contact points to avoid adverse interactions during the experiment. The entire jig was then wrapped in tantalum foil and placed into the furnace. Figure 5.2 (b) shows an assembled diffusion jig before the final tantalum foil wrap is applied and a diagram of the experimental diffusion couple jig setup is shown in Figure 5.2 (c). With the diffusion couple jig placed within the furnace chamber, the high purity argon is flowed into the furnace chamber 30 min prior to initiating the diffusion experiment. The furnace was then heated at a rate of 1,000 °C/h (0.28 K/s) up to the experiment temperature and held for the length of the diffusion experiment. Upon completion of the experiment, the jig was immediately removed from the furnace chamber and allowed to cool in the open glovebox environment. The cooling rate of the jig in this experiment was not measured directly but similar experiments exhibited a cooling rate of 22°C/min (0.37 K/s), i.e. cools to 373K (100°C) in ~26 min.

5.2.2 Characterization methodology

The diffusion couple was sectioned and mounted in epoxy for microstructural characterization. Samples were then prepared by grinding using sequential grits of SiC papers followed by polishing down to a 1 μm finish using diamond-based suspensions. All sample preparation steps were performed within an inert argon glovebox to avoid oxidation on the analysis surface. The polished surfaces were then coated with a thin layer of gold to control charging of the metallographic mount during electron microscopy analysis.

Scanning electron microscopy was performed using a JEOL JSM-6610LV scanning electron microscope (SEM) operated at an accelerating voltage of 20 kV. Imaging was primarily conducted in backscatter electron (BSE) imaging mode to get better contrast of phase formations. Energy dispersive X-ray spectroscopy (EDS) was conducted using an EDAX Apollo X silicon drift detector (SDD) and EDAX TEAM v4.4 (2016) software. The amp time was adjusted for each analysis to generate a dead time of between 20% to 30%. In conducting point analysis, elemental spectra were collected for 50 live seconds per analysis location. For elemental spectra mapping, a dwell time of 200 μs was used. Elemental data collected from EDS was quantified based on the standardless ZAF method using the EDAX TEAM library of spectra standards. X-ray diffraction (XRD) was performed using a Rigaku SmartLab X-Ray

Diffractometer paired with SmartLab Guidance software (v 2.0.4.7). XRD was conducted using a parallel beam (PB) optics configuration, Cu Kα radiation at a tube current of 44 mA, and a D/tex Ultra 250 1D silicon strip detector. Focused XRD $\theta/2\theta$ scans were performed using a 0.04° step size and a 5°/min scan speed. Data was analyzed and indexed using Rigaku's PDXL 2 software (v2.3.1.0) and the International Centre for Diffraction Data (ICDD) (PDF-2 Release 2016) database.

5.3 Results and Discussion

5.3.1 As-cast and annealed structure

The U-10Zr-2.6As-4Nd (wt.%) alloy in its as-cast and annealed conditions can be found in the SEM micrographs of Figures 5.3 and 5.4, respectively. To determine elemental information of the precipitate and matrix formations, EDS point analysis was conducted at the locations indicated in Figure 5.3 (b), (d) and Figure 5.4 (b), with the results listed in Table 5.2. In the as-cast condition (Figure 5.3) two unique precipitate formations are observed to have formed. Based on the EDS data, the large precipitates are likely the NdAs phase (pts. 1–6) but with areas that are very Nd-rich (in excess of 96 at.% Nd) spread throughout (pts. 7 and 8). This multi-phase precipitate may be a non-equilibrium formation due to the quick solidification of the alloy from a liquid during the arc-melting process. Alternatively, the formation may be the result of excess Nd being dissolved within the Nd-As liquid phase during arc-melting and upon cooling the NdAs phase initially solidifies followed by the Nd-rich regions. The Nd-As binary phase diagram is shown in Figure 5.6 and it demonstrates that the NdAs phase has a much greater melting temperature compared to that of elemental Nd. In addition to Nd-rich regions, there are also lighter phase regions observed within the large precipitates (pts. 9–12). EDS analysis indicates these are likely the U-Zr matrix material and appear to be Zr-rich compared to the surrounding matrix (pts. 20 and 21). The smaller precipitates observed within the as-cast alloy (Figure 5.3 (d)) have a unique amoeba-like structure with what appears to be the U-Zr matrix contained within as well. It is not fully understood at this time what led to such a precipitate formation nor why it deviates from the larger precipitate shown in Figure 5.3 (b). From the EDS analysis these smaller precipitates are likely the NdAs phase (pts. 13–19) as well and there is no indication of Nd-rich regions being contained within. However, some of the smaller inclusions within the matrix (pts. 24 and 25) are primarily Nd, containing only a

small concentration of As (~7 at.%) but they do not align with a stoichiometric Nd-As compound. As for the U-Zr phase contained within the precipitates, the region is observed to be U-rich, aligning with the matrix phase.

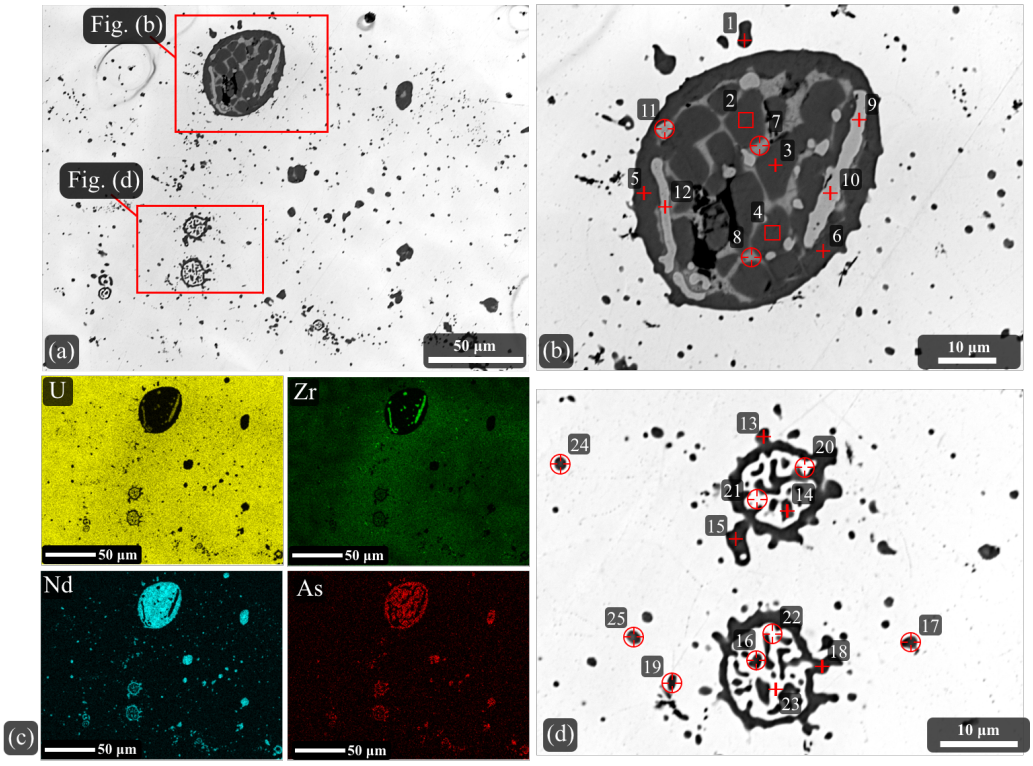

Figure 5.3. SEM/EDS characterization of the U-10Zr-2.6As-4Nd alloy in the as-cast condition. (a) BSE micrograph of different precipitate formations within the alloy. (b) high magnification BSE micrograph of the area indicated in (a). (c) EDS elemental map results of the area imaged in (a). (d) high magnification BSE micrograph of the area indicated in (a). EDS point analysis of the locations indicated in (b) and (d) are listed in Table 5.2.

The presence of elemental Nd throughout the matrix, as well as the presence of Nd-rich phases within the precipitates, may be an indication that the As concentration in the fabricated alloy fell below the targeted 1:1 (additive-lanthanide) atom ratio, i.e. more As may have been lost during arc melting then initially planned. However, it is encouraging that As is not observed to bind with any other elements within the matrix, e.g. U or Zr, an indication of its favored binding with Nd. Previous research characterizing a U-As-Nd alloy observed the formation of a UAs phase when the alloy was fabricated at a 2:1 (additive-lanthanide) atom ratio [1]. Such a formation is shown in Figure B.1 of Appendix B, where the UAs phase is observed to form around the NdAs phase. It should be noted however that all of the Nd was

observed to be bound with As and only then would As bind to U. This was evident by the UAs phase forming around the NdAs phase.

In its annealed condition, the U-10Zr-2.6As-4Nd (wt.%) alloy (Figure 5.4) was observed to contain large precipitates, similar to those in Figure 5.3 (b). These precipitates are again likely the NdAs phase (pts. 1–7). These large precipitates appear to continue to exhibit a multi-phase structure wherein Nd-rich regions are still observed (pts. 8–10). It is interesting that the large precipitates continue to maintain a two-phase morphology through the annealing process as the higher temperatures would have provided the necessary energy to allow them to fully homogenize. This indicates that the formation is likely thermodynamically stable. The stability of such a precipitate suggests their initial formation, as observed in the as-cast alloy, was not the result of a non-equilibrium process. Again, this may indicate that the alloy composition ended up being additive-poor. However, such multi-phase precipitates are not uncommon, research evaluating palladium (Pd) as an additive in a U-10Zr (wt.%) alloy from Benson *et al.* [11] also observed multi-phase precipitates where lanthanide-rich regions formed within additive-lanthanide precipitates.

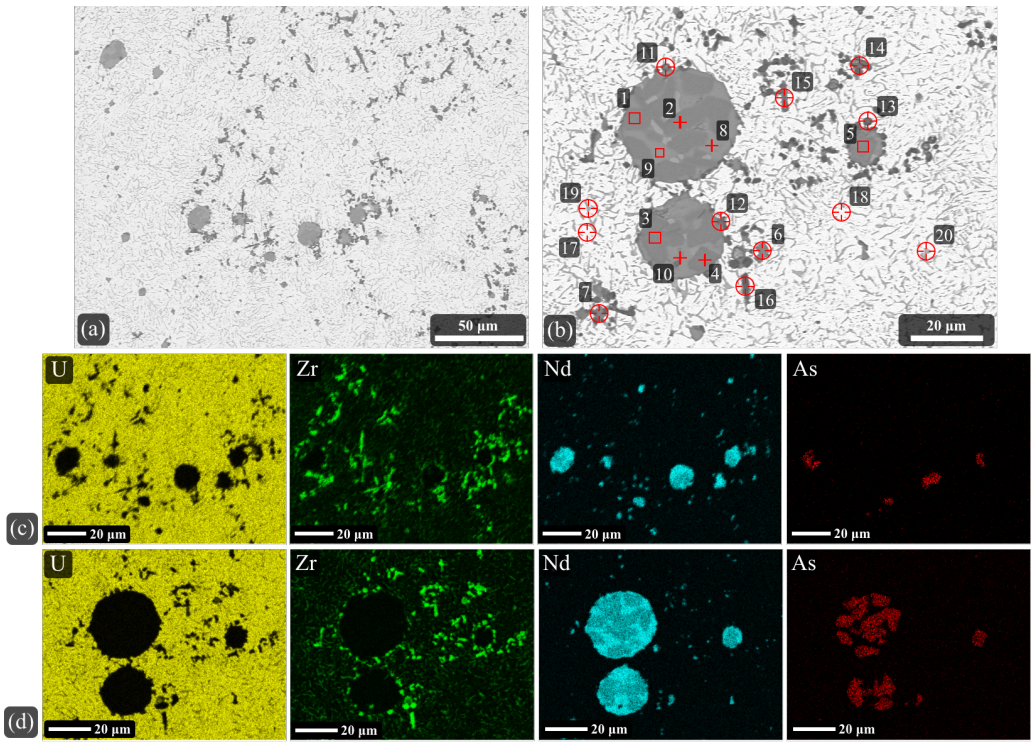

Figure 5.4. SEM/EDS characterization of the U-10Zr-2.6AS-4Nd alloy in the annealed condition. (a) and (b) BSE micrographs of different precipitate formations within the alloy. (c) EDS elemental map results of the area imaged in (a). (d) EDS elemental map results of the area imaged in (b). EDS point analysis of locations indicated in (b) are listed in Table 5.2.

Table 5.2. EDS point analysis results, in at.%, corresponding to locations indicated in Figure 5.3 (b) and (d) and in Figure 5.4 (b).

Pt.	U	Zr	As	Nd	Phase[a]	Pt.	U	Zr	As	Nd	Phase[a]
Figure 5.3 (b) & (d)						*Figure 5.4 (b)*					
1	1	0.2	49	50	*NdAs*	**1**	0.1	5	43	50	*NdAs*
2	0	0	47	53	*NdAs*	**2**	0.1	4	45	49	*NdAs*
3	0	0	48	52	*NdAs*	**3**	0.1	5	44	49	*NdAs*
4	0.2	2.7	45	52	*NdAs*	**4**	0.1	4	45	49	*NdAs*
5	0	0	46	54	*NdAs*	**5**	0.1	5	42	52	*NdAs*
6	0	0	47	53	*NdAs*	**6**	0.1	5	43	50	*NdAs*
7	0	0	4	96	*Nd-rich region*	**7**	2	20	35	41	*NdAs*
8	0	0	5	95	*Nd-rich region*	**8**	0.1	6	4	88	*Nd-rich region*
9	29	66	4	2	*U-Zr soln. (Zr-rich)*	**9**	0.1	6	2	89	*Nd-rich region*
10	29	66	3	2	*U-Zr soln. (Zr-rich)*	**10**	0.1	6	13	78	*Nd-rich region*
11	24	67	4	5	*U-Zr soln. (Zr-rich)*	**11**	16	79	3	2	*Zr incl.*
12	24	68	4	4	*U-Zr soln. (Zr-rich)*	**12**	4	86	2	7	*Zr incl.*
13	5	4	45	46	*NdAs*	**13**	4	81	2	12	*Zr incl.*
14	13	8	39	40	*NdAs*	**14**	9	87	2	0.6	*Zr incl.*
15	0.1	0	49	50	*NdAs*	**15**	13	84	2	0.5	*Zr incl.*
16	6	5	44	45	*NdAs*	**16**	2	96	2	0.4	*Zr incl.*
17	11	7	40	41	*NdAs*	**17**	81	7	7	2	*α-U*
18	5	5	42	48	*NdAs*	**18**	86	7	3	1	*α-U*
19	9	7	41	44	*NdAs*	**19**	36	58	3	1	*δ-Zr_2U*
20	55	37	5	3	*U-Zr soln.*	**20**	35	60	2	1	*δ-Zr_2U*
21	51	35	9	5	*U-Zr soln.*						
22	56	35	6	3	*U-Zr soln.*						
23	57	36	5	1	*U-Zr soln.*						
24	6	7	7	80	*Nd prec.*						
25	12	11	7	71	*Nd prec.*						

[a]*suggested phase based on EDS results*

The other primary changes observed in the annealed alloy are the presence of Zr-rich inclusions (pts. 11–16) and the precipitation of the δ-Zr_2U (light grey) phase throughout the matrix (pts. 19 and 20). Further, the remaining matrix of the alloy in its annealed condition is likely that of the α-U phase (pts. 17 and 18), having a concentration that is primarily U. As for the formation of Zr-rich inclusions, they have been previously documented to form at the edge of lanthanide-containing precipitates and are typically stabilized by trace impurities, such as nitrogen, in the alloy [12].

Overall, it is encouraging that the large NdAs precipitates are not observed to change or degrade through the annealing process. Further, the lack of As interaction with other matrix constituents, e.g. U or Zr, is also encouraging for its use as an additive. It is important to note that if arc melting is utilized as the fuel fabrication method for such a fuel alloy, even greater concentrations of As need to be utilized to compensate for vaporization losses. As arsenic continues to be evaluated as an additive, a U-10Zr-2.6As (wt.%) alloy should be characterized in order to evaluate how it interacts within the U-Zr matrix without lanthanide additions.

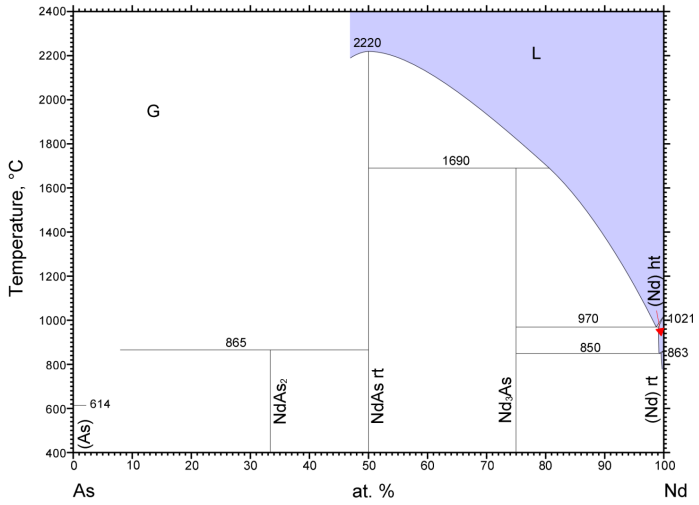

Figure 5.5. Nd-As binary phase diagram [13].

XRD analysis was carried out on the U-10Zr-2.6As-4Nd (wt.%) alloy both in its as-cast and annealed condition and the results are plotted in Figure 5.6. From the corresponding XRD patterns, the NdAs phase was identified in the alloy in both the as-cast and annealed conditions. An elemental Nd phase was also detected in the as-cast condition, whereas the δ-

Zr_2U phase is evident in the annealed condition. Both α-U and UO_2 are observed in both alloy conditions with α-U being the dominant phase, typical of a U-10Zr (wt.%) alloy. The presence of UO_2 is likely due to surface oxidation from air exposure during XRD analysis. Additional crystallographic details of the phases identified through XRD are summarized in Table 5.3.

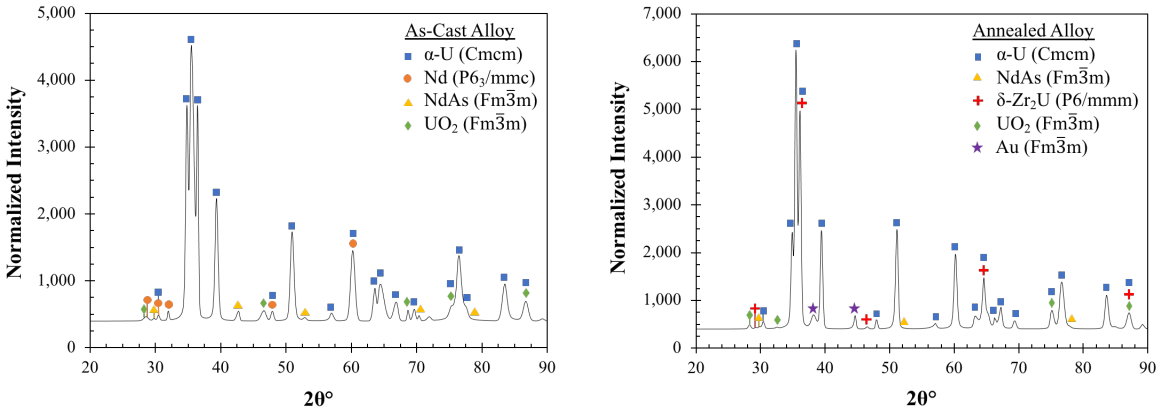

(a) (b)

Figure 5.6. XRD results of the U-Zr-As-Nd alloy in its (a) as-cast condition and (b) annealed condition.

Table 5.3. Crystallographic information of phases identified through XRD analysis shown in Figure 5.6.

Phase	**Space Group, Structure**	**Cell Parameters**
α-U [14]	Cmcm (63), Orthorhombic	a=0.287, b=0.587, c=0.496 [nm] $\alpha=\beta=\gamma=90°$
Nd [15]	$P6_3/mmc$ (194), Hexagonal	a=b=0.366, c=1.18 [nm] $\alpha=\beta=90°$, $\gamma=120°$
NdAs [16]	$Fm\bar{3}m$ (225), Cubic	a=b=c=0.599 [nm] $\alpha=\beta=\gamma=90°$
δ-Zr_2U [17]	P6/mmm (191), Hexagonal	a=b=0.503, c=0.308 [nm] $\alpha=\beta=90°$, $\gamma=120°$
UO_2 [18]	$Fm\bar{3}m$ (225), Cubic	a=b=c=0.547 [nm] $\alpha=\beta=\gamma=90°$
Au [19]	$Fm\bar{3}m$ (225), Cubic	a=b=c=0.408 [nm] $\alpha=\beta=\gamma=90°$

5.3.2 Interactions with HT9

During the cross-sectioning of the U-10Zr-2.6As-4Nd/HT9 diffusion couple the bond fractured, thus when the two components were mounted in epoxy, a gap was formed between

the two sections. This gap is denoted in the SEM micrographs of Figures 5.7 and 5.8 as "Resin". Figure 5.7 shows SEM micrographs of the interaction region that formed between the fuel and cladding alloys. In Figure 5.7 (a) the interaction region was found to stretch into the fuel alloy ~70 µm and appears to be comprised of three distinct layers each containing unique phase formations. These layers are more discernible in the higher magnification SEM micrograph shown in Figure 5.7 (b). To gain insight into the elemental concentration of the various phase formations within the interaction region, EDS analysis was conducted. EDS point analysis data of the locations indicated in Figure 5.7 (b) are listed in Table 5.4. Further, an EDS line scan was conducted across a section of the interaction region as indicated in Figure 5.7 (a), and its concentration profile is plotted in Figure 5.7 (c). EDS elemental mapping of the area imaged in Figure 5.7 (b) is shown in Figure 5.7 (d).

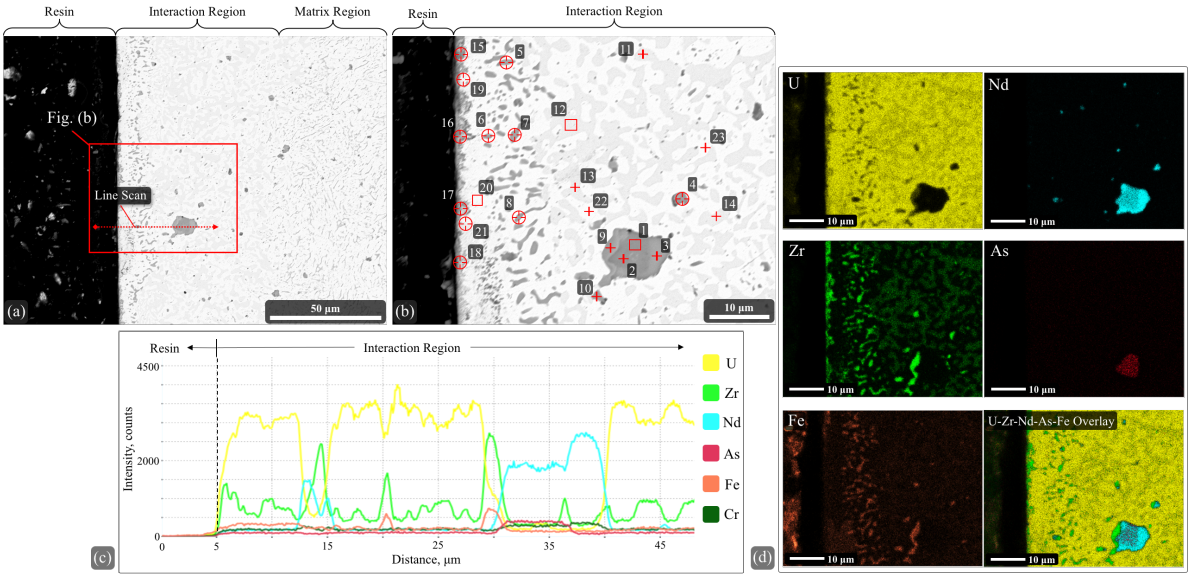

Figure 5.7. SEM/EDS characterization of the U-10Zr-2.6As-4Nd/HT9 diffusion couple. (a) and (b) BSE micrographs of the interaction region at varying magnifications. (c) EDS elemental line scan plot of the location indicated in (a). (d) EDS elemental map results of the region imaged in (b). EDS point analysis of the locations indicated in (b) are listed in Table 5.4.

Directly at the diffusion couple interface there appears to be a Zr-rich layer (pts. 15–18), that is only a few microns thick and is observed to be comprised of both U and Fe at varying concentrations, 18–51 at.% and 6–37 at.%, respectively. The Zr-rich layer is followed by a layer that stretches ~10 µm into the fuel alloy which contains dark grey precipitates (pts. 5–8) within a light matrix phase. Based on the elemental ratios from the EDS data, these dark grey precipitates are likely the U-Zr-Fe ε-phase, as described by Nakamura *et al.* [20] with a

nominal composition of U-(33–50)Zr-33Fe (at.%). In evaluating the Fe elemental map in Figure 5.7 (c), its concentration is noticeable at the locations that correspond to the ε-phase precipitates. The light matrix phase is likely that of the α-U phase (pts. 19–21). Beyond this second layer, the remainder of the interaction region appears to be comprised of a two-phase morphology. The light grey phase (pts. 11–14) is likely the U-Zr-Fe λ-phase, having a nominal composition of U-(21–25)Zr-6Fe (at.%) [20] and the light phase is likely the α-U phase as well (pts. 19–23). At this analysis location a precipitate, which appears to be comprised of multiple phases, is present but not directly at the interface. The precipitate appears to be primarily comprised of the NdAs phase (pts. 1 and 2), but also contains Nd-rich regions (pts. 3 and 4). Interestingly, a section of the precipitate appears to correlate with the ε-phase (pt. 9), but this formation appears to be restricted to one side of the precipitate.

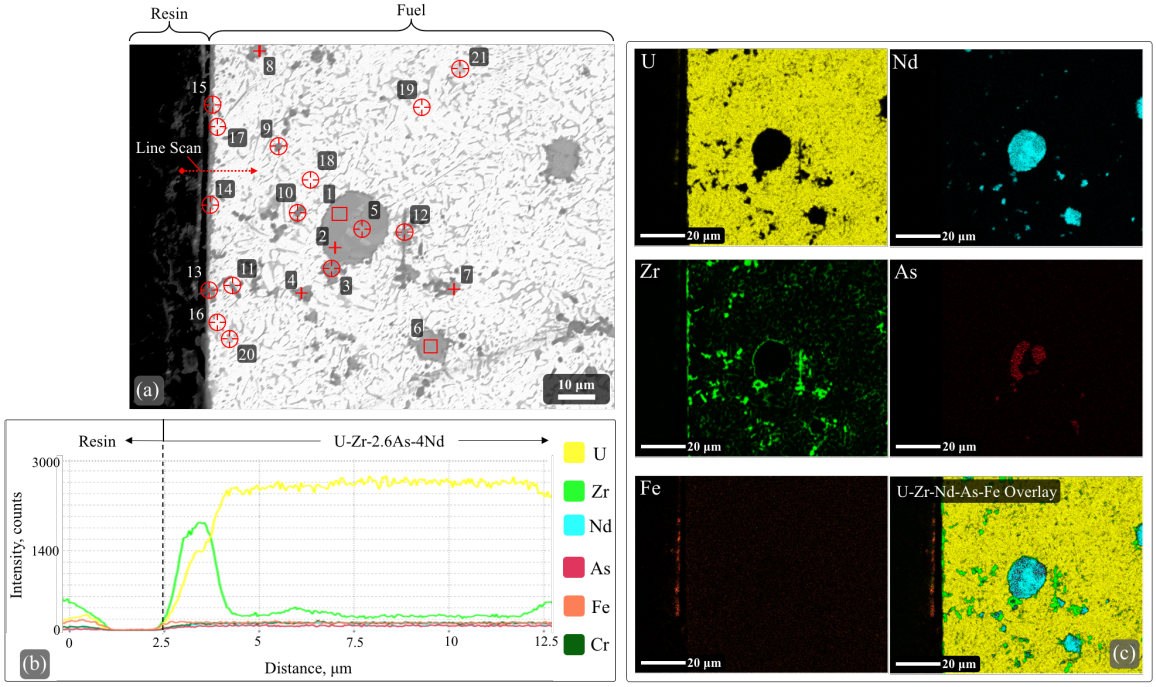

Figure 5.8. SEM/EDS characterization of a separate section of the U-10Zr-2.6As-4Nd/HT9 diffusion couple. (a) BSE micrograph of the diffusion couple interface. (b) EDS elemental line scan plot of the location indicated in (a). (c) EDS elemental map results of the region imaged in (a). EDS point analysis of the locations indicated in part (a) are summarized in Table 5.4.

In general, the matrix phase of the interaction region appears to be that of the αU phase (pts. 22 and 23), however, the locations nearest the interface (pts. 19 and 21) exhibit appreciable concentrations of Fe (5 at.% and 3at.%, respectively) compared to locations away from the interface. Beyond the evidence of U-Zr-Fe ternary phase formations, the degree of Fe

diffusion into the alloy can be further discerned in the elemental line scan plot in Figure 5.7 (c). The Fe intensity is observed to be elevated in general through the matrix and intensifies in areas of the line scan that cross over the ε- and λ-phases. Overall, the fuel-side of the diffusion couple can be summarized as containing four distinct phase regions: (1) Zr-rich layer (containing varying concentrations of U and Fe) at the bonding interface, (2) αU + ε, (3) αU + λ, and (4) αU + δZr_2U, which extends through the remainder of the fuel. To discuss on these region formations, Figure 5.9 contains a U-Zr-Fe isothermal ternary phase diagram constructed at 680°C (953K) that was recreated from Nakamura *et al.* [21]. This isotherm aligns closely to the 675°C temperature used in this diffusion experiment. Because the Zr-rich layer does not align with an equilibrium phase, its location on the ternary isotherm cannot be determined. However, the binary αU + ε and αU + λ regions are shown, denoted as the dotted regions on the phase tie lines. This is followed by the presence of the αU + δZr_2U region on the U-Zr tie line. It should be noted that although the ternary phase diagram denotes the βU and γ_2 phases, given the relatively low cooling rate of the diffusion couple at the completion of the experiment, these phases are expected to transform to αU and δZr_2U phases upon cooling, respectively. It can be seen from the ternary isotherm, that both U-Fe and Fe-Zr phases are lacking and Nakamura *et al.* [21] may further offer a rationalization for their lack of formation. They found that Zr-Fe and U-Fe phases near the bonding interface tend to exhibit slow growth rates, thus the 96h annealing time used in this diffusion experiment may not have provided sufficient time for such layers to fully develop.

A separate section of the interface of the U-10Zr-2.6As-4Nd/HT9 diffusion couple is shown in Figure 5.8. At this location, interaction between the two alloys appear to be drastically different compared to that observed in Figure 5.7; here no interaction region is observed to have formed. Results from EDS point analysis of locations indicated in Figure 5.8 (a) is listed in Table 5.4 and results of EDS line scan analysis of the section indicated in Figure 5.8 (a) is plotted in Figure 5.8 (b). Further, EDS elemental mapping results of the area imaged in Figure 5.8 (a) is shown in Figure 5.8 (c). At this location, again a Zr-rich layer is observed to have formed at the diffusing interface, but the concentrations were found to be different compared to the Zr-rich layer observed in Figure 5.7. Here the concentration of U and Fe are found to be much less, measuring 5–14 at.% and 2–5 at.%, respectively. There are several globular light grey precipitates near the interface, and they appear to be comprised of multiple phases as well.

The largest precipitate is likely the NdAs phase (pts. 1–3) but it also contains an Nd-rich region (pt. 5). There are also several instances of Nd-rich precipitates having varying concentrations of As (pts. 6–8), none of which aligns with a stoichiometric Nd-As compound.

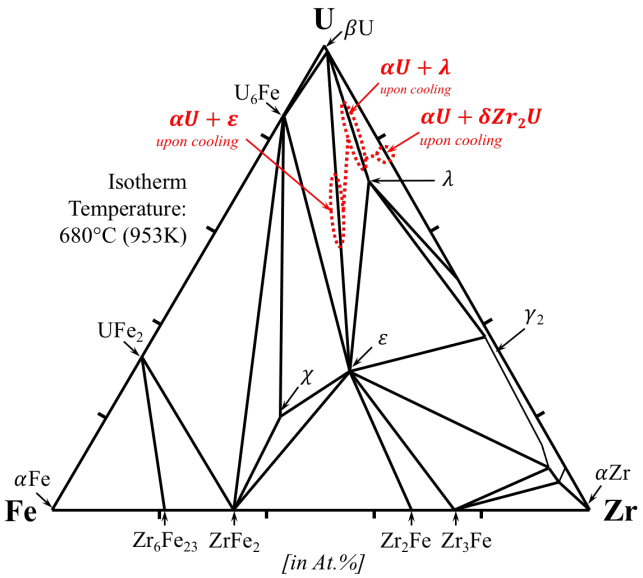

Figure 5.9. U-Zr-Fe ternary isotherm at 680°C (953K) showing the phase layers observed through the interaction region in Figure 5.7. *Recreated from the calculated ternary isotherm reported in Nakamura et al.* [21].

A unique formation observed in this section of the diffusion couple is that of Zr-inclusions (pts. 9–13), which were not observed in the interaction region imaged in Figure 5.7. Similar formations, however, were observed in the fuel alloy in the annealed condition (Figure 5.4). The primary matrix phase is again likely the αU phase (pts. 16–19), but sections of the matrix phase near the interface were observed to contain elevated Fe concentrations, 5 and 4 at.% (pts. 16 and 17), compared to 1 and 2 at.% at locations away from the bonding interface (pts. 18 and 19). Another formation that was not previously observed near the interface is the formation of the light grey phase which is likely the δZr_2U phase (pts. 20 and 21). From EDS line scan results reported in Figure 5.8 (b), it is apparent that the diffusion of Fe into the fuel did not readily occur at this location. The line scan results indicate a slight increase in Fe concentration at the diffusion interface, which correlates with the Zr-rich layer, but then remains low through the rest of the scan. The absence of Fe diffusion can be further hypothesized due to the apparent lack of U-Zr-Fe ternary phase formations within the fuel alloy, which was readily observed within the interaction region of the U-10Zr-2.6As-4Nd alloy

in Figure 5.7. The only presence of Fe is the limited concentration observed within the Zr-rich layer and slightly elevated Fe concentrations within the αU phase near the interface.

Table 5.4. EDS point analysis results, in at.%, corresponding to locations indicated in Figure 5.7 (b) and Figure 5.8 (a).

Pt.	U	Zr	As	Nd	Fe	Cr	Phase[a]	Pt.	U	Zr	As	Nd	Fe	Cr	Phase[a]
Figure 5.7 (b)								*Figure 5.8 (a)*							
1	0.2	6	44	49	0.6	0.7	*NdAs*	**1**	0.1	5	45	49	0.7	0.7	*NdAs*
2	1	6	44	47	0.7	0.8	*NdAs*	**2**	0.1	5	44	49	0.7	1	*NdAs*
3	0	8	2	88	0.9	0.9	*Nd-rich region*	**3**	0.4	27	34	38	0.5	0.5	*NdAs*
4	6	11	4	76	2	1	*Nd prec.*	**4**	0.1	9	43	47	0.2	0.3	*NdAs*
5	23	42	2	0.3	32	0.8	ε	**5**	0.1	7	4	87	0.9	1	*Nd-rich region*
6	29	40	3	0.5	28	0.7	ε	**6**	0.1	8	17	73	0.9	1	*Nd-rich prec.*
7	19	45	1	0.4	33	0.4	ε	**7**	0.1	9	13	77	0.4	1	*Nd-rich prec.*
8	23	41	3	0.4	31	1	ε	**8**	0.2	9	33	56	0.7	1	*Nd-rich prec.*
9	14	51	2	2	31	0.5	ε	**9**	4	94	1	0.3	0.5	0.2	*Zr incl.*
10	18	45	3	3	30	0.7	ε	**10**	3	94	2	0.4	0.3	0.1	*Zr incl.*
11	58	29	4	1	8	1	λ	**11**	7	90	2	0.3	0.3	0.3	*Zr incl.*
12	58	28	4	1	8	2	λ	**12**	12	84	2	1	0.3	0.3	*Zr incl.*
13	58	27	4	1	2	8	λ	**13**	7	88	3	0.2	2	0.1	*Zr layer*
14	58	29	4	1	8	1	λ	**14**	14	78	3	0.3	5	0.4	*Zr layer*
15	18	41	2	0.5	37	2	*Zr layer*	**15**	5	86	2	0.6	5	0.8	*Zr layer*
16	35	52	3	3	6	1	*Zr layer*	**16**	76	12	5	1	5	1	*α-U*
17	41	48	3	1	6	1	*Zr layer*	**17**	80	10	5	1	4	1	*α-U*
18	51	33	3	1	10	1	*Zr layer*	**18**	83	10	4	1	1	0.8	*α-U*
19	75	12	5	2	5	2	*α-U*	**19**	78	14	4	0.9	2	0.8	*α-U*
20	82	9	5	1	3	1	*α-U*	**20**	37	59	2	0.3	1	0.2	*δ-Zr_2U*
21	70	8	6	1	14	1	*α-U*	**21**	36	60	2	0.7	0.7	0.4	*δ-Zr_2U*
22	81	9	6	1	2	0.6	*α-U*								
23	82	11	3	1	3	0.8	*α-U*								

[a]*suggested phase based on EDS results*

In comparing the different sections of the U-10Zr-2.6As-4Nd/HT9 diffusion couple shown in Figures 5.7 and 5.8, some theories can be put forward regarding the different phase formations. The primary differences between the two sections of the diffusion couple is the presence of the U-Zr-Fe ternary ε- and λ-phases at one section (Figure 5.7) and Zr-rich inclusions and the δZr_2U phase at the other (Figure 5.8). It is likely that as Fe diffuses into the fuel alloy, the formation of both Zr-rich inclusions and the δZr_2U phase are suppressed and with the addition of Fe both the ε- and λ-phases form within the interaction region. The limited degree of Fe diffusion at the location in Figure 5.8 could be the result of a more robust Zr-layer formation but the layer formation appears to be similar to the Zr-layer observed in Figure 5.7 and neither appear to be overly continuous. Thus, an alternative explanation for the lack of Fe diffusion at the location observed in Figure 5.8 may be due to limited contact being achieved with the HT9 alloy, which is difficult to determine due to the bond fracturing during sectioning. However, it's worth noting again that both EDS point analysis of the αU phase (pts. 16 and 17) and the EDS line scan results, Figure 5.8 (b), indicate elevated Fe concentrations near the bonding interface and thus diffusion of Fe has occurred, but the depth of its diffusion into the fuel alloy appears to be minimal.

The HT9 side of the bonding interface was also analyzed (not shown here) and it was not apparent that any U-based phases, such as the UFe_2 phase, had developed. The UFe_2 phase was previously observed to form at the diffusing interface in diffusion couple experiments carried out between U-10Zr-4Nd (wt.%) and HT9 but it was not observed in other additive-based diffusion couple experiments (Chapter 4). This may be attributed to the observation that the Zr-rich layer in the U-Zr-As-Nd/HT9 diffusion couple appears to be different than the Zr-rich layers observed to form in other additive-based diffusion couple experiments, e.g. U-10Zr-3.6Sb-4Nd/HT9 and U-10Zr-4.3Te-4Nd/HT9 (Chapter 4). The Zr-rich layer analyzed in Figure 5.7, for example, appears to have a greater U and Fe concentration than the Zr-layers of the previous experiments. The presence of U and Fe may be an indication of their diffusion through the Zr-rich layer of this study. The presence of Fe, of course can be linked to its diffusion into the fuel alloy where U-Zr-Fe phases were observed to form. Whereas the presence of U within the layer may indicate an agreement with a hypothesis proposed by others that U atoms would diffuse through the Zr-layer to interact with the cladding. Therefore, it could be that the experiment time in this study was not adequate to allow for a sufficient

concentration of U to diffuse through the Zr-layer and for a U-Fe layer to fully develop. It is not understood at this time, however, why the experiment time appears to be sufficient for Fe diffusion into the fuel but not for the diffusion of U out of the fuel. This variation in diffusion may be attributed to the Zr-layer formation, which was unable to be determined here.

5.5 Conclusion

The proposed fuel-based additive As is observed to bind with Nd within the U-Zr matrix to preferentially form the NdAs compound. The NdAs compound remained unchanged when annealed at elevated temperatures, an indication of its thermal stability. Further, As was only observed to bind with Nd and not with any other fuel-based constituents, which is an important function of fuel-based additives being proposed to mitigate FCCI. However, great care must be taken in alloying As into the fuel given its low boiling point, this led to the alloys in this study being As-poor. Fabrication techniques beyond arc-melting should be explored or ways to better implement the arc melting process with As-bearing alloys should be evaluated. Alternatively, As may need to be alloyed at even greater concentrations to account for potential losses, but care must be taken here as well to avoid As forming undesired phases with fuel constituents, i.e. U and Zr.

It is apparent in the U-10Zr-2.6As-4Nd/HT9 diffusion couple that Fe is clearly diffusing into the fuel alloy at certain locations forming different U-Zr-Fe ternary phases within the interaction region. It is important to note that the intention of the As additive is to prevent lanthanide interactions with the cladding alloy, and no Fe-Nd interactions were observed in this study even with Nd-rich precipitates observed to form near the bonding interface. It should be further noted no NdAs precipitates were observed at the bonding interface, which would be more ideal to evaluate the stability of such precipitates in the presence of Fe. However, based on the results here the NdAs phase does appear to be stable. Additionally, it is unknown at this time why Fe diffuses so readily into the U-10Zr-2.6As-4Nd fuel alloy when its diffusion was not observed to have occurred in previous diffusion experiments carried out with Sb- and Te-containing fuel alloys. However, the diffusion of Fe into the U-Zr-As-Nd alloy should not be used as a reason to discount the effectiveness of As as an additive and further experimentation should be carried out to continue to investigate its efficacy to mitigate FCCI in U-Zr fuels.

References

[1] R. Khanal, N. Jerred, M.T. Benson, D.A. Andersson, R.D. Mariani, I. Charit, S. Choudhury, A novel approach to selection of dopant to immobilize neodymium in uranium-based metallic fuels, Journal of Nuclear Materials. 529 (2020) 151922. https://doi.org/10.1016/j.jnucmat.2019.151922.

[2] R. Khanal, N. Jerred, M.T. Benson, Y. Xie, R.D. Mariani, Interactions and immobilization of lanthanides with dopants in uranium-based metallic fuels, Journal of Nuclear Materials. 540 (2020) 152372. https://doi.org/10.1016/j.jnucmat.2020.152372.

[3] R. Khanal, N. Ayers, N. Jerred, M.T. Benson, R.D. Mariani, I. Charit, S. Choudhury, Role of zirconium in neodymium-dopants interactions within uranium-based metallic fuels, Nuclear Materials and Energy. 26 (2021) 100912. https://doi.org/10.1016/j.nme.2021.100912.

[4] WebElements Periodic Table, University of Sheffield. (n.d.). https://webelements.com (accessed January 14, 2021).

[5] R.D. Mariani, D.L. Porter, T.P. O'Holleran, S.L. Hayes, J.R. Kennedy, Lanthanides in metallic nuclear fuels: Their behavior and methods for their control, Journal of Nuclear Materials. 419 (2011) 263–271. https://doi.org/10.1016/j.jnucmat.2011.08.036.

[6] D.D. Keiser Jr., Metal fuel-cladding interaction, Comprehensive Nuclear Materials. 3 (2012) 423–441. https://doi.org/10.1016/B978-0-08-056033-5.00067-7.

[7] W. Zhuo, Y. Xie, M.T. Benson, Q. Yang, R.D. Mariani, J. Zhang, Experimental investigation of FCCI using diffusion couple test between UZr fuel with Sb additive and cladding, Nuclear Science and Engineering. (2020) 1–15. https://doi.org/10.1080/00295639.2020.1713656.

[8] Y. Xie, J. Zhang, M.T. Benson, R.D. Mariani, Diffusion behavior of lanthanide-additive compounds (Ce 4 Sb 3 , Ce 2 Sb, and CeTe) against HT9 and Fe, Materials Characterization. 150 (2019) 107–117. https://doi.org/10.1016/j.matchar.2019.02.012.

[9] G.W. Egeland, R.D. Mariani, T. Hartmann, D.L. Porter, S.L. Hayes, J.R. Kennedy, Reducing fuel-cladding chemical interaction: The effect of palladium on the reactivity of neodymium on iron in diffusion couples, Journal of Nuclear Materials. 432 (2013) 539–544. https://doi.org/10.1016/j.jnucmat.2012.07.028.

[10] G.W. Egeland, R.D. Mariani, T. Hartmann, D.L. Porter, S.L. Hayes, J.R. Kennedy, Reduction of FCCI effects in lanthanide-iron diffusion couples by doping with palladium, Journal of Nuclear Materials. 440 (2013) 178–192. https://doi.org/10.1016/j.jnucmat.2013.04.060.

[11] M.T. Benson, L. He, J.A. King, R.D. Mariani, Microstructural characterization of annealed U-12Zr-4Pd and U-12Zr-4Pd-5Ln: Investigating Pd as a metallic fuel additive, Journal of Nuclear Materials. 502 (2018) 106–112. https://doi.org/10.1016/j.jnucmat.2018.02.012.

[12] D.E. Janney, T.P. O'Holleran, Zr inclusions in actinide-Zr alloys: New data and ideas about how they form, Journal of Nuclear Materials. 460 (2015) 13–15. https://doi.org/10.1016/j.jnucmat.2015.01.065.

[13] K.A. Gschneider Jr., F.W. Calderwood, As-Nd (Aresenic-Neodymium), in: T. Massalski, H. Okamoto, P. Subramanian, L. Kacprzak (Eds.), Binary Alloy Phase Diagrams, II, ASM International, 1990.

[14] S. la Placa, ICDD, New York, 1959.

[15] F.H. Spedding, A.H. Daane, K.W. Herrmann, The crystal structures and lattice parameters of high-purity scandium, yttrium and the rare earth metals, Acta Crystallographica. 9 (1956) 559–563. https://doi.org/10.1107/S0365110X5600156X.

[16] J.B. Taylor, L.D. Calvert, J.G. Despault, E.J. Gabe, J.J. Murray, The rare-earth arsenides: Non-stoichiometry in the rocksalt phases, Journal of the Less Common Metals. 37 (1974) 217–232. https://doi.org/10.1016/0022-5088(74)90038-1.

[17] J.M. Silcock, Intermediate phase in the uranium-zirconium system, Transaction of AIME. 209 (1957) 521.

[18] M.J. Cooper, The analysis of powder diffraction data, Acta Crystallographica Section A. 38 (1982) 264–269. https://doi.org/10.1107/S0567739482000564.

[19] I.K. Suh, H. Ohta, Y. Waseda, High-temperature thermal expansion of six metallic elements measured by dilatation method and X-ray diffraction, Journal of Materials Science. 23 (1988) 757–760. https://doi.org/10.1007/BF01174717.

[20] K. Nakamura, M. Kurata, T. Ogata, A. Itoh, M. Akabori, Equilibrium phase relations in the U–Zr–Fe ternary system, Journal of Nuclear Materials. 275 (1999) 151–157. https://doi.org/10.1016/S0022-3115(99)00116-6.

[21] K. Nakamura, T. Ogata, M. Kurata, A. Itoh, M. Akabori, Reactions of U–Zr alloy with Fe and Fe–Cr alloy, Journal of Nuclear Materials. 275 (1999) 246–254. https://doi.org/10.1016/S0022-3115(99)00227-5.

CONCLUDING REMARKS

This research work was initially focused on evaluating both antimony (Sb) and tellurium (Te) as potential additives for the U-Zr fuel system to mitigate the deleterious effects of the fuel cladding chemical interaction (FCCI) phenomenon. Because previous research has shown lanthanides as being the most problematic solid fission products in FCCI, neodymium (Nd) was also utilized in this research to evaluate additive-lanthanide interactions. Further, atomistic-based modeling based on the density functional theory (DFT) method was used to identify other potential additives. Based on electronic structure and enthalpy of mixing calculations, both arsenic (As) and selenium (Se) were found to exhibit a favorable tendency to bind with lanthanide fission products. Although initial experimental work was carried out with both As and Se, more extensive experimentation reported in this work was carried out with As.

It was necessary to develop a baseline understanding for the propensity of Nd to interact with the cladding alloy HT9. Prior research by others demonstrated Nd interacts strongly with elemental iron (Fe) through Nd/Fe diffusion couple experiments. Similar research was performed here, i.e. Nd/Fe diffusion couple experiments, but was also expanded to include isothermal diffusion experiments between elemental Nd and HT9. It was found that even against HT9, Nd strongly interacts with Fe to form two distinct phases at the diffusion interface, $Fe_{17}Nd_2$ and $Fe_{17}Nd_5$. When Nd was alloyed directly with Sb, i.e. Sb-Nd alloy, and diffusion experiments were again carried out against HT9, no interaction between the two alloys was observed indicating the stabilizing effects that Sb has on Nd.

Progressing into fuel-based experiments it was critical to extensively evaluate the interactions of both the additives and additive-lanthanide compounds within the U-Zr matrix. First, it is important to evaluate the U-Zr-X alloys, where ‘X’ denotes the additive component, in order to gain an understanding of how the additive will interact with the matrix in a *fresh fuel* condition. In evaluating Sb and Te, both additives showed preferential interaction with Zr within the U-Zr matrix. Research by others on alternative additives, e.g. Sn and Pd, have also demonstrated a similar propensity for those additives to bind with Zr within a U-Zr-X alloy. A U-Zr-As alloy was not evaluated directly in this research and thus it is difficult to determine

exactly how As will form within the U-Zr matrix. However, it should be noted that experimental work was carried out to evaluate U-As-Nd alloys, i.e. without Zr in the matrix, and As was observed to bind with U is some instances (Appendix B.2). Thus, it is not guaranteed that As would interact with Zr in a U-Zr-X alloy, however, in later experiments evaluating U-Zr-As-Nd alloys (Chapter 5), no interactions were observed between As and Zr nor between As and U. Regarding the implications of additives interacting with Zr, it should be understood that the use of Zr within the U-10Zr (wt.%) fuel system is to primarily elevate the solidus temperature of the alloy. As a result, X-Zr interactions would remove Zr from the U-Zr matrix, which can be detrimental to the fuels in-reactor performance. To compensate for the potential loss of Zr from alloying with U, the concentration of Zr will need to be increased the degree of which may likely be additive dependent. Thus, although the X-Zr interaction is problematic, it is not entirely detrimental, as the fuel alloy can be adjusted accordingly. Evaluation of U-Zr-X alloys was followed by fabricating U-Zr-X-Nd alloys, to evaluate additive-lanthanide interactions within the U-Zr matrix. The alloys evaluated included U-Zr-Sb-Nd, U-Zr-Te-Nd and U-Zr-As-Nd, and each exhibited strong additive-lanthanide interaction where SbNd/Sb_3Nd_4, TeNd, and NdAs phases were all observed to form, respectively. In the case of each alloy, these X-Nd phases exhibit favorable formation energies and high temperature stability having melting temperatures of 2203 K (SbNd), 2298 K (TeNd) and 2473 K (NdAs). Further, annealing experiments of the U-Zr-X-Nd alloys in excess of 948 K resulted in no observed degradation of these X-Nd phases, an indication of their thermodynamic stability within the U-Zr matrix. In some of the U-Zr-X-Nd alloys, X-Zr interactions were still observed to form, e.g. Zr_2Sb, Zr_2Te and Zr_3Te, but only where X-Nd compounds were also observed, i.e. no elemental Nd was observed. Therefore, formation of X-Zr compounds within U-Zr-X-Nd alloys suggests that these alloys were likely additive-rich and X-Zr compounds would form only after X-Nd compounds and sufficient additive concentrations remained in the alloy. Further, when elemental Nd was observed only X-Nd compounds were observed to have formed. In these instances, the alloys were likely additive-poor. Therefore, this is most likely an indication of the preferential binding of Sb, Te and As with Nd. This was further supported through enthalpy of mixing calculations, which indicated the X-Nd interaction is highly favorable within the U-Zr matrix.

To further evaluate the the efficacy of the additives to stabilize Nd within the U-Zr matrix, isothermal diffusion couple experiments were carried out between U-Zr-X-Nd alloys and HT9 and then compared against isothermal diffusion couple experiments between U-Zr-Nd and HT9. In the case of the latter experiments, Nd precipitates located on the diffusing interface were observed to somewhat interact with the Fe constituent of the HT9 alloy, although their interaction did not lead to the formation of stoichiometric Nd-Fe compounds. Additionally, Fe was observed to diffuse well into the U-Zr-Nd alloy forming an interaction region in excess of 60 μm, where the δZr_2U phase was notably absent and the formation of several U-Zr-Fe ternary phases were observed. Further, the diffusion and interaction of U with Fe was also observed with the formation of a distinct UFe_2 phase at the diffusing interface. In the execution of diffusion couple experiments with additive-containing fuel alloys, the observed interactions changed drastically. In the case of Sb and Te additives, the formation of X-Nd phases were observed within the fuel alloy but no interaction was observed to have occurred between any of these phases and HT9 constituents. Further, the formation of a robust Zr-rich layer directly at the interface was observed, which is believed to have limited the diffusion of Fe into the fuel alloy. It has previously been documented that the formation of a Zr layer at the diffusing interface can act as a diffusion barrier and deter interaction between the alloys. However, it is not understood why the layer was so prevalent within the additive-containing fuel alloys and not in the U-Zr-Nd alloy, although a small Zr-rich layer was observed to form in the latter experiment as well. One theory is the additive-based fuel alloys may contain a higher concentration of impurities, such as nitrogen, which has been documented to stabilize the Zr-rich layer and thus more effectively limit the diffusion of Fe. It is also plausible that the presence of Sb and Te within the matrix phases is affecting the thermodynamic drive of Fe to diffuse into the fuel alloy. More extensive analysis and experimentation is needed to fully investigate these observed variations and to fully determine how these additives, once alloyed within the fuel, affect the diffusion of Fe. In the case of diffusion experiments containing the As additive, no interaction was observed to occur between Nd and HT9 constituents and a Zr-rich layer was again observed to have formed. However, Fe was observed to have diffused well into the fuel alloy at some locations along the diffusion interface forming an interaction region measuring up to ~70 μm wide, but the level of Fe diffusion was not consistent through the diffusion couple. Within regions that exhibited

the greatest level of Fe diffusion, U-Zr-Fe ternary phases were again observed to have formed but Fe was not observed to interact with NdAs precipitates also present within the region. Additionally, no interaction between U and Fe was observed in the U-Zr-As-Nd diffusion experiments.

Overall, the use of fuel-based additives continues to show promise with only slight adjustments likely needed in the Zr content of the U-10Zr (wt.%) fuel alloy. With respect to the lanthanide Nd, all three additives evaluated in this work, Sb, Te and As, show promise, but additional work is needed to evaluate their interactions with other lanthanide elements, i.e. cerium (Ce), praseodymium (Pr) and lanthanum (La). Both Sb and Te were evaluated as additives in the presence of Ce by a separate research group. In their evaluation, they found that Sb would preferentially bind with Ce, exhibiting similar favorable results to what was observed here with Nd. However, in their evaluation of diffusion experiments between a U-Zr-Te-Ce alloy and HT9, the interaction of Te and Cr was observed at the diffusing interface, indicating Te may not be ideal for binding Ce. As for arsenic, this work indicates As may also be a promising candidate to mitigate FCCI, but additional experiments should be carried out. Overall, Sb exhibits great promise as a fuel-based additive and through this research it has demonstrated a strong interaction with Nd both as a standalone alloy, e.g. Sb-Nd, and within the U-Zr matrix. Due to its promise as an additive, a separate research program will irradiate a U-Zr-Sb fuel alloy to evaluate the effectiveness of Sb under irradiation conditions. As part of the Advanced Fuels Campaign (AFC) Fission Accelerated Steady-State Test (FAST) series of experiments, an experimental U-Zr-Sb fuel alloy will be irradiated in the Advanced Test Reactor (ATR) at Idaho National Laboratory (INL) in the coming years.

FUTURE WORK AND RECOMMENDATIONS

In continuing research from where this work ends, there are a few areas that are noteworthy. In this research, the additive interactions were only evaluated against Nd. Although Nd is found to form in the greatest concentration as a solid fission product in the U-Zr fuel system, Ce, Pr and La also form as fission products in appreciable concentrations. As previously stated, both Sb and Te have been evaluated with respect to Ce, but research should be undertaken with respect to Pr and La. Although it is largely believed that Pr and La will behave in a similar manner as Nd and Ce, respectively, *out-of-pile* experiments should be carried out nonetheless. This work should then progress into evaluating the interaction of additives within U-Zr having a combined concentration of Nd, Ce, Pr and La all alloyed at their expected formation concentrations. This is especially needed for As being a newly proposed additive.

The primary alloy fabrication method used in this experiment was arc melting, which can be a difficult processing method to gather critical processing conditions when executed, e.g. alloying temperature, cooling rate, etc. Accurate measurement of such conditions can aid in better understanding the thermodynamics of the alloying process. Thus, additional work may consider how to incorporate the measurement of such conditions during the fabrication process. Additionally, metallic fuel slugs were historically fabricated through injection casting processes and there are some thoughts that the fabrication process may play a factor in its susceptibility to FCCI. Therefore, additional fabrication methods could be evaluated to carry out a sensitivities study on the effects the fabrication process has on a fuels FCCI performance.

This research, and most research work to-date incorporating fuel-based additives, has focused on the additive-lanthanide interactions within the U-Zr matrix. However, as work progresses in this area, it will be important to understand the macro effects the additive additions have on the overall performance of the fuel alloy. In particular, metal fuel systems, such as U-10Zr (wt.%), are favorable due to their exceptional thermal properties and thus understanding how such alloying additions affect these properties will be of importance.

This work performed isothermal diffusion-based experiments exclusively, however, such experimental conditions do not fully capture the thermal conditions of the fuel and

cladding structure within a reactor system. Specifically, reactor systems exhibit thermal gradients extending radially outward from the fuel centerline, where it is hottest, to the cladding surface, where it is coldest. Such thermal conditions can induce different diffusion kinetics compared to isothermal-based experiments. In particular, lanthanide transport through the fuel and into the cladding appears to be strongly dependent on such thermal gradients. Thus, it is recommended that additional diffusion experiments be carried out, which incorporate prototypic thermal gradients. It is likely that such experiments would require development of unique equipment to simulate such thermal conditions. The lack of thermal gradients and use of isothermal conditions in this research, for example, is believed to have resulted in a lack of drive for Nd to migrate into the HT9 alloy, which in-turn led to only limited interaction between Nd and HT9 being observed. Although Fe diffusion into the fuel alloy was observed, the limited Nd-HT9 interaction reduced the baseline understanding of this study, i.e. interactions of U-Zr-Nd alloy and HT9. This in-turn limited the full understanding of the effectiveness of the additives being evaluated. It is believed that different results would have likely been observed if the thermal conditions were more prototypic of a reactor system.

Finally, evaluating additive-based fuels contained within claddings, e.g. HT9, under irradiation conditions will be necessary to fully capture the complex kinetics and thermodynamics of a reactor system. Such experiments would lead to lanthanides being burned-in to the fuel and thus lead to the FCCI phenomenon. Furthermore, such reactor conditions can induce changes in the kinetics behavior of the different materials, e.g. radiation enhanced diffusion (RED), which will be important to capture and better understand. However, prior to executing targeted irradiation experiments in reactors such as ATR, ion-based irradiation experiments can be performed first as scoping studies. Although such experiments would not capture the thermal conditions or the diffusion kinetics of a reactor system, they can be used to further evaluate the irradiation properties of additive-based fuel alloys. Such experiments can provide initial insight into the irradiation effects on additives in a fresh fuel condition, i.e. U-Zr-X, and on the additive-lanthanide interactions within fuel alloys containing lanthanides, i.e. U-Zr-X-Ln. Ion irradiation experiments would further facilitate the measurement of important fuel performance metrics, such as fuel swelling, thermal conductivity, etc., on additive-based fuel alloys; building a knowledge-base on their expected in-reactor performance.

Overall, the fuel metrics gleaned through post irradiation examination (PIE) of such irradiation experiments will be quite useful in understanding the performance of additives within metal fuel systems. Additionally, PIE observations can be used in conjunction with the Nuclear Energy Advanced Modeling and Simulation (NEAMS) program to validate fuel-performance modeling and simulation codes. This will lead to an overall improvement in the effective use of such codes, which will be even more important as fuel-based additives inevitably become more widely explored.

APPENDICES

Appendix A

Chapter 4 Supplemental Information

Evaluation of Sb-Nd and Te-Nd Phases within the U-Zr Fuel Matrix and their Interactions with HT9

Figure A-1 shows SEM micrographs of a large precipitate found in the U-10Zr-3.6Sb-4Nd (Sb-Nd) alloy in its as-cast condition. Results of the EDS point analysis locations depicted in Figure A.1 (b) can be found in Table A.1.

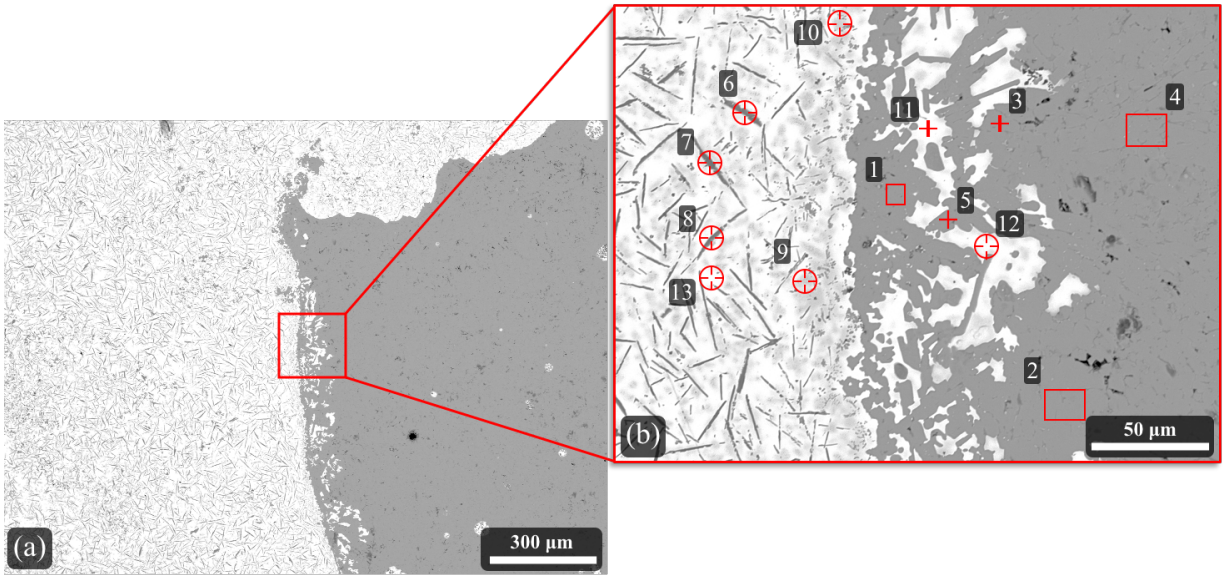

Figure A.1. (a) and (b) BSE micrographs of the large precipitate found in the as-cast Sb-Nd alloy. EDS point analysis results can be found in Table A.1.

Table A.1. EDS points analysis results, in at.%, of the locations depicted in Figure A.1 (b).

Pt.	U	Zr	Sb	Nd	Phase[a]	Pt.	U	Zr	Sb	Nd	Phase[a]
1	0.2	4	30	66	$SbNd_2$	**8**	13	55	29	2	Zr_5Sb_3/Zr_2Sb
2	0.2	6	29	65	$SbNd_2$	**9**	55	40	4	0.6	$U\text{-}Zr^b$
3	0.1	4	29	67	$SbNd_2$	**10**	56	41	2	0.8	$U\text{-}Zr^b$
4	0.2	6	28	66	$SbNd_2$	**11**	84	12	3	1	$\alpha\text{-}U$
5	0.6	4	30	66	$SbNd_2$	**12**	79	17	3	0.8	$\alpha\text{-}U$
6	10	56	31	3	Zr_5Sb_3/Zr_2Sb	**13**	79	16	3	1	$\alpha\text{-}U$
7	5	59	33	3	Zr_5Sb_3/Zr_2Sb						

[a]*suggested phase based on EDS results*

XRD analysis was performed in the vicinity of the large precipitate observed in Figure A.1 and the results are shown in Figure A.2. Additional crystallographic information of indexed phases can be found in Table A.2.

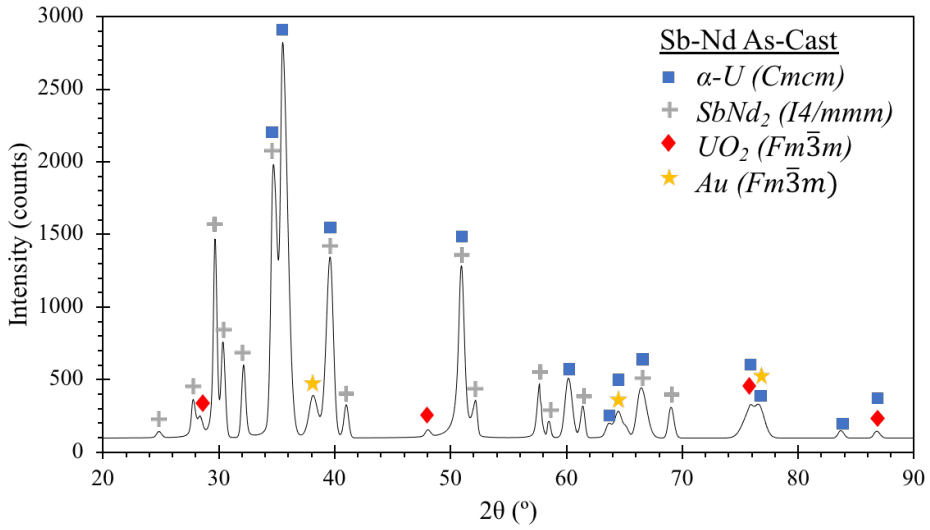

Figure A.2. XRD results of the Sb-Nd alloy in a region near the large precipitate imaged in Figure A.1.

Table A.2. Crystallographic information of phases identified through XRD analysis in Figure A.2.

Compound	Space Group, Structure	Cell Parameters
α-U [1]	Cmcm (63), orthorhombic	a = 0.2854, b = 0.587, c = 0.496 [nm] $\alpha = \beta = \gamma = 90°$
$SbNd_2$ [2]	I4/mmm (139), tetragonal	a = b = 0.451, c = 1.758 [nm] $\alpha = \beta = \gamma = 90°$
UO_2 [3]	$Fm\bar{3}m$ (225), cubic	a = b = c = 0.548 [nm] $\alpha = \beta = \gamma = 90°$
Au [4]	$Fm\bar{3}m$ (225), cubic	a = b = c = 0.408 [nm] $\alpha = \beta = \gamma = 90°$

Figure A.3 (a) shows a SEM micrograph of the U-10Zr-4Nd (wt.%) base material section of the Nd/HT9 diffusion couple sample. The micrograph depicts the alloys microstructure after annealing at 675ºC for 96h. EDS elemental maps of the region imaged in Figure A.3 (a) can be found in Figure A.3 (b).

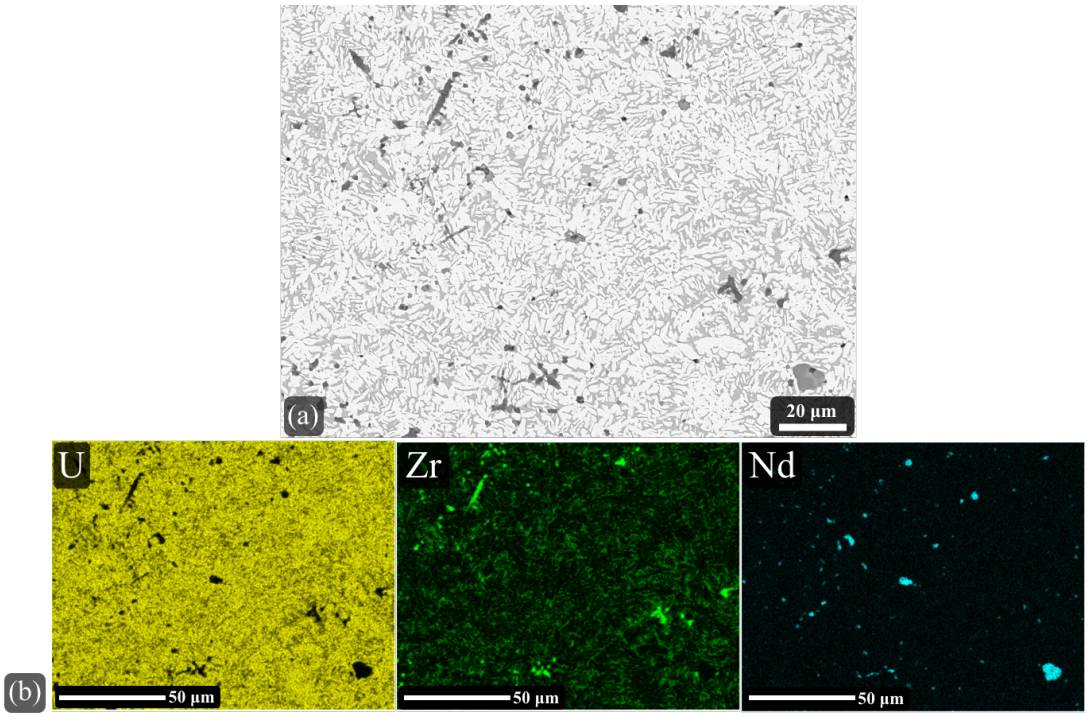

Figure A.3. (a) BSE micrograph of the Nd/HT9 diffusion couple in the annealed section of the U-10Zr-4Nd (wt.%) alloy well away from the diffusion interface. (b) EDS elemental maps of the region in (a).

References

[1] G. H. Lander and M. H. Mueller, Neutron diffraction study of α-uranium at low temperatures, *Acta Cryst. Sect. B.* 26(2):129–136, 1970. https://doi.org/10.1107/S0567740870002066

[2] J. Nuss and M. Jansen, Crystal structure of dineodymium antimonide, Nd_2Sb, *Z. Kristallogr. NCS* 220(1–4):529–530, 2005. https://doi.org/10.1524/ncrs.2005.220.14.559

[3] V. M. Goldschmidt and L. Thomassen, Geochemische Verteilungsgesetze der Elemente III Die Kristallstruktur Natürlicher und Synthetischer Oxyde von Uran, Thorium und Cerium, *Skr. Nor. Visensk.-Akad. Mat.-Nat.* 2:1–48, 1923.

[4] H. Swanson and E. Tatge, Standard x-ray diffraction patterns (gold), *Natl. Bur. Stand. (U.S.)* circ. 539, vol. 1, pp.33, 1953.

Appendix B
Experimental Validation of Arsenic and Selenium as Additives

B.1 Introduction

Through the research program that funded this work, atomistic modeling was carried out to evaluate other potential additives beyond antimony (Sb) and tellurium (Te). This effort led to the identification of both arsenic (As) and selenium (Se) as potential additives for lanthanide fission products. Although the modeling effort was carried out by others within the research group and therefore is not fully contained within this dissertation, experimental-based work was carried out to aid in validating these efforts which is provided in the subsequent sections of this appendix.

Initially, the modeling work aimed to simplify the calculations by eliminating zirconium (Zr) from the modeling matrix, i.e. evaluate just U-X-Nd alloys, where 'X' denotes the additive. This was done to isolate the interactions of the additives and lanthanides within the uranium (U) matrix with the primary lanthanide being neodymium (Nd). As a result, the As-Nd interactions within the uranium matrix observed experimentally matched the calculations. This was then followed by experimental work to validate Se-Nd interactions as well as validate As and its tendency to interact with cerium (Ce), being another prominent lanthanide element to form within U-Zr fuel at significant concentrations. Although a specimen containing Se was eventually fabricated, its use proved to be challenging as significant vaporization losses of the element would occur during the arc melting process. However, with the promising results observed with As, in the presence of both Nd and Ce, more extensive modeling was carried out to incorporate Zr, i.e. evaluation of a U-Zr-As-Nd alloy. Thus, experimental work was carried out to evaluate As-Nd interactions within the U-10Zr (wt.%) matrix. Initial experimental work carried out on a U-Zr-As-Nd alloy was aimed at validating the latest modeling efforts, but the encouraging results culminated into more extensive experiments being carried out with the alloy which is detailed in Chapter 5.

The subsequent sections contain excerpts, detailing the experimental work only, from corresponding journal publications. The journal publications should be further reviewed for additional context on the modeling efforts.

B.2 Experimental Evaluation of U-As-Nd Alloy

Excerpt of manuscript published in Journal of Nuclear Materials in December 2019.
"A novel approach to selection of dopant to immobilize neodymium in uranium-based metallic fuels." *J. Nucl. Mater.* 529:151922 (2020). https://doi.org/10.1016/j.jnucmat.2019.151922
0022-3115

B.2.1 Experimental results and discussion

In-reactor conditions lead to the continuous generation of fission products, such as Nd, within the U-matrix. In order to verify the formation of *ab-initio* predicted Nd-As intermetallic and its stability within the U-matrix, two alloys were cast alloy1, U-4As-4Nd (wt.%) and alloy2 U-2As-4Nd (wt.%). Alloy1, representing initial stages of the formation of fission products when the externally added concentration of dopant As is higher than Nd (Nd:As atomic ratio of 1:2) and alloy2 with equal atomic ratio of As to Nd (Nd:As atomic ratio of 1:1) representing later stage of the formation of fission product. Backscattered electron (BSE) SEM images (Figure B-1(a-b)) of these U-Nd-As alloys reveals the formation of two precipitated phases within the matrix, dark-grey and light-grey precipitates. The precipitated phases are observed to be evenly distributed throughout the microstructure and range in size between 5 to 20 μm. EDS point chemical analysis was conducted on several precipitates of interest in both the alloys; selected points are shown in Figure B-1 (a) and (b); the corresponding compositions of each analysis point are listed in Table B-1. The dark-grey precipitates are found to be consisted of Nd and As at roughly a 1:1 atomic ratio; indicating that they are likely the NdAs phase. The light-grey precipitates consisting of U and As and are observed to bind at an atomic ratio of roughly 3:4 (or possibly 1:1), which would correspond to the U_3As_4 (or UAs) phase. Based on our *ab-initio* calculated negative enthalpy of mixing for As in the α-U matrix is $\approx$ -1eV, as compared to greater negative mixing enthalpy of As in Nd-U matrix (-4.26 eV), it is intuitive that in alloy1 any excess As remains after binding with Nd may form compound with U matrix. For the same reason no U-As compound is observed in alloy2, which has a lower As content

than Nd, Table B-1. Overall, the presence of the NdAs precipitates in both these alloys indicate its formation is more favorable within the U matrix. Based on the results of mixing enthalpy and the experimental observations in both alloy1 and alloy2, we suggest that for in-reactor applications, U-based alloys should have excess As compared to the expected Nd generated at maximum burnup. From thermodynamic consideration it is expected that as Nd is continuously generated within the matrix, As would be released from the U and bind with Nd, as seen from the preference of As for Nd over U from our calculated enthalpy of mixing of As in U and Nd-U matrix. Finally, it should be pointed out that NdAs, U_3As_4, and UAs phases are stable, equilibrium phases as found in their corresponding binary phase diagrams[1,2].

For accurate identification of the phases formed in these U-Nd-As alloys (Figure B-1(c) and (d)) XRD was performed. Beside confirming the EDS point chemical analysis predicted formation of NdAs phase, diffraction data confirms that the U-As precipitates observed in the alloy1 sample are actually comprised of the UAs phase (1:1 atomic ratio) with peaks indexed at of 2θ angles of 30.8° and 44.0°. In analyzing the diffraction pattern of the alloy2, a peak is identified for the NdAs phase at the 2θ angles of 29.8° which is better observed in the inset of Fig. B-1 (d). Due to their proximity, the NdAs peak could not to be completely deconvoluted from the α-U peak, which is at 30.3°; nevertheless, its existence can still be discerned. Overall, the formation of NdAs intermetallic compound in both these alloys is further verified by our elemental EDS mapping as presented in the supplementary information section of the corresponding journal publication. It should be pointed out that the SEM image of alloy2 (Figure B-1(b)) also indicates numerous sub-micron sized round precipitates. Our elemental EDS maps of Nd and As reveal that these sub-micron precipitates have only high concentration of Nd and no As. Given our *ab-initio* calculated positive enthalpy of mixing (4.26 eV) of Nd in U, no Nd-U phase is expected to form. However, higher resolution analysis techniques would be necessary to infer the elemental compositions of such precipitates accurately.

References from journal publication:

[1] [20] J.K.A Gschneidner and F. Calderwood, The As-Nd (Arsenic-Neodymium) System, *Bull. Alloy Phase Diagr.,* 7 (1986) 345–346

[2] [21] H. Okamoto, As-U (Aresnic-Uranium), *Binary Alloy Phase Diagrams II,* 1 (1990) 330–334

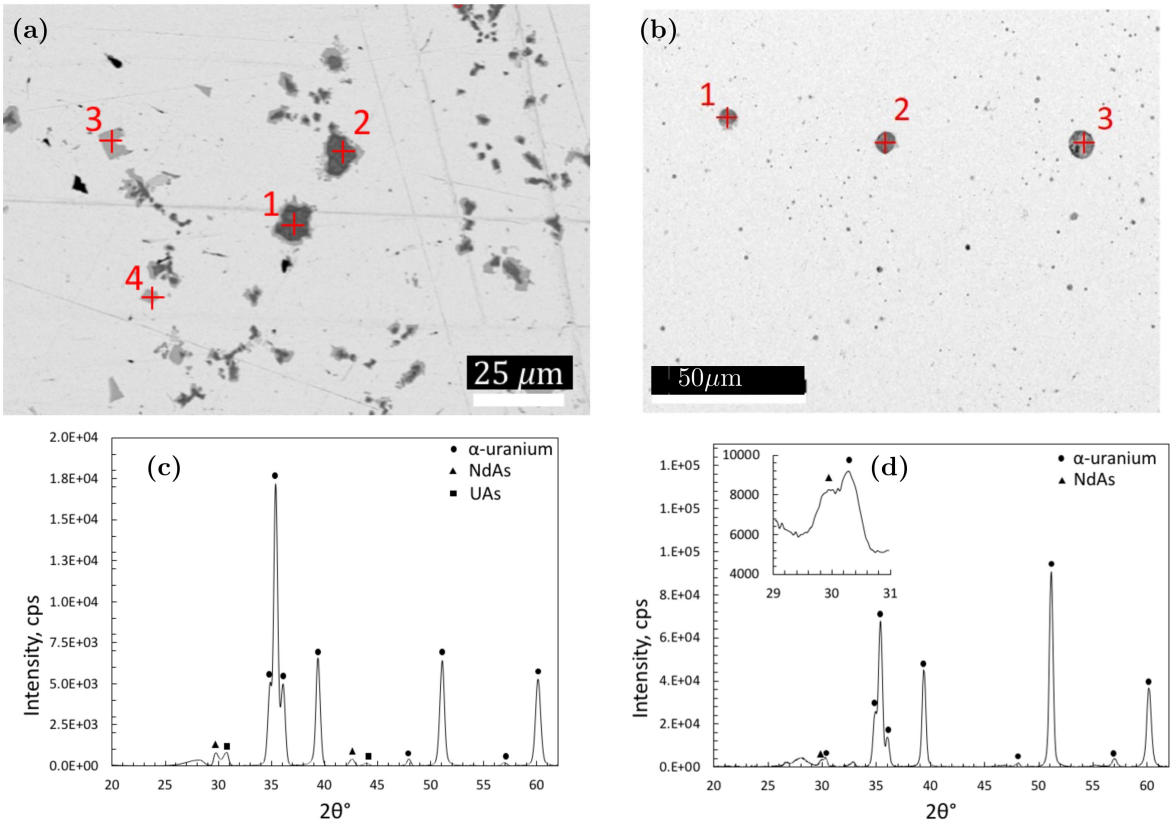

Figure B.1. Backscattered electron SEM image indicating locations of EDS point analysis (a) alloy1 (92U4Nd-4As, wt.%) (b) alloy2 (94U-4Nd-2As, wt.%). XRD patterns of (c) alloy1 and (d) alloy2 samples.

Table B.1. EDS point analysis compositions of precipitates (at.%) in reference to Fig. B.1 (a) alloy1 (92U-4Nd-4As, wt.%) and (b) alloy2 (94U-4Nd-2As, wt.%).

Alloys	Pt #	Precipitate	U	Nd	As	Suggested Phase
alloy1	1	dark grey	4	45	50	*NdAs*
	2	dark grey	5	45	50	*NdAs*
	3	light grey	43	2	55	*UAs*
	4	light grey	44	1	55	*U_3As_4 or UAs*
alloy2	1	dark grey	4	52	45	*NdAs*
	2	dark grey	0	57	43	*NdAs*
	3	dark grey	1	59	40	*NdAs*

In this study, using *ab-initio* calculations, we have developed simple alloy design principles primarily based on electronic configurations, electronegativities and covalent radius of elements involved. These principles were used to demonstrate the tendency of externally

added dopants to form intermetallic within a metallic matrix in a more comprehensive manner than typically used thermodynamic approaches such as Hume-Rothery rules or Darken-Gurry map. The uniqueness of our guiding principles is that they are based on readily available elemental features without creating complicated binary/ternary phase-diagrams, as previously needed. We showed that our proposed principles are successful in correctly identifying previously known effective dopants such as Pd, Sb and less effective ones such as Tl to form intermetallic within the U-matrix. Also, guided by the same principles we identified two highly effective novel dopants, namely, As and Se as potential dopants and experimentally verified the compound forming tendency of Nd with As inside the U-matrix.

B.3 Experimental Evaluation of U-Se-Nd and U-As-Ce Alloys

Reproduced from section of manuscript published in the Journal of Nuclear Materials in June 2020.
"Interactions and immobilization of lanthanides with dopants in uranium-based metallic fuels." *J. Nucl. Mater.* (2020). https://doi.org/10.1016/j.jnucmat.2020.152372.

B.3.1 Characterization of U-2.1Se-3.8Nd alloy

The 2Se alloy was cast by arc melting and later characterized using backscatter electron (BSE) and energy-dispersive X-ray spectroscopy (EDS). A BSE image of the periphery region of the 2Se alloy is shown in Figure B.2. The EDS map analysis indicates the grey-contrast area that has formed at the periphery of the alloy is the combination of Nd and Se. EDS point analysis was also conducted to determine the approximate ratio of the Nd and Se elements within the grey-contrast region. The point analysis locations are indicated on the BSE image in Figure B.2, the results of which are shown in Table B.2. The EDS point analysis indicates the grey-contrast region is comprised primarily of Nd and Se at an atomic ratio of between 2:1 and 1.5:1 (Nd:Se), indicating the phase is Nd-rich. However, our literature search does not indicate the existence of an equilibrium Nd-Se phase that is Nd-rich.

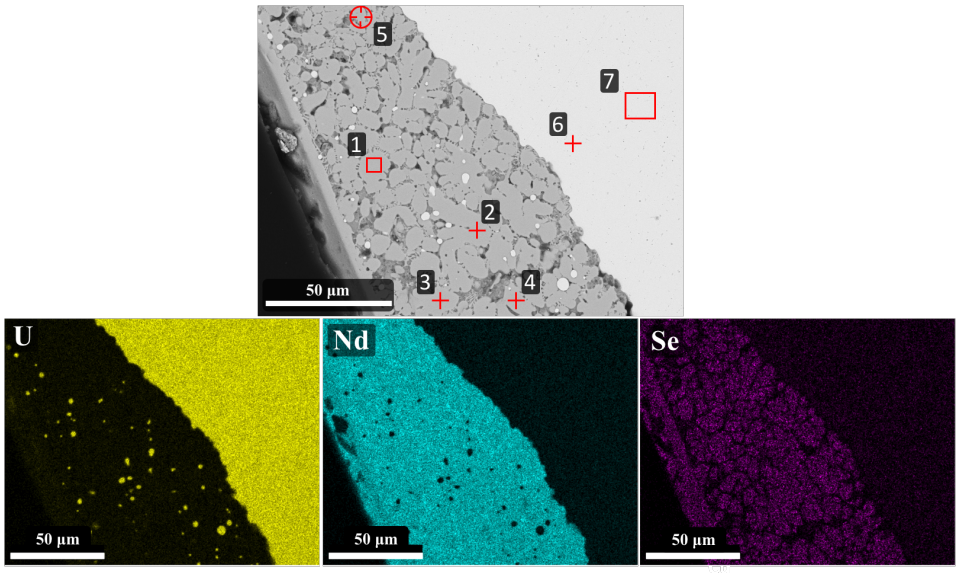

Figure B.2. BSE SEM image of the 2Se alloy, (a), with elemental maps, (b)–(d). Elemental map analysis was conducted at higher magnification on a portion of the grey-contrast region of (a). Corresponding EDS point data listed in Table B-2.

Table B.2. EDS point (Pt.) analysis compositions of locations (atom %) identified in the BSE image shown in Figure B.2 (a).

Pt. #	U	Nd	Se	Ratio (Nd:Se)	Pt. #	U	Nd	Se	Ratio (Nd:Se)
1	0.1	66	34	~2:1	5	0.1	60	40	~1.5:1
2	0.4	62	38	~1.6:1	6	95	1	4	n/a
3	0.1	60	40	~1.5:1	7	94	2	4	n/a
4	0.3	60	40	~1.5:1					

X-ray diffraction (XRD) was performed on the area of interest in the 2Se alloy to determine the Nd-Se phase. It is shown in the diffraction pattern of Figure B.3 that the Nd-Se phase formed is the NdSe phase (1:1 atomic ratio) with peaks at 30.2° and 43.2° 2θ angles. It should be noted, the peak observed at the 2θ angle of 30.2° is convoluted with an α-U peak, but the peak at the 2θ angle of 43.2° is only indexed with the NdSe phase and has been utilized to verify the grey-contrast region as the NdSe phase. The excess Nd within the grey-contrast region (beyond Nd:Se 1:1 ratio) may be a result of interaction volume during the EDS analysis or an indication of Nd dissolved in the NdSe phase. Investigation of the general matrix region of the 2Se alloy (Figure B.2 and Table B.2, locations # 6 and 7) revealed the Se and Nd concentrations were insignificant. It appears Se has strictly bonded with Nd to form the NdSe phase, at the periphery of the alloy as observed in Figure B.2. Se binding with Nd, to form the

NdSe phase, agrees with our DFT calculations, which indicated highly negative enthalpy of mixing, -4.18 eV, between each element.

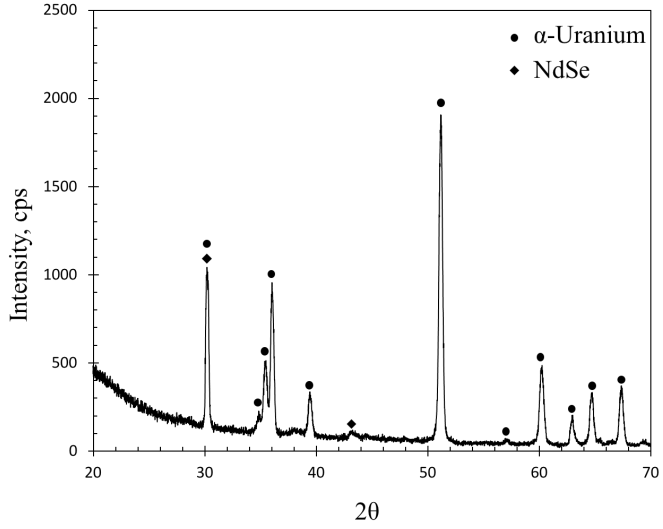

Figure B.3. X-ray diffraction pattern of the light grey-contrast region in the 2Se alloy confirming the formation of NdSe phase within α-U matrix.

B.3.2 Characterization of the U-3As-4Ce alloy

Figure B.4 shows BSE images of the 3As alloy (U-3As-4Ce, wt.%) along with the EDS elemental maps. Figure B.4 (a) indicates the formation of spheroidal precipitates within the general matrix of the alloy. The result of the EDS point analysis conducted on the various locations in Figure B.4 (a) is tabulated in Table B.3. The large spheroidal precipitates observed in Figure B.4 (a) appear to be the combination of multiple phases, making it a ternary compound microstructure and not a simple precipitate. For simplicity, however, these spheroidal regions will still be referred to as precipitates. Points # 1–5 indicate these areas consist of different Ce-As phases. Based on EDS analysis these phases appear to be either the CeAs or the slightly Ce-rich, Ce_4As_3 phase. Further analysis of these spheroidal precipitates observed in Figure B.4 (a) indicates a large portion of these precipitates appear to consist of pure Ce (points # 6–10). The presence of pure Ce was expected based on the positive enthalpy of mixing, of Ce in U-matrix. EDS elemental maps for the area imaged in Figure B.4 (a), are shown in Figure B.4 (b)–(d), which confirms the precipitate consist primarily of Ce, where As is present in parts of the precipitates.

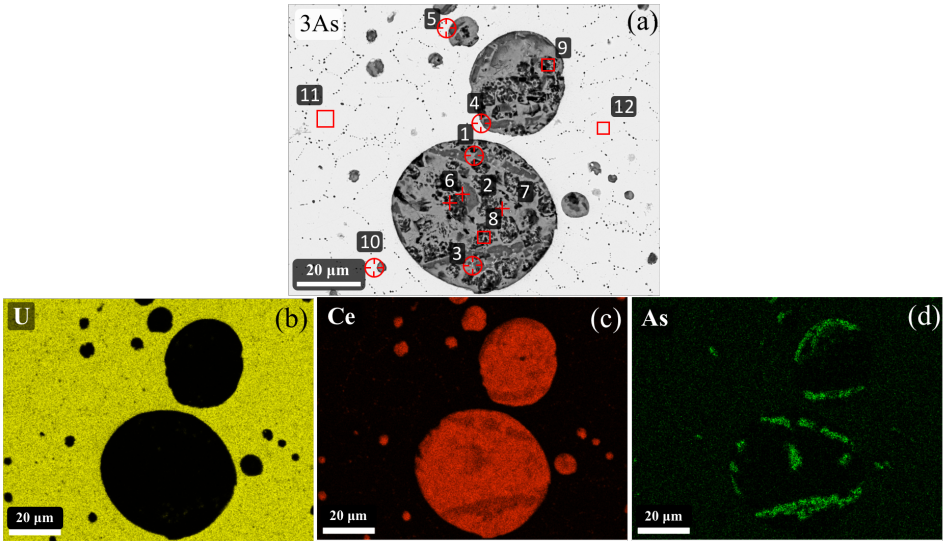

Figure B.4. Backscatter SEM image of the 3As alloy, (a), with elemental maps, (b)–(d). Corresponding EDS point data listed in Table B-3.

Table B.3. EDS point (Pt.) analysis compositions of locations (atom %) identified in the BSE images of Figure B.4 (a).

Pt. #	U (at.%)	Ce (at.%)	As (at.%)	Phase(s)[a]
1	0.1	56	44	*CeAs/Ce_4As_3*
2	0.1	53	47	*CeAs/Ce_4As_3*
3	0.1	52	48	*CeAs*
4	0.2	58	42	*Ce_4As_3*
5	0.1	50	50	*CeAs*
6	0.3	97	3	*Pure Ce*
7	0.8	98	1	*Pure Ce*
8	0.1	98	2	*Pure Ce*
9	0.1	98	2	*Pure Ce*
10	0.1	99	1	*Pure Ce*
11	96	0.3	4	*Pure U*
12	97	0.4	2	*Pure U*

[a]*suggested phase(s) induced by atomic ratios from EDS analysis*

To confirm phase formations in the 3As alloy, micro-XRD analysis was performed on the matrix region contained in the alloy. Figure B.5 contains the diffraction plots of the XRD analysis. The matrix region is mainly comprised of the α-U phase. It is also evident that CeAs precipitates is forming within the matrix region, likely formed as precipitates similar to those

shown in Figure B.4 (a). There are a few peaks in the diffraction pattern which indicate the formation of the Ce_4As_3 phase as well, but this phase is only slightly above the diffraction background. In addition to these phases, CeO_2 and UO_2 phases were also found, likely due to surface oxidation during analysis. Overall, the primary phase formations found in the matrix region of the 3As alloy are α-U and CeAs phases with a small amount of the Ce_4As_3 phase.

Experiments performed with Nd-Se and Ce-As confirm the formation of NdSe and CeAs phases inside the α-U matrix, as predicted by our DFT calculations. We also note that our calculated enthalpy of mixing of As and Se within the α-U matrix is -1.04 and -0.94 eV, respectively, whereas the enthalpy of mixing of As in Ce-U system is -1.21 eV and Se in Nd-U system is -4.18 eV. Due to the close value of the enthalpy of mixing of As in both the U-matrix and the U-Ce matrix, U-As phase can also form in the presence of Ce in the U-As-Ce system. In the case of the U-Nd system, we do not expect to form U-As/Se compounds in the presence of Nd due to a significant difference in enthalpy of mixing between As/Se in the U-matrix and the Nd-U matrix. However, diffusion couple experiments of UAs against the lanthanides may help to understand the comparative stability of U-As and Ln-As compounds.

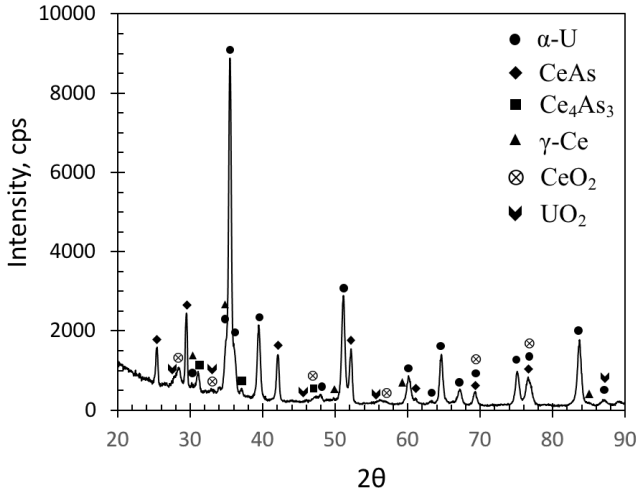

Figure B.5. XRD diffraction plots of the 3As alloy shown in Figure B.4 confirming the formation of CeAs and Ce_4As_3 phases within the α-U matrix.

B.4 Experimental Evaluation of U-Zr-As-Nd alloy

Reproduced from section of manuscript published in the journal Nuclear Materials and Energy in January 2021.
"Role of Zr in lanthanides-dopants interactions within uranium-based metallic fuels" *Nucl. Mater. Energy* (2021). https://doi.org/10.1016/j.nme.2021.100912

B.4.1 Experimental results and discussion

To verify the computationally predicted dominant interactions, i.e., between elements in the U-Zr-Nd-X system, we selectively cast and characterize a U-10Zr-2.6As-4Nd (wt.%) alloy, where As was selected as a representative dopant. The SEM analysis of our synthesized U-Zr-Nd-As alloy reveals the formation of precipitates of varying sizes, Figure B.6. The larger precipitates were found to measure ∼10 μm in size, which were surrounded by a finer precipitate dispersion measuring < 2 μm in size. The EDS point analysis and area elemental mapping were both performed in an area showing both types of precipitates, and the results are shown in Figure B.6. Figure B.6 (a) and (b) show a BSE/SEM micrograph of the alloy and precipitate formations, respectively, Figure B.6 (b) also shows the EDS point analysis locations, the results of which are tabulated in Table B.4, and Figure B.6 (c) displays the EDS area elemental mapping results. From the EDS area elemental mapping as shown in Figure B.6 (c), it is observed that the larger (∼10 μm) precipitates contain both Nd and As, whereas the smaller precipitates (< 2 μm) are a dispersion of pure Nd precipitates. The larger precipitates appear to be comprised of a multi-phase structure, where two different contrast regions are seen in the BSE SEM micrograph of Figure B.6 (b). EDS point analysis of the various phases as indicated in Figure B.6 (b) and Table B.4 shows the medium gray contrast regions (pts. 1–3) appear to be a nearly equal mixture of both Nd and As indicating the likely formation of the NdAs phase. Further, the light gray contrast regions (pts. 4–7) appear to be primarily Nd.

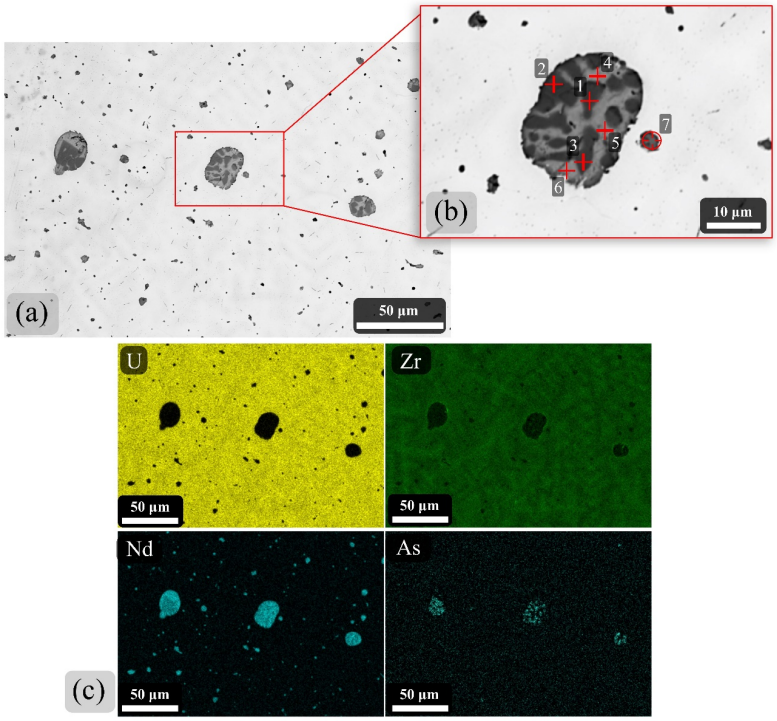

Figure B.6. (a) BSE SEM micrograph of U-10Zr-2.6As-4Nd alloy showing precipitate formation. (b) BSE SEM micrograph of precipitate from section (a) inlay. (c) EDS elemental map of area imaged in section (a).

Table B.4. EDS point analysis results of Figure B-6 (b) in at.%.

Pts	**U**	**Zr**	**Nd**	**As**	**Phase[a]**
1	0	0	55	45	*NdAs*
2	0	0	54	46	*NdAs*
3	0	0	54	46	*NdAs*
4	0	0	96	4	*Nd*
5	0	0	96	4	*Nd*
6	0	0	97	3	*Nd*
7	0	0	97	3	*Nd*

[a]*suggested phase from EDS analysis*

XRD analysis was also performed on the U-Zr-Nd-As alloy, and the results are shown in Figure B.7. The main phase detected is that of the α-U phase, which is typical in U-10Zr (wt.%) alloys. Additionally, both the Nd and NdAs (atomic ratio Nd:As 1:1) were also detected

in the analysis confirming their formation within the alloy. There is also evidence of the formation of the UO_2 phase, which may be the result of some residual oxygen in the original uranium metal used to fabricate the alloy button or may have formed during XRD analysis which is performed in an open-air containment. Additional crystallographic details of the indexed phases from Figure B.7 can be found in the supplemental information section of the journal publication.

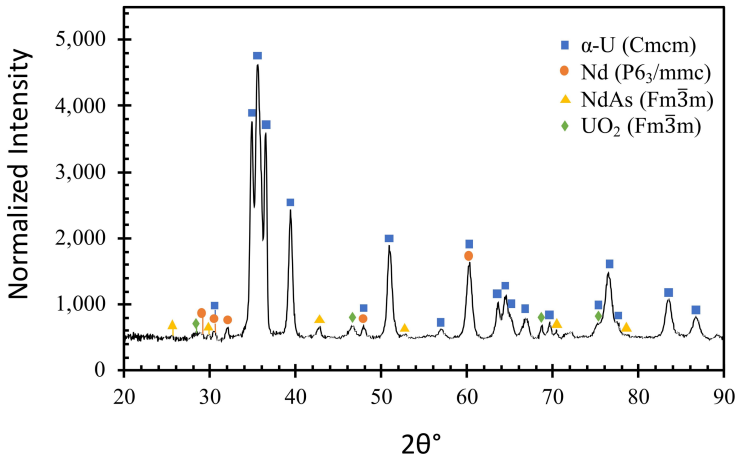

Figure B.7. Plot of XRD data collected on U-10Zr-2.6As-4Nd alloy. Crystallographic details of phases are reported in supplemental information of the journal publication, Table S1.

The presence of pure Nd precipitates and the formation of multi-phase larger precipitates appear to indicate that the cast alloy is dopant poor, and there is not enough As present to combine with the available Nd. The limited As concentration at this analysis location may indicate homogeneity of the alloy was not fully realized during alloy fabrication, and this analysis plane is As-deficient, or As loss during the arc-melting process may have led to the whole alloy being As-deficient. However, it should be noted that all the As appears to be combining with Nd, and there is no evidence of the formation of either a Zr-As phase or U-As phase, which agrees with negligible Zr-As interactions predicted in U-Zr-Nd-As system based on calculations. Further, calculated Nd-As binding energy (-3.23 eV) is significantly stronger than Nd-Zr binding energy (-1.27 eV), resulting in experimentally observed formation of Nd-As phase, as expected from electronic structure calculations. Thus, even in the presence of Zr, Nd-As phase is the most favorable in U-Zr-Nd-As system as predicted by our calculations. It is expected that As may help to mitigate FCCI even in the presence of Zr in U-Zr-based metallic fuel.

Appendix C

List of Journal Publications and Conference Presentations

List of First Author Journal Publications

N.D. Jerred, R. Khanal, M.T. Benson, R.D. Mariani, S. Choudhury, and I. Charit, "Nd, SbNd, and Sb_3Nd_4, and their interactions with the cladding alloy HT9," *Journal of Nuclear Materials*, 541 (2020) 152387.

N. Jerred, R. Khanal, M.T. Benson, E.E. Perez, J.A. King, M. Dubey, J. Burns, I. Charit, S. Choudhury, and Robert D. Mariani, "Evaluation of Tellurium as a Fuel Additive in Neodymium-Containing U-Zr Metallic Fuel," *Scientific Reports* (Nature Publishing Group), 9 (2019) 16403.

List of Co-Author Journal Publications

R. Khanal, N. Ayers, **N. Jerred**, M.T. Benson, R.D. Mariani, I. Charit, and S. Choudhury, "Role of Zr in Lanthanides-Dopants Interactions within Uranium-Based Metallic Fuels," *Nuclear Materials and Energy*, 26 (2021) 100912.

R. Khanal, **N. Jerred**, Michael T. Benson, Y. Xie, R.D. Mariani, I. Charit, and S. Choudhury, "Interactions and Immobilization of Lanthanides with Dopants in Uranium-based Metallic Fuels," *Journal of Nuclear Materials*, 540 (2020) 152372.

R. Khanal, **N. Jerred**, M.T. Benson, D.A. Andersson, R.D. Mariani, I. Charit, and S. Choudhury, "A Novel Approach to Selection of Dopant to Immobilize Neodymium in Uranium-Based Metallic Fuels," *Journal of Nuclear Materials*, 529 (2020) 151922.

M.T. Benson, Y. Xie, J.A. King, K.T. Tolman, R.D. Mariani, I. Charit, J. Zhang, M.P. Short, S. Choudhury, R. Khanal, and **N. Jerred**, "Characterization of U-10Zr-2Sn-2Sb and U-10Zr-2Sn-4Ln to Assess Sn+Sb as a Mixed Additive System to Bind Lanthanides," *Journal of Nuclear Materials*, 510 (2018) 210-218.

List of Conference Presentations as Primary Presenter

N. Jerred, I. Charit, R. Khanal, S. Choudhury, M. Benson, and R. Mariani, "Use of Tellurium and Antimony as Potential Metallic Fuel Dopants in Preventing the Onset of FCCI," Symposium: Research by US-DOE NEUP-Sponsored Students, American Nuclear Society (ANS) Winter Meeting & Expo, Oct. 29 to Nov. 2, 2017, Washington DC (corresponding manuscript published in ANS Transactions).

List of Conference Presentations as Contributing Author

R. Khanal, **N. Jerred**, M. Benson, R. Mariani, I. Charit, and S. Choudhury, "Effect of Dopants on Uranium-Based Metallic Fuels to Mitigate Fuel-Cladding Chemical Interactions," Symposium: Computational Materials Science & Engineering for Nuclear Energy, TMS 2018 Annual Meeting, March 11-15, 2018, Phoenix, AZ.

R. Khanal, **N. Jerred**, I. Charit, M. Benson, R. Mariani, and S. Choudhury, "Design of Alloy Chemistry to Mitigate Fuel-Cladding Chemical Interactions in Uranium-Based Metallic Fuels," Symposium: Materials for Nuclear Applications, Materials Science & Technology Conference 2019, Sep. 29-Oct. 3, 2019, Portland, Oregon, USA.

R. Khanal, **N. Jerred**, M. Benson, R. Mariani, I. Charit, and S. Choudhury, "Effect of Dopants on Uranium-Based Metallic Fuels to Mitigate Fuel-Cladding Chemical Interactions," Symposium: Computational Materials Science & Engineering for Nuclear Energy, TMS 2018 Annual Meeting, March 11-15, 2018, Phoenix, AZ.

R. Khanal, **N. Jerred**, I. Charit, M. Benson, R. Mariani, and S. Choudhury, "Dopant Selection to Immobilize Fission Products in Uranium-Based Metallic Fuel," Symposium: Advanced Nuclear Materials: Design, Development and Deployment, Materials Research Society (MRS) Fall Meeting & Exhibit, Nov. 26 to Dec. 1, 2017, Boston, MA.

N. Ayers, R. Khanal, **N. Jerred**, I. Charit, M. Benson, R. Mariani, and S. Choudhury, "Study of Dopants in U-Zr Metallic Fuels for Limiting Fuel-Cladding-Chemical-Interaction," 2019 Technical Division Undergraduate Student Poster Contest, TMS 2019 Annual Meeting, March 10-14, 2019, San Antonio, TX.

R. Khanal, **N. Jerred**, M. Benson, R. Mariani, I. Charit, S. Choudhury, "The Guiding Principles of the Dopants Selection to Immobilize Lanthanide Fission Products in Uranium Based Metallic Fuels," 2019 Technical Division Young Professional Poster Contest – Structural Materials Division (SMD), TMS 2019 Annual Meeting, March 10-14, 2019, San Antonio, TX.

R. Khanal, **N. Jerred**, I. Charit, M. Benson, R. Mariani, and S. Choudhury, "A Novel Approach of Dopant Selection to Immobilize Lanthanides in Uranium-Based Metallic Fuels," MRS Fall Meeting & Exhibit, Boston, MA, USA, Nov. 25-30, 2018.

R. Khanal, **N. Jerred**, I. Charit, M. Benson, R. Mariani and S. Choudhury, "An Ab-initio Study in Selecting dopants to Arrest Lanthandies within Uranium-Based Metallic Fuels," The Nuclear Materials Conference (NuMat), Seattle, WA, USA, Oct. 14-18, 2018.

N. Ayers, R. Khanal, **N. Jerred**, I. Charit, M. Benson, R. Mariani, S. Choudhury, "Effectiveness of Sn and Sb to mitigate fuel-cladding-chemical-interactions in U-based metallic fuels," The Nuclear Materials Conference (NuMat), Seattle, WA, USA, Oct. 14-18, 2018.